Advance on Non-Destructive Evaluation methodologies for the material characterization and damage monitoring of masonry structures

Shuang Peng

université de BORDEAUX

Thèse présentée pour obtenir le grade de

Docteur de l'Université de Bordeaux

École doctorale des Sciences Physiques et de l'Ingénieur
Spécialité "Mécanique"

par

Shuang PENG

Advance on Non-Destructive Evaluation methodologies for the material characterization and damage monitoring of masonry structures

Sous la direction de

Mehdi Sbartaï

Soutenue le 03 décembre 2020

Membres du jury:

M. Jean Paul BALAYSSAC	Professeur	Université de Toulouse	Rapporteur
M. Emmanuel FERRIER	Professeur	Université Claude Bernard Lyon 1	Rapporteur
M. Vincent GARNIER	Professeur	Université Aix Marseille	Examinateur
M. Takarli MOKHFI	Maître de Conférences	Université de Limoges	Examinateur
M. Mehdi SBARTAÏ	Professeur	Université de Bordeaux	Directeur de thèse
M. Thomas PARENT	Maître de Conférences	Université de Bordeaux	Encadrant

Acknowledgement

Firstly, I would like to express my sincere gratitude to my advisors, Mehdi Sbartaï, Thomas Parent, for the continuous support of my Ph.D study and related research. Mehdi, I am really appreciated for your patience, confidence, optimism, motivation and immense knowledge during these three years. Your guidance helped me in all the time of research and writing of this thesis. Your optimism is particularly impressed for me that will always be a treasure during my whole life. You always have new and interesting ideas to a further discovery. Thomas, thank you for your kindness and patience, also for your support, encouragement and valuable advice whenever I encountered difficulties, particularly in the last year. Without you I couldn't imagine if I can finish my thesis successfully. You had always the brilliant ideas to provide to me. Your immense knowledge helped me a lot to advance my work. The period working with you at this laboratory is unforgettable for me.

Besides my advisors, I would like to thank the rest of my thesis committee: Jean Paul Balayssac and Emmanuel Ferrier for reading my manuscript and giving their comments, as well as Vincent Garnier, Takarli Mokhfi to have accepted to participate in my thesis committee. I would like to express my appreciation for their interest in my research work, as well as for their very encouraging and interesting comments.

Thanks should also go to Jean-luc Coureau, Emmanuel Maurin, Myriam Chaplain, Alain Cointe, Philippe Galimard, Jacqueline Saliba, we have exchanged a lot ideas for my thesis as well as in other aspects. I would also like to extend my deepest gratitude to the atelier team, thanks to Bernard, Philippe Taris, Olivier Lagardere, Sylvain Mateo, Bouchra El Oifi to support my experimental tests, for the design, fabrication as well as setup. Thanks to Jean-Marc Sibaud to solve the computer problem. I would like thank the administrative persons of I2M, Elise Keou, Ophelie Sallat and Isabelle Dusanier for my administrative affaire.

Also thanks to Antoine who have finished his thesis the same year when I came to this laboratory. I am so glad that you are interested in Chinese culture. Thanks To Edouard, thank you for guiding me to visit Bordeaux, and discovery the interesting places in this beautiful city. A good thanks to Marie, you are so cool and thank you for all the efforts you have made to improve the test setup design, to Renau who helped me a lot to deal with my rest things in France. Thanks to my CMI student Lilas, this program is a new experience for me and I really appreciate the work have finished together. Thanks to Nathalie, Seif Eddine for the discussion about our work and our life.

A special thanks to Stéphane Morel for providing brilliant ideas which help me

advance my thesis. Thanks to Vincent from whom I have taken advantage of his experimental tests. I learned a lot each time after discussion with you. Thanks to Cédric, your kindness and humor impressed me, you always have some interesting options for science and also for life. Thanks to Bernard, you have a lot of ideas to make a better experimental test. Each time I struggled with problems, we had the 'brain storm' which offered more possibilities to solve the problem.

I would like to express my deepest appreciation to all the PhD students and post doctorates of I2M GCE, It is an unforgettable memory of staying in such dynamic, friendly and enjoyable group. Finally, I would like also thank to my whole family who have provided me a far but huge support from China. Particularly I would like to express my deepest gratefulness to my husband, Zou it's the best thing of my whole life to have met you.

Contents

List of Figures

List of Tables

Développement d'outils d'évaluation des ouvrages maçonnés - Apport du contrôle non destructif

Résumé : La France est dotée d'un très large patrimoine historique en maçonnerie de pierre. La sauvegarde de ce patrimoine historique constitue un enjeu culturel et économique. Ce type d'édifice, à forte valeur architecturale, limite l'emploi d'essais destructifs. Le besoin exprimé concerne l'absence d'une méthodologie fiable pour l'évaluation des structures à l'échelle du matériau et de la structure. Cette thèse se propose donc de répondre à deux verrous : (i) comment fiabiliser l'Evaluation Non Destructive (END) des matériaux sur ouvrages, (ii) comment mieux détecter, localiser et suivre les défauts dans le matériau au cours de l'endommagement mécanique. Le matériau étudié dans cette thèse se concentre sur la maçonnerie de pierre calcaire appareillée par un mortier de chaux hydraulique.

Premièrement, une campagne de caractérisation non destructive sur des blocs de pierre calcaire est mise en œuvre. Trois types de mesures d'END sont réalisées : électromagnétique aux fréquences radar, les ultrasons, la mesure de la résistivité électrique ainsi qu'une campagne de caractérisation mécanique sur ces mêmes blocs (module de Young et résistance mécanique). De par la dépendance du degré de saturation sur les mesures CND et sur les caractéristiques mécaniques, l'influence du degré de saturation a été étudiée. Les modèles analytiques de mesure de CND en fonction du degré de saturation ont montré des résultats satisfaisant vis-à-vis de résultats expérimentaux.

Deuxièmement, la performance de la méthode d'émission acoustique pour le suivi de l'endommagent a été mise en œuvre sur le matériau maçonnerie à différentes échelles : de l'échelle mésoscopique, c'est-à-dire de l'assemblage pierre-mortier pierre à l'échelle de la structure i.e. mur (échelle 1) en cisaillement. A l'échelle mésoscopique, une série d'essai de cisaillement et traction directe sollicitant l'interface pierre-mortier a permis de discriminer les signaux acoustiques relatifs au mode de rupture par traction directe (mode I) et par cisaillement (mode II). De plus une corrélation entre énergie acoustique et énergie mécanique a été mise en évidence. Enfin, ces résultats ont été validés à l'échelle macroscopique à travers une série d'essais sur mur de pierre appareillée de cisaillement sous chargement vertical constant. Le suivi de déformations par corrélation d'image a notamment permis de valider la capacité de la méthode d'émission acoustique dans le suivi de l'endommagement et de la fissuration d'une structure maçonnée.

Mots-clés : END, ,caractérisation du matériau, suivi d'endommagent, maçonnerie

Advance on Non-Destructive Evaluation techniques for the material characterization and damage monitoring of masonry structures

Abstract: In the context of the preservation of masonry heritage, the structure diagnosis is essential for two main aims: (i) material assessment (ii) damage assessment. The non-destructive techniques (NDT) are privileged for the investigation and the assessment of structure condition, particularly in masonry architectural heritage field. The present work aims to understand the process of material deterioration and to investigate the performance of NDT at the material physico-mechanical characterization and crack monitoring.

The first study addresses the material characterization by different types of non-destructive techniques. As water is considered as a crucial parameter in the material deterioration, the influence of water saturation degree on the physico-mechanical properties of different types of limestone is firstly discussed. Three NDT methods including ultrasound, electrical resistivity and radar are performed to explore the relationship between the non-destructive parameters and the physico-mechanical properties. A good agreement is observed between the ND parameters, porosity, and water saturation. Different analytical modeling of NDT behaviors was also proposed that showed satisfactory results in comparison with experimental tests.

The second study focus on the performance of acoustic emission technique (AET) for the mechanical damage monitoring in the masonry structure. This technique is investigated at multiscale experimental tests from the mesoscopic scale (bloc-mortar-bloc) to the macroscopic scale (shear wall). At the mesoscopic scale, the AET was applied to a series of small-scale laboratory specimens under tensile and shear loading. A mechanical analysis is firstly required to characterize both cracking modes. Different AE indices (hit number and hit energy) are correlated with damage accumulation to identify its response to each loading. AE duration parameter is found distinctive to discriminate signal from different sources. To validate these observations at the macroscopic scale, a series of full-scale test as a shear wall under compression was carried out in parallel with the AET and the digital image correlation (DIC). Comparing with the DIC results, the AET shows a good performance of damage assessment as well as source characterization in masonry at a more complex mechanism of failure.
Keywords: NDT, material characterization, crack monitoring, masonry

---

Unité de recherche
UMR 5295 Université de Bordeaux, 33000 Bordeaux, France.

Introduction

The conservation and restoration of historical monuments is an important topic in terms of culture, history, science and economy. However, some disastrous events such as fire, floods and earthquake have threaten the health of the historic heritage, leading to the material degradation and the structure deterioration. The recent example that cathedral of Notre-Dame which was ravaged by a fire have provoked a worldwide concern in the conservation of culture heritage. More scientific researches have been devoted in the wide range from the damage assessment to the restoration plan in the framework of conservation. Indeed, many aspects have been involved in the conservation and a multidisciplinary approach is required. And the diagnostic is a fundamental phase to evaluate the actual condition of structures for a final decisive conservation plan.

The diagnostic involves a wide range analysis in order to deepen the knowledge of degradation causes and the structural assessment, etc. In the framework of diagnosis, the archive study is firstly required to understand the environment and the history of the building. Some obvious defects, cracks can be observed by the visual inspection. The methods such destructive test, demi-destructive method and non-destructive methods are also applied for the material condition evaluation. And the use of the non-destructive tests is more significant for the diagnostic, particularly in the historical building with a high heritage value. The non-destructive methods can maintain the authenticity and integrity of studied structure. This investigation is designed for two main objectives: (i) the mechanical characterization of material; (ii) the damage characterization. For the former one, the intrinsic properties such as the porosity, the physical property as the degree of saturation and the mechanical properties, the strength and the deformation capacity are also the crucial parameters for the material evaluation. For the latter one, the cracks nature, the location and the damage monitoring are some investigation aspects.

The historical monument were widely constructed in masonry in the past hundred years in France as well as in the whole Europe. In the Bordeaux region (France), the

masonry is usually made of the stone and the mortar. Certainly, different types of stone and mortar can be characterized by the origin, these different stones shows a great variability in the mechanical characteristics. The mortar, due to the different composition, performs as well as a different mechanical behavior. Many studies have been devoted to understand the masonry material and the failure processes and failure mode of masonry structures subjected to different loadings. Due to the complexity of material and the typology of masonry, it is still difficult to model the masonry structure.

This thesis aims to deepen the understanding of the process of material deterioration and to investigate the performance of NDT at the material physico-mechanical characterization and crack monitoring of stone masonry. In order to achieve these objectives, we will firstly present a review of the available literature concerning the mechanics of masonry structure and the non-destructive techniques for the material and damage evaluation. The mechanics of masonry involve the mechanical characterization of masonry components and the mechanical behavior of masonryunder different loadings.

The study in this thesis consists of two main axes. The first one (Chapter 2) focus on the material degradation by moisture and the material evaluation by 3 different non-destructive techniques including Ultrasounic Pulse Velocity, GPR (radar) and the electrical resistivity. The material degradation is discussed from the evolution of physico-mechanical properties of stone at different degrees of saturation. These mechanical characteristics of stone are obtained from a series of mechanical tests at laboratory. Besides, the influence of moisture in the NDT measurement is also investigated from the experimental results and the modeling results.

The second axis of is to investigate the acoustic emission technique (AET) for the damage evaluation from the mescoscale (Chapter 3) and the macroscale (Chapter 4). The chapter 3 focuses on the performance of AET for the damage monitoring to get a further understanding of damage process of small-scale masonry specimen under tensile and shear loading. The monotone and cyclic tensile test offers a deeper understanding of non-linear damage mechanics. The AE parameters are used to be correlated with the damage process. Moreover, the fracture energy and the acoustic emission energy are consulted and compared for the objective of source discrimination. In the shear test, the damage process is also compared with the acoustic emission indices. Besides, three factors influencing the acoustic recording is also discussed.

The last chapter (Chapter 4) concerns a validation test to confirm the capacity of AET of damage monitoring in a shear wall test, in the basis of results in the

chapter 3. The mechanical behavior and the failure mode of shear wall subjected to a horizontal load under a constant stress are firstly presented, consisting of the DIC results as well as AE results. The source discrimination from the AE is also studied at the different damaged areas.

Chapter ends with general conclusions including these two main aspects and some suggestions about the future research are also proposed.

Chapter 1

Literature review

1.1 Introduction

In the context of preservation of historical masonry construction, the experimental investigation for the mechanical assessment of building is indispensable as shown in Fig 1.1. This thesis focuses on the masonry construction assessment by non-destructive techniques (NDT). The understanding of the mechanical behavior of masonry and the investigation of NDT are the two main aspects in our study. In this section, the literature study consists of two parts: (i) the mechanical behavior of masonry at different scales; (ii) the application of non-destructive techniques (NDT) in material characterization and cracking monitoring.

The study of masonry at large scale such as masonry wall consists of two aspects: the masonry morphology and materials characterization. These two elements are the essential factors leading to the different failure modes. Besides, the failure of masonry wall can be conducted by in-plane loading or out-plane loading or the combined two loadings. The failure modes studied in our work focus on the failure under the in-plane loading.

For the morphology, the typology represents the way how the masonry elements are arranged and built. The constitutive materials in themselves are not taken into account. In the masonry structure, according to the Italian code[MIT, 2009], five typologies of stone masonry are characterized and shown in the Fig 1.2:

- Class A: irregular stone masonry, with pebbles, erratic and irregular stone units;
- Class B: uncut stone masonry, with external leaves of limited thickness and

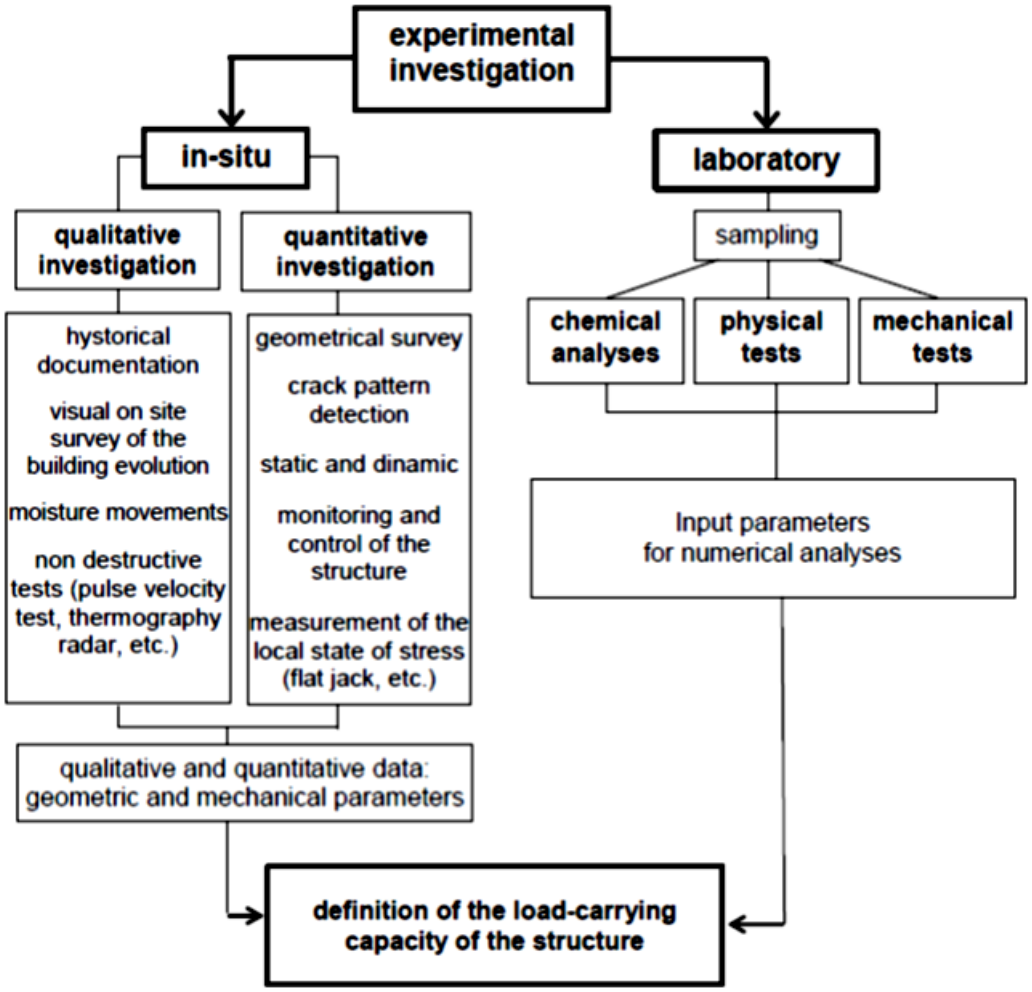

Figure 1.1: Information required and corresponding investigation[Binda et al., 1994]

infill core (three-leaf stone masonry).

- Class C: cut stone masonry with good bond.
- Class D: soft stone regular masonry (built with tuff or sandstone blocks).
- Class E: ashlar masonry, built with sufficiently resistant blocks (i.e. blocks with higher resistance than those of class D). This class was further subdivided into regular squared block masonry with mortar joints (E) and dry-joint ashlar masonry (E1).

In the first part 1.2, the mechanical behavior of masonry elements is studied. Considering masonry is a composite material, the multi-scale study is indispensable from the masonry element scale to the assemblage scale and finally to the masonry structure scale.

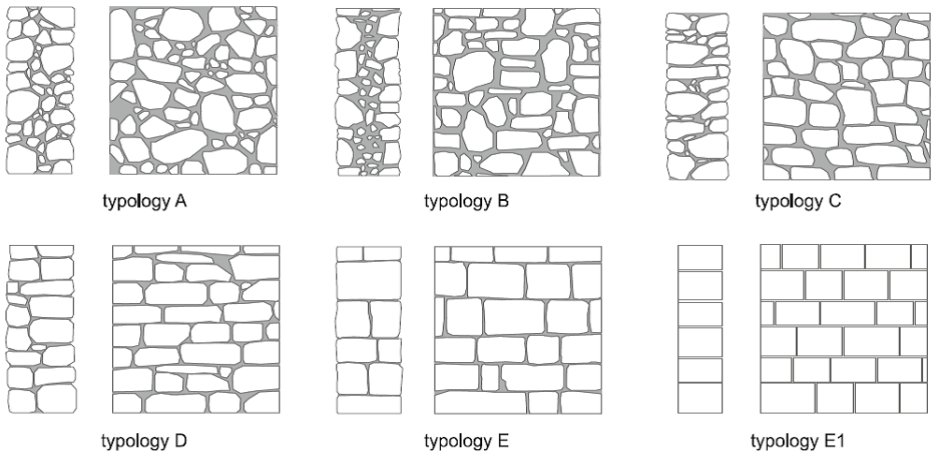

Figure 1.2: Stone masonry typologies: sketches of typical textures and cross-sections

For the study at masonry element scale, the study of the binder material and the bloc are involved to characterize the masonry constitutive elements. Indeed, the binder material is usually a mortar and the blocks are often stone/bricks. Mortars can be characterized by the physical–chemical composition of the binder and aggregates, besides the mineralogical composition of aggregates are also participated influencing the properties. The building stone can be distinguished as the igneous stones, sedimentary stones and metamorphic stones, which are formed in a different way. These type stones are characterized by their appearance and the chemo-mechanical properties.

The masonry elements in our study consist of limestone block and lime mortar. Limestone, as a type of sedimentary stones, is essentially composed of calcium carbonate mineral, $CaCO_3$, as a common type of the sedimentary rocks, it shows a high anisotropy and heterogeneity in the mechanical behavior. The lime mortar is also a composite material which is used to associate the stone blocks, providing a coherence between the blocks and redistributing the stress between the blocks under loading and avoiding block punching.

Firstly, the physic-mechanical properties of limestone and lime mortar are studied (Part 1.2.1). These properties include the porosity, the bulk density, the compressive strength and the modulus of elasticity, etc. Aforementioned, the limestone is a heterogeneous material which shows a great variability in the porosity, also influencing the mechanical characteristics. Besides, as the water is a crucial parameter in the material deterioration, the influence of different degrees of saturation on the stone mechanical properties is also investigated.

It is observed that cracking due to tensile or shear stress is in most case the

major cause of failure. Most of time the bond between the block and mortar is the weakest link [Van der Pluijm, 1997], so that the tensile failure and shear failure are often observed at the block-mortar interface. Thus, these two types of failure modes will be studied in the literature review (Part 1.2.2). Besides, the failure mode of masonry subjected to compressive loading is also presented in the same part.

Furthermore, the acknowledge of failure mode in a structure scale is necessary. Some efforts have been done for decades in the experimental tests and simulation, providing a deeper understanding of ruin mechanisms at a real masonry structure (Part 1.2.3).

Then, in the part 1.3, different non-destructive techniques are investigated. In fact, some techniques were initially performed in other domains such as soil, rock, and other building materials. These studies provided the ability of the non-destructive techniques in the material condition assessment.

The ultrasonic method (Part 1.3.1.1), the electrical method (Part 1.3.1.3), and electromagnetic methods (Part 1.3.1.2) are the methods frequently used in the material characterization, particularly in the water detection. So each method is discussed to understand its performance in the assessment of physico-mechanical properties of limestone.

Several methods can be used in the damage characterization such as damage detection, damage localization, and damage source identification. The acoustics emission technique is will be discussed in part 1.3.2 because it provides the ability in the damage characterization and moreover the damage monitoring in the terms of time in civil engineering.

1.2 Mechanical behavior of masonry

In this section, the review focuses on the mechanical behavior of masonry element in different scale studies. The limestone block is firstly studied to understand the nature and mechanical properties in different degrees of saturation. And then the mechanical behavior of assemblage block-mortar under compressive, tensile loading and shear loading are discussed. Finally, more complex failure mechanisms, observed in shearing wall is presented.

1.2.1 Masonry element

The material characterization on the limestone and lime mortar are firstly introduced. The stone can be usually distinguished by the observation, the mineralogical composition analysis and the geotechnical properties. Lime mortar can be classified, depending on the qualitative determination of the chemical element according to the results of SEM-ENDS analysis[Vanin et al., 2017]. In our study, the geotechnical properties such as the physical properties (density, porosity) and the mechanical properties (modulus of elasticity and strength) are mainly presented.

1.2.1.1 Limestone block

Compression

For all the building material, the mechanical properties in compression is indispensable to be taken into consideration. [Lourenço and Rots, 1994] in his study shows a characteristic stress-displacement response of a quasi-brittle material under uniaxial compressive loading as shown Fig 1.3. A linear phase is firstly observed, indicating an elastic behavior of material. This phase with reversible displacement is characterized by the modulus of elasticity can be deduced. Then, then the micro cracks are progressively formed, corresponding to the convex form in this curve before reaching to the maximal stress. This peak stress is regarded as the compressive strength of material. Beyond the peak stress, the stress decreases meanwhile the displacement increases, indicating a softening behavior due to the formation and propagation of macro cracks.

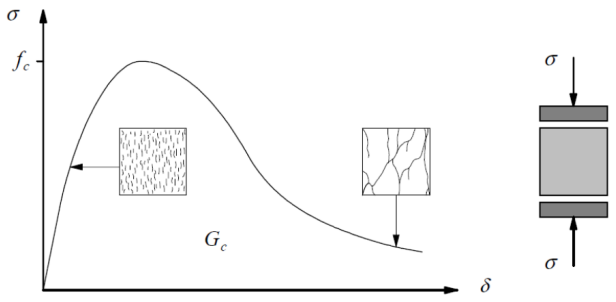

Figure 1.3: Typical behavior of quasi-brittle materials under uniaxial compressive loading[Lourenço and Rots, 1994]

Based on the recommendation of the standards [NF EN 1926, 1999], [NF EN ISO 14580, 2011], a series of compression tests were carried out to measure the elastic properties as the Young's modulus and the compressive strength in the

work of [Bisoffi-Sauve, 2016]. The stone studied in our work shows a similarity in mechanical characteristic as that in the author's work.

In fact, the limestone shows a great variability on the physical observation as well as the mechanical properties. [Mohammed and Mahmood, 2018] collected 184 data on limestone from different quarries to quantify this variability on the physical properties (density and porosity) as well as on the mechanical properties, exhibited in the Tab 1.1. A great variability is observed in all the characteristics, thus the correlation between them is necessary, allowing a basic prediction of the strength of an unmeasured stone.

Table 1.1: Statistical variation of limestone properties from [Mohammed and Mahmood, 2018]

	Statistical parameters	Density (gm/cm3)	Compressive strength σcv (MPa)	Tensile strength σt (MPa)	Compression modulus E (GPa)	Flexural strength σf (MPa)	Porosity n
Limestone	No.of Data	184	184	96	107	21	35
	Range	1.71-2.75	6-250	1.6-25	7.0-70	4-12	0.2-0.7
	Mean (µ)	2.49	68.4	6.5	25.00	8.1	0.38
	Std. Deviation(σ)	0.26	36.6	1.5	11.65	2.30	0.135
	COV(%)	10.4	53.5	23.1	46.6	28.3	35

[Parent et al., 2015] summarized in his work a series of correlations between some principal mechanical properties such as bulk density, compressive strength, static elasticity modulus. These correlations allows a general understanding of characteristic of limestone. In the Fig 1.4, a correlation is presented between the compressive strength of limestone and its bulk density. In fact, this correlation can be also used to predict the compressive strength of a type of stone according to its density.

Impact of porosity on mechanical properties

The porosity is an essential nature characteristic of limestone. Some compression tests have been carried out on the limestone to verify if it can be used in a reconstruction[Pappalardo et al., 2016],[Saba et al., 2019]. Indeed the porosity in the heterogeneous material is formed through non-connected air bubbles, the capillary porosity and also the hydrated porosity[Bennacer et al., 2014]. Two types of porosity are observed: total or absolute porosity and effective or accessible porosity. The former involves all the pores and the latter refers to the pores transferring the fluid. A strict linear correlation is observed between the accessible porosity and the bulk density (i.e. ratio of the grain mass to the specimen volume) in the summarized

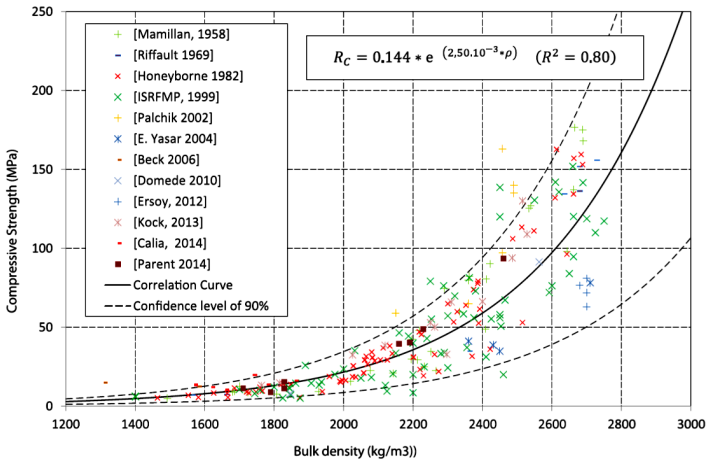

Figure 1.4: Compressive strength vs. bulk density [Parent et al., 2015]

Fig 1.5 [Parent et al., 2015].

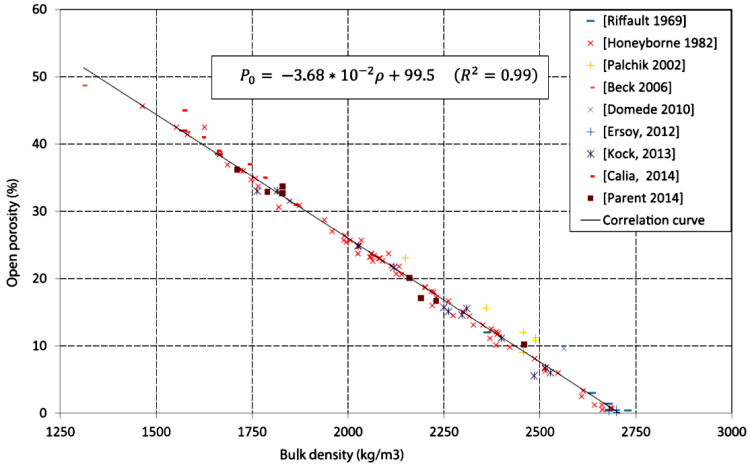

Figure 1.5: Open porosity vs. bulk density[Parent et al., 2015]

In the study of [Pappalardo et al., 2016], the investigation focuses on two types of limestone which are used in the restoration of Baroque buildings. One type stone is a white-cream limestone, namely Palazzolo Stone (PS), the other type is a yellowish limestone, named Noto Stone (NS). Bulk density, water absorption, total and effective porosity were estimated according to [ISRM, 2007] recommendations. The main properties of studied stones are summarized in the Tab 1.2 at a dry state. These two type stones show a similarity in the color and in the real density, however the PS performs better on the compressive strength and deformability, which are related to the microfossiliferous content and the porosity.

The statistical correlation between the selected properties underlies the dependency of mechanical properties as compressive strength and modulus of elasticity on

Table 1.2: Summarized mechanical properties of studies samples

Stone	Real Density (gm/cm3)	Bulk Density (gm/cm3)	Compressive strength UCS (MPa)	compression modulus E (GPa)	Porosity n (%)
PS	2.65	1.89	20.91	4.33	28.6
D-NS	2.56	1.67	9.92	2.57	37.3
B-NS	2.69	1.64	9.54	2.23	38.6

the porosity of stone. In the Fig 1.6, an exponential law illustrates the decrease of the compressive strength with an increasing porosity, the similar tendency is observed in the modulus of elasticity (Fig 1.7). Meanwhile due to the heterogeneity of material and the non-uniform distribution of microfossils, the average value is not always representative, thus he suggested that the extreme value must be taken into consideration for the engineering characterization, in order to avoid either underestimation or overestimation of rock mechanical properties[Pappalardo et al., 2016].

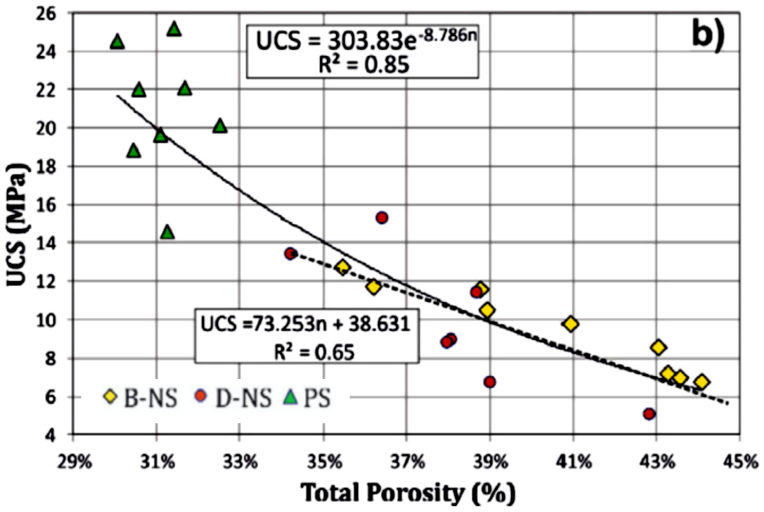

Figure 1.6: Evolution of UCS with porosity[Pappalardo et al., 2016]

The relation between the mechanical properties and porosity have also been studied by other researches on the different types of stone [Beck et al., 2007],[Saba et al., 2019] of which the porosity is not in the same range. These results highlight the significant dependency of mechanical behavior of stone with the porosity and the mineralogical composition of material.

Impact of water saturation on mechanical properties

Another important factor leading the material degradation is water. Many

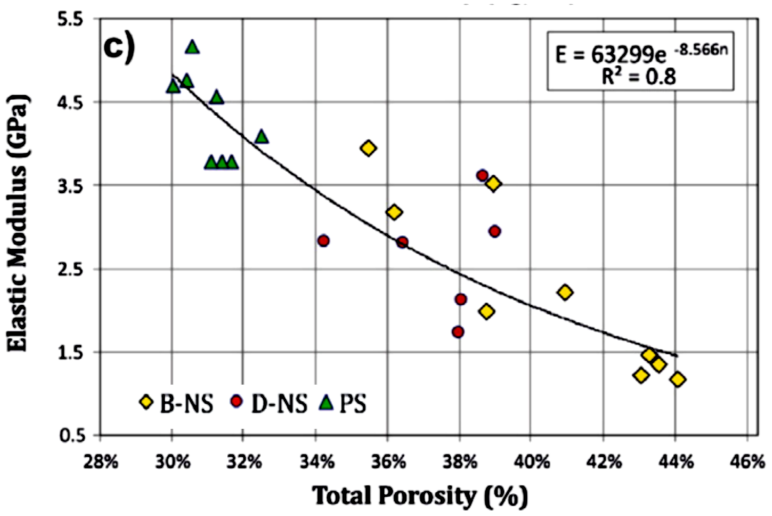

Figure 1.7: Elastic modulus vs. porosity[Pappalardo et al., 2016]

authors have examined the effect of moisture on the strength of various rocks. They found that the degrees of reduction in compressive strength range from 6% to 85% with increasing moisture content[Ojo and Brook, 1990]. The reasons for the material degradation by water content have been discussed from the different points of view as the chemical[Ruedrich et al., 2011] and mechanical explications[Beck et al., 2007],[Khamrat et al., 2016]. Representative examples of mechanism are [Matsushita and Onoue, 2006]: (1) pore water pressure helps separation at the tip of the microcracks because incompressible water gets wedged into the cracks, and (2) the surface energy that forms new microcracks decreases because moisture adheres to the surface of microcracks.

In the research of [Beck, 2006], two types of limestone with a high porosity have been studied. The evolution of compressive strength and modulus of elasticity following the degree of saturation are demonstrated in the Fig 1.8. It is shown that the mechanical strength as well as modulus are greater at the dry state than that at saturated state. Besides more pronounced decrease is observed at the initial presence of water, besides this decrease is no longer evident while the degree of saturation exceeds to a certain value. This phenomenon have also been reported by other researchers on different types of stone [Han et al., 1986],[Rezaei et al., 2019],[Si et al., 2016]

Another relations of mechanical parameters between the saturated and dry were established by [Vasarhelyi, 2003] (Fig 1.9) . The compressive strength and the modulus were obtained from 35 British sandstones from different sites. It showed a linear regression of between the dry and saturated strength and modulus. The decrease of value of mechanical parameters is observed with the presence of water from the

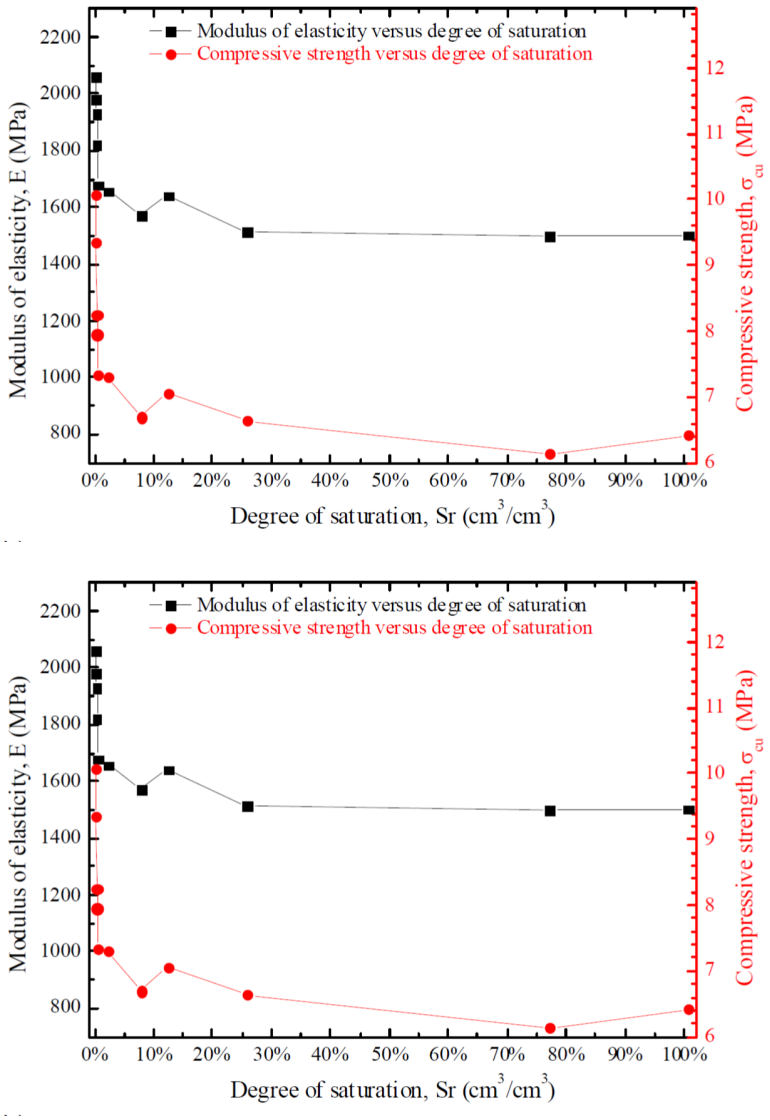

Figure 1.8: Compressive strength/modulus of elasticity vs. degree of saturation for (a) 'White Tuffeau' and (b) 'Sébastopol' stone[Beck et al., 2007]

different samples of sandstone. Besides, he suggested the dry or saturated properties can be estimated if one of these is known.

1.2.1.2 Mortar joints

The mortar is usually composed by aggregate such as sands and the binder (lime, cement), mixed with the water. The hydration process means the hydraulic binder sets by reaction with water, while aggregates participate in the compactness of hardened mortar.

Different types of hydraulic binder are usually used [Venzal et al., 2020], each

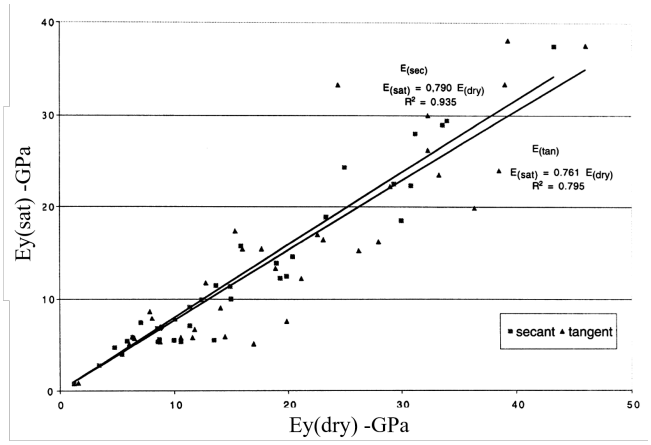

(a)

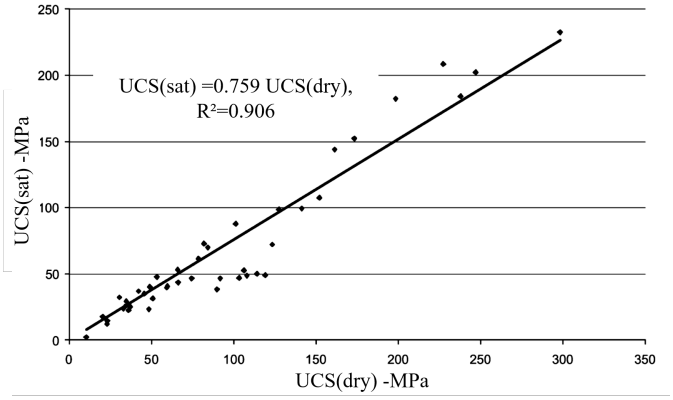

(b)

Figure 1.9: Relationship between the dry and saturated UCS and secant Young's modulus[Vasarhelyi, 2003]

types have its advantages and disadvantages. The cement mortar is the most used in modern building due to its better mechanical properties and shorter hardening time. However, the high rigidity as well as the weak capillarity result in an unsatisfactory adaption for the natural stones and the historic building restoration. Thus the hydraulic lime mortar is chosen for masonry construction built with soft limestone[Popinet et al., 2018].

The size of grains as well as its proportion in a total volume are also important and will influence the mechanical properties of mortar. Indeed, the compressive strength and the modulus of elasticity of mortar decrease with the reduction of grain size[Bisoffi-Sauve, 2016]. Besides the proposition of water is also considered, more extra water will result in increasing the porosity, as the result, the compressive strength of mortar decreases.

Based on the analysis of the type of hydraulic lime, the hardening time [Costigan and Pavía, 2012], the mortar used in our experimental tests is composed by the crushed fin sands (0-2mm), the hydraulic lime (NHL3.5). Taking into account the proposition of mortar used in actual restoration and the tests carried by [Bisoffi-Sauve, 2016] and [Venzal et al., 2020], the composition of the fresh mortar determined in our tests is shown in Tab 1.1. The compressive strength of this type of mortar was determined on 8 samples in their study in Tab 1.1, according to the standard material testing [NF EN 1015-11, 2000].

Table 1.3: Designed mortar mix proportions

Volume (L)	Total weight (g)	Lime NHL3.5(g)	Sand (g)	Water (g)
1	2018.6	233.2	1445.4	340

Table 1.4: Mechanical properties of limestone and lime mortar determined by [Bisoffi-Sauve, 2016]

	Compressive strength UCS (MPa)	compression modulus E (GPa)	Flexural strength σf (MPa)
Limestone	9.5 (26%)	11.1 (15%)	-
NHL mortar	1.9 (14%)	3.95	0.6 (6%)

1.2.2 Assemblage

The masonry consists of stones bonded with mortar, it is indispensable to understand the mechanical behavior of an assemblage and the interface which is most of time the weakest link [Van der Pluijm, 1997]. The compression test on the masonry assemblage will be firstly discussed to understand the mechanical response and failure mode under compression. Besides, [Laurenco et al., 1995] have observed in his work the cracking due to tensile or shear stress is in most case the major cause failure of a masonry structural element. Thus, in this section the tensile failure and shear failure at the block-mortar interface are studied.

1.2.2.1 Mechanical behavior of block-interface under compression

A series of compressive tests were conducted by [Kaushik et al., 2007] on the brick, the mortar and the masonry prism to characterize the mechanical behavior of each

element. The compressive stress-strain curves are summarized as the results of bricks from different manufacture (Fig 1.10 a), the different grade mortar and the masonry prism, respectively. The compressive strength of masonry prism is not greater than that of each element. Indeed, the mechanical behavior and the failure mode is also associated with the state of stress at the block-mortar interface as shown in the Fig 1.10.

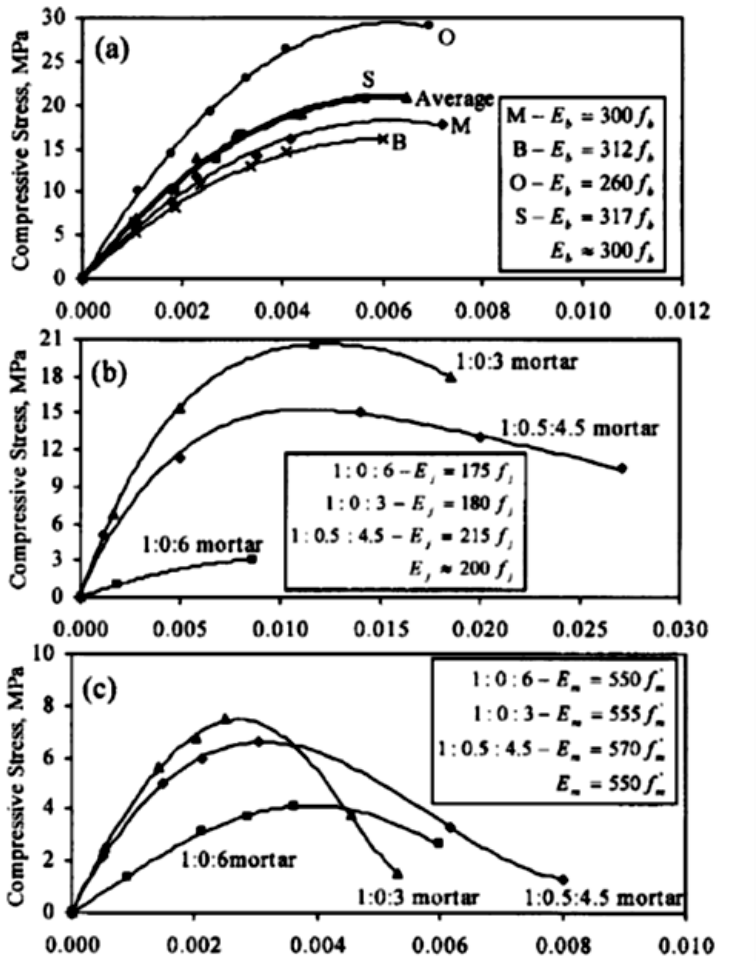

Figure 1.10: Compressive stress-strain curves for: (a) brick units; (b) mortar cubes; and (c) masonry prisms [Kaushik et al., 2007]

Under the compressive loading of masonry prism as illustrated in the Fig 1.11, mortar of bed joint trends to expand laterally than the blocks due to the lower stiffness of mortar. However the adjacent block provides a confining stress on the mortar, impeding the deformation of mortar. The shear stress at the block-mortar interface induces the stress concentration at the block contrarily. This bilateral tension result in a crack in the block due to its weak tensile strength.

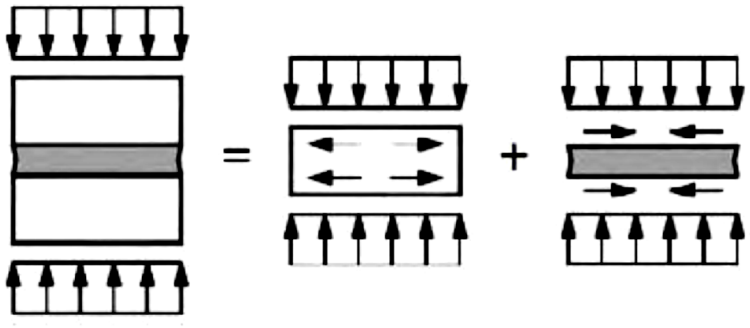

Figure 1.11: Schematic plane representation of stresses in masonry components under compressive loading[Lourenço and Pina-Henriques, 2006]

1.2.2.2 Mechanical behavior of block-interface under tensile loading

Direct tensile test[Bisoffi-Sauve et al., 2019] and indirect tensile test, including three-point bending test as well as Brazilian splitting test are used to characterize the mode I interface mechanical behavior. However, regarding the literature review, direct tensile test seems to be the most appropriate test to characterize the pure failure mechanism (mode I) of quasi-brittle material [van Mier and van Vliet, 2002]. In fact, the technical problems faced in tensile test include the secondary flexure, the gripping problem, the liberated rotation problem[Venzal, 2020] and stabilities of imposed displacement control system at the post-peak behavior, which limit advanced experimental research. Besides Lourenço proposed the preferred location of opening displacement for direct tensile test[Lourenço et al., 2005] in Fig 1.12. The typical stress-displacement response to tensile loading is show in Fig 1.13. [Almeida et al., 2014] conducted a series of direct tensile tests, performed on specimens composed of bricks and mortar, describing the softening branch, which is a typical feature of quasi-brittle material. The results of this study show that the interface fracture energy is only on tenth of brick fracture energy and the bond tensile strength is influenced by material and geometric homogeneity as well as the process of the specimen preparation.

Among the limited literature in tensile test, the research on cyclic tensile test carried on masonry is still needed, and the mechanical behavior remains unclear. In fact, some studies [Li et al., 2018] have been devoted in concrete in cyclic tensile test, showing the envelop curves under cyclic tension are approximately the same as the monotonic curves, and emphasizing the hysteresis phenomena and an empirical relation between the unloading displacement and residual displacement. He also stated that the plastic strain (or residual strain) can be expressed as a function of the unloading strain (Fig 1.14), regardless of stress and the load-strain curve

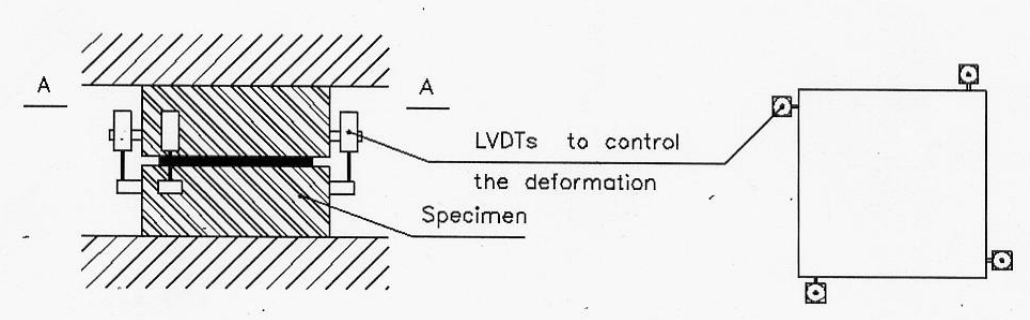

Figure 1.12: Preferred location of LVDTs for direct tensile tests [Lourenço et al., 2005]

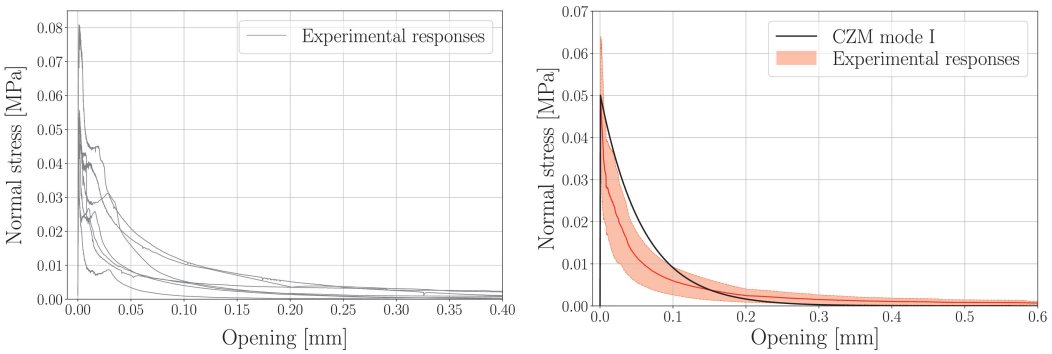

(a) (b)

Figure 1.13: Mechanical response stress-opening displacement in direct tensile test [Venzal, 2020]

form (Fig 1.15). The experience in describing this mechanical behavior of concrete could be used in masonry to discover and explain the fracture behavior under cyclic tension, due to the similar behavior of quasi brittle material.

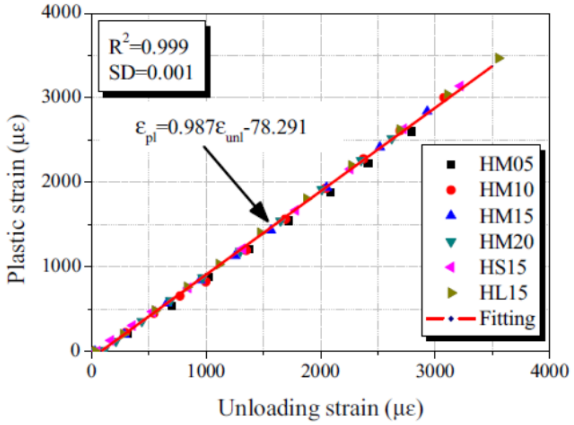

Figure 1.14: Plastic strain versus envelope unloading strain of SFRC for various fiber volume fractions and aspect ratios[Li et al., 2018]

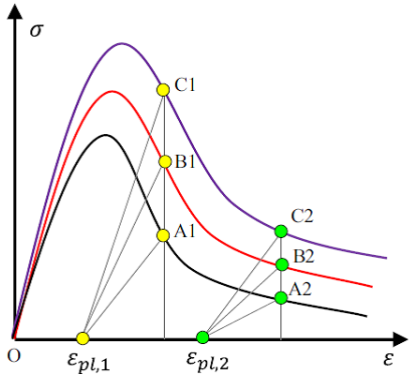

Figure 1.15: Schematic of the stiffness for variable concrete mixture at the same unloading strain[Li et al., 2018]

1.2.2.3 Mechanical behavior of block-mortar interface under shear loading

The shear behavior of block-mortar interface is generally characterized by applying a normal loading to joint. Different test set-ups are summarized in the Fig 3.27(a), according to the standards recommendation [EN 1052-3, 2002]. The reasons for this participated compressive loading are to: (1) make sure of the stabilization of the samples; (2) identify the frictional behavior of interface.

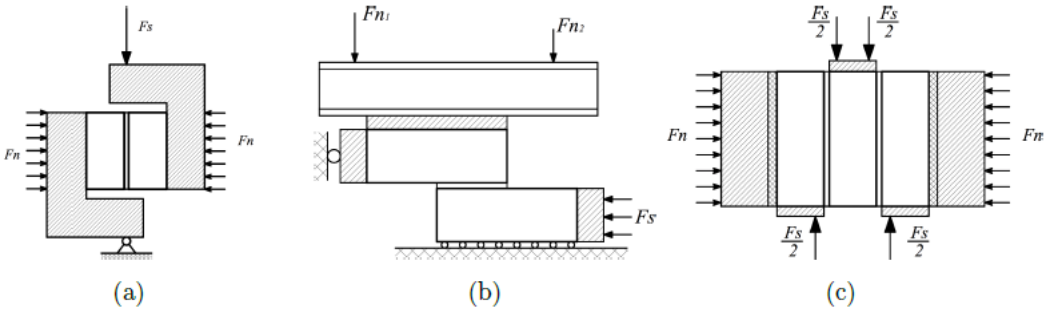

Figure 1.16: Set-up of shear test under compression: (a) proposed by [Pluijm, 1999], (b) test on duo (c) test on triplet[Lourenço and Ramos, 2004]

In the study of Van der Pluijm[Pluijm, 1999], the failure at one joint was characterized under combined loadings. As shown in the Fig 1.17, mechanical response stress-displacement highlights firstly a linear domain before the peak stress. Then the stress reduces gradually to a relative constant stress value, call residual shear strength. This can be explained by the participation of compression stress, resulting in a frictional behavior. It is also observed that more normal compression contributes to a higher shear strength and a higher residual shear strength.

Some similar observations are also found in the tests using the triplet samples by other researchers[Lourenço and Ramos, 2004], [Bisoffi-Sauve, 2016], [Venzal et al., 2020]. The Fig 1.17(b) shows the mechanical behavior of triplet samples under shear and compressive loading[Venzal et al., 2020]. Besides the shear test on triplet is recommended by some standard for the shear strength assessment.

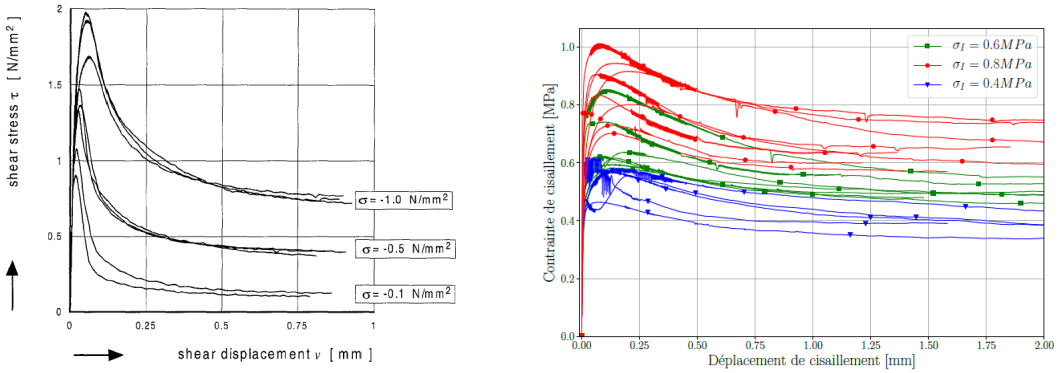

(a) (b)

Figure 1.17: Mechanical response of shear loading under a normal stress from (a) Van der Pluijm[Pluijm, 1999] and (b) Venzal[Venzal et al., 2020]

1.2.3 Mechanical behavior of shear wall

Some studies have been conducted to understand the mechanical behavior of masonry wall panels under different solicitations such as traction, compression and shear loading at a larger scale. In this part, we focus on the shearing wall under compressive load: masonry wall panels with bed joints in horizontal direction is fixed on the bottom, an in-plan horizontal force and a compressive force were applied at the upper side. Some effort have been devoted to discuss the applied boundary conditions, including the way in which the load is introduced and the principle of the test set-up at last several decades[Broekmanweg et al., 2004].

With reference to the boundary conditions, [Lang, 2002] and [Petry and Beyer, 2014] took into account of the coupling effect due to the fact that the walls are joined by the horizontal elements in a masonry building. Indeed three coupling level were distinguished and the bending moment distribution are demonstrated in the Fig 1.18 respectively: (1) weak coupling where the wall can be regarded as interacting cantilever walls, the shear stress and the moment is not transferred by horizontal elements;(2)intermediate coupling, where the transferred moments are limited(3) strong coupling where the wall is considered as coupling

wall, the overturning moment is changed due to the shear force transmit by the horizontal element (spandrels).

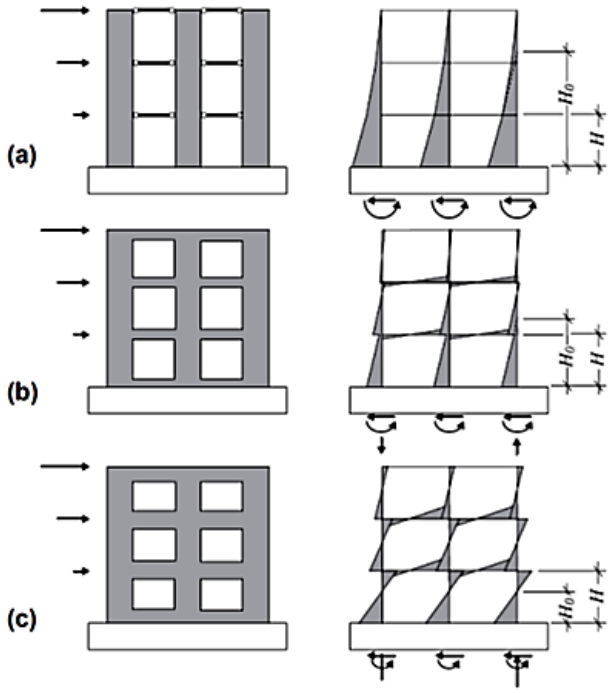

Figure 1.18: Moment profiles of masonry wall structures with (a) weak coupling, (b) intermediate coupling and (c) strong coupling, taken from [Lang, 2002],[Petry and Beyer, 2014].

Different experimental set-up of the shear wall have been carried out to reveal the mechanical behavior of a shearing wall subjected to different boundary conditions. The Fig 1.19 offers an example of a test set-up of a quasi-static cyclic shear-compression tests on six plastered single-leaf stone masonry walls[Godio et al., 2019]. By varying the axial load ratio on the tested wall, the stiffness as well as the force capacity were investigated. He has underlined the increase of stiffness with an increasing load ratio.

Besides, some other experimental test didn't take into account the coupling effect and another example of this type test is demonstrated in the Fig 1.20. It shows the test set-up, a constant normal stress distributed uniformly via a steel roller bearings was applied at the top of the wall.

When subjected to compressive and shear loading, four failure mechanisms can be observed according to the horizontal load level as shown in the Fig 1.21[Oliveira et al., 2007]. Rocking occurs at a heavy solicitation while the compressive stress is below the compressive strength. The propagation of horizontal crack at the bottom provoked by traction is observed, the rest wall remains nearly

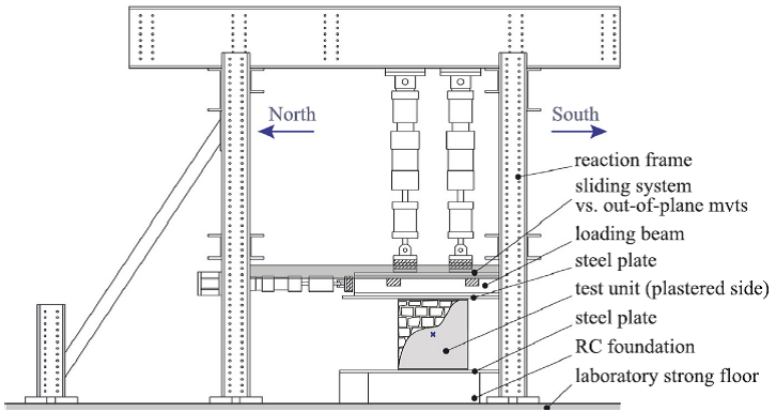

Figure 1.19: Test setup used for the tests at the École Polythecnique Fédérale de Lausanne (EPFL): illustrative sketch, front view on the plaster side.[Godio et al., 2019]

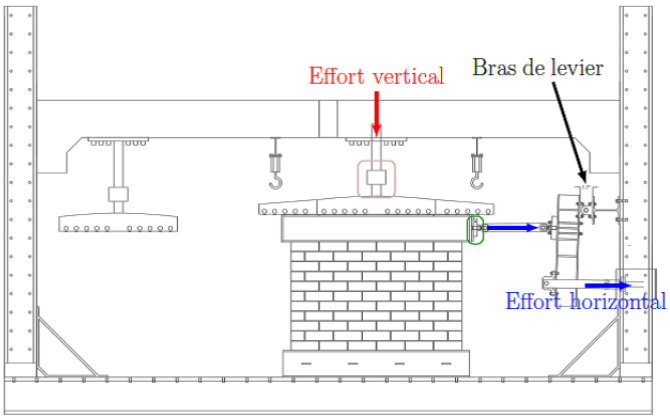

FIGURE 4.4 – Schéma du protocole expérimental d'essai

Figure 1.20: Test setup proposed by [Venzal, 2020] for a shearing wall under compression

a rigid body rotating about the toe Fig 1.21a). Toe crushing failure (Fig 1.21b) is resulted from compressive failure at the area of toe where the compressive strength is exceeded. While the solicitation is relatively less important, the sliding occurs at the cracked interface of block-mortar (Fig 1.21c). And the diagonal cracking (Fig 1.21d) is usually formed at the center of wall and develops towards to the corners with the increasing loading. In this case, the vertical joint suffers traction while the horizontal joint is subjected to shear loading.

Besides, [Vanin et al., 2017] has summarized 123 quasi-static static shear-compression reported in the literature in order to estimate the stiffness and strength of different types of stone masonry. A statistical analysis was carried out to find the

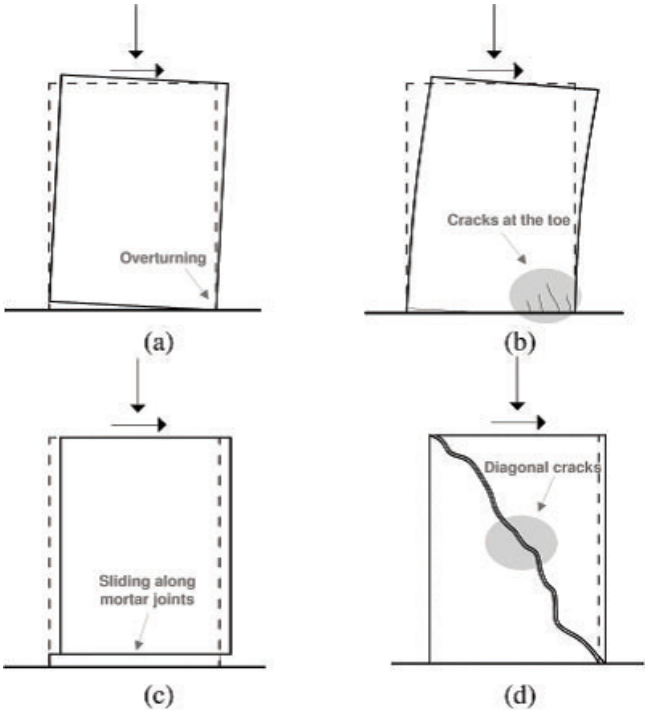

Figure 1.21: Typical failure mechanisms of masonry piers: (a) rocking; (b) toe crushing; (c) sliding; (d) diagonal cracking.[Oliveira et al., 2007]

median value and coefficient of variation of studied parameters from the different masonry typology as shown in Fig 1.2 and failure mode.

He concluded that most of the masonry typologies that were tested had a compressive strength less than 5 MPa while few tests of dry stone masonry had a strength larger than 50 MPa; note that the latter value was obtained from tests on masonry prisms rather than masonry walls or wallettes.

Consisted with the literature data provided by [Lourenço and Rots, 1997] and by [Macorini and Izzuddin, 2011], [D'Altri et al., 2018] summarized the experimental and numerical mechanical response of shearing walls subjected to different compressive loading level Pv in the Fig 1.22. He underlined a good agreement between experimental and numerical results which can be observed up to collapse, including initial stiffness, maximum capacity and the post-peak response of the panels.

In the basis of experimental results, the mechanical characterization of masonry element and the mechanical behavior of masonry subjected to different solicitations are presented in this part. On the other hand, the material properties can be also characterized by the non- destructive tests which will be presented in the following part.

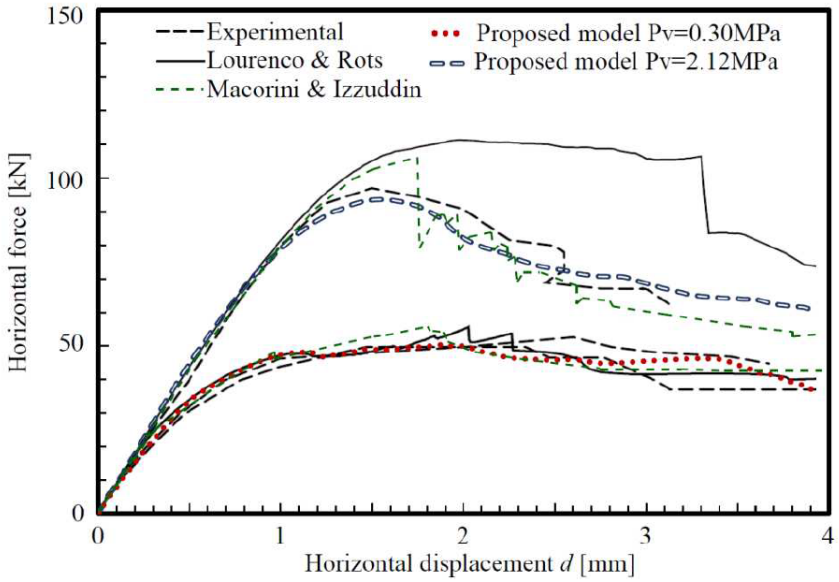

Figure 1.22: Experimental – numerical comparisons of the load – displacement curves for the masonry wall panels loaded in plane[D'Altri et al., 2018]

1.3 Methodology of masonry auscultation

For a better conservation of masonry construction, the auscultation of structure actual condition is necessary in short and long terms. The methodology of auscultation consists of visual inspection, instrumentation, the not destructive evaluation and destructive evaluation. The material characterization of masonry is an essential step for the building condition assessment. Thus the properties measurement of a large number of samples are required for a representative characterization in stonework. However the destructive tests are limited on the samples as a conflict to the necessary requirement of historical building preservation. Alternately, the not destructive techniques are widely used for recent years in the material condition assessment, particularly in the historic building. Thus, in this part, some not destructive techniques will be discussed in two fields: (1) mechanical characterization, (2) damage monitoring. For the former objective, we are interested in how the NDT performs in the characterization of physico-mechanical properties of limestone such as porosity, modulus of elasticity, and compressive strength as well as the water content. For the latter one, the studies of the acoustic emission technique (AET) for damage monitoring are presented. In order to get a better understanding of each NDT, more interest is paid on the laboratory and is-situ NDT assessment.

1.3.1 Material characterization by Non-destructive techniques (NDT)

1.3.1.1 Ultrasound

The ultrasonic method, as a non-destructive method have been used for material characterization, due to its repetitive and reproductive manner. Some studied have been devoted at the last decades to discover the relation between the ultrasonic parameter with physico-mechanical properties such as porosity(ϕ), water transport and storage capacity, uniaxial compressive strength(Rc) as well as static and dynamic moduli of elasticity (Estatic, Edym). The most common parameter used in ultrasound method is the ultrasonic pulse velocity (UPV). And UPV can be measured in different type of test: direct, semi direct, indirect and reflection modes (Fig 1.23). In direct mode, emitting and receiving transducers are placed on opposite surfaces of the tested element. In the semidirect method, transducers are located at 90° angle, and in the indirect (surface) mode, transmitter and receiver are arranged on the same surface of tested element[Aydin, 2014]. In each type of test, different types of wave are involved, including compressive wave, shear wave, surface wave.

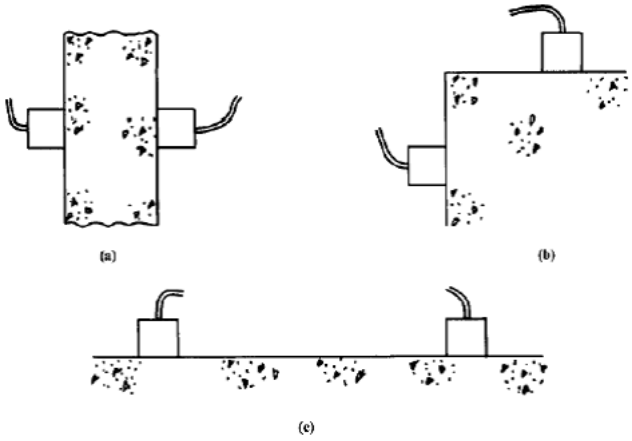

Figure 1.23: Types of ultrasonic method configuration (a) direct, (b) semi-indirect et (c) indirect[Bungey et al., 2006]

The measurement of ultrasonic compressive velocity in the direct transmission mode is mostly performed at laboratory for the primary understanding of characteristics of studied material. The velocity is calculated as the following Eq 1.1.

$$V = \frac{D}{t} \tag{1.1}$$

Where D is the distance between the tested points and the t is the travel time

of p-wave between these two points corresponding to the position of the transmitter and receiver. [Parent et al., 2015] have summarized the correlation between the compressive and the ultrasonic velocity of a wide range of limestones with the variance with a confidence level of 90%. These data were extracted from 12 references. It can be observed from the Fig 1.24, the ultrasonic velocity is generally higher in the stone with greater strength. Moreover, some experimental and theoretical studies are dedicated addressing the relationship of the velocity-saturation in sandstones[El-Husseiny et al., 2019].

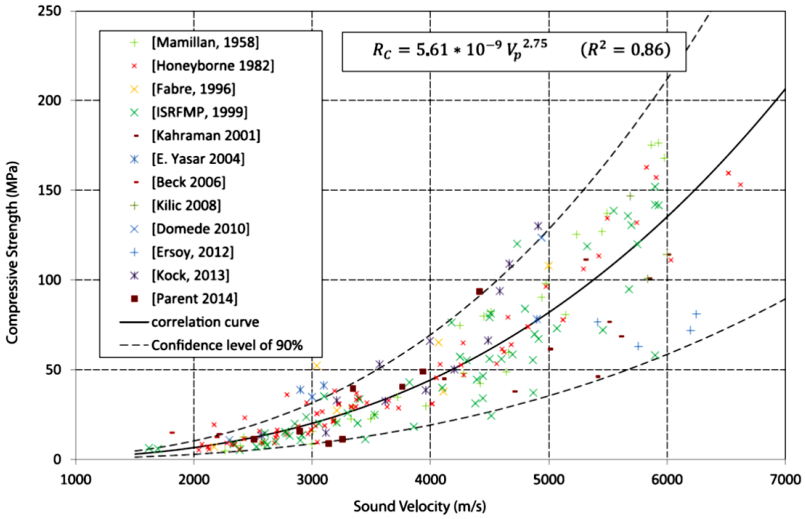

Figure 1.24: Compressive strength vs. sound velocity[Parent et al., 2015]

Beck in his study[Beck, 2006] illustrated the evolution of ultrasonic velocity of compressive in different degrees of saturation for two high porous limestone (48% for white tuffeau stone and 42% for 'Sébastopol' stone) in Fig 1.25. The curves in these two stones present a nonlinear evolution. The velocity in dry state is a litter higher than that in full-saturated stage, a 'convex' form is observed at the partially saturated state. Regardless of the velocity value, it can be seen that lowest value of velocity is at about 75% of degree of saturation in these two stones.

in the study of [Si et al., 2016], the measurement of velocity was performed on seven sandstone samples. The relationship of water saturation degree and its related velocity is presented in three typical samples. These samples represent the different porosity of stone, including high, medium and low porosity. He observed that for a sample of high porosity ($\Phi = 29.1\%$) (Fig 1.26(a)), P-wave velocity was almost unchanged when the water saturation changed from 0 to nearly 80%. With further increase of water saturation P-wave velocity began to increase significantly until the sample was fully water-saturated. Fig 1.26(b) showed the velocity curves of a sample with medium porosity ($\Phi = 15.0\%$), P-wave velocity increased near-linearly

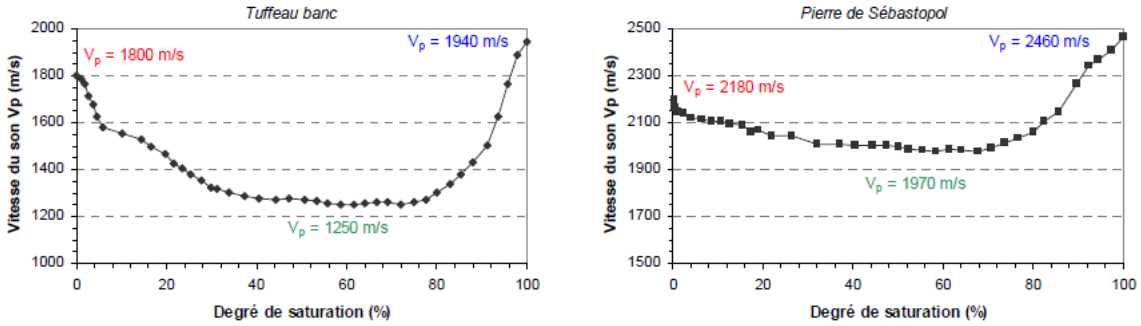

(a): tuffeau blanc (b) : pierre de Sébastopol

Figure 1.25: Evolution of ultrasound velocity (P-wave) following the degree of saturation pour White Tuffeau /' Sébastopol' stone (perpendicular to bedding)[Beck, 2006]

with water saturation changing from 0 to nearly 50%, after which a dramatic increase can be observed. For a sample with low porosity ($\Phi = 8.1\%$). P-wave velocity increased near-linearly with water saturation during all saturation process. He also compared the experimental results with different models (Gassmann-Wood (G-W) and Gassmann-Hill (G-H) boundaries and Gassmann-Brie (G-B) trends with different e-coefficients). The overall results showed P-wave velocity trend with saturation was closely related to porosity.

1.3.1.2 Radar

Grand Penetration Radar (GPR) is also a non-destructive technique which is wildly used in civil engineering. This technique was initially applied in the geophysical investigation[Neyrat, 2009], and nowadays has been used in different domains[Daniels, 2004]. This application is used in masonry assessment[Binda et al., 1998],[Orr et al., 2019] and healthy monitoring[Alani et al., 2020],[Orr et al., 2020] in masonry construction.

The design for repair and strengthening of historic masonry structures is based on this diagnosis [Binda et al., 1998]. Thus this technique was also applied in masonry for the diagnosis of the state of damage, including detection of voids or inclusion of different materials, and material characterization such as the level of moisture.

The general principle of radar have been reported by many authors[Sbartaï et al., 2006]. It is based on the propagation of electromagnetic wave, more common studies have focused on reflectometric interpretation. The common method used in Radar is shown in Fig 1.27, an electromagnetic pulse

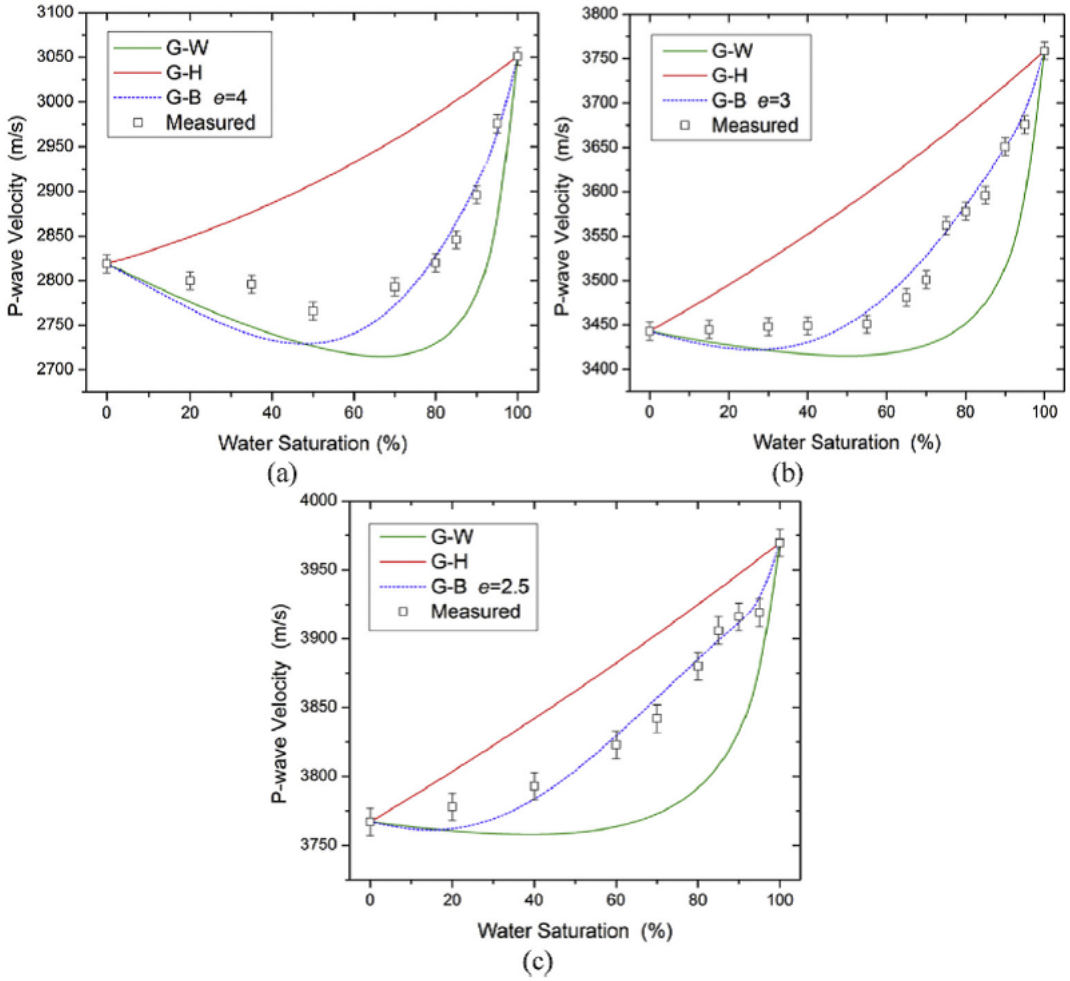

Figure 1.26: Comparison of theoretical and measured P-wave velocity trends (a: sample 6-2, Φ= 29.1%, b: sample 6-5, Φ= 15.0%, b: sample 6-7, Φ=8.1%) [Si et al., 2016]

is emitted from the transmitter antenna, and another receiver antenna records the reflection wave through the surface of tested material. The parameter as velocity, amplitude as well as dielectric constant are commonly studied for the different objectives.

The dielectric constant is an intrinsic parameter which cannot be obtain directly, The velocity with which the electromagnetic wave travels through a substance depends on the dielectric constant and is calculated as shown below:

$$V = \frac{c}{\sqrt{e_r}} \tag{1.2}$$

Where C is the speed of light and V is the velocity of the wave though the material with relative dielectric constant e_r.

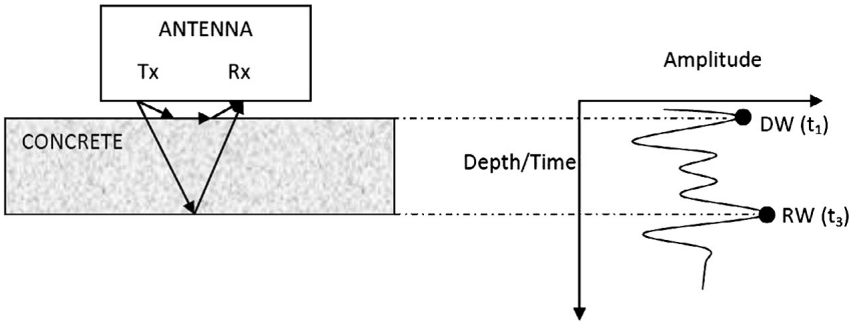

Figure 1.27: Identification of direct and reflected waves from the GPR scan on concrete.[Senin and Hamid, 2016]

Many tests have proved the radar wave is sensitive to moisture condition of material. Binda have carried out a test in situ to find the presence of moisture in a stone masonry wall. The transmitter and receiver antenna were positioned at two opposite sides of wall, the direct wave was then studied. The Fig 1.28 illustrated the time delay and amplitude reduction in a single recorded at the bottom of a wall at wet state compared to dry state. And the velocity of dry area was 13 $cm.s^{-1}$, while that of wet area was 11 $cm.s^{-1}$.

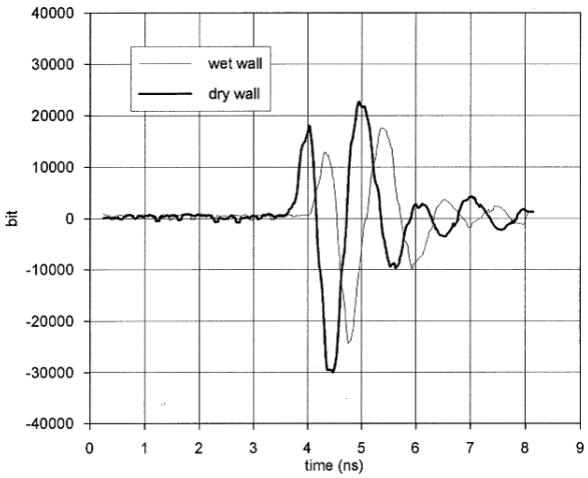

Figure 1.28: Signals recorded at ICITE full-scale models in a wet and dry part of the wall[Binda et al., 1998]

[Cardani et al., 2013] in his study showed a relation between the radar velocity and the moisture degree of stone in a masonry building as shown in Fig 1.29. The moisture degrees were obtained by the powder drilling test. The points consist of the different tested material: sand stone masonry panel and brick masonry panels with or without treatment. The velocity decreased with the increasing moisture by overall of tested points.

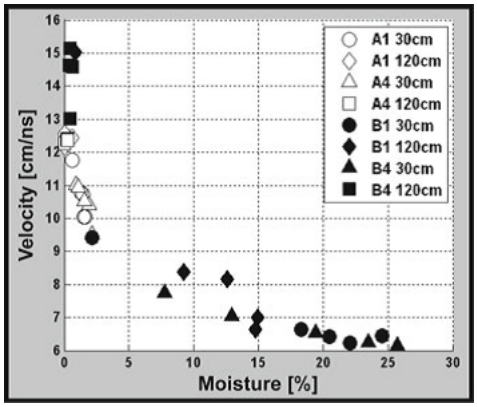

Figure 1.29: Radar velocity vs. moisture from the powder drilling method[Cardani et al., 2013]

Many experimental tests have been carried out to find the empirical relationship between the moisture and velocity or dielectric constant in concrete[Laurens et al., 2005],[Sbartaï et al., 2006],[Senin and Hamid, 2016]. However more experimental research is needed in the masonry.

Some empirical equations were developed to underline the relationship between the dielectric permittivity with the water content or degree of saturation, these empirical correlations were established for different type of material, such the soil, concrete, the stone, etc. on the other hand, different models were also proposed by researchers[Anbazhagan et al., 2020],[Laurens et al., 2005] to simulate the bulk permittivity of a studied sample, by using the permittivity of mixture components. The recommended permittivity of material is summarized in the Fig 1.30.

In fact, in the ND parameters, both empirical correlation and models are commonly used in the prediction of water content of degree of saturation by the inversion method. However compared with the empirical correlation, the models is more frequently used due to its advantages: (1) the model equation is based on the theoretical analysis and it offers a better understanding by a physical explanation (2) the physical parameter or coefficient can be obtain from experiment data or a commended value table as in the Fig 1.30 . This provide a possible to get the appropriate coefficient of each material or texture component.

As the radar parameters are usually used to be lined with the liquid solution of porous material, which also lacks the relationship between the radar parameter with the mechanical parameters.

Material	Dielectric permittivity
Vacuum	1
Air	1.0005
Fresh water	$78.54 \times (1 - 4.579 \times 10^{-3}(T - 25))$
Fresh water ice	3.2
Quartz	4–6
Concrete dry	4–10
Sand Dry	2–6
Sandstone dry	2–5
Soil Dry Clay	4–10
Granite Dry	5
Limestone dry	7

Figure 1.30: Dielectric permittivity of materials at 100 MHz from [Daniels, 2004].

1.3.1.3 Resistivity

The electrical resistivity was firstly used in geology for petroleum reservoirs researching, and nowadays this technique is more widely used in soil science[Samouëlian et al., 2005], rock science[Griffiths, 1976],[Hassine et al., 2018] and other materials[Li et al., 2012],[Nguyen, 2014]. These researches prove that the electrical resistivity is sensitive to the physical and chemical change particularly to the water transfer in porous materials. Different methods have been used to determine the electrical resistivity of material such as by applying two plate electrodes[Lataste et al., 2018], a multi-ring resistivity cell[du Plooy et al., 2013], the Wenner probe[Sbartaï et al., 2007], etc[Nilsson, 2018]. It is a parameter characterizing the ability for a material to impede the flow of electrical current.

The two-plate electrodes technique is often used for the laboratory resistivity assessment[Weydert and Gehlen, 1999]. This technique is to circuit a current between the two probes on the two faces of tested materiel. Thus the resistivity obtain can be considered representative of the average material's property. Based on the Ohm's laws and the geometry of tested sample, the electrical resistivity is calculated as the following equation:

$$\rho = \frac{R \cdot S}{L} with R = \frac{\Delta V}{I} \tag{1.3}$$

Where ρ (Ω.m) is electrical resistivity, the resistance R (Ω) is derived from the protein drop Δ V(V) by applying a current (A), S (m^2) refers to the cross-sectional area and L is the length of the tested sample as shown in Fig 1.31.

In building materials (stone, concrete, wood) the electrical conduction

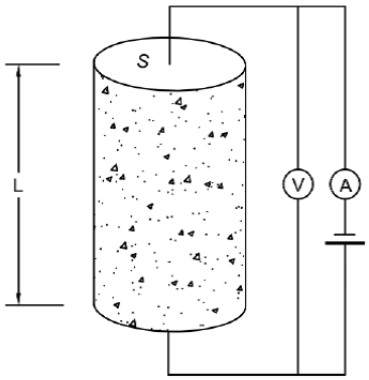

Figure 1.31: Illustration of principle of resistivity measurement[Nguyen, 2014]

is essentially an electrolytical phenomenon, linked to the fluid phase in porosity[Nilsson, 2018]. Many studies have been carried out on the relation between the resistivity and the porosity as well as water content. Note that the porosity discussed here is open porosity (effective porosity). An empirical correlation between the resistivity and porosity was firstly proposed by [Archie, 1942], based on the measurement of sandstones. And then this relation was modified, taking consideration of the pore containing fluid such as water, oil, etc. Some efforts have also been devoted to modify this Eq 1.4 to fit better the experimental results[Li et al., 2016].

$$\rho = a\Phi^{-m}\rho_f S^{-N} \tag{1.4}$$

In this equation, ρ_f is the resistivity of pore fluid, Φ is the porosity of material and S is the saturation degree, for a given material, a, m and n was fixed and in a range as shown in Fig 1.32. For most geological units, a=1, n=1 and m=2 are commonly used.

	a	*m*	*n*
Shape factor on rocks	Function of lithology	Function of cementation	–
On rocks (Telford *et al.*, 1990)	Increase when porosity decreases 0.6 to 2	Increase with pore tortuosity 1.3 to 2.2	~2
On concrete (Naar, 2006)	0.1 to 0.8	2 to 7	1 to 2.4

Figure 1.32: Archie's law parameters[Lataste, 2010]

In fact, this method have been used in water infiltration or salinity assessment

into the soil[Rhoades et al., 1999],[Samouëlian et al., 2005]. Recently this method have been applied in the concrete[Nguyen et al., 2017],[Sbartaï et al., 2007]. However limited study have been used to monitor water content in rocks. One case is found in Sass's research[Sass and Viles, 2010], the resistivity method has also been used in masonry for the moisture determination on the historic stonework, in his study, a calibration curve was established using several cuboid specimen of different limestones and dolomites from Alps mountain[Sass, 1998].

$$w = 7.11\rho^{-1} + 0.0021 \tag{1.5}$$

Where w is the gravimetric water content in % and ρ is the bulk resistivity in Ω.m.

This Eq 1.5 is consistent with Archie's law in case of simplifying assumptions. Besides, he compared this measurement calibration with the theoretical curve from Archie's law. He found a better accordance between them at a higher water content. In the Fig 1.33, a decrease of resistivity is observed with an increase water.

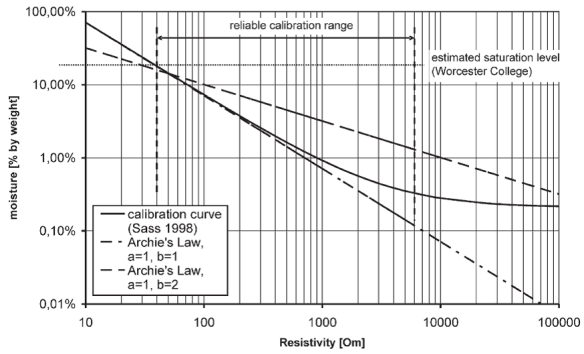

Figure 1.33: Moisture–resistivity conversion curve for limestones[Sass, 1998], together with theoretical curves based on Archie's Law[Sass and Viles, 2010]

The relationship between resistivity and degree of saturation related to different porosity have been also studied by many authors[Lataste and Göller, 2018],[Nguyen, 2014]. However these studies focus on the soil [Bai et al., 2013],[G. et al., 2002],[Kazmi et al., 2016] or concrete (Fig 1.34). These relations highlight a great loss of resistivity with an increasing saturation degree. And the decrease of porosity enhances the connectivity of pore fluid and soil particles, which results in increasing electric current path and, consequently, resistivity decreases.

Besides, the most common model to predict the resistivity parameter of unsaturated material is based on the Archie equation. Some modifications have also

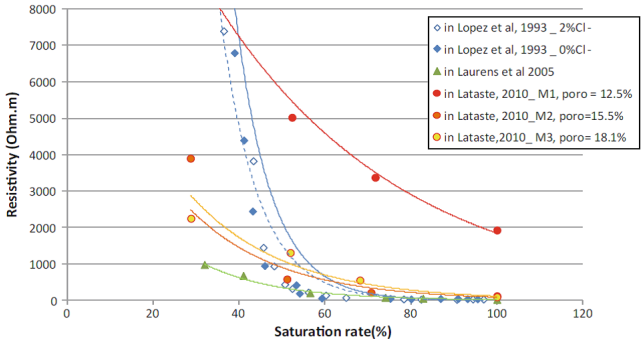

Figure 1.34: Saturation rate versus electrical resistivity[Lataste and Göller, 2018]

been taken into account for adapting to each etude case[Li et al., 2016]. The error analysis is also an important technique to assess the reliability of suggested model, by comparing with the experimental data. In the basis of study of the resistivity technique, the electrical resistivity of liquid phase is lower several orders than the solid and gas phase, thus this technique is often applied to assess the unsaturated porous material such as the porosity, the liquid content, etc. However limited studies focused on the relationship between the resistivity parameters and the mechanical parameters. This relation will be studied in the following analysis.

1.3.2 Damage characterization by acoustic emission technique (AET)

Several non-destructive techniques can be use for the damage characterization, such as the method of ultrasound. The choice of the method corresponds to the demand and the objective. In our study, the acoustic emission technique is studied as a passive method which perfomence well on the damage monitoring.

Acoustic Emission technique, is one of the useful and cost-efficiently method for investigating and monitoring the local damage and localization in civil engineering structure. When a material is damaged, energy is released and delivered in form of an elastic wave, this specific impulsion can be recorded by sensors as acoustic signal, namely hit. Some parameters referring to the hit-based features, can be extracted or deduced from the waveform, in time or frequency domain such as amplitude, energy, frequency (AF), ... etc. for the damage assessment.

1.3.2.1 Monitoring of damage evolution

The basic acoustic emission (AE) counting, considering the cumulative or averaged number of AE hits or AE energy, proves the capacity of AET for damage assessment in masonry[De Santis and Tomor, 2013],[Ghiassi et al., 2014],[Tomor and Verstrynge, 2013]. In this context, [De Santis and Tomor, 2013] conducted an experimental research on prism of masonry under compression, identifying the stage of fracture development process by amplitude(Fig 1.35). It is generally observed that micro-cracks generate a large amount of low amplitude emission, while less emission with great amplitude are related to macro crack.

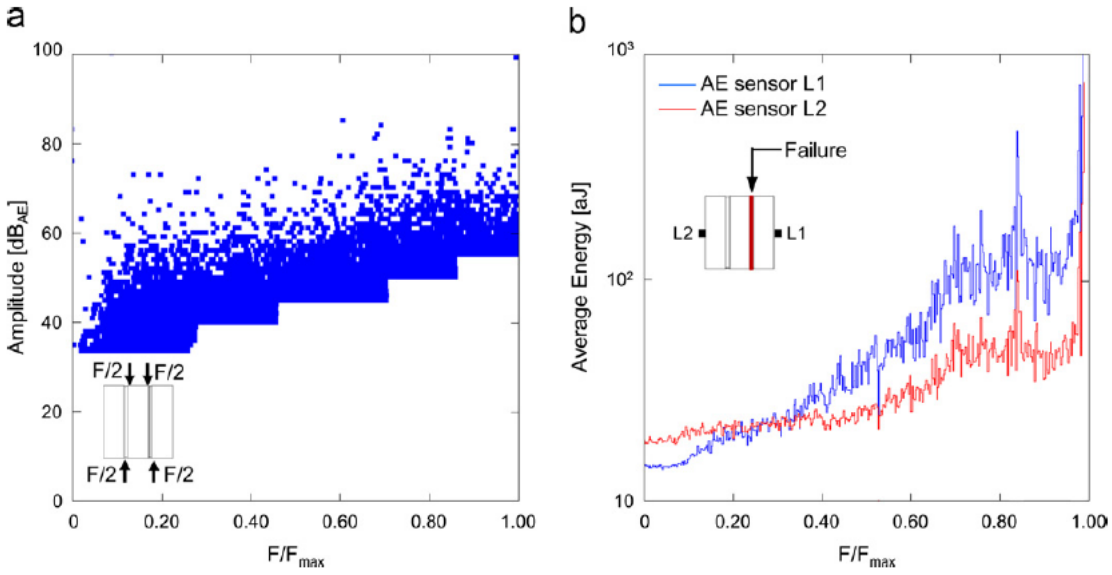

Figure 1.35: AE recording during quasi-static shear of a triplet: amplitude vs. load (a) and average energy vs. load (b).[De Santis and Tomor, 2013]

Besides, some studies focused on the AE energy which is highly correlated with debonding phenomena on strengthen bricks. For this type of composite material, the debonding phases in FRP-strengthened masonry were characterized by AET in the study of [Ghiassi et al., 2014](Fig 1.36). He found that at the stage of micro crack formation, the AE energy is relatively smaller and the rate of AE energy is lower than the rate of hit number. Besides the sudden jump of energy can be related to the formation of macro crack formation. At the moment of full debonding, a huge release of energy is observed. In the basis of these observations, the micro and macro cracks due to the debonding phenomena can be characterized by the AE hits and energy.

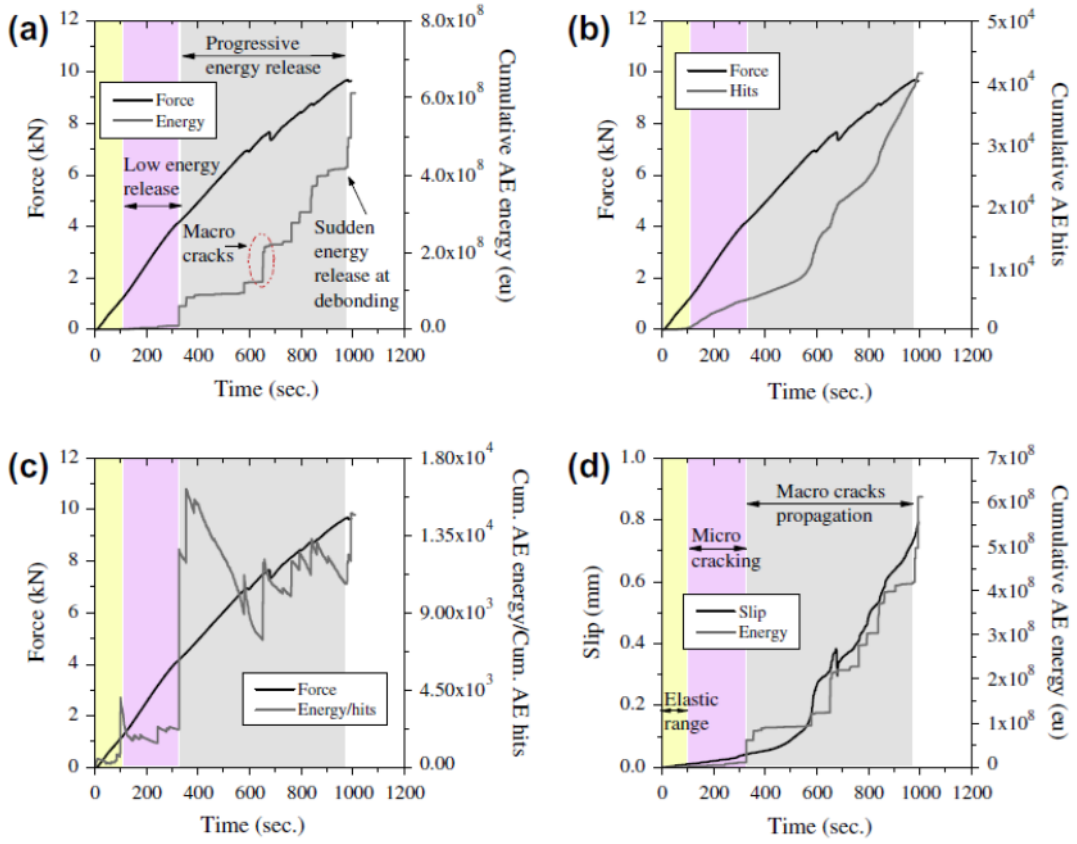

Figure 1.36: Typical AE results in reference GFRP-strengthened brick specimens[Ghiassi et al., 2014]: (a) force-cumulative AE energy; (b) force-cumulative AE hits; (c) force-energy/hits, E/h; and (d) slip-cumulative AE energy.

Among these hit based parameters, AE energy seems a crucial parameter, which could be directly compared with fracture energy. In the limited publications which discussed the quantitative correlation between these two sources of energies, [Benavent-Climent et al., 2012] conducted a test in a reinforced concrete under dynamic loading, illustrating a good correlation between the plastic energy and AE energy (Fig 1.37). [Landis and Baillon, 2002] conducted a three-point bend test in mortar and concrete specimen, showing a reasonable proportionality between AE energy and fracture energy. Besides, an empirical correlation between AE index and damage index in concrete was also proposed[Nguyen-Tat et al., 2018]. These observations are mostly based on the fracture energy derived from an entire test, deeper investigation on quantitative correlation is needed to uncover the realistic energy of emission emitted by damage source.

Furthermore, Carpinteni in his work observed the occurrence of AE activities when the snap-back instability takes place at the softening phase (Fig 1.38). Indeed,

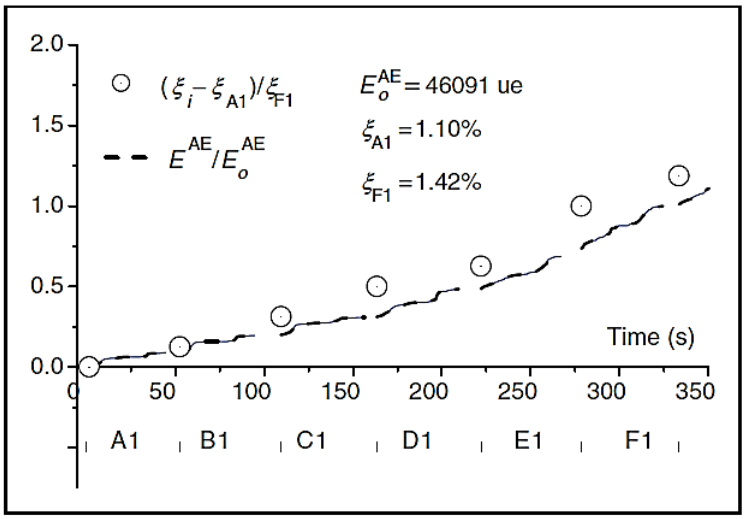

Figure 1.37: Comparison between the cumulative AE energy[Landis and Baillon, 2001]

these instabilities or snapback occur when the energy dissipated through material damage is less than all the elastic energy stored in the sample. As shown in the illustration, three different energy components can be distinguished: the energy dissipated by material damage (gray area), the surplus of elastic energy with respect to the dissipated one (red dashed area), and the total released energy, which is the sum of the two previous areas. He has explained the amount of AE energy is only a part of the dissipated energy because the energy dissipated through material viscosity, impact of fragments and heats should also be taken in to account.

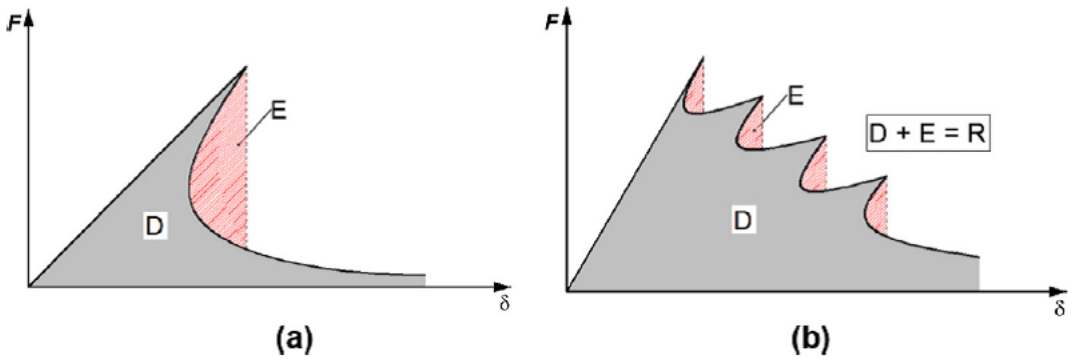

Figure 1.38: Load–displacement curves representing: (a) a catastrophic failure (single snap-back); (b) a global softening behavior perturbed by multiple local instabilities (snap-back). The gray areas identify the dissipated energy, D, whereas the dashed ones represent the emitted energy, E. The total released energy, R, is the summation of the two previous areas: D + E = R. [Carpinteri et al., 2016]

Besides, analysis based on amplitude distribution, namely b-value or improved b-value have been successfully used for investigation of damage process evolution[Rao and Lakshmi, 2005]. Besides, studies conducted in concrete also show other AE indices as AF and RA correlated with the damage deterioration[Aggelis et al., 2011]. Most of these observations were based on time-dependent failure, some of them lacked the deeper link with the mechanical behavior of material, particularly in the softening process.

In the cyclic tests, Kaiser Effect and felicity effect are frequently discussed to interpreter the onset of damage and the damage accumulation. The notion of Kaiser effect is explained [Lavrov, 2003]. "Kaiser Effect is related to the fact that AE activity increases dramatically as soon as the largest previously experienced stress level is exceeded", means that emission activities occur when the stress level is exceeded, that is also to say the capacity of storing stress of material is exceeded, particularly at pre-peak phase. The felicity effect demonstrates the occurrences of acoustic activities at a stress lever lower than the maximal stress of the previous cycle, which has been reported by the other researchers[Fowler, 2017, Shetty et al., 2019].

1.3.2.2 Source discrimination

Fracture mode discrimination is also an important issue in recent studies, particularly in concrete. The conventional method [Ohtsu et al., 2007],[RILEM Technical Committee (Masayasu Ohtsu), 2010] presented in Fig 1.39, suggest the RA(rise time/amplitude) and AF(counting/duration) could classify the failure mode in mode I (tensile crack) and in mode II (shear crack). As signal from mode I crack shows a higher AF and lower RA, whereas signal from mode II shows a lower AF and RA, however, the empirical discrimination line is determined by user's experience, which depends on the specimen geometry, the materiel homogenization and the distance from source to sensor[Aggelis et al., 2017].

Some other parameters are also studied by Farhidzadeh and Aggelis [Farhidzadeh et al., 2014],[Aggelis et al., 2017] such as duration. The authors reported that the AE duration is strongly sensitive to the fracture pattern, and the presentation of amplitude vs. duration exhibits high classification potential Fig 1.40. It is observed from the above studies that tensile and shear phenomena are successful distinguished by their AE signature, however this distinction of fracture signature are induced by various kinds of fracture phenomena resulted from composite material and not by the different fracture mode of the material itself[Aggelis et al., 2013].

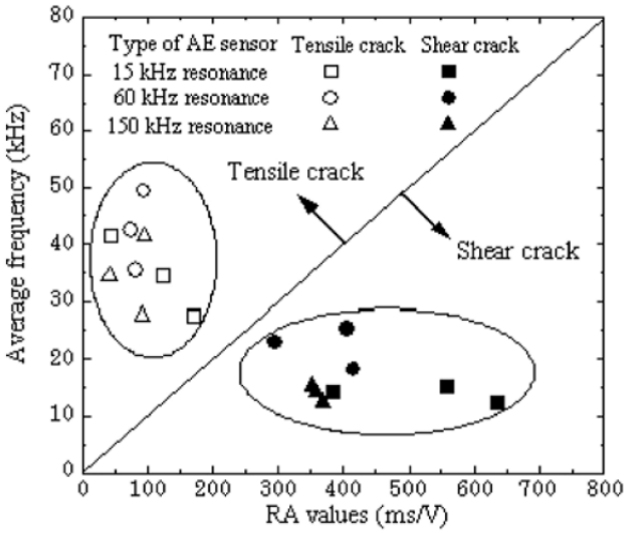

Figure 1.39: Relationship between average frequency AF and RA values for crack classification[Ohtsu et al., 2007].

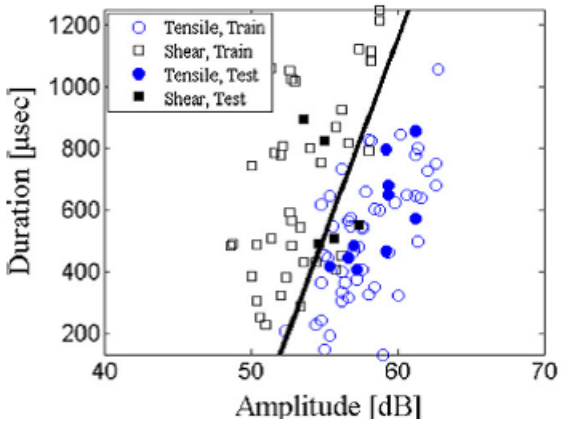

Figure 1.40: Presentation of duration-amplitude from tensile and shear signals

1.3.2.3 Unsupervised pattern recognition

In general, the discrimination of damage source is accomplished with a cluster method. Different cluster methods applied on the AE signature were also studied, such as k-mean[Pashmforoush et al., 2014],[Tang et al., 2017], gauss mixed modeling[Prem et al., 2018], Support Vector Machine[Farhidzadeh et al., 2014] and other cluster methods. These pattern recognition algorithms are helpful to cluster the signals from tensile crack to shear crack. Among these methods, K-mean method is often used due to its simplicity and efficiency. The task of k-means algorithm is to partition an N×n input dimensional dataset into k number of classes. This partition is done by minimizing the within-cluster sum of squares which is resulted from

the distance from the data points from the relevant cluster center point as in the equation

$$\sum_{i=1}^{k} \sum_{m \in C_i} \|X_m - z_i\|^2 \tag{1.6}$$

Where Ci is the N×n dimensional dataset in the i^th cluster and the z_i is the center of the points within the i^th cluster, which is calculated as in the following:

$$Z_i = \frac{\sum_{m=1}^{N_i} x_m}{N_i}, x_m \in C_i \tag{1.7}$$

This clustering method is often used in the source discrimination in the composite material, where the cluster number is determined related to the damage modes. On the other hand, some other methods[Saitta et al., 2007] are compared and applied to determine the cluster number such as the Davis–Bouldin (DB) index[L. Davies and Bouldin, 1979].

1.3.2.4 Factors influencing AE parameter

The damage accumulation and the source discrimination are interpreted by the physical observation and the AE parameters. However it is difficult to set a universal boundary or rule to quantify these AE results due to the geometric effects. In the work of Aggelis[Aggelis et al., 2012],[Aggelis et al., 2017], he has highlighted the effect of wave propagation distance on the signal waveform and the AE parameters. This observation is taken from the three-points bending tests on the textile reinforced cement. By analysis the averaged value of AF and RA at the tensile and shear cracking, he has observed the frequency parameter is strongly downshifted and RA increase for just a few cm of additional propagation as shown in the Fig 1.41.

Besides, Carpinterie has outlined the size effects on the dissipated energy as well as the AE energy. He has compared the fracture energy (dissipated energy) and the AE energy and found that the former energy increases with the specimen size whereas the latter one decreases[Carpinteri et al., 2016]. These comparisons have carried out on a three-bending test on a concrete beam by varying the height of beams. However due to the heterogeneity of material, it is difficult to evidence the reproducibility of a test monitored by AET, leading to similar AE parameters.

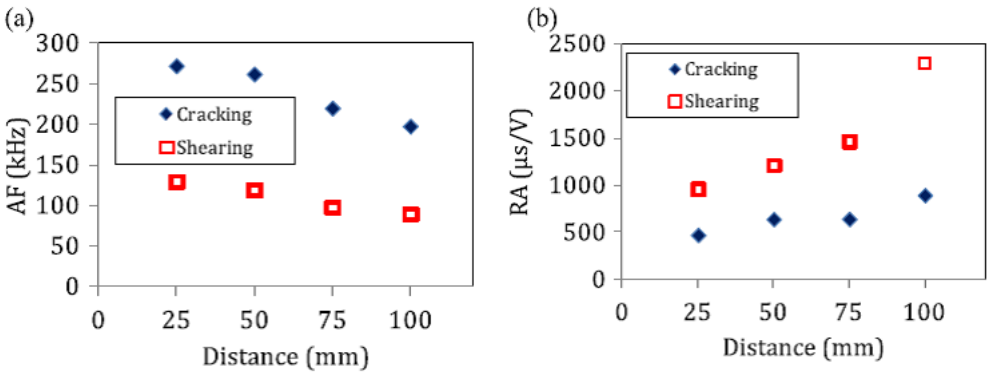

Figure 1.41: Dependence of average value of (a) AF and (b) RA on the distance between sensor and fracture zone[Aggelis et al., 2017]

1.4 Conclusion

Stone masonry is an important part of monumental heritage in France and also in Europe, from the point of view of history, economy and culture. More studies optimizing the material characterization have been devoted to the preservation and repair of historic construction. The non-destructive technique is the preferred method applied in the historical masonry construction. To get a better understanding of the performance of each ND technique for the investigation of the material condition. The mechanical behavior of masonry is necessary to understand. Besides ability of non-destructive techniques for material characterization and damage monitoring should also be acknowledged.

In order to understand the mechanical behavior and failure process of masonry, the literature studies were carried out from the masonry element scale to assemblage scale and to a structure scale. The masonry element focuses on the mechanical characteristics of limestone and mortar. Moreover, the influence of water content and the porosity on the mechanical properties of stone were also studied. Then the mechanical behavior of assemblage (block-interface) under a tensile or shear loading were discussed. Besides, it should be noticed that the experience in the cyclic tensile test provides a good insight for a further understanding of failure process in masonry assemblage. The failure mode in the shear wall have been also studied and the mechanical properties of masonry were summarized.

Different non-destructive techniques including ultrasonic velocity, electrical resistivity and electromagnetic techniques were discussed. The relationship of these non-destructive parameters and mechanical parameters are established from experimental tests, however limited researches are found in limestone. More experimental

results are needed to establish the correlation which can be used as a calibration correlation in situ. For the damage monitoring, the acoustic emission technique is usually performed in the civil engineering. The studies of this technique prove its ability in the damage characterization, including damage monitoring, damage source characterization and damage localization. However some conventional methods are not appropriate in the damage analysis of masonry as that in other building material structure. There is a need for better analysis of the performance of this technique in masonry at a multiscale.

Chapter 2

Material characterization

2.1 Introduction

In the context of conservation of masonry heritage, the structural evaluation requires firstly the mechanical characterization of masonry components: the stone and mortar. These mechanical properties are helpful for a potential use in the structure analysis. According to the literature review, it is found that the water is a crucial parameter on the weakening the strength as well as the deformation of stone. Some destructive tests have been devoted to establish the correlation between the degree of saturation and the mechanical properties of stone. Nowadays, more Nondestructive techniques (NDT) are applied to investigate the physical and mechanical properties of stone. The NDT as a non-invasive methods can respect the integrity of historic heritage.

In this chapter, we will firstly mainly discuss the influence of water on the mechanic properties and non-destructive (ND) parameters. The objective is then to estimate the influence of water on the mechanical characteristics and the non-destructive (ND) parameters. Based on the correlation between the ND parameters and degree of saturation, it offers a possibility to combine the information from the different techniques for a better water content assessment. Furthermore, the estimated water content can predict the mechanical characteristic of auscultated stone structure in-situ.

In this study, three different type stones (marble, non-marble and sireuil) are firstly characterized by its nature and mechanical properties. A series of compression test and the determination of the modulus of elasticity of material at different degree of saturation were carried out. The compressive strength of dry and saturated

sample were obtained from another compression test. The influence of porosity on the modulus of elasticity will be discussed according to the experimental data and the involved literature data. The evolution of modulus of elasticity is discussed in terms of different degree of saturation.

With respect to the ND parameters, three different nondestructive methods (ultrasound, radar and resistivity) are involved providing a good insight of the evolution of the ND parameters in terms of degree of saturation. The repeatability of ND measurement is firstly analyzed, ensuring the reliability of data. Then the effect of material anisotropy is discussed in terms of ND measurement in the direction parallel and perpendicular to the bedding planes. The evolution between the experimental ND parameter and the degree of saturation is compared with modeling. And two estimators are used to evaluate the goodness of modeling fitting.

2.2 Materials and methods

2.2.1 Materials

For each type stone Marble(M), Non-marble(NM) and Sireuil(S), 6 samples with the dimension of $10\times10\times10cm^3$ were used. The first two types of stone were carried from the quarry 'Frontenac', the last one is from the quarry Sireuil. The two sites are at the region of Bordeaux, France. The three types of stones show a visible difference from each other in terms of color, weight and porosity. Note that the marble and the Sireuil seem more homogeneous while the non-marble seems some evident bedding planes visually as shown in the Fig 2.1.

The schema (Fig 2.2) illustrates the bedding plane of stone and the relationship between the loading direction and bedding direction. The left one indicates the bedding plane parallel to the loading direction while the right one indicates the bedding plane perpendicular to the loading direction.

2.2.2 Methodology

This experimental campaign (Fig 2.3) aims to investigate the influence of water on the mechanical properties of stone sample as well as on the ND measurement. To achieve these goals, different kinds of experimental tests are performed on the samples at different degrees of saturation (Sr). The first step is to prepare the samples at a desired degree of saturation. Then three different no destructive tests

(a) (b) (c)

Figure 2.1: Sample of stones used in the experimental tests: (a) Marble, (b) Non-marble (c) Sireuil

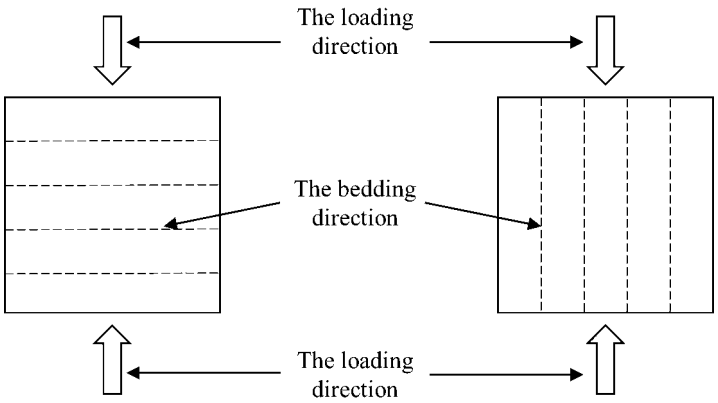

Figure 2.2: Illustration of bedding and relationship between the loading and bedding direction

were conducted to obtain the ND measurement on the specimen at each desired Sr. Then a series of mechanical tests were carried out to obtain the modulus of elasticity of each sample. The last step aims at getting the compressive strength of specimen. More details will be presented in each different tests in the following part.

2.2.2.1 Physical characterization and sample preparation

The physical feature as the bulk density (kg/m^3) were characterized by a series of laboratory test, according to the specifications[NF EN 1936, 2007]. The specimens were dried in an oven of 105 °C for 24 h up to a constant weight. The dry mass, noted Md, was measured after the specimen cooled down to a temperature of 20 °C. The capacity of balance used to measure the mass is 3kg with a precision of 0.1g.

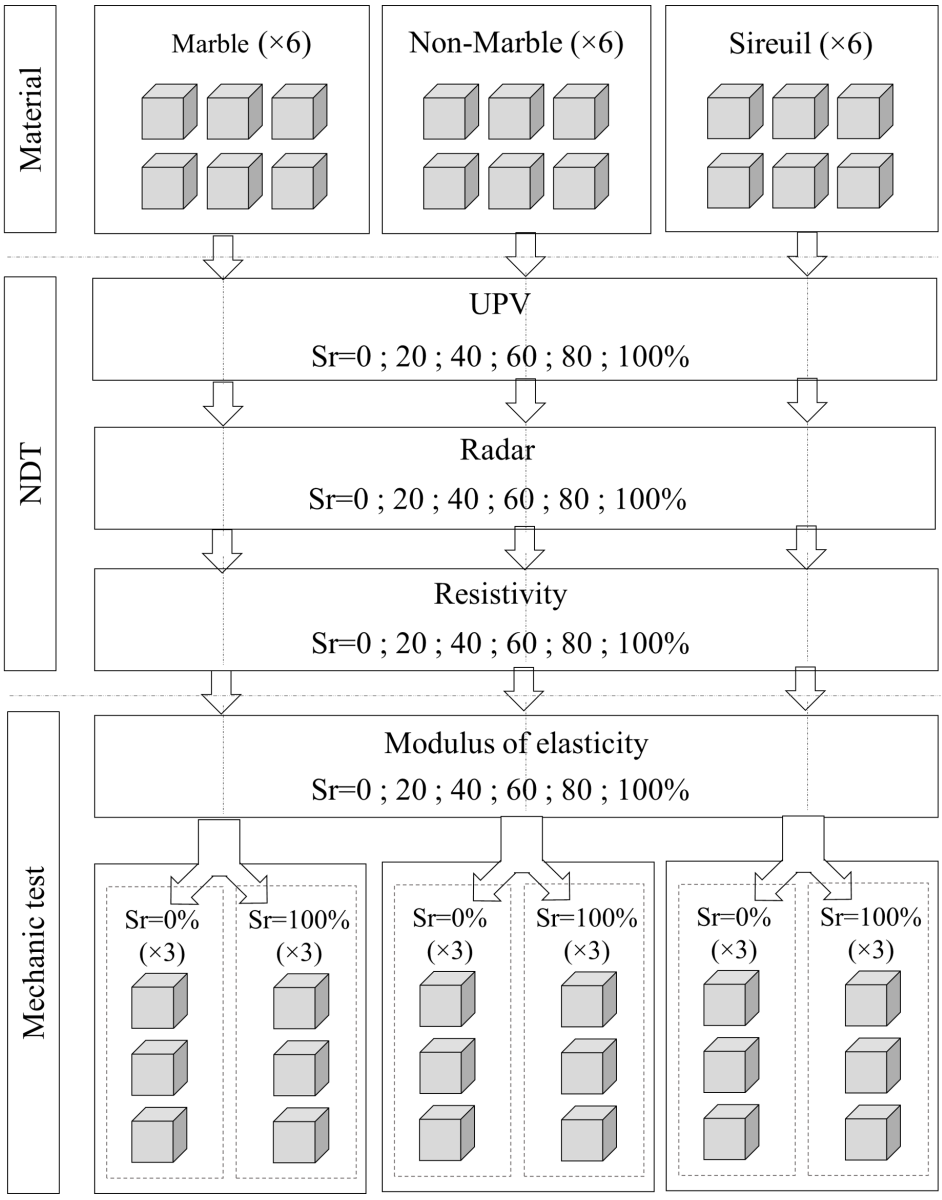

Figure 2.3: Test methodology

Figure 2.4: Packaged specimens

Then the specimens were immerged in the water for more than 30 days to get full saturated mass noted Ms and the full water saturation is then obtain. Considering the influence of water pressure on the water absorption of stones, water is added to a height of 2cm every day until to full immersion. The samples were placed at a room temperature to get dried to a desire saturation of degree, 6 degrees were considered: 0-20-40-60-80-100%. For each desired degree of saturation, the relative error between the real degrees of saturation from the desired degree should be less than 5%. And then each sample was packaged by a plastic film and an aluminum films to avoid the desiccation during the homogenization process for 7 days as shown in Fig 2.4.

A necessary step prior to the sample preparation is to measure the porosity of each sample. According to the standards recommendation, the porosity is calculated from the Eq 2.1:

$$\rho = \frac{M_s - M_d}{V} \tag{2.1}$$

Where Ms and Md are saturated and dry weight of sample, V is the volume which is considered as 0.1*0.1*0.1m^3. Note that the porosity measured here is the open porosity. The degree of saturation Sr is defined in the Eq 2.2:

$$S_r = \frac{V_w}{V_v} \tag{2.2}$$

Where Vw is the water volume in the pore and Vv is the volume of pore.

2.2.2.2 Compressive tests

The mechanical properties as uniaxial compressive strength (UCS) and modulus of elasticity (E) were estimated through uniaxial compression test, according to the standards[NF EN 1926, 1999]. These compression tests were conducted on the specimen at different degrees of saturation to evaluate the influence of water on these mechanical parameters.

Compression test for modulus of elasticity

For each degree of saturation, 18 specimens were tested to estimate the modulus of elasticity on the direction perpendicular and parallel to the bedding.

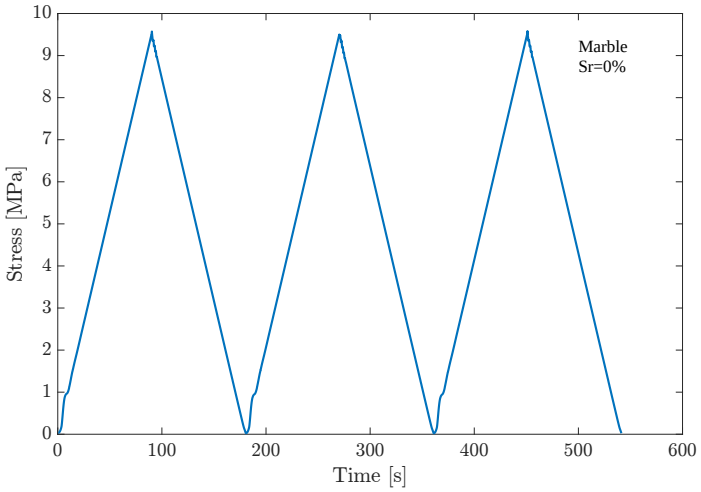

Figure 2.5: Loading rate of 3 cycles

This uniaxial compression test was conducted on studied specimen by using an electro-hydraulic servo mechanics test machine MTS, with a capacity of 10t, as show in the Fig 2.6(b). The specimen was placed on the center of a steel plate, the load was applied on the upper side of stone. Before each test, a preload of 200N was applied on the sample to ensure a good contact. 3 cycle of loading and unloading phases was conducted and the test was load-controlled with the same loading rate in both phases as shown in the Fig 2.5. The maximal load was set differently, depending to the estimated compressive strength of each type of stone at different degree of saturation, according to the correlation reported by [Vasarhelyi, 2003],[Vasarhelyi and Davarpanah, 2018]. The maximal load was determined as 50% of the estimated compressive strength. Besides the test with load

direction perpendicular to the bedding is prior to that parallel to the bedding. And the maximal load is greater at the former one. Note that this maximal load was set, ensuring that the sample is always in the elastic domain. The duration of an overall test was fixed at 90 s, thus the loading rate was variable which can be calculated from the applied maximal load. Two summarized Tab 2.1 and Tab 2.2 exhibit the loading rate for each type of stone sample at different degrees of saturation and 2 directions to the bedding.

Table 2.1: Loading rate of in the direction perpendicular to bedding

	Marble		**Non-marble**		**Sireuil**	
	Maximal load (MPa)	Loading rate (kN/s)	Maximal load (MPa)	Loading rate (kN/s)	Maximal load (MPa)	Loading rate (kN/s)
Sr=0%	9.5	1.06	9.9	1.1	4	0.44
Sr=20%	8	0.89	9	1	3	0.33
Sr=40%	7.5	0.83	8	0.89	2	0.22
Sr=60%	7	0.78	8	0.89	1.5	0.17
Sr=80%	6.5	0.72	8	0.89	1.5	0.17
Sr=100%	6	0.67	6	0.67	1.5	0.17

Traditionally, the displacement is measured by displacement measurement device. However this method is not applicable in our test because the device cannot be glued on a wet surface. Besides, considering the loss of water of tested sample at room temperature, the preparation and device set-up should be efficient to minimize the influence of lost water on the measured degree of saturation. Thus, an optical method was applied in our tests to measure the vertical applied displacement. This technique focus on the displacement between the 2 virtual gauges by using the software Vic 2d gauge. The gauge points were selected as the center point A and B of targets which were positioned in the midline of upper and down metallic platen as shown in the Fig 2.6(a). This displacement measurement includes the deformation of metallic platen of 2mm and the total deformation of stone, however the deformation of platen is 0.2μm which can be neglected comparing to the deformation of stone. Before the test, a calibration test was needed to convert the pixel coordinates to a meter coordinate. By putting a ruler upright and against the sample surface as shown in the Fig 2.6(a), the coefficient was derived from the pixel coordinates and its corresponding length which can be read from the ruler. The displacements of points A and B are denoted by V_A and V_B(mm), respectively. Accordingly, the strain can be expressed as $\epsilon = \frac{(V_A - V_B)}{L_{AB}}$, the L_{AB} is the original length from the point A to B.

Table 2.2: Loading rate in the direction parallel to bedding

	Marble		**Non-marble**		**Sireuil**	
	Maximal load (MPa)	Loading rate (kN/s)	Maximal load (MPa)	Loading rate (kN/s)	Maximal load (MPa)	Loading rate (kN/s)
Sr=0%	9	1	9.9	1.1	3	0.33
Sr=20%	7	0.78	8	0.89	2	0.22
Sr=40%	6.5	0.72	8	0.89	1.5	0.17
Sr=60%	6	0.67	7	0.78	1	0.11
Sr=80%	5.5	0.61	5	0.56	1	0.11
Sr=100%	5	0.56	5	0.56	1	0.11

In order to minimize the error of calculated modulus of elasticity of a material which is related directly to the measured strain. This method was applied at both of sides, equipped with one camera 'Manta' with lens 28mm for each side as shown in the Fig 2.6(b).

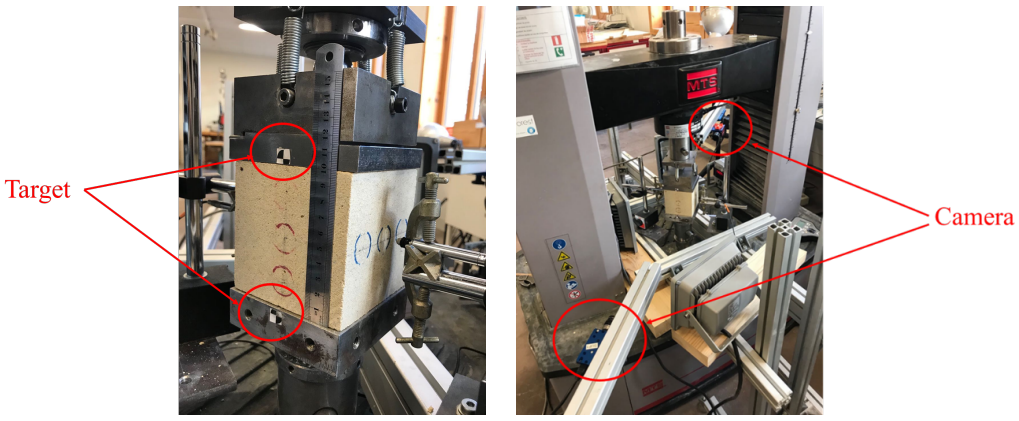

(a) (b)

Figure 2.6: (a)Calibration test (b) experimental setup

Comparison between the displacement measurement methods

Before determining the optic method to measure the deformation of specimen under compression, different methods have been tried and compared with a referent method. The referent method is to use the displacement measurement transducer to measure the deformation of the center area of a specimen. Finally we will see that the optic method prove a good agreement with the displacement measurement in the referent method.

To validate the optic measurement, the displacement measurement by the optic method and the referent method were both carried on the same stone sample as shown in the Fig 2.7. The displacement mesured in the optic method is resulted from the displacement of the gauges while that measured in the referent method is obtain by a displacement measurement transducer (HBM). This validation tests were carried out on the 3 samples of different type stone. And a good agreement of calculated modulus of elasticity in both methods confirms the possibility to use the optic method in the deformation measurement in our test.

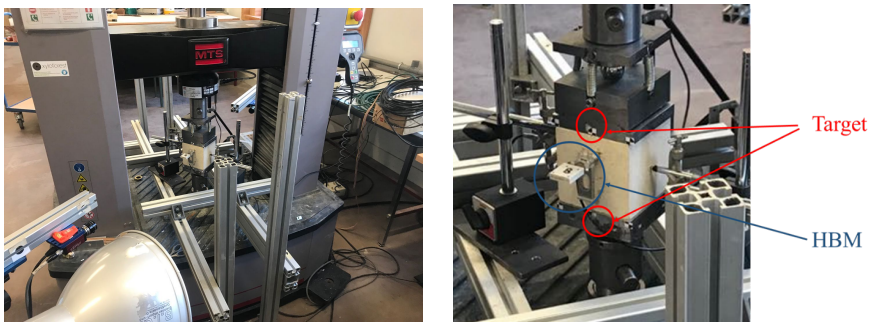

(a) (b)

Figure 2.7: Validation test and referent test setup

Compression test for compressive strength

For each type of stone, the 6 samples were divided into 2 groups: three samples were conserved in dry condition and the other three were conserved in saturated condition before the compression test. An ascending order can be obtained according to the results of elastic modulus of each dry sample. The specimen with even-numbered modulus order belong to the former group while the rest belong to the latter group.

Table 2.3: Loading rate of compression test

Loading rate (MPa/s)	Marbe	Non-marble	Sireuil
Dry condition	0.3	0.3	0.05
Saturated condition	0.3	0.15	0.05

The dry or saturated sample was placed at the center of the metal platen as shown in the Fig 2.8. The sample was then subjected to a uniform vertical loading, provided by a machine testing MEH with the capacity of 3000kN.This test was also load-controlled until the ruin of sample. According to the standards, the loading rate depends on the compressive strength. The following Tab 2.3 summarizes the

Figure 2.8: Experimental setup for compression test

loading rate for each type of stone in dry or saturated conditions. The Fig 2.9 demonstrates the failure mode of dry or saturated sireuil sample.

(a) (b)

Figure 2.9: Failure mode of dry and saturated sireuil sample

2.2.2.3 Non-destructive tests

Three different non-destructive techniques were applied to obtain the different non-destructive (ND) parameter at different degrees of saturation, to analyze the sensibility of each ND parameter to the material, the anisotropy and the degree of saturation. Besides, the correlation between the NDT parameter with different degree of saturation is also obtained and compared with model. The discussion will be conducted to the experimental results and the simulation results.

Ultrasound

The direct transmission time through a sample was measured by PUNDIT 7(Fig 2.10), equipped with two transducers operating at 200 kHz and an accuracy of ± 0.1µs. Meanwhile the associated waveforms were recorded by an oscilloscope (PicoScope 2000). For the PUNDIT 7, the frequency was set at 1 Hz. The sampling rate and the signal length in the oscilloscope were set at 200MHz and 5ms, respectively.

Each transmission time was measured from emitter to receiver which were positioned at the same position of the opposite sides. 6 signals were recorded simultaneously at the same point of measure. The Fig 2.11(a) shows an example of an emitting signal in blue and a receiving signal in red. Another zoomed figure demonstrates the travailing time corresponds to the width of an emitting signal. The advantage to recalculate the transmission time is to reduce the error due to the bad adherence between the sensor surface and tested sample surface even with the Vaseline as a coupling.

Due to the material heterogeneity, 3 points of measure were undertaken through one direction as shown in the Fig 2.10. The distance between the sensors near the side to the sensor at the center remains 2cm. To evaluate the sensitivity of ultrasound velocity on the material anisotropy, the measurements were repeated through 3 directions of each sample at a controlled degree of saturation.

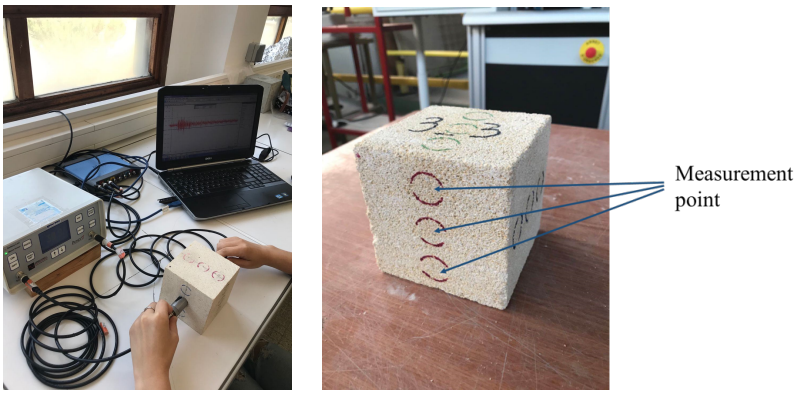

(a) (b)

Figure 2.10: Ultrasound measurement setup

Radar A GSSI TeraSIRch SIR System-3000 developed by Geophysical Survey Systems was used, equipped with two antennas operating at the frequency 2.6GHz. The two antennas consist of a transmitter and a receiver. They were fixed with a distance 10 cm for all the tests as shown in the Fig 2.12. The transmission signals

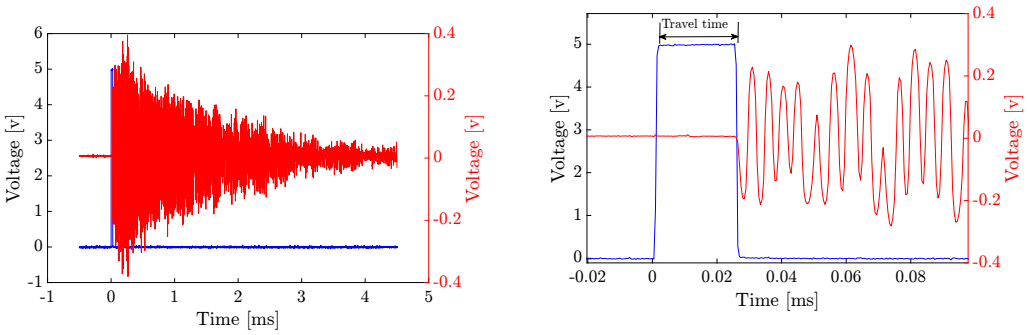

(a) (b)

Figure 2.11: Recorded emitting (blue curve) and receiving (red curve) signal (b) zoomed figure

through the sample were firstly recorded when the specimen was positioned between these two antennas as demonstrated in the Fig 2.12(a). Then the transmission signals through the air were recorded when the specimen was moved (Fig 2.12(b)). The recording process of a test was repeated in three direction of all the degrees of saturation. Note that some important parameters influencing the recorded signals should be noticed. In our test, the recording sampling was fixed at 50 scans/s. The sampling rate was set at 512 sample/scan with a 10 ns range of length of a signal.

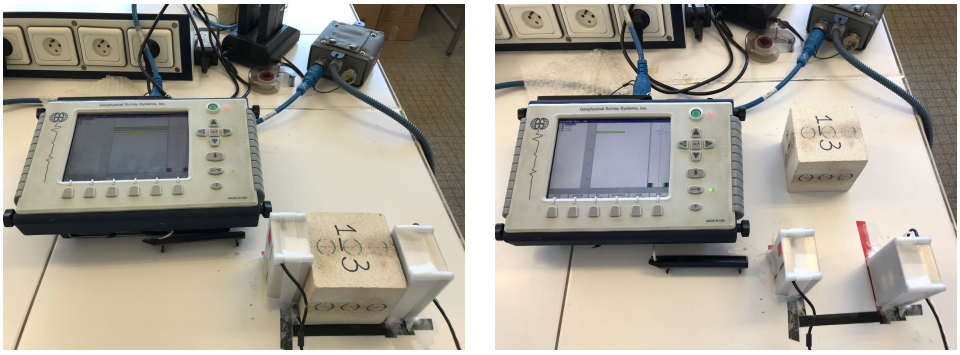

(a) (b)

Figure 2.12: Experimental setup for the signal recording by Radar (a) through the sample (c) through the air

Once the signal through the tested sample was recorded, it is important to calculate the travel time leading to the radar transmission velocity as well as the dielectric permittivity of the overall sample. However the onset of signal is not clear, only the time delay Δt from the signal through the specimen to the signal through the air at the same distance can be obtain from the Fig 2.13. That is explained why the

two type of signal needed to be recorded in the file, ensuring the onset of signal is the same through the two materials. The Δt is the time difference corresponding to the first negative peak of the two signals. Thus the real transmission time through a sample $t_{s,real}$ should be adjusted by adding a real time of air $t_{a,real}$) through the fixed distance (D) 10.5cm, which is written as the Eq 2.3-Eq 2.4:

$$t_{s,real} = \Delta t + t_{a,real} \tag{2.3}$$

$$t_{a,real} = \frac{D}{c} \tag{2.4}$$

Where c is the speed of light, 310^8 m/s. And the velocity of a wave travailing through a material of length of d (m), is given by:

$$v = \frac{D}{t_{s,real}} \tag{2.5}$$

The dielectric permittivity ϵ can be derived from the velocity v (ms^{-1}) of an electromagnetic wave, according to the Eq 2.11:

$$\epsilon = (\frac{c}{v})^2 \tag{2.6}$$

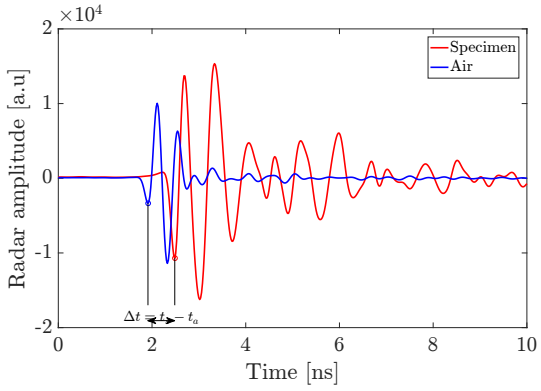

Figure 2.13: Waveform of radar signal through specimen and air

Resistivity

The measurement of the electrical resistance of material is undertaken by two devices: the LCR meter (LCR 819, a device for assigning Inductance 'L', Capacitance 'C' and Resistance 'R') and MEGGER DET5/4D. The former one with a larger measurement rang of resistance from 0 to 999k which can be used for sample at a lower degree of saturation. The latter one was used as a referent method to

check the resistance measured by the LCR. The resistance and the capacitance are both recorded with 1 V terminal voltage at 128 Hz which is the same as applied in MEGGER. Before each test, a calibration test should be taken into consideration. Note that even for the LCR meter, the resistivity can be only obtain at the degree of saturation ranging from 20% to 100%. Because the sample in dry condition has a high resistivity which has exceeded the measurement range of LCR meter.

The test setup is shown in the Fig 2.14, two wet sponge were put at the upper and bottom side of specimen to raise the conductivity of electricity through the material. Two probes were connected with the metal plate to inject the electrical current. Another two probes was also connected with the plates to measure the potential voltage. For each test, the resistance value and the capacitance value were recorded. In order to evaluate the repeatability of the measurement, 3 repeated tests were carried out through one direction. For each tested sample at the controlled degree of saturation, the resistance through 3 direction were measured.

The electrical resistivity of a tested sample is then calculated as the following Eq 2.7:

$$\rho = \frac{R \cdot S}{L} \tag{2.7}$$

Where ρ (Ω.m) is electrical resistivity, the resistance R (Ω) is resistance measured by LCR, S (m2) refers to the cross-sectional area (0.01m2) and L is the length of the tested sample (0.1m) as shown in Fig 2.14.

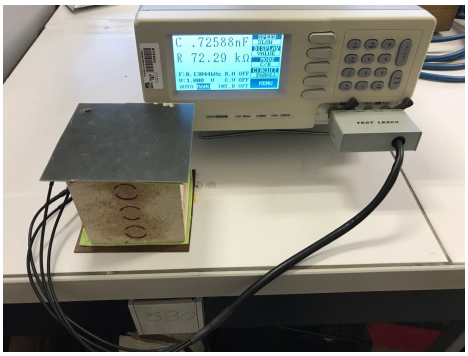

Figure 2.14: Experiential setup for the measurement of resistivity by LCR

2.3 Results and discussions

2.3.1 Physical properties

The porosity and the bulk density of all the 18 specimens were measured and the averaged value with its relevant coefficient of variation are demonstrated in the Tab 2.4. The marble and non-marble shows a similar in terms of bulk density and porosity. The bulk density of sireuil is significantly lower while the porosity is higher. A general low CV indicate a low variability of material of each type stone. A correlation is established between these two parameters in the Fig 2.15. The Marble and Non-marble show similar features in terms of these two parameters. The sireuil is more porous and the bulk density is also lower than the other types of stones.

Table 2.4: Physic properties of stone

	Marble	Non-marble	Sireuil
Bulk density (g/cm^3)	2.33 ($\pm$0.76%)	2.13 ($\pm$1.17%)	1.82 ($\pm$0.77%)
Porosity	0.14 ($\pm$5%)	0.15 ($\pm$3%)	0.26 ($\pm$1%)

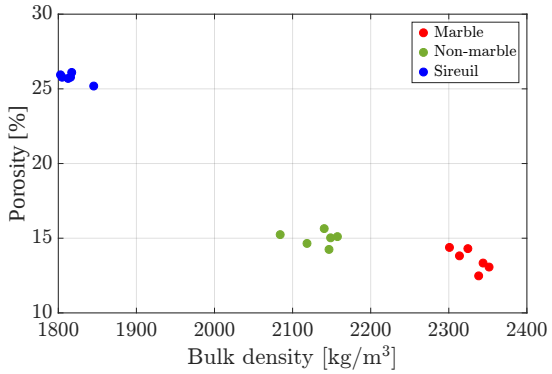

Figure 2.15: Correlation between the porosity and bulk density

2.3.2 Mechanical characterization

2.3.2.1 Modulus of elasticity

Determination of modulus of elasticity

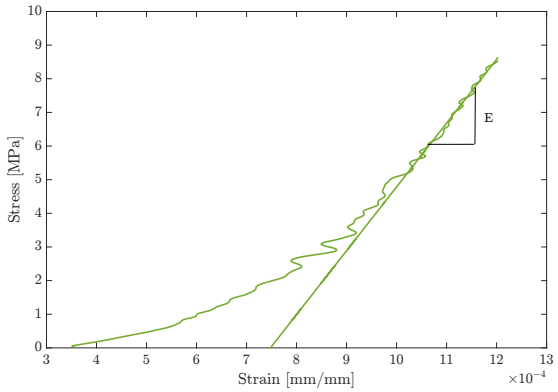

Figure 2.16: Modulus of elasticity determination from increasing branch of stress strain curve of compression test

The modulus of elasticity is derived from the stress-strain curve of the last cycle of each test, shown in the Fig 2.16. In this figure, only the increasing branch is presented to obtain the modulus. The stress is calculated by computing the load at the applied surface. In our test, the surface of specimen is $0.01m^2$. The modulus of elasticity is calculated as the slope (E in the Fig 2.16) of the linear fitting corresponding to zone between the 60% to 100% of the maximal stress in each test. However, the data noise is noticed on the raw data, it is necessary to apply the method of moving average to decrease the influence brought by the noised data in image acquisition.

In fact, an analysis have been conducted to demonstrate the influence of moving number on the two following parameters. The first one is the coefficient of determination (R^2) of the linear fitting and the second one is the calculated modulus of elasticity as shown in the Fig 2.17. It is seen the value of R^2 and the value of modulus of elasticity perform well when the moving number is approximately equal to 20. This determined moving number is finally applied in the moving average for all the stress-strain curves in our study.

As mentioned in the part of materials and methods (Part 2.2), the displacement of material is measured for both opposite sides. The modulus of elasticity studied in the following section is the averaged value of computed modulus from the two sides.

Influence of Degree of saturation on the modulus of elasticity

The Fig 2.18 illustrate the evolution of module of marble with degree of saturation, the modulus is obtained from the test with loading direction perpendicular and

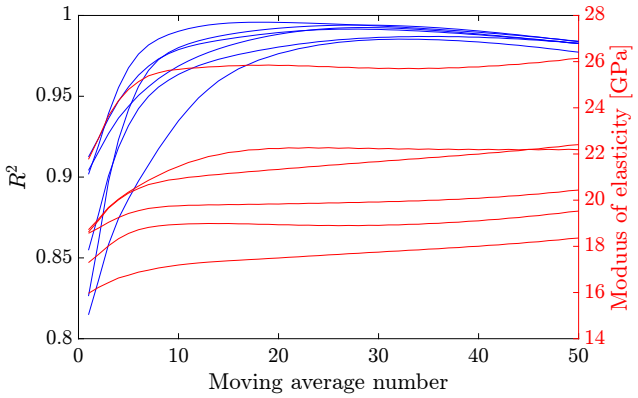

Figure 2.17: Influence of moving average number of coffecient of determination of fitting and the modulus of elasticity

parallel to the bedding planes. In these figure, the modulus of each of the 6 marble samples is plotted in different colors. As seen in these two figures, the modulus decreases with increasing degree of saturation in both directions. All the sample illustrate the same tendency of modulus in terms of degree of saturation. Note that, this decrease is more pronounced when the degree of saturation shift from 0% to 20%. For the other degrees of saturation, this decrease seems relatively stable.

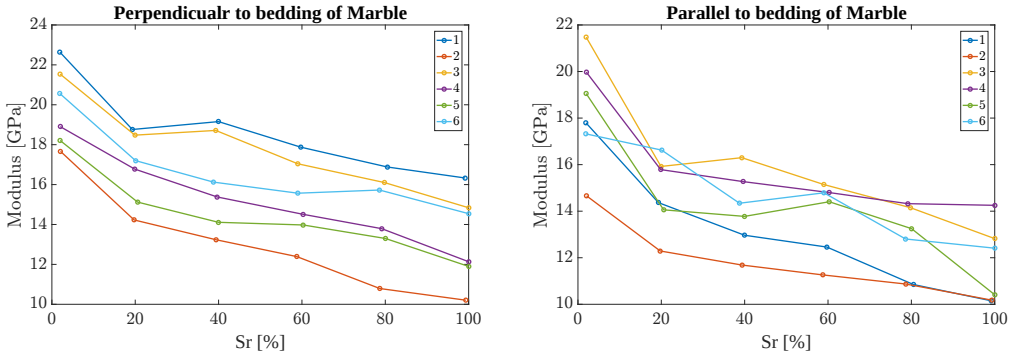

(a) (b)

Figure 2.18: Evolution of modulus of elasticity in terms of degree of saturation in the direction (a) perpendicular (b) parallel to bedding planes of marble 1-6

This evolution of modulus in each type of stone in terms of degree of saturation is summarized in the Fig 2.19. The modulus of each point is calculated as the averaged value of modulus of 6 specimens of the same type. The horizontal and vertical error bar represents the standard deviation of the degree of saturation and the modulus of elasticity, respectively. It can be observed that more variability of modulus is

found in the direction parallel to bedding than in the perpendicular direction for the three types of stone. For all the type of stones in the two directions, the modulus of elasticity of sample decreases with an increasing degree of saturation. And more than 30% of decrease of modulus is observed from the dry condition to saturated condition of samples. For the sireuil, this percentage of reduced modulus is still higher in both directions. This decrease of modulus is more significant than that observed in the sandstone[Kim and Changani, 2016].

Some researchers[Beck, 2006],[Zhang et al., 2012] have reported the effect of suction, one factor can explain the decreasing modulus of elasticity with the increasing water content. They have also demonstrated the suction curve which shows a negative trend of suction with an increasing degree of saturation[Zhang et al., 2012]. And the suction generates a confining pressure, increasing the elastic stiffness of material consequently. At a high saturation degree, the confinement pressure due to suction is reduced, resulting in a decrease of elastic stiffness.

For the marble and sireuil stone, the modulus in direction perpendicular to bedding are generally greater than that parallel to bedding. In fact, due to the heterogeneity of stone, a relative great variability is observed. However the evolution of the modulus in the two directions show a similar tendency in terms of degree of saturation. It indicates that the decreasing modulus between the two directions are generally constant for all the tested degrees of saturation. However this phenomena cannot be observed in non-marble stone. The modulus in two directions are quite almost the same when the degree of saturation is below 60%, and a greater difference between the two modulus when the non-marble sample is saturated.

Note that the marble and non-marble are similar and homogeneous in terms of porosity and bulk density. However, the marble is more isotropic than the non-marble. It is questioned why the modulus of elasticity of non-marble show a great similarity at the low degree of saturation and huge difference at the high degree. This question can be explained by the suction effect which seems more important on anisotropic structure which have been reported by other researchers[Zhang et al., 2012]. In our test, the structure anisotropy can be characterized by the presence of parallel bedding planes and also by the non-destructive parameter detailed in the following analysis. In fact, the bedding plans(Fig 2.2) of non-marble is closed progressively under a perpendicular loading while they are more likely opened under a parallel loading. The micro cracks are more easily induced when the bedding plans opens. Thus the opening bedding plans are more sensitive to the confining stress resulted from the suction effect rather that the closing ones. That is why the more decrease of modulus of elasticity is observed with parallel loading than that with perpendicular

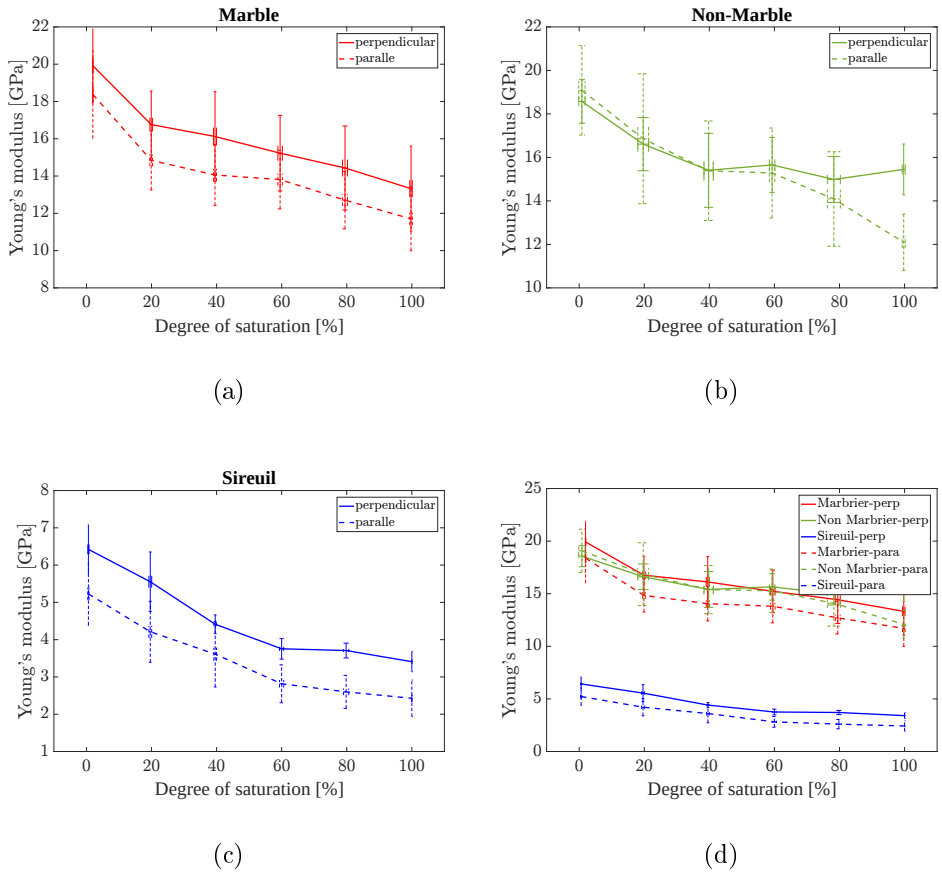

Figure 2.19: Summarized evolution of modulus of elasticity in terms of degree of saturation in the direction (a) perpendicular (b) parallel to bedding planes of three type stones

loading when the dry non-marble sample is saturated.

Besides, a summarized Fig 2.20 and Tab 2.5 quantify the reduction of modulus of elasticity of dry and saturated sample. This comparison focus this parameter with loading direction perpendicular to bedding (Fig 2.20(a))) and the direction parallel to the bedding (Fig 2.20(b)). The modulus of elasticity are similar for the marble and non-marble stone both in dry and saturated condition in these two directions. More percentage decrease of modulus (47%) is found in the sireuil against that in the other types of stone (about 20%). Moreover, more decrease of modulus between dry and saturated condition is observed in the direction parallel to the bedding for all types of stone. This observation confirms that the modulus in the direction parallel to the bedding is more sensitive to the water content.

Effect of anisotropy

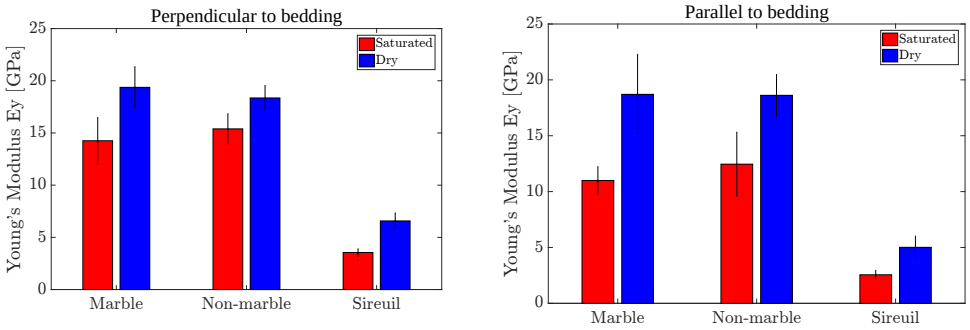

(a) (b)

Figure 2.20: Modulus of elasticity of dry and saturated sample

Table 2.5: Modulus of elasticity of dry and saturated sample

Modulus of elasticity Ey (GPa)	Marble		No marble		Sireuil	
	Dry	Saturated	Dry	Saturated	Dry	Saturated
Perpendicular to bedding	19.4 (±8.3%)	14.3 (±12.8%)	18.4 (±5.3%)	15.4 (±7.7%)	6.6 (±9.5%)	3.5 (±8.1%)
Parallel to bedding	18.7 (±15.6%)	11.0 (±9.2%)	18.6 (±8.2%)	12.5 (±18.8%)	5.0 (±16.3%)	2.6 (±12.5%)

The effects of anisotropy on the modulus of elasticity is analyzed in this part. The same data processing is applied to obtain the modulus of elasticity at different degrees of saturation of each 18 specimen in both the two directions. As shown in the Fig 2.21, the modulus of elasticity of each specimen of the same type are plotted in the same color. The color of point fades with a decrease degree of saturation. It can be firstly concluded that the modulus of marble and non-marble sample are significantly greater than that of sireuil sample in both two directions and in all the degrees of saturation. The modulus of elasticity of the former ones are around about 15GPa while that of the latter one are around 5GPa. Besides the modulus of elasticity of marble and sireuil sample in the direction perpendicular to bedding are generally greater than that in the other direction. For the non-marble stone, this observation is still found in the mostly modulus of non-marble sample. However some points present the opposite correlation between these two modulus. In the following part, more details will be discussed to answer this question.

Influence of porosity and bulk density on modulus of elasticity

The modulus of elasticity (E) in dry condition is presented in terms of the porosity (ρ_0), as the blue dot in the Fig 2.22. It can be seen that the modulus of elasticity decreases with an increasing porosity ranging from 10% to 25%. In fact, some studies have been devoted to discover the relationship between the modulus and the porosity as shown in the Fig 2.22. The data extracted from the work of Pappalardo

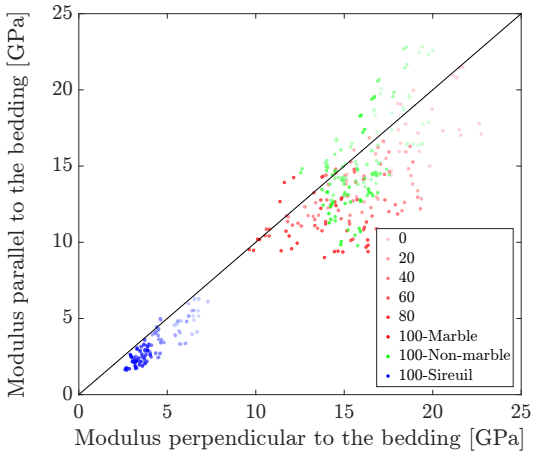

Figure 2.21: Relationship of modulus measured in the direction parallel and perpendicular to bedding planes

are also presented in the form of black point in the same plot. In fact, the stone studied in his work is more porous with the porosity ranging from 30% to 50%. Besides, he illustrated a good correlation between these two parameters. This good correlation plotted in the black line is well fitted with the experiential data. So it is interesting to reconstruct a new correlation considering the data in the literature and the data obtain in our test to validate this correlation if it is suitable for the low porous stone. Thus an exponential correlation is reestablished with a good coefficient of determination. This new correlation is exhibited in a red line in this Fig 2.22.

By comparing the correlation in the literature and the correlation obtain by adding our experimental data, these two correlations show a quite similarity in terms of empirical equation (Eq 2.8). It can be concluded that this correlation can be used to estimate the modulus of elasticity if the porosity of stone is known ranging from 10% to 50%. Of course, more experimental tests should be conducted to investigate this correlation at other porosity to validate this correlation. Moreover, in ranging porosity from 10% to 50%, as the porosity is highly correlated to the bulk density[Parent et al., 2015]. It can also be concluded that the elastic modulus can be estimated from the bulk density.

$$E = 64.895e^{-8.07} \tag{2.8}$$

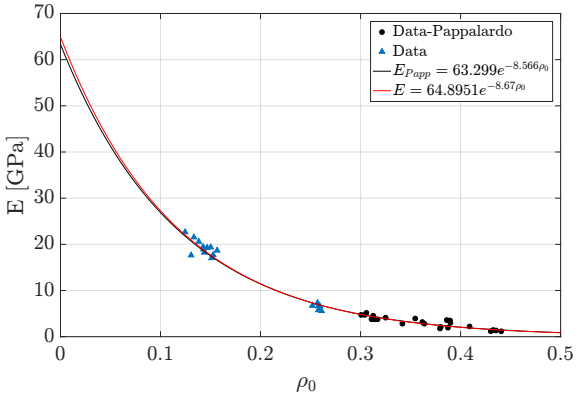

Figure 2.22: Correlation between the modulus of elasticity and porosity

2.3.2.2 Compressive strength UCS

The effect of water saturation on the compressive strength (UCS) of these three types of stone is discussed in this part. As presented in the methodology part, only the compressive strength of sample in the dry and saturated condition are concerned. Three samples of the same type stone are tested for each condition. In the Fig 2.23, each bar refers to the averaged value of compressive strength of each type stone at the dry and saturated condition. The error bar is calculated as the standard deviation of 3 values in each condition. It is observed that the UCS is generally higher when the sample is dry for all the types. Besides, a summarized Tab 2.6 offers the more detailed value including the averaged UCS of dry and saturated sample and its corresponding coefficient of variation. More than 25% of compressive strength decreases in the marble and non-marble from the dry condition to saturated condition. This decrease percentage is about 20% in the sireuil stone. This observation confirms the importance of water in weakening the strength of stone.

Table 2.6: Compressive strength of dry and saturated sample

Marble		Non-marble		Sireuil	
Dry	Saturated	Dry	Saturated	Dry	Saturated
37.7 (±4.6%)	26.7 (±25.9%)	23.1 (±5.6%)	16.3 (±15.3%)	6.2 (±1.4%)	5.0 (±14.6%)

A great difference in the strength is observed between the different type stones in both condition. Another presentation Fig 2.24 underlines the correlation between the compressive strength and the porosity. The decrease trend indicates the porosity of stone contribute to a weaken effect on the strength of stone. This strength decreases with an increasing porosity whatever in dry or saturated condition.

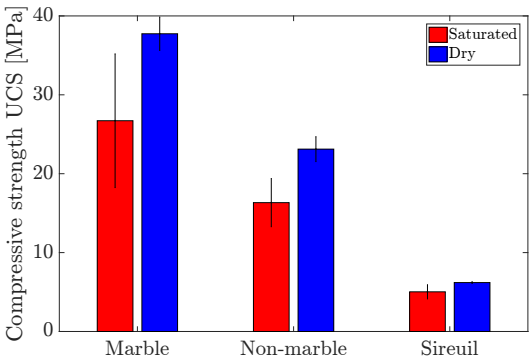

Figure 2.23: Compressive strength of three type stones at dry and saturated condition

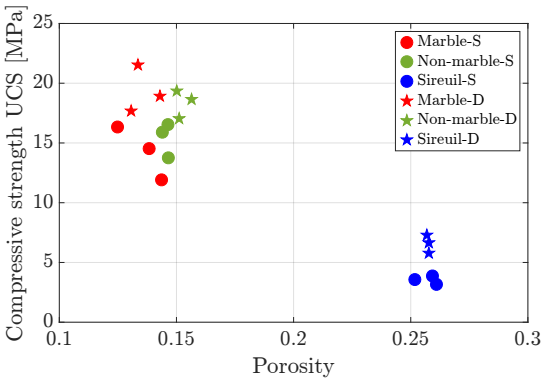

Figure 2.24: Correlation between the compressive strength and porosity

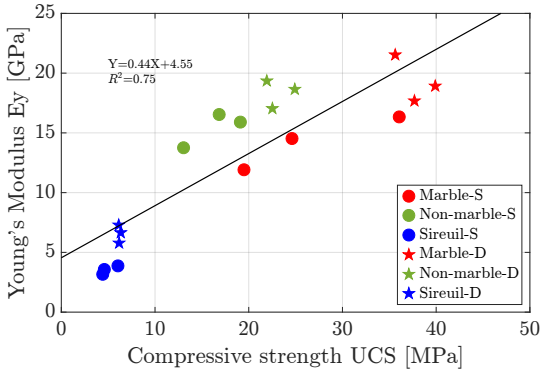

Figure 2.25: Correlation between the modulus of elasticity and compressive strength, S : saturated and D : dry.

2.3.2.3 Correlation between compressive strength and modulus

In the basis of previous observation, stone with lower porosity may result in a weaker compressive strength, along with poorer modulus of elasticity both in dry and saturated condition. And some studies[Pappalardo et al., 2016] have highlighted a correlation in an exponential or linear trend between these two mechanical parameters. According to the curve-fitting obtained in our test, an empirical equation (Eq 2.9) can be obtained between the modulus of elasticity and the compressive strength of dry and saturated sample (Fig 2.25).

$$E(GPa) = 0.4UCS(MPa) + 4.55 \tag{2.9}$$

2.3.3 Influence of water on ND parameters

Whereas the previous analysis has highlighted the influence of isotropy, porosity and degree of saturation on the mechanical properties. In this section, three non-destructive method (ultrasound, radar and resistivity) are involved to demonstrate the relationship between the non-destructive (ND) parameter and the degree of saturation and the porosity. These ND parameters are resulted from the ND measurement in each technique.

2.3.3.1 Influence of water on ultrasound velocity

The first analysis focuses on the variation of ultrasound velocity in terms of the porosity and the degree of saturation. For each specimen at any controlled degree of saturation, the velocity through 3 directions on each 3 faces are concerned (9 points per sample are concerned). The velocity represented at each point is the averaged value of 6 repeat at same point. And its relevant coefficient of variation (CV1) related to the repeatability can be also obtain. Taking into consideration of all the measurements at the 9 points , for the 18 samples at each 6 targeted degree of saturation (in total: 972 point), an average CV1 0.69% shows a good repeatability in the ultrasound velocity determination. Besides, for each direction, the velocity used in the following analysis is the averaged value of the 3 points at the same surface. This CV2 is regarded as an indicator which describes the homogeneity of a studied sample. The averaged CV2 2.44% confirms a good homogeneity of the limestone at the 10cm sample scale in terms of ultrasound velocity.

As the stone is an anisotropic material, the velocity through the 3 directions for each controlled degree of saturation is summarized in the Fig 2.26. The Fig 2.26a-c correspond to the summarized velocity of marble, non-marble and sireuil, respectively. In each of these three figures, each point represents the ultrasound velocity through one direction of one specimen at a given degree of saturation. And the velocity through one direction of one type stone is calculated as the averaged value of 6 samples, plotted in a solid line. The legend 'parallele1' and 'parallele2' refers to the two directions parallel to the bedding plane while the 'perpendicular' correspond to the direction perpendicular to the bedding.

It can be found that only the non-marble shows a different in the direction: parallel and perpendicular of bedding. And the other two types of stone show there is no evident difference in these two directions. This observation is also summeraised in the Tab 2.7. With regarding to the evolution, for the sireuil the UPV decrease from 2100m/s to 2000m/s when the degree of saturation increase from 0% to 80%, then the upv increases from 80% to 100%. It can be seen that for the marble, an increasing velocity is observed from 0% to 20%, and this UPV remains constant from 20% to 100% in both the 2 directions. For the non-marble, the same tendency is observed as marble. In the summarized Fig 2.26(d), the value of velocity in the marble and non-marble is similar and higher than that in sireuil, indicating the velocity is related to porosity. However due to a low porosity of studied stones (10%-30%), it is quite difficult to observe the evolution of ultrasound velocity in terms of degree of saturation.

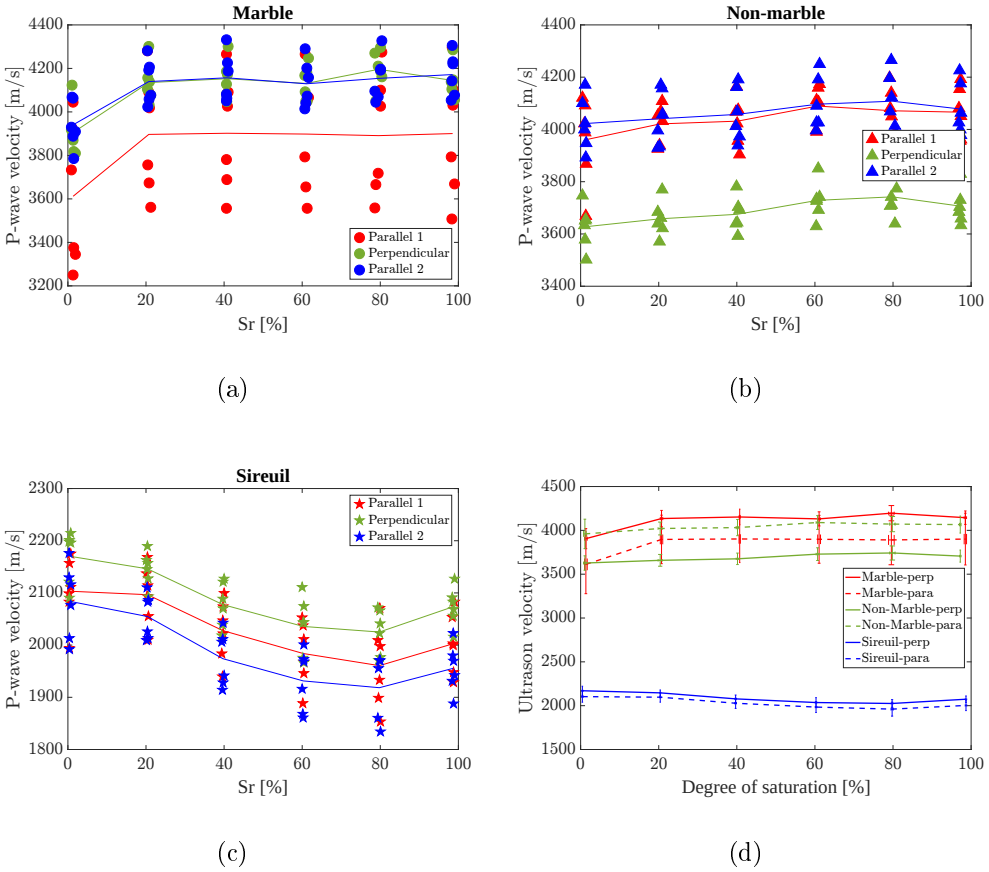

Figure 2.26: Evolution of p wave velocity in (a) marble (b) non-marble (c) sireuil (d) summaised results

2.3.3.2 Influence of water on dielectric permittivity

The dielectric constant (permittivity) is one basic parameter of radar method. This ND parameter is derived from the propagation time of radar wave though the material, based on the equation (Eq 2.5). For each sample at a given degree of saturation, the travailing time through the 3 directions were investigated. The time through one direction is calculated from the equation (Eq 2.10) which is modified according to the equation:

$$t = \bar{t_s} - \bar{t_a} + t_0 \tag{2.10}$$

Where $\bar{t_s}$ is the averaged traveling time through the specimen calculated from the first 50 recorded signals, $\bar{t_a}$ is averaged traveling time through the air calculated from the last 50 recorded signals. Recall the method to calculate the travel time from the signal waveform in the part 2.2.2.3. The dielectric constant is then obtained

Table 2.7: Ultrasound velocity measured in the two directions of dry and saturated samples.

UPV (m/s)	Marble		Non-marbe		Sireuil	
	direcion ⊥	direction //	direcion ⊥	direction //	direcion ⊥	direction //
Dry	3905 (±2.9%)	3776 (±5.7%)	3627 (±2.3%)	3991 (±3.3%)	2170 (±2.4%)	2094 (±2.3%)
Saturated	4145 (±1.9%)	4036 (±4.7%)	3707 (±1.9%)	4072 (±2.4%)	2074 (±1.8%)	1979 (±1.9%)

with the radar travel time through the specimen. Recall this equation (Eq 2.11):

$$\epsilon = (\frac{c}{v})^2 \tag{2.11}$$

Experimental results

As the same manner of presentation, the Fig 2.27 a-c show the evolution of dielectric constant in the 3 directions in terms of saturation for the marble, non-marble and Sireuil respectively. For the marble, the three lines are highly overlapped, indicating material anisotropy of the marble highlighted by the young modulus measurement, is not detected in terms of radar measurement. For the non-marble and sireuil, the two trended lines show a great similarity in the directions parallel to the bedding. While the dielectric constant value is generally higher in the direction perpendicular to bedding when degree of saturation exceeds 20%. Indeed, the coefficient of variation of measurement through the 3 directions is only 1.1% for all tests including 18 samples at 6 degrees of saturation. This small variation offers the possibility to use averaged dielectric constant value through the three directions as the dielectric constant of a sample in the modelling approach.

Besides, a summarized Fig 2.27(d) shows the averaged value of 6 samples of one type stone in the direction perpendicular or parallel to bedding plane. The vertical and horizontal error bar refers to the variability of material and the variability of the measured degree of saturation, respectively. It can be also observed that the variability of material is more important at a higher degree of saturation. The radar measurement is more sensitive to high water content.

Moreover, the trend line of dielectric constant in marble and non-marble shows a quite similarity. Unlike these two stones, this line in the sireuil is shaper resulted from the lowest value of sample in dry condition and the highest value of that in saturated condition. Indeed, the dielectric constant of a sample depends strongly on the water content. Because water has a high dielectric constant. As a polar molecule, water molecules electric dipoles are more easily to be aligned along the direction of an applied electric field[Physics, University of Louisiana at Monroe and McGRAW Jr., 2020]. On con-

trast, air has the poorest dielectric constant. As sireuil is a more porous stone, its dielectric constant is higher when the pore is full of water and it is lower when the pore is full of air.

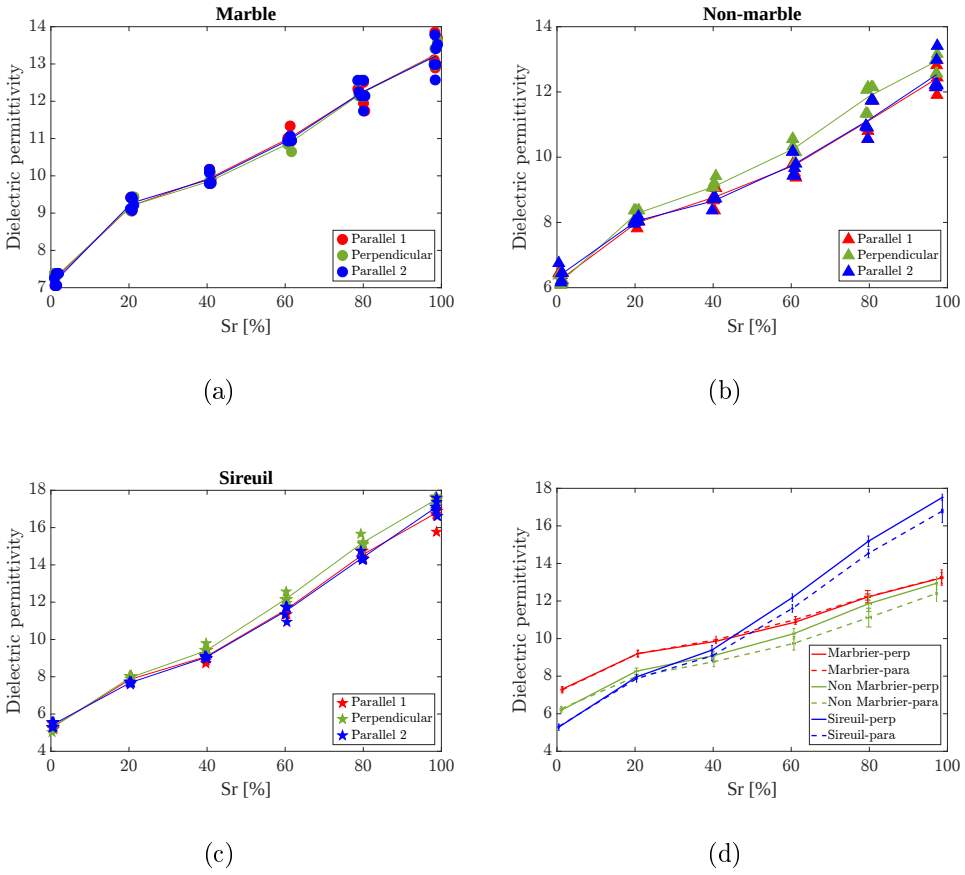

Figure 2.27: Evolution of dielectric permittivity of Sr in (a) marble (b) non-marble (c) sireuil (d) summarized results

Modeling dielectric permittivity

With respect to the degree of saturation, the increasing trend in the Fig 2.27(d) confirms the effect of water content on the dielectric permittivity. The permittivity of dry specimen is generally around 7 while that of saturated specimen increase to 18 for the most porous stone of the three against about 12 of the other type stones.

Besides, the model used in our study is the complex refractive index model (CRIM)[Laurens et al., 2005]. This model has already implanted in the concrete water content assessment and a promising agreement was observed between the modelled and measured data. The effective dielectric permittivity of each tested

specimen can be simulated, according to the Eq 2.12:

$$\sqrt{\varepsilon_r} = (1-\Phi)\sqrt{\varepsilon_m} + (1-S_w)\Phi\sqrt{\varepsilon_a} + S_w\Phi\sqrt{\varepsilon_{sw}} \tag{2.12}$$

Where:

- ϵ_r relative effective permittivity of resulting stone mixture
- ϵ_m relative permittivity of the solid phase (matrix)
- ϵ_a relative permittivity of the gaseous phase (air)
- ϵ_{sw} relative permittivity of the liquid phase (fresh water)
- Φ effective porosity
- S_w degree of saturation

The dielectric constant of air and fresh water are (at 1 and 80, according to the dielectric constant table[Martinez and Byrnes, 2001]. The estimation of the permittivity of solid phase is the key role to simulate the effective permittivity.

For each type stone, the Eq 2.12 can be also rearranged as the Eq 2.13, the subscripts i refers to the specimen number and the j refers to the degree of saturation. Φ_i is the porosity of each sample.

$$\sqrt{\varepsilon_{r,ij}} = (1-\Phi_i)\sqrt{\varepsilon_m} + (1-S_{w,j})\Phi\sqrt{\varepsilon_a} + S_{w,j}\Phi_i\sqrt{\varepsilon_{sw}} \tag{2.13}$$

Thus the $\sqrt{\epsilon_m}$ can be obtained by solving the equation. The ϵ_m as the permittivity of the solid phase of one type stone is then calculated. Besides, a homogenized permittivity is also estimated by using the same equation with Φ_i as an averaged porosity of all the samples.

A summarized Tab 2.8 demonstrate the estimated permittivity of solid phase of each type stone.

Table 2.8: Dielectric permittivity modeling parameter

	Marble	Non-marble	Sireuil	homogenized
ϵ_m	8.67	7.32	6.98	7.71

In the scatter plot of Fig 2.28, for each type stone, the averaged value of three directions of one tested specimen corresponds to one point. And the model line

plotted in dashed line is calculated from the equation with the averaged porosity of each type stone and the dielectric constant of fresh water and air. In order to evaluate the goodness of fit of model, two parameters are used: root mean squared error (RMSE) and coefficient of determination R^2, based on the experimental data and the model results.

The RMSE and the coefficient of determination R^2 are calculated based on the equations (Eq 2.14-Eq 2.15):

$$R^2 = \frac{\left[\left(\sigma_{mod,i} - \bar{\sigma}\right)\left(\sigma_{mod,i} - \bar{\sigma}\right)\right]^2}{\sum_{i=1}^{N}\left(\sigma_{mod,i} - \bar{\sigma}\right)^2 \sum_{i=1}^{N}\left(\sigma_{exp,i} - \bar{\sigma}\right)^2} \tag{2.14}$$

$$RMSE = \left[\frac{1}{N}\sum_{i=1}^{N}\left(\sigma_{mod,i} - \sigma_{exp,i}\right)^2\right]^{1/2} \tag{2.15}$$

Where the subscripts 'mod' and 'exp' refer to the model-based data and experimental data. $\bar{\sigma}$ Is the averaged value of relative dielectric constant calculated from the experimental test, 'i' indicates the number of tested samples. When the RMSE is lower and the coefficient of determination is closer to 1, better agreement is found between the model and experiment.

The modelling results show a good agreement with the experimental data, with a coefficient of determination more than 0.95. By using homogenized permittivity of solid phase, the RMSE increasing and the coefficient of determination decrease, however it is still in a reasonable range, suggesting that the homogenized permittivity of solid phase can be applied and the degree of saturation can be predicted for a given dielectric permittivity of a studied stone sample.

2.3.3.3 Influence of water on resistivity

Prior to the analysis of effect of water content on the resistivity, an estimation of the repeatability of the measurement is necessary to ensure the variability of the measurement is small enough for the following analysis. The averaged variability is calculated, taking account of 3 repeated measurement of resistivity through each direction for all the samples at all given degree of saturation. In total, 972 points are involved to the calculated of coefficient of variation of repeatability. The average coefficient of variation of repeatability is 0.73%, proving a good reproduction of the measurement.

Anisotropy effect on the resistivity

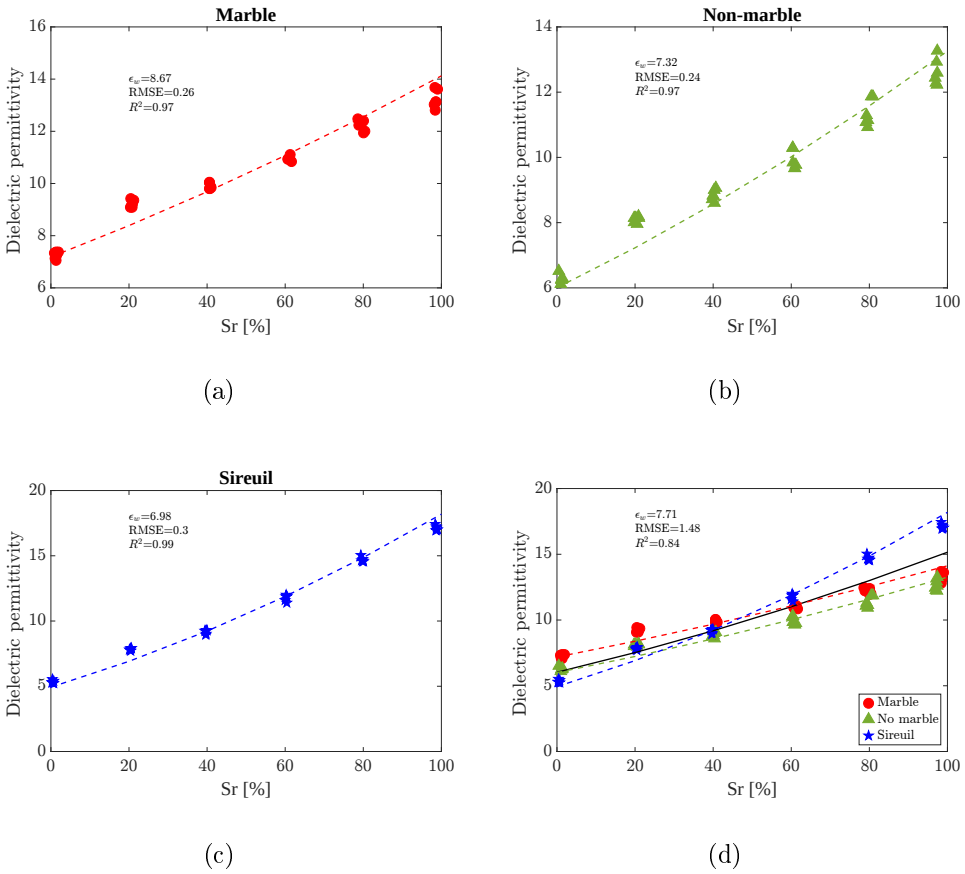

Figure 2.28: Modelling dielectric permittivity in (a) marble (b) non-marble (c) sireuil (d) all the type stone

Remember that for each type stone, the scatters in Fig 2.30 show the resistivity of material through one direction at a given degree saturation. The solid line links the averaged resistivity of 6 samples measured through one direction from different degree of saturation. For the marble and sireuil, no evident variation or small variation is observed in the three directions. For non-marble, the resistivity in the direction perpendicular is significantly higher than the direction parallel to the bedding for all the degrees of saturation.

It can be seen that there is a difference between the resistivity in the direction of parallel and perpendicular of bedding, particularly for the non-marble. Thus in the following analysis, we will separate the data in these two directions.

For the marble, no evident variation is found in the three directions. For the other types of stones, the resistivity in the direction of perpendicular is higher than the direction of parallel to the bedding. It can be seen that more dispersion of resistivity of different specimen is higher with a decreasing degree of saturation. In

the summarized Fig 2.29(d), the averaged value of resistivity in the face 1 and face 3 will represent the resistivity in the direction of parallel to bedding.

The effective porosity as a measure of the pore and void connectivity offers the fluid and current flow pathway. That is why the effective resistivity of sireuil is much less than the other two type stones due to a higher porosity (Fig 2.29(d)). However the porosity is a non-directional parameter which cannot describe the material's resistivity in different direction[Nabawy, 2018]. That is normal to obtain the resistivity in the direction parallel to bedding different from that in the direction perpendicular to bedding. Besides, more connectives of pore are accessible for a current flow in the direction parallel to bedding, suggesting the resistivity in this direction is smaller than that in the direction perpendicular to bedding. That explain the resistivity of non-marble in the parallel direction is similar as that in the marble, due to a close porosity.

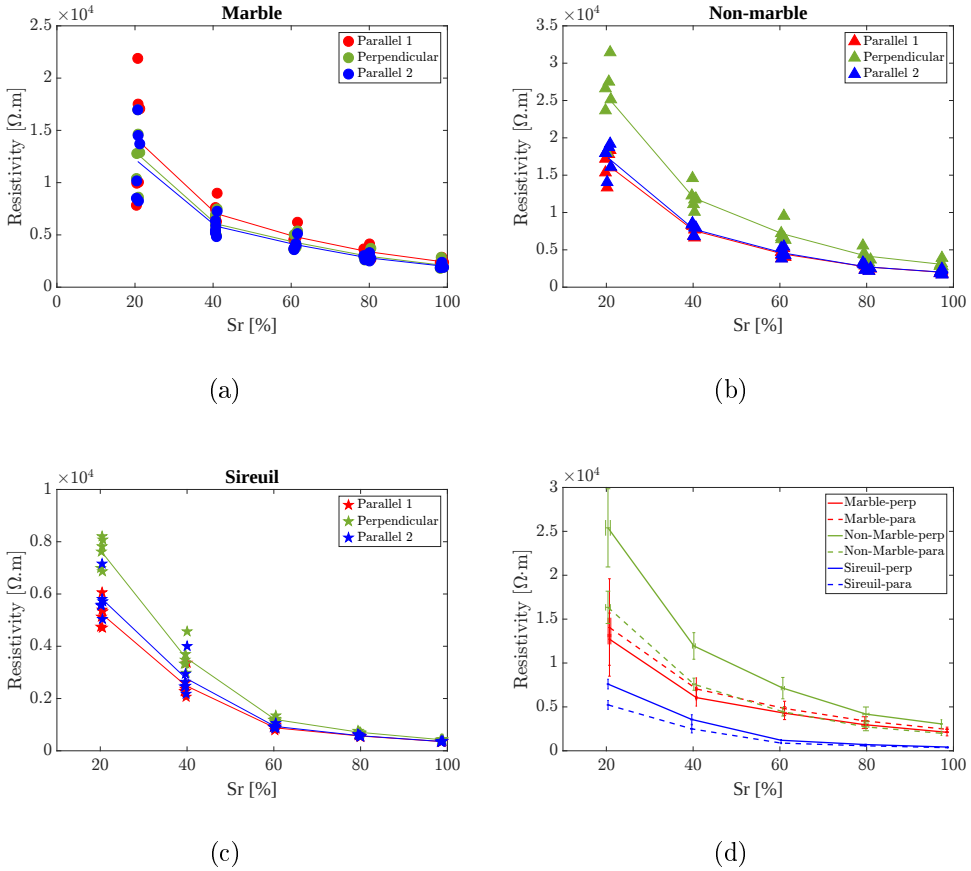

Figure 2.29: Evolution of resistivity of Sr in (a) marble (b) non-marble (c) sireuil (d) summaised results

Correlation between Degree of saturation and dielectric constant

The air medium is an insulator (i.e. infinitively resistive), the water solution resistivity is a function of the ionic concentration, and the resistivity of the solid grains is related to the electrical charges density at the surface of the constituents. These parameters affect the electrical resistivity. Electrical resistivity experiments have been performed to establish relationships between the electrical resistivity and each of these soil characteristics. And the modelling will enable a prediction of degree of saturation for a given resistivity of studied sample.

The modelling is performed on the resistivity of material measured through the direction perpendicular to bedding. The determination of the resistivity of water used in our test is derived from the Eq 2.16 called Archie's first law which is only employed on the saturated sample.

$$\rho_0 = \rho_w \Phi^{-m} \tag{2.16}$$

ρ_0 is resistivity of material, the ρ_w is the resistivity of water The factor m is the cementation index, the higher value m indicates the current is forced to take a tortuous pathways through the conducting fluid, resulting in an increasing resistivity. Which, when rearranged, becomes

$$log\rho_0 = log\rho_w - m\Phi \tag{2.17}$$

The log ρ_w can be obtain by a solving the linear equations, taking account the value of ρ_0 and Φ of all the saturated samples. Thus the resistivity can be also deducted. Then the Archie's second law (Eq 2.18) concerning the partial water saturation is used to deduce the both the cementation index m and the saturation exponent n.

$$\rho_0 = \rho_w \Phi^{-m} S_w^{-n} \tag{2.18}$$

Which, when rearranged, becomes

$$log\rho_0 = log\rho_w - m\Phi - nS_w \tag{2.19}$$

The two determined coefficient m and n differs from the type stone. They can be obtain by solving a series of linear equations with the value of S_w and Φ and its corresponding resistivity ρ_0 of each sample in the same type. Besides a homogenized factor m and n are also calculated applying for all the tested sample. The modelling data are summarized in the Tab 2.9. And the modeling results are exhibited in the Fig 2.30.

The scatter points refer to effective resistivity in the direction perpendicular to bedding planes. The modelling line is form resulting from a calculation of resistivity

Table 2.9: Resistivity modeling parameter

	Marbe	Non-marble	Sireuil	Homogezied
m	2.55	2.87	2.59	2.64
n	1.11	1.38	1.85	1.49
ρ_w (Ωm)	13.67			
RSME ($\times 10\hat{6}$)	1.87	6.95	0.57	14.56
R_2	0.88	0.92	0.95	0

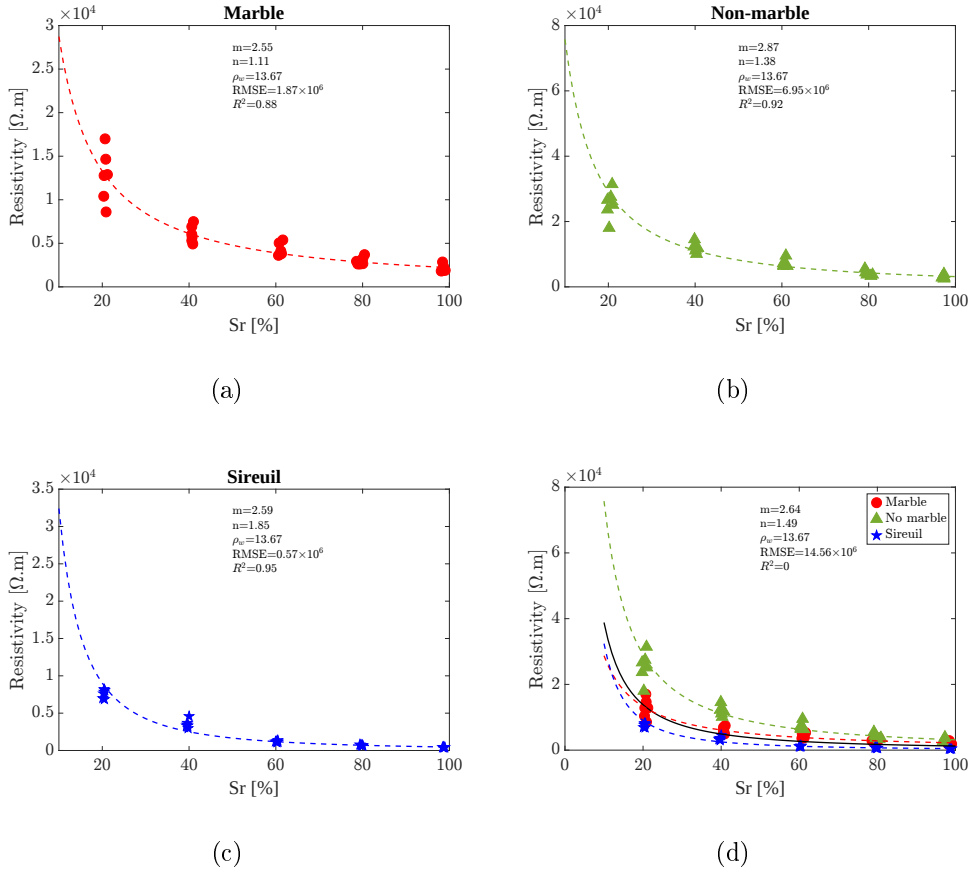

Figure 2.30: Modelling resistivity in (a) marble (b) non-marble (c) sireuil (d) summaised results in the perpendicular to the bedding

with an averaged porosity of each type sample as well its corresponding factor m and n.

A good agreement is observed between the modeling-estimated and the measured resistivity with the coefficient of determination 0.88, 0.92 and 0.95 for the marble, non-marble and sireuil, respectively. The last Fig 2.30(d) shows the modelling with homogenized coefficient pass through the 3 separate modelling line. However, the

great variability of resistivity of different type stones results in a poor coefficient of determination.

With regarding to the factor m, this value of non-marble is the highest among them, indicating this factor is not only related to the porosity of material. Indeed the anisotropy should be another factor increasing the resistivity as explained previously. Besides, a factor n shows an increasing trend with the porosity.

2.3.4 Mechanical characterization by ND parameters

2.3.4.1 Mechanical characterization by ultrasound velocity

In the previous part, the relationship between the ND parameters and the degree of saturation is discussed. And it is observed water content shows a strong influence on weakening the modulus of elasticity and the compressive strength. In this part, we will discover the relationship between the ND parameter and the modulus and compressive strength.

The relation between the ultrasound velocity and the modulus of elasticity of dry and saturated sample are exhibited in the Fig 2.31, correspondingly. At the degree of saturation of 0%, two parts of points are characterized, the modulus of elasticity of sireuil and its corresponding ultrasound velocity are both at a low value, compared with that of the other type of stones. It is difficult to separate the marble and non-marble. The similar observation are observed on the saturate samples.

Regarding to the compressive strength of the dry and saturated samples (Fig 2.32). The ultrasound velocity shows an increasing trend linked with the compressive strength in the both degree of saturation. However, a great variability of strength is observed at a relative constant ultrasound velocity. In the basis of the observations, the ultrasound shows an increasing trend in both the mechanical parameters, besides the ultrasound is more sensitive to the modulus increasing than the compressive strength. Unfortunately, 3 non-marble sample lacked the NDT tests, leading to an incomplete evolution in the ND parameters and compressive strength.

2.3.4.2 Mechanical characterization by dielectric permittivity

Unlike the similar trend of velocity of dry or saturated sample in terms of modulus of elasticity, the dielectric permittivity of dry and saturated sample shows an inversing trend in the Fig 2.33. For the dry samples, the dielectric permittivity

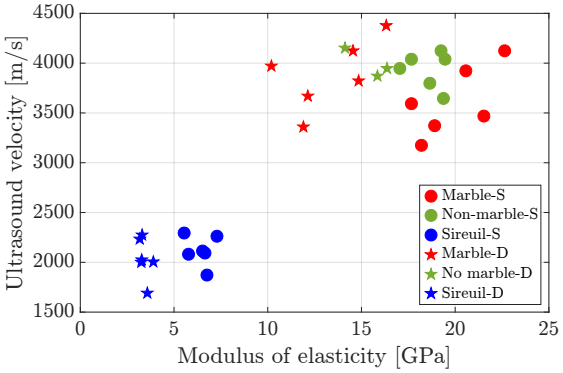

Figure 2.31: Correlation between ultrasound velocity and modulus of elasticity of dry(D) and saturated(S) samples

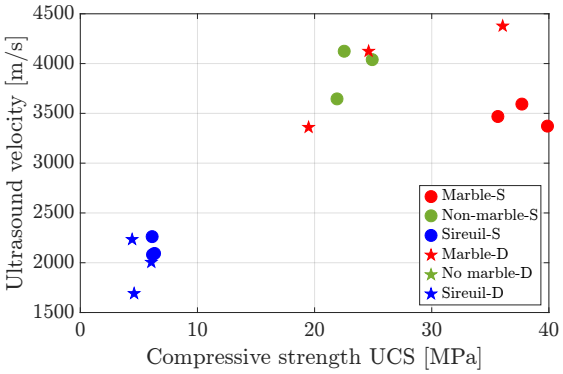

Figure 2.32: Correlation between ultrasound velocity and compressive strength of dry(D) and saturated(S) samples

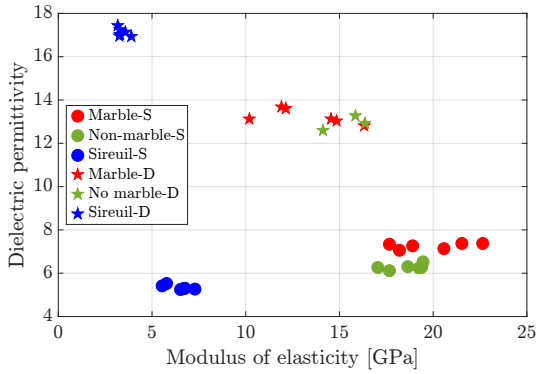

Figure 2.33: Correlation between dielectric permittivity and modulus of elasticity of dry(D) and saturated(S) samples

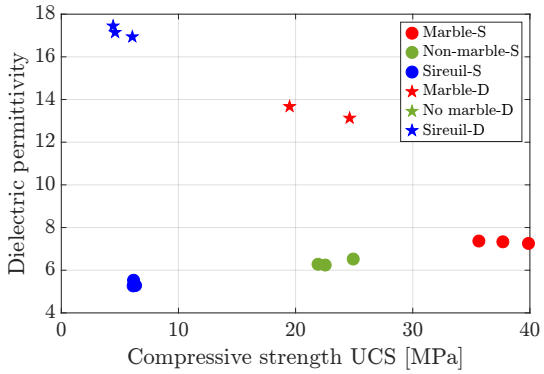

Figure 2.34: Correlation between dielectric permittivity and compressive strength of dry(D) and saturated(S) samples

increases with higher modulus of elasticity. While the negative trend of dielectric permittivity is linked with and increasing modulus. The inverse trend is related to the presence of water, with the same pore volume, water shows a good ability to be polarized by the external electric field, thus increasing the dielectric permittivity of bulk material. Besides, for the saturated samples, the dielectric permittivity of non-marble is less than that of marble, indicating the permittivity is not only influenced by the porosity, it is probably related to the pore distribution and pore orientation[Endres and Bertrand, 2006]. These factors also influence the modulus with same trend as in the dielectric permittivity.

The similar trends exhibit a good correlation between the dielectric permittivity

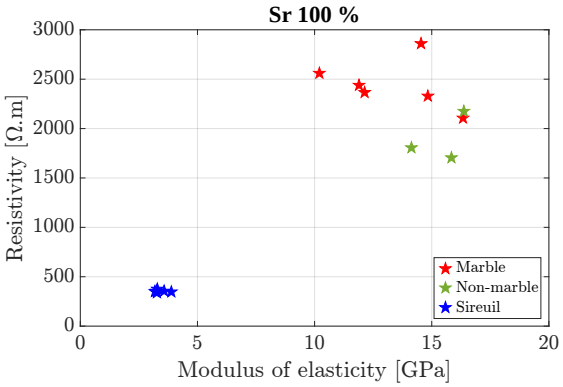

Figure 2.35: Correlation between resistivity and modulus of elasticity of saturated samples

with the compressive strength in both dry and saturated condition (Fig 2.34).

2.3.4.3 Mechanical characterization by resistivity

Due to the lack of measurement of resistivity of dry sample, the Fig 2.35 and Fig 2.36 show the relationship of resistivity of saturated sample and the modulus and compressive strength, respectively. Greater value of resistivity is measured with greater Modulus of elasticity. However an evident variability both in the modulus and the resistivity when the stone shows a great difference in the porosity.

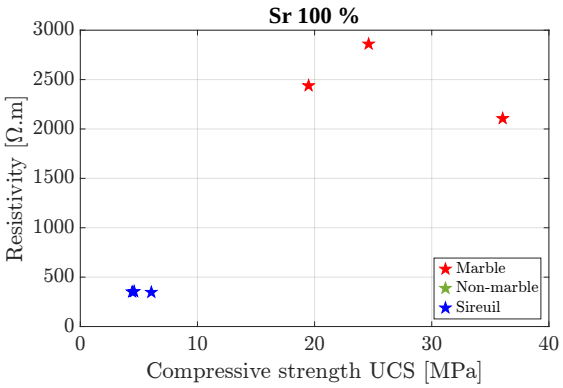

Figure 2.36: Correlation between resistivity and compressive strength of saturated samples

2.4 Conclusion

In this chapter, the influence of water on the mechanical characteristic of stone have been investigated. Firstly, the physic and mechanical properties as the porosity, the bulk density were obtained from a series of test. And a good correlation was found between the porosity and the bulk density. Then the modulus of elasticity of stone sample at different degree of saturation were derived from the load-displacement curve. These experimental curve were obtained from the compressive tests, which were also carried out in two directions: parallel and perpendicular to the bedding. It shows that the modulus of elasticity in direction perpendicular to the bedding is generally greater than that in direction parallel to bedding at the tested degree of saturation. And generally, the modulus of elasticity decreases with an increasing degree of saturation. However, because of the anisotropy of non-marble, the modulus is more sensitive to the degree of saturation in the parallel direction than the perpendicular directions. Besides the correlation between the porosity and the modulus of elasticity are consistent with literature data, showing the deformability characteristic decreases as the porosity increases, following an exponential trend.

A series of compressive test were carried out the stone sample either at dry or at full saturated state to obtain the compressive strength of each sample at one state. The compressive at dry state is greater than that at full saturated state. Besides, the relationship between the compressive strength and the modulus of elasticity is described by the empirical correlation. The influence of water on the no-destructive measurement was also investigated. For the ultrasonic method, the ultrasound velocity was measured through the different sides at the variable degree of saturation. The results show that no significant variability in the velocity in terms of degree of saturation for the low porous stone. For the stone with relative higher porosity, the evolution of ultrasound velocity follows a trend in the form of 'convex' with the increasing water content.

Regarding to the radar, the dielectric permittivity of a studied sample is mainly influenced by the presence of water. With the increasing degree of saturation, the permittivity of material shows a relative linear increasing value. A modelling is also implanted, comparing with the experimental-measured data. A good agreement is observed based on the coefficient of determination and RMSE.

With reference to the resistivity, an exponential relation is outlined, with a decrease trend as the degree of saturation increases. Comparing with the measured resistivity, the model-calculated resistivity is well predicted by the model of each type stone. However, this model is not a general model for all type stones, because

of the great variability of resistivity of stone under a relativity dry condition.

Besides, the relations between the ND parameters and modulus of elasticity and compressive strength under dry and saturated condition are also discussed, supporting the observations and conclusion obtain in the previous part.

Chapter 3

Damage monitoring at an assemblage scale

3.1 Introduction

The previous chapter studies the mechanical properties of stone and the material deterioration with the increasing degree of saturation. In fact, in the most of time the bond between the stone bloc and mortar is the weakest link[Van der Pluijm, 1997]. And as presented in the literature review, cracking due to tensile or shear stress is in most cases the major cause of failure. The tensile failure and shear failure are often observed at the bloc-mortar interface in masonry structure. Several methods can be used to characterize the damage occurring in the block mortar interface. The Acoustic emission technique (AET) is one of the non-destructive methods usually implemented to investigate the damage onset, damage evolution, damage nature and damage location in civil engineering structures[Boniface et al., 2019],[Carpinteri and Lacidogna, 2007],
[Ghiassi et al., 2014],[Reboul et al., 2020]. In this chapter, these two failure modes are studied by the means of AET for a better understanding of the failure process of interface under tensile and shear loading.

We will firstly introduce the experimental tests, including direct tensile test and shear test. The direct tensile test is performed under monotone and cyclic loading of which limited number is found in the existing research literature. The mechanical behavior of interface in these two tests is discussed, according to the cyclic load-displacement curve. Then, the acoustic emission parameters will be studied to be correlated with the damage process, underlying more

detailed information in the failure process. Some AE parameters have already proved the capacity of AET for damage assessment in masonry structures [De Santis and Tomor, 2013],[Ghiassi et al., 2014],[Tomor and Verstrynge, 2013]. Besides the discrimination of signal source will also be studied in these tests.

The direct tensile test will be firstly studied. Some nonlinear phenomena as the stiffness degradation residual displacement and hysteresis effect will be discussed. This observation helps a further understanding of the material deterioration of masonry assemblage subjected to tensile loading. The AET is used to monitor the damage process, the parameters such as the hits number and hits' energy provide another insight to explain the damage process, particularly at the softening phase. Besides, another ultrasonic method is also studied, and compared with AE parameters analysis.

Regarding to the shear test, the specimen submitted a shear loading under a normal compressive stress applied perpendicularly to the bed mortar interface. Thus, the damage process as well as friction phase will be discussed by the mean of AET. The mechanical behavior of materiel and the AE signature are also discussed by varying the compressive stress level.

The discrimination of signals from the different sources (micro crack, macro crack and friction) is presented. The discrimination of signals from the micro to macro crack is studied only in the tensile test, of which the friction is seldom observed. Then, the discrimination of signals from the crack to friction is based on the analysis of AE parameters by comparing that in tensile and shear test.

Before presenting these two different tests, the specimen and the materiel we used in the tests will be firstly introduced.

3.2 Materials and materiel

3.2.1 Specimen preparation

The specimen used in the tensile test was composed by two limestone blocks bonded by thin lime mortar as shown in Fig 3.1(a). Stone blocks of $0.07\times0.1\times0.1m^3$ dimensions were carried from the Frontenac limestone quarry. The specimen used in shear test (Fig 3.1(b)) was composed by three blocks ($0.1\times0.1\times0.1m^3$) bonded by the same lime mortar. Their main mechanical characteristic are 9.5 MPa average compressive strength (Coefficient of Variation CV=26%) and 11.1 GPa average

Young's Modulus (CV=15%)[Bisoffi-Sauve, 2016].

Bed joint thickness was 7 mm and the mortar was realized using crushed fine sand (0-2 mm), Hydraulic Lime (NHL3.5) and water. Proportions by volume of the lime, sand and water in the mixture are estimated by a master stonemason on the basis to 1 part of lime and 3 parts of sand. After that, water was added in the mixture until reaching desired traditional workability. The proportions of compositions for the fresh mortar are shown in Tab 3.1. Standard material testing [NF EN 1015-11, 2000] indicated 1.9 MPa average compressive strength (CV=12%) and 3.32 GPa average Young's Modulus (CV=16%)[Bisoffi-Sauve, 2016] for this mortar. Specimens were cured at ambient temperature for 3 months before testing.

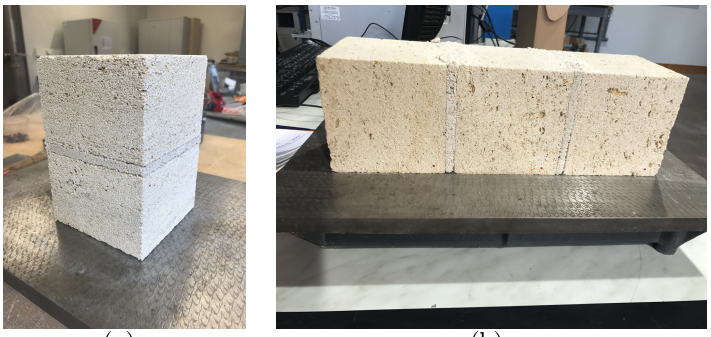

(a) (b)

Figure 3.1: Specimen used in (a) tensile/(b) shear test

Table 3.1: Designed mortar composition proportions

Volume (L)	Total weight (g)	Lime NHL3.5(g)	Sand (g)	Water (g)
1	2018.6	233.2	1445.4	340

3.2.2 Acoustic emission technique

The acquisition system of AET was equipped with a Peripheral Component interface (PCI) with 8 channels boards for the data acquisition and a software for data collection and processing. The setup parameters, according to the signal recorded by Pencil Lead break (PLB), were given in Tab 3.2. These parameters are crucial to determine each recorded hit[Moradian and Li, 2017]. It should be noted that the peak definition time (PDT) is the duration between the first threshold crossing and the peak amplitude, and the hit is automatically ended when an amount time equal to the hit definition time (HDT) has elapsed without any threshold crossings, during the hit lockout time (HLT), any new threshold crossings which could start a new hit are ignored. These important setup parameters are demonstrated in the Fig 3.2.

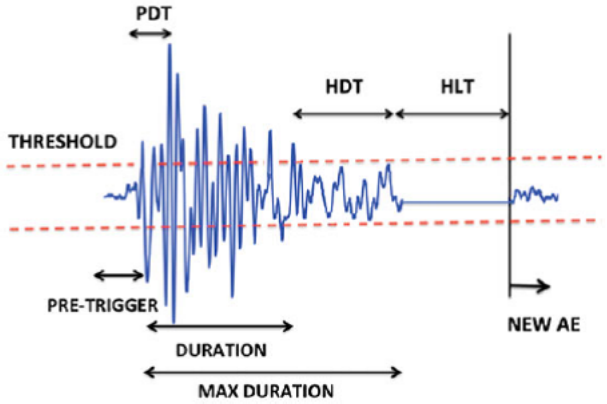

Figure 3.2: Important parameters[Moradian and Li, 2017] in hit-based data acquisition setup

Table 3.2: AE setup parameter

Sampling rate	1MHz
Waveform time length	2048μs
Pre-trigger	256μs
PDT	200μs
HDT	800μs
HLT	1000μs

The sensors with a resonant frequency of about 150 kHz were thinly glued by a silicone grease to ensure a good contact. The pre-amplifier gain was set at 40dB with amplitude threshold of 35dB. The signal was filtered by a pass-band filter ranging 100-400 kHz, to eliminate the no-sensitive frequencies signal and noise. A typical recorded signal in time and frequency domain is presented in Fig 3.3.

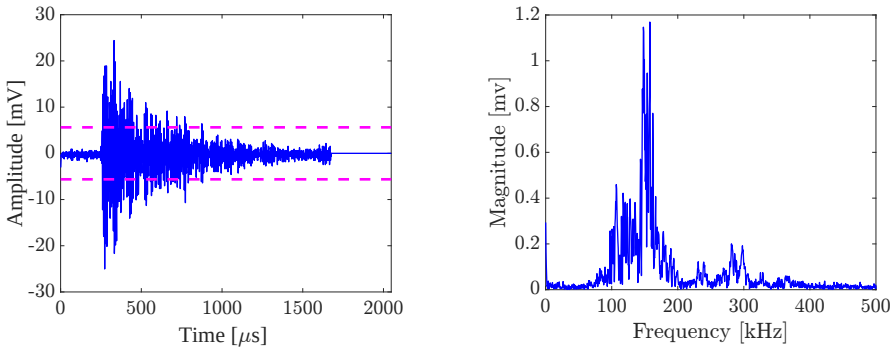

(a) (b)

Figure 3.3: A representative signal in the time domain and frequency domain

3.3 Tensile test

in this section, the performance of AET on a series of direct tensile tests under monotonic and cyclic loadings are analyzed to get a better understanding of fracture damage development in a duo of limestone blocks assembled by thin lime mortar joint. Different AE indices (hit number and hit energy) are correlated with damage accumulation to identify its response to tensile loading and the relation between the fracture energy and the recorded AE energy is analyzed. Some AE parameters as amplitude and duration are studied to show the distinctive signature of acoustic emission reflected to failure mode. A method of discrimination from micro crack to macro crack is also proposed.

3.3.1 Experimental equipment setup

Two types of tensile tests were carried out on the duo samples: 5 monotonic tests (samples T1 to T5) and 4 cyclic loading tests (samples TC1 to TC4). For each test, acoustic emission technique (AET) was performed. The specimens and setup configuration were the same in both two types of tests and are analogous to those proposed by [Bisoffi-Sauve, 2016] and [Venzal, 2020].

Under a compressive preloading of about 0.2 MPa, the specimen was glued inside the upper and down metallic cage, the used resin glue gets a good adherence quickly to assure the tensile loading during the whole test. The MTS machine applied a vertical load on the specimen, in a perpendicular direction of the bed mortar. At four corners of the specimen, four displacement transducers (HBM, accuracy of 0.5 μm, measurement range of 5 mm) were positioned at the vicinity of the upper and lower interface block-mortar and crossing the bed-mortar interface to measure crack opening displacement, which was expected to initialize at one of the four corners (Fig 3.4). The mechanical test was displacement-rate controlled, ensuring the post-peak softening behavior of a completed load-displacement curve, required for the determination of fracture energy. The test set-up and instruments are shown in Fig 3.4.

Four AE sensors, formed into three-dimensional space were placed at the four corners of specimen, near the expected initial crack (Fig 3.4). They were distributed at two sides of mortar, to localize the acoustic events at a minimized error. Each sensor was deviated 20mm from the boundary of stone and the interface to avoid side effects. Before each test, the PLB test was necessary to check the coupling of sensor and wave attenuation in the tested specimen. Ultrasonic tests using the same

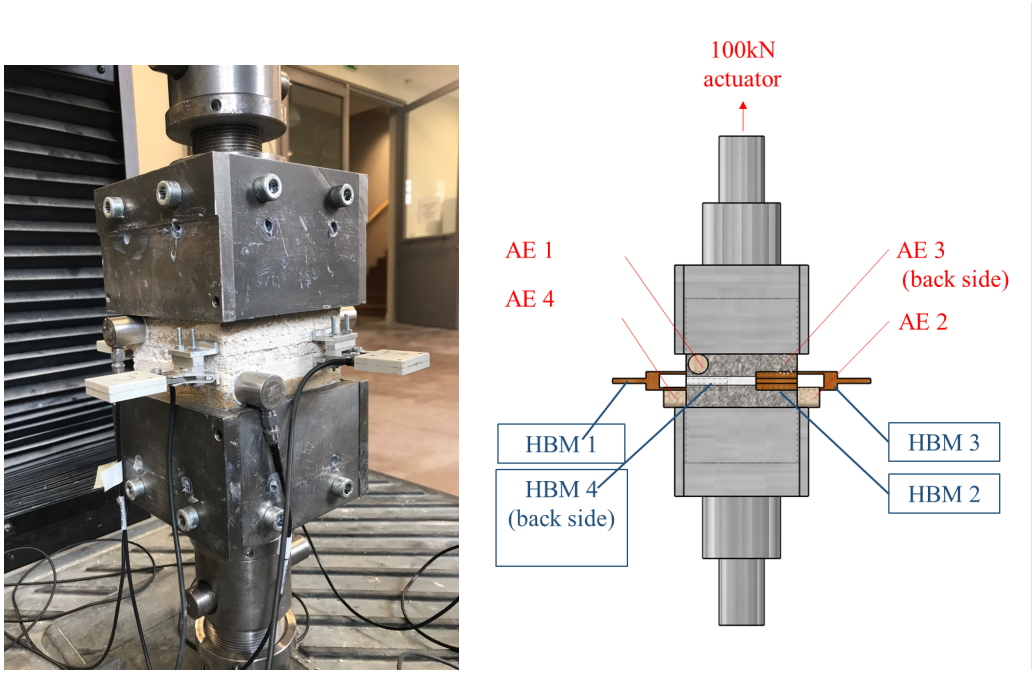

(a) (b)

Figure 3.4: Test setup and instrumentation.

sensors was also carried out preliminarily to ensure no variation of sensor sensitivity. In the cyclic test, the ultrasonic test was also carried out between each two cycles to show the signal evolution between the cycles recorded at the null stress level.

3.3.2 Load test procedure

Two loading regimes were performed in this study. In monotone tensile test, the initial displacement rate was set at a low value of 0.3μm/min to avoid instability phenomena at peak load and to ensure the nominal displacement. Then, the rate was doubled in each 9 minutes to reduce the whole test duration when the load peak was reached. Finally, the rate at the end of the test was 25μm/min. The test was ended automatically when the averaged displacement reachedt0.8mm, ensuring that the interface was separated completely for all test. In the cyclic test, before the peak stress, the specimen was loaded to 0.018 MPa and 0.036 MPa and then unloaded at the first two cycles by applying a displacement rate of 0.3μm/min. Nine cycles were involved at the post-peak phase. For each cycle, the specimen was firstly loaded to the same stress level as the unloading stress of previous cycle. During the softening phase, the decreasing stress corresponded to 10% of peak stress of overall test. And then the specimen was unloaded to a zero-stress level. Each cycle is performed for

a constant displacement rate but this rate was set varying from 0.6 μm/min to 25 μm/min in order to ensure an equal duration for each cycle thus limiting effects of creep phenomena.

3.3.3 Results and discussions

3.3.3.1 Mechanic behavior

Fig 3.5 exhibits the mechanical behavior which is firstly characterized by tensile stress-displacement curve, containing 5 monotonic tests and 4 envelope curves corresponding to cyclic tests. The displacement is estimated as the averaged value of crack opening displacement measured by the four displacement transducers (HBM). These monotonic and cyclic envelope curves show a typical quasi-brittle material fracture process. An elastic domain before the peak stress followed by a softening curve beyond the peak stress. However, some irregular points can be pointed out at the softening part, due to the non-uniform crack opening at the corner resulted from specimen rotation, that have been reported by other researchers[Almeida et al., 2014],[Lourenço et al., 2005]. All the curves exhibit a quite similar tendency, regardless of the maximum stress. In particular, it is observed that the cyclic envelope curves show a similar tendency as the monotonic ones. As a consequence, it can be assumed that the imposed cyclic loading procedure does not influence the typical load-displacement response observed from the monotonic loading test. The initial elastic stiffness of each specimen is defined as the best-fit slope in ascending branch, resulted from the least squares method. Moreover, the mode I fracture energy is calculated as the area under the stress-displacement curve. The detailed information with respect to the peak load, stiffness, and fracture energy are summarized in Tab 3.3. The difference in peak strength between specimens is related to the variability of the used materials and manual preparation of samples.

For a further understanding of the nonlinear phenomenon occurring along a block-mortar interface subjected to tensile load, the mechanical behavior observed from cyclic loading is investigated in the following parts. Fig 3.6 shows the global cyclic test response of the TC2 sample. Prior to the peak stress, the material exhibits an elastic behavior as shown by the linear domain observed in Figure 3. Beyond the peak stress, the softening phase formed by the envelope curve is observed as similar as that in the monotonic test. For each cycle plotted through different colors in Fig 3.6, three distinctive phases can be identified, including loading, softening and unloading phase. Moreover, a hysteresis effect can be observed from the loop formed

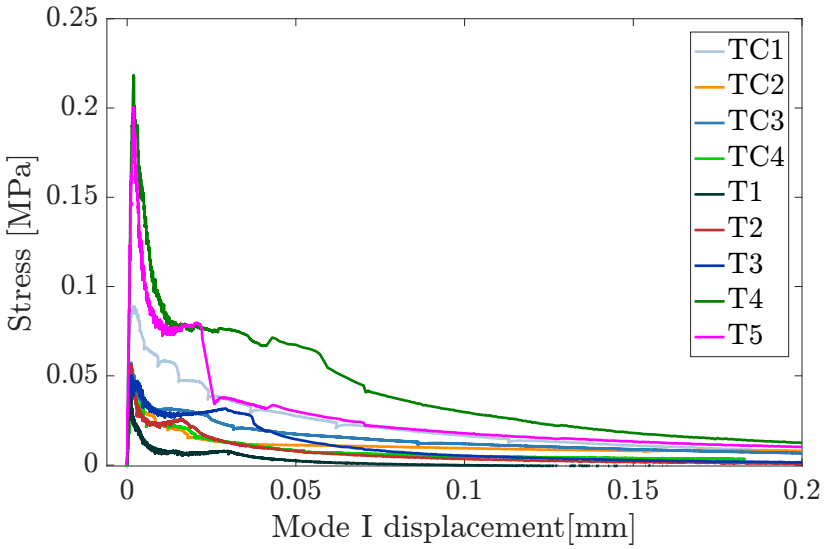

Figure 3.5: Mode I Stress vs. displacement curves of mortar/unit interface

Table 3.3: Mode I mechanical properties of mortar/unit interface

Specimen	**Peak stress (MPa)**	**Stiffness K0(Mpa/mm)**	**Fracture energy (J/m2)**
TC1	0.089	158.8	4.95
TC2	0.045	76.9	2.6
TC3	0.057	90.1	3.24
TC4	0.046	33.5	1.48
T1	0.048	79.7	0.28
T2	0.056	64.7	1.28
T3	0.05	63	2.31
T4	0.218	147.9	10.46
T5	0.201	128.6	7.23
Mean (CV)	0.090 (±72%)	93.6 (±43%)	3.76 (±82%)

during the unloading of a given cycle i and the loading of the following cycle i+1.

Fig 3.7 focuses on the mechanical behavior exhibited by the cycle 7 (i =7) which can be considered as the typical mechanical response observed from each cycle located in the post-peak behavior. From the point A, the sample is loaded and exhibits a maximum stress at the point B from which the softening behavior takes place. The softening branch of the cycle i ends at the point C which corresponds to the point from which the sample is unloaded up to a zero-stress corresponding to the point D (end of the cycle i). This procedure of loading-unloading was repeated 9 times in the post-peak phase. The initial stiffness of this typical cycle i, plotted from a blue solid line in Fig 3.7, is determined as the slope of approximate linear part of ascending

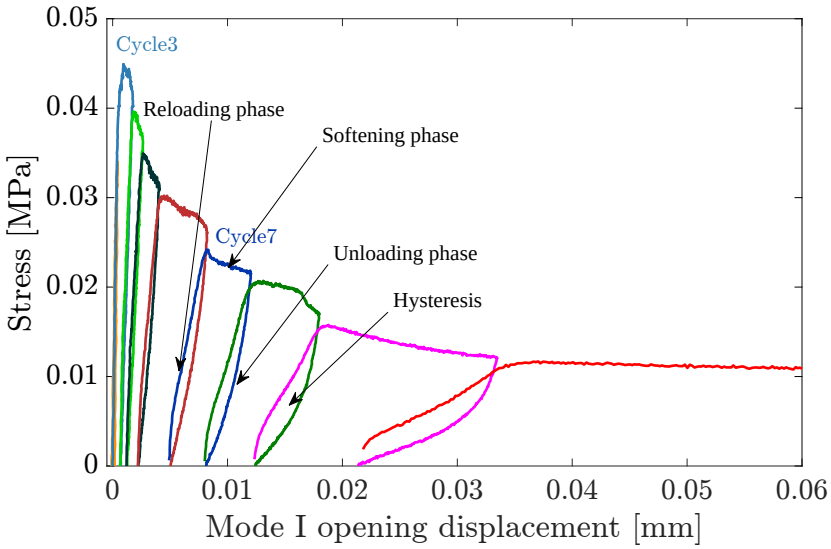

Figure 3.6: Mode I stress vs. displacement curves in cyclic test on TC2 sample.

phase where the material shows an elastic behavior. The bounds of this linear part are determined as following: the starting point was chosen manually and the ending point was determined corresponding to a good-fit linear regression, resulted from least squares method. It can be observed in Fig 3.7 that the intersection between the straight line of slope Ki and the previous cycle i-1 corresponds approximately to the unloading point of the cycle i-1. As a consequence, the initial stiffness Ki of a given cycle i corresponds to the elastic stiffness of the sample at the onset of cycle i or, similarly, to the elastic stiffness of the sample corresponding to the unloading of the previous cycle i-1. This emphasizes the fact that the slope of the unloading branch of a given cycle does not reflect the elastic stiffness of the specimen because of hysteresis effect caused by crack closure problem and/or dissipative mechanism such as plasticity or more exactly friction which takes place in fracture process zone. Thus, in the absence of hysteresis effect, the residual displacement of a given cycle i will not be associated to the abscissa of the point D but should be estimated from the displacement corresponding to the intersection of the straight line of slope Ki+1 and the abscissa axis, i.e., the abscissa of the point D' (analogously, the residual displacement of cycle i-1 will correspond to the abscissa of the point A' as shown in Fig 3.7).

In order to estimate the damage level emphasized by the decreasing of the elastic stiffness observed from successive cycles, the damage variable d (scalar) is usually used and is defined as:

$$d = 1 - \frac{K_i}{K_0} \tag{3.1}$$

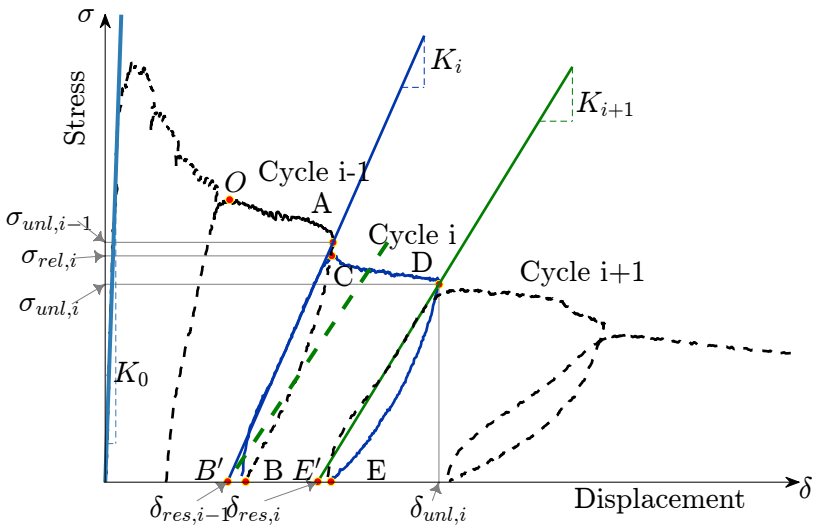

Figure 3.7: Illustration of elastic stiffness in Mode I stress vs. displacement curves in cyclic test on TC2 sample

It varies from 0 to 1, corresponding to undamaged and complete failure, respectively.

The loading-unloading cycle highlights two phenomena: the stiffness of the sample decreases progressively during the test which is caused by rising quasi-brittle damage, meanwhile an irreversible displacement δ_{res} takes place induced by another dissipative mechanisms such as plasticity or more exactly friction phenomenon which takes place between the microcrack lips and during the grain locking mechanism leading to crack bridging phenomenon. According to the loading-unloading cycles, residual displacements δ_{res} are almost negligible in the pre-peak regime while they increase strongly in the post-peak one. In the same way, hysteresis loops are more notable in post-pic regime than in the pre-peak one.

The residual displacement δ_{res} is a relevant parameter in the description of the quasi-brittle fracture of the block-mortar interface. However, the evolution of the residual displacement cannot be accurately observed without performing a cyclic fracture test. As a consequence, it appears interesting to study the relationship between the residual displacement δ_{res} and the unloading displacement δ_{unl} which corresponds to the displacement of the envelop curve of the block-mortar interface, i.e., the response which will be obtained in the case of a monotonic fracture test. Thus, the evolution of the residual displacement δ_{res} is plotted in Fig 3.8 with respect to the unloading displacement δ_{unl} ant it can be observed a strong correlation between both these quantities. In the same way, the elastic stiffness can be well

predicted from unloading displacement according to an exponential correlation as shown in Fig 3.9(a). In addition, the damage variable d, estimated according to Eq 3.1 is also correlated to the unloading displacement as shown in Fig 3.9(b).

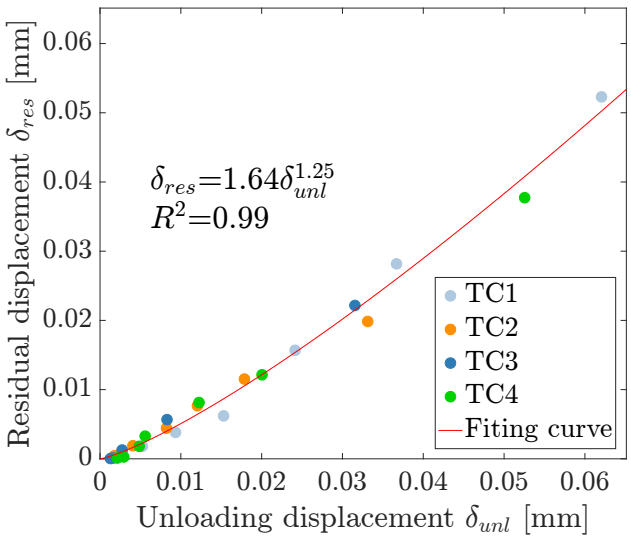

Figure 3.8: Correlation between residual and unloading displacements

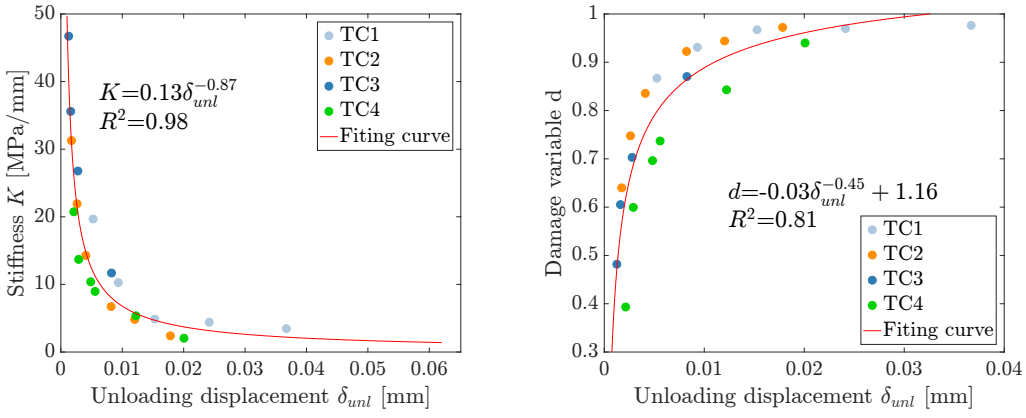

(a) (b)

Figure 3.9: (a) Stiffness and (b) damage variable vs. unloading displacement

If the correlations shown in Fig 3.7 and Fig 3.9 would be confirmed in the future from assembly of different natures of stone blocks and mortars, then these correlations should be useful to calibrate mechanical model from simple monotonic fracture tests.

From the previous study, it can be observed that envelope curve derived from the cyclic test are similar as the load-displacement curve of monotonic tensile test.

However, from cyclic test, the stiffness evolution as well as the residual displacement can be obtained only in each cycle. This detailed information enables a better understanding of the material deterioration under tensile loading and these relations can be implemented in a mechanical modeling in a possible future study.

3.3.3.2 Acoustic emission activities analysis

Signal filtering

An important step is to remove the undesired signal before the analysis to quantify the damage severity or classify the damage source. The unwanted signals are noisy signals or signals with too long duration, noise can be generated from external environment source or due to instrumentation sources, including thermal noise, leakage currents instability etc. A filtering on duration (>10 μs) and on counts (>3) was applied, due to the low magnitude that could be related to a background noise[Traore et al., 2017]. Examples of filtered signal are shown in Fig 3.10. The dashed magenta line illustrates the threshold corresponding to 35dB.The cause of long signal is complex, some of these are caused by the superposition of more than one signal (Fig 3.10(a)), resulted from the inappropriate setup parameter, however it is impossible to adjust the introductory parameter for each hit. Some of these long signals (Fig 3.10(b)) are probably resulted from a continuous movement as sliding, which remains difficult to identify. However, in direct tensile test, most signals are induced by tensile damage process, which will be discussed in the following parts, and the signal with extreme long duration is not discussed in our study. Thus, another filtering on rise time ($<500\mu$s) and on duration ($<2000\mu$s) is also applied, ensuring only the appropriate signals are studied. These results demonstrate the importance of waveforms treatment before analysis of the signal parameters.

Monotonic test

In order to analyze the damage process of masonry, the typical relation between the AE hits number and energy, stress versus mode I opening displacement under monotonic loading is illustrated in Fig 3.11. The displacement ends at 0.35mm corresponding to a null stress is shown in this figure. Each bar corresponds to the sum of hit number or the sum of AE absolute energy within one micrometer. The hits number is the first parameter to be considered since no dislocation generates no signal. Therefore this parameter could be correlated with cracking incidents. The signal emitted from micro cracking is generally less energetic than that from the macro crack formation and propagation, since the AE signal energy depends on the dislocation displacement. Three stages can be identified according to the hit number

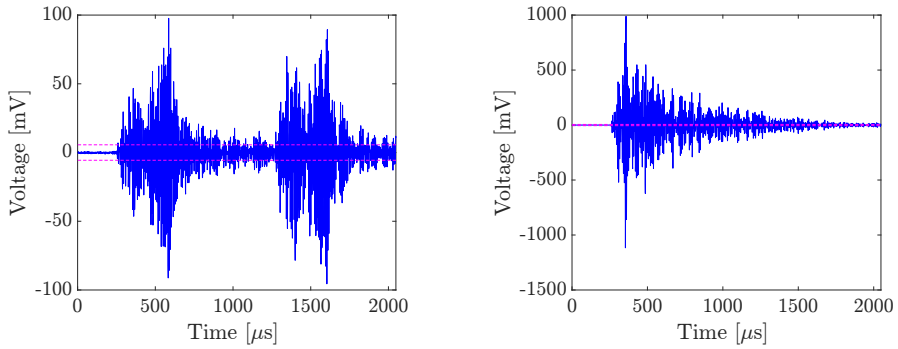

(a) (b)

Figure 3.10: Examples of filtered signal (a) superposition of signal (b) signal with long duration

and hit energy.

Elastic stage and micro cracking initiation (Path OA). At the early stage, no signal was detected, indicating at the elastic stage, no damage is induced and no dislocation takes place under the loading. However, the stress-displacement curve was no longer linear from the 90% of peak stress, at this interval up to peak stress, few signals with very low energy were recorded, indicating the initiation of micro crack in the interface, or a small quantity of matrix cracking in the mortar.

Macro crack coalescence (Path AB): at the softening stage, the stress dropped sharply and then more slowly, a continuously increasing number of AE signals were observed. However, from the energy of AE signal, it is interesting to show that the energy is smaller at the peak stress zone than the latter descending curve, as the masonry is a quasi-brittle material, when a slight load applied after the peak stress, the micro cracking dominates at the peak stress and then the crack is initially formed resulting from micro crack bridging, which emit more energetic signals.

Macro crack propagation (Path BC): at this stage, the load dropped more slowly, less signals were observed continuously, however, at several instant, signals with very high energy were observed, indicating crack propagation with more formed cracks or micro friction inducing potential residual displacement, which have be reported by [Carpinteri et al., 2007],[Ghiassi et al., 2014]. It should be noticed that the interface could be considered to be separated completely at the point C, beyond this point few signals with low energy, resulting from imbalance of specimen, crack roughness and the spring force of extensometer was not taken into account.

As the studied specimen is a composite and a heterogeneous natural material,

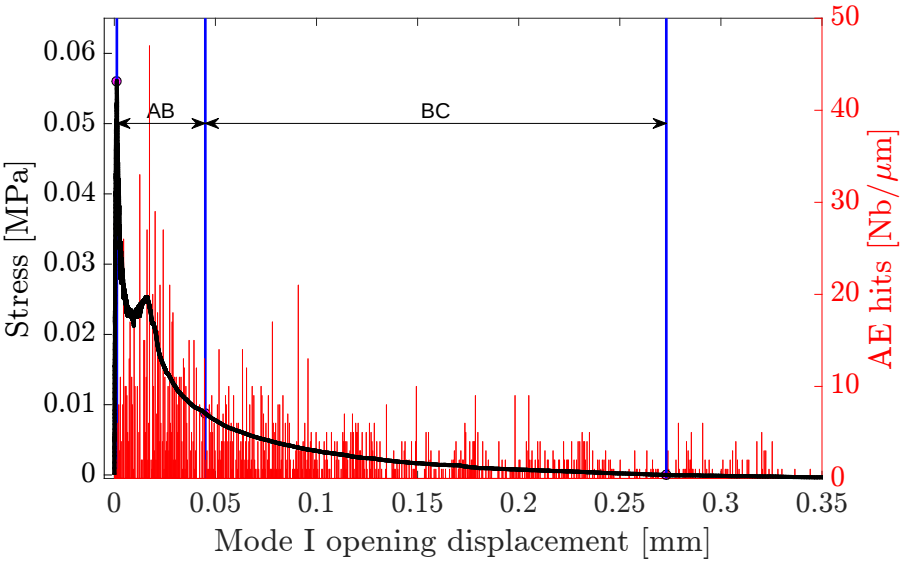

(a)

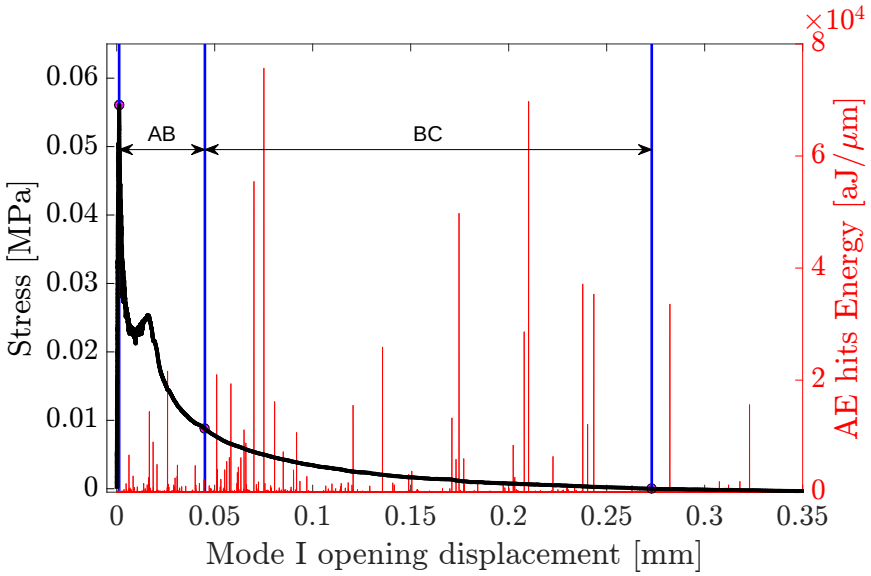

(b)

Figure 3.11: Stress and AE hit number/ AE energy vs. displacement of specimen T2

the cracking is impossible to be identical between different tests. Besides the attenuation due to material heterogeneity, wave propagation path and the presence of crack affect signal detection as well as signal waveform, consequently the AE hits number and its energy are also influenced. However, the cumulative curves of hits number and energy after data normalization seem similar between each direct

tensile test according to Fig 3.12. The slope of cumulative curve decreases gradually, corresponding to increasing deterioration, until the failure of material, the interface is completely separated and the slope sifts to almost horizontal and stable. As the same reason, the energy curves are also accumulated and normalized. These curves are not as smooth as the former. Their evolution increases steeply, corresponding to the moment where the crack is nucleated or cross through the aggregate or micro friction. It is noticed that a few signals were also recorded after the failure of material (Point C), some of them are energetic, because of the complexity of source of acoustic emission, as some phenomena as debris falling, sliding between the crack lips, etc. The summarized Tab 3.4 illustrates displacement corresponding to the 3 important points of each specimen. The displacement at point C is likely related to the peak stress, and more than 70% of signal are taken into account within this displacement.

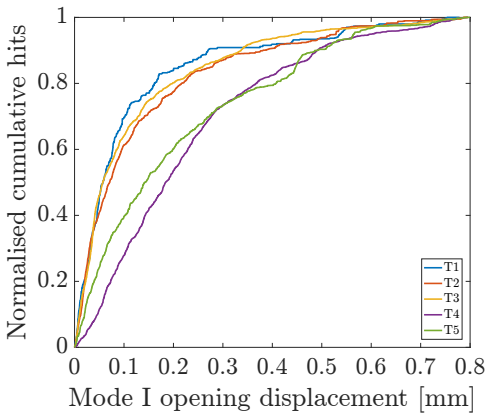

(a)

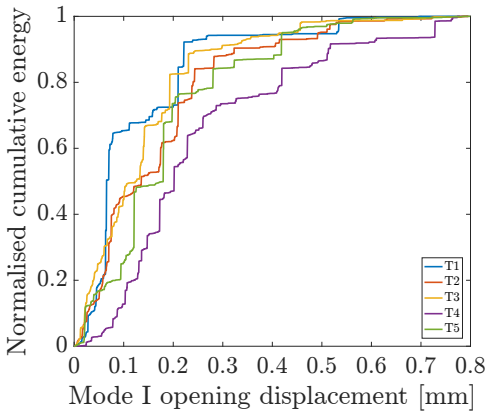

(b)

Figure 3.12: Summary of cumulative hits number/ hits energy vs. displacement

A summarized table Tab 3.5 exhibits the hits and and the total energy of signals recorded in the tensile test. In fact, the hits number rang from 600 to 3000 and a great variance is also observed. This variance is related to the material and the crack path, thus the normalized number is suggested in the repeated test analysis.

Table 3.4: Summary of displacement corresponding to point A, B, C

Specime n	**Displacement (mm)**		
	Point A	**Point B**	**Point C**
T1	0.0008	0,059	0.0963
T2	0.0013	0,045	0.2720
T3	0.0012	0,119	0.7951
T4	0.0019	0,07	0.7735
T5	0.0019	0,089	0.5753

Table 3.5: Summary of hit and hit energy

	Hit number	Hit energy (aJ)
T1	602	2.72E+05
T2	2235	9.72E+05
T3	3383	1.82E+06
T4	3847	3.98E+06
T5	2015	1.35E+06

Crack re-closure

At the end of tensile loading, a compressive load is applied on the specimen T2, as shown in Fig 3.13, the material trended to close and the progressive stiffness restitution of material due to closing was observed, corresponds to the increasing slope of curve. The stiffness of material was then increased to the initial value as before damage in tensile test. With respect to the acoustic emission, the Fig 3.14 illustrates the evolution of amplitude of acoustic emission in the compression phase. Before the crack re-closure, the signal of acoustic emission was seldom detected, and then an increasing number of signals are observed with increasing crack reclosure. It can be seen that some signals with greater amplitude are received at the beginning of crack reclosure than that at the end of the compressive phase. This can be explained by the fact that more slip and dislocation of grains was involved while the crack lips start to close. With the increasing crack closing surface, more signals are generated, however, the maximal amplitude is less than that of the previous phase.

Cyclic test

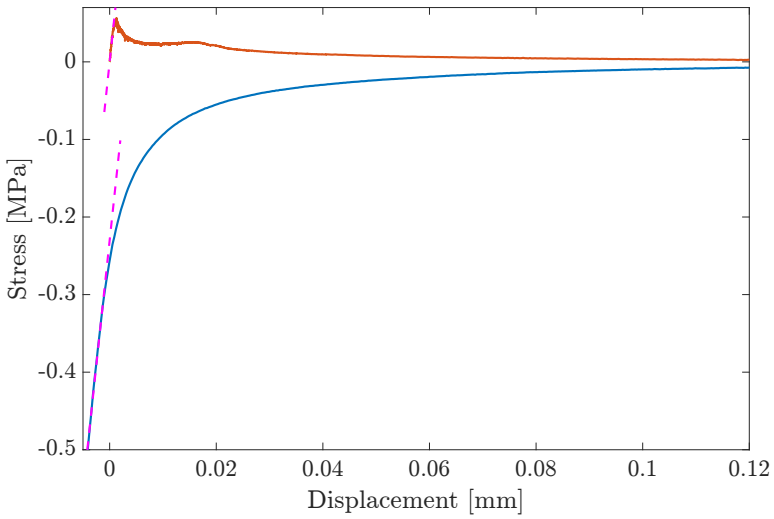

Figure 3.13: Tensile-compressive stress vs. displacement.

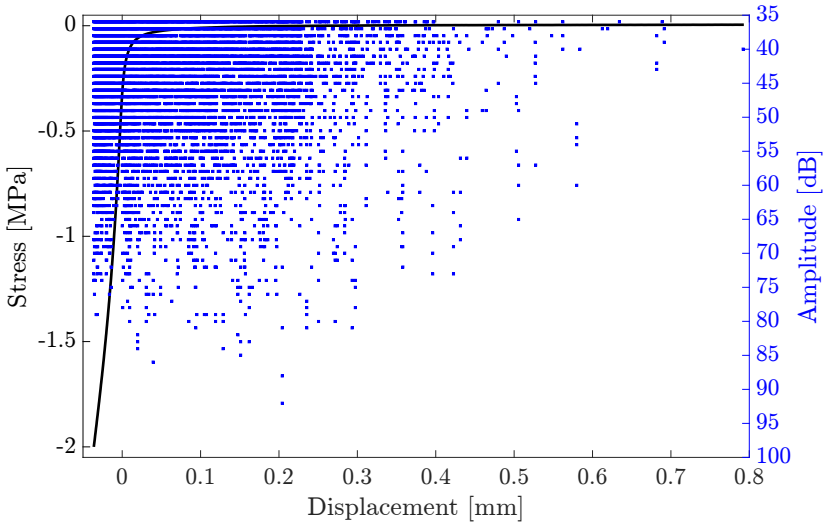

Figure 3.14: AE amplitude /compressive stress vs. displacement.

The damage process was monitored by AET on cyclic tests. Fig 3.15 illustrates the stress level and AE Amplitude versus time in a cyclic test on TC2 sample. Before to the 3^{th} cycle, where the material remained almost in a linear behavior, few signals were detected, both in the reloading, and unloading branches. Beyond this cycle, signals were recorded only after the previous damage level was exceeded. The maximal amplitude increased with damage accumulation, particularly in the last

2 cycles, where the maximal amplitude was significantly greater. This observation indicates that the macro crack coalescence, which liberates more AE energy as shown in Fig 3.15, generate signals with greater amplitude. In fact, a stable increase of AE energy is observed from cycle 5 and this energy raises brutally at the last cycles in Fig 3.16. Besides, the signals occur mostly at the softening phase, observed in the Fig 3.11. Other illustration shows this observation more clearly in Fig 3.17, which presents the event location in the 3 phases of all the cycles. In fact, due to the low amplitude of recorded signals, only a few number of events can be obtain. However, it is clear that more events are recorded at the softening phase (Fig 3.17(b)) than that at the reloading and unloading phase (Fig 3.17(a) and Fig 3.17(c)). The felicity effect can be also observed beyond the peak stress (cycle 3) in the Fig 3.18. This effect demonstrates the occurrences of acoustic activities at a stress lever lower than the maximal stress of the previous cycle, which has been reported by the other researchers[Fowler, 2017],[Shetty et al., 2019].

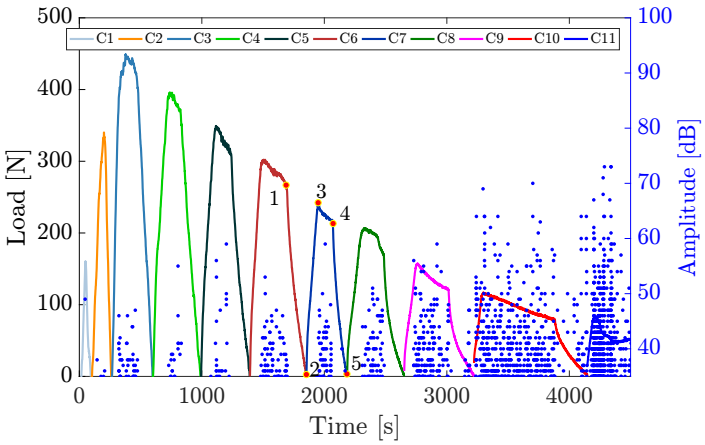

Figure 3.15: Stress and amplitude vs. time of TC2

With respect to AE hit, another attempt is carried out to show the evolution of normalized cumulative hits following the damage variable in each cycle in Fig 3.19. This relation have been analyzed in concrete[Nguyen-Tat et al., 2018]. Only the signals under the load-displacement envelop (e.g. Branch CD in cycle 7) can be considered. The number of hits in each cycle is expressed as a percentage, compared with the hits number within overall envelop. It can be observed a pronounced increase in hits number when the damage variable exceeds 0.9. Compared to concrete, the damage variable increases more sharply, inducing a pronounced number of hits at a greater damage variable level.

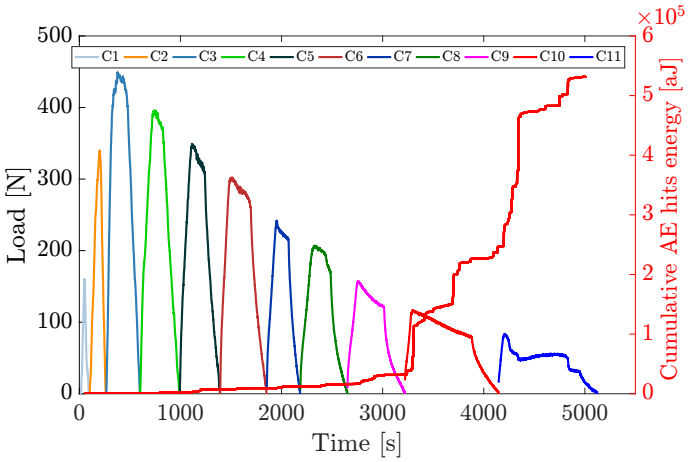

Figure 3.16: Stress and cumulative AE energy vs. time

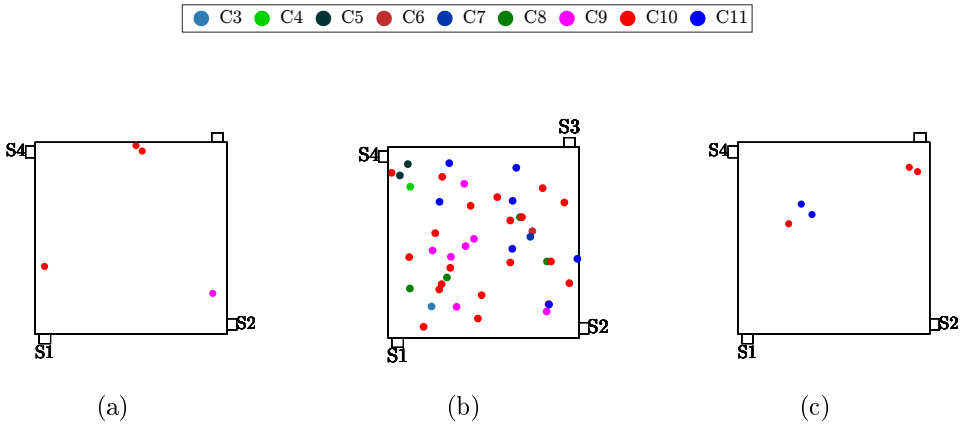

(a) (b) (c)

Figure 3.17: Event location at the (a) reloading, (b) softening, (c) unloading phase of cycle 9

3.3.3.3 Ultrasonic parameter analysis

As mentioned previously, the ultrasonic test can also be used to be correlated with material mechanical damage. For each ultrasonic test, one of all sensors (i.e. Sensor 2, namely S2) in turn emit an impulsion as shown in Fig 3.20(a), meanwhile the others receive this signal, and the waveform as well as the related parameters are then recorded. Fig 3.20(b) illustrates the wave of ultrasound signal received by sensor 1. The wave velocity can be also derived from the distance and the propagation time between the sensors.

Fig 3.21 illustrates the evolution of amplitude and velocity of signals generated by sensor 2 at the end of each corresponding cycle i.e. when the interface is fully

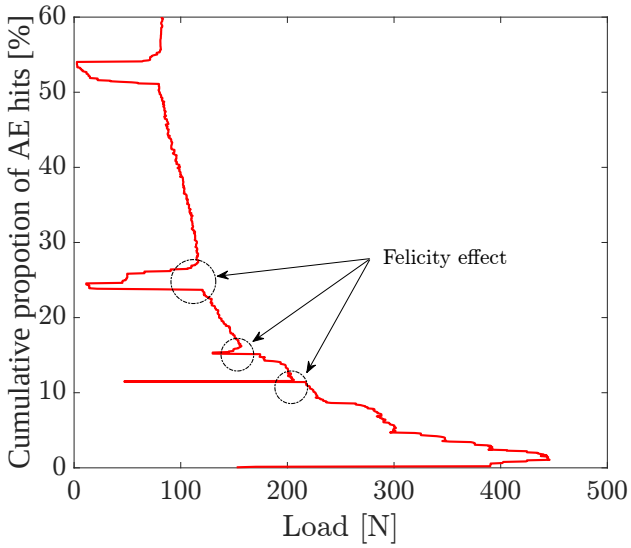

Figure 3.18: Felicity effect observed at the post peak phase

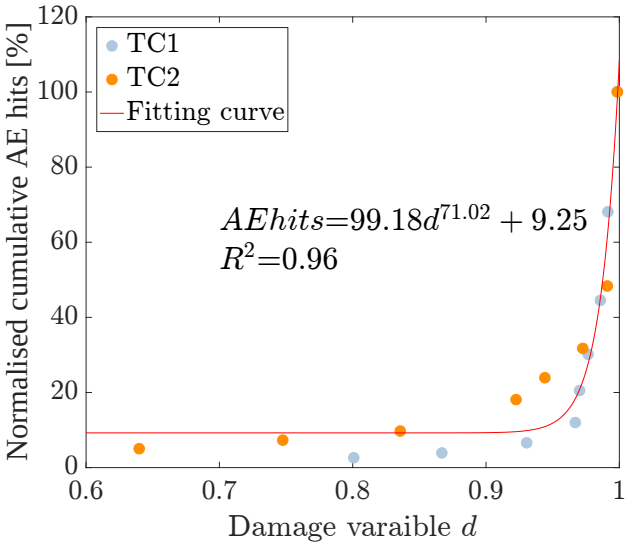

Figure 3.19: Normalized cumulative AE hits vs. damage variable

unloaded. The cycle 0 refers to the initial state before the test. The amplitudes of signal recorded by the sensor 1 and 3, decrease notably with accumulative damage in the interface after the 5th cycle, however, the amplitude of signal recorded by S4 remains almost constant. This can be attributed to the fact that sensors S2 and S4 are placed on the bottom block while S1 and S3 on the upper block. Then, the signal propagating across the interface is affected by the crack propagation, while the signal propagating in the stone is not affected. The similar observation

is found in the wave velocity evolution. The velocity in the stone is measures at 3030m/s (Coefficient of variation=0.5%) for all the cycles, while that across the mortar interface is about 2036m/s and 1337m/s at initial state and then get smaller with crack propagation. The difference value between the sensor 1 and 3 is resulted from the different wave propagation path due to the material heterogeneity. In order to compare the sensibility of these two parameters regarding to the sensitivity to damage, the percentage decrease is considered in the Fig 3.22, which is calculates according to the following equation (Eq 3.2):

$$Percentagedecrease = \frac{V_i - V_1}{V_1} \times 100 \tag{3.2}$$

Where V_i is the value at the initial state and V_i is the value at the i^{th} cycle. A pronounced decrease is observed after the cycle 7 in both these two ultrasonic parameters, referring to the detection of macro crack. Compared to the cumulative number of hits in the cycles in Fig 3.23, it can be seen that the linear ultrasonic parameter is more sensitive to detect macro crack, and the AE parameters are sensitive to both micro and macro crack.

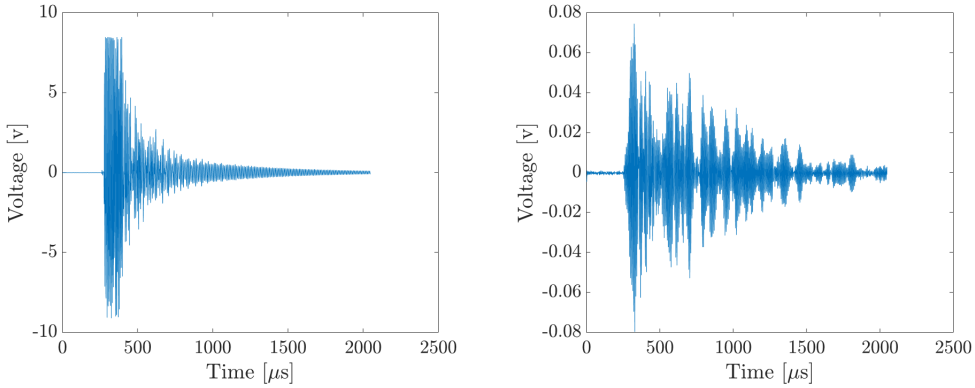

Figure 3.20: Waveform of ultrasound (a) emitted by sensor 2 (b) received by sensor 1 in the cycle 0

Cross-correlation of signal waveform

In each cycle, each sensor can receive the signal emitted from the same sensor, so it is questioned how the receiving signal changes in different cycle, and if this change is correlated with the damage in the material. To answer these questions, a method named 'Normalized Cross-correlation' (NCC) is applied to estimate the similarity of two signals between the cycles. In fact, this method is used widely to calculate the

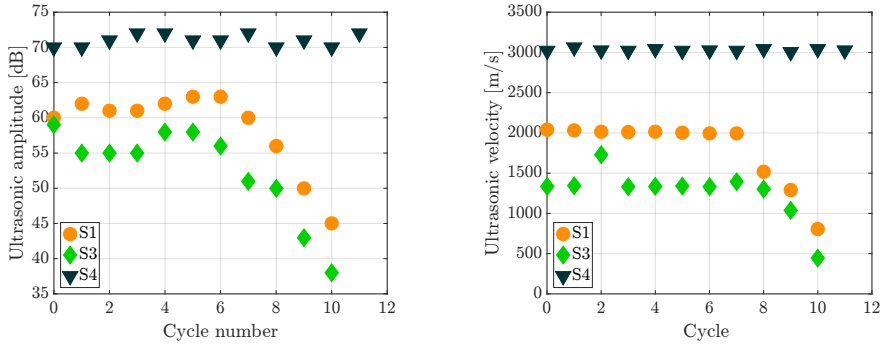

Figure 3.21: Amplitude/ ultrasonic velocity vs. cycle number

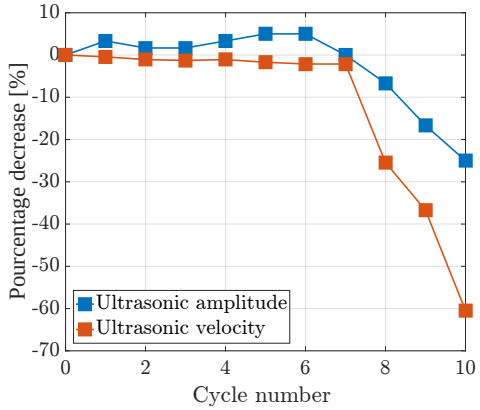

Figure 3.22: Percentage decrease vs. cycle in sensor 1

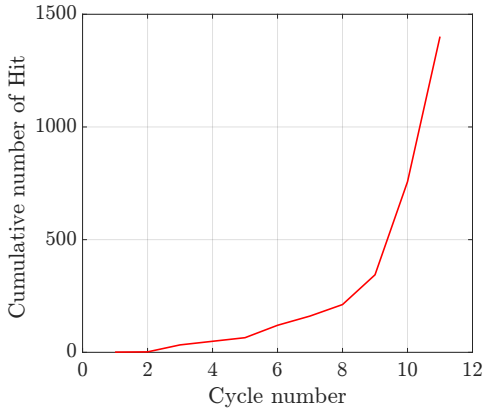

Figure 3.23: Cumulative hits vs. cycle

cosine of the angle θ between the two vectors a and b as in the following equation:

$$NCC = cos\theta = \frac{a \cdot b}{|a|\,|b|} = \frac{\sum_i a_i b_i}{\sqrt{\sum_i a_i^2}\sqrt{\sum_i b_i^2}}, -1 \leq NCC \leq 1. \tag{3.3}$$

The NCC index is also known as the correlation coefficient. This coefficient is near 1 when two signals are more similar. In our case, we focus on the signal received by sensor 1 in each cycle which is emitted by sensor 2. The two signals to estimate the similarity are both the receiving signals by sensor 1, the first one is the receiving signal in cycle 0 which is considered as a referent signal. The second one is the receiving signal in each different cycle. In the Fig 3.24, 4 examples show the signal waveform recorded by sensor 1 in 4 different cycles. And the correlation coefficient is calculated between recorded signal of each cycle and the referent signal as show in Fig 3.25.

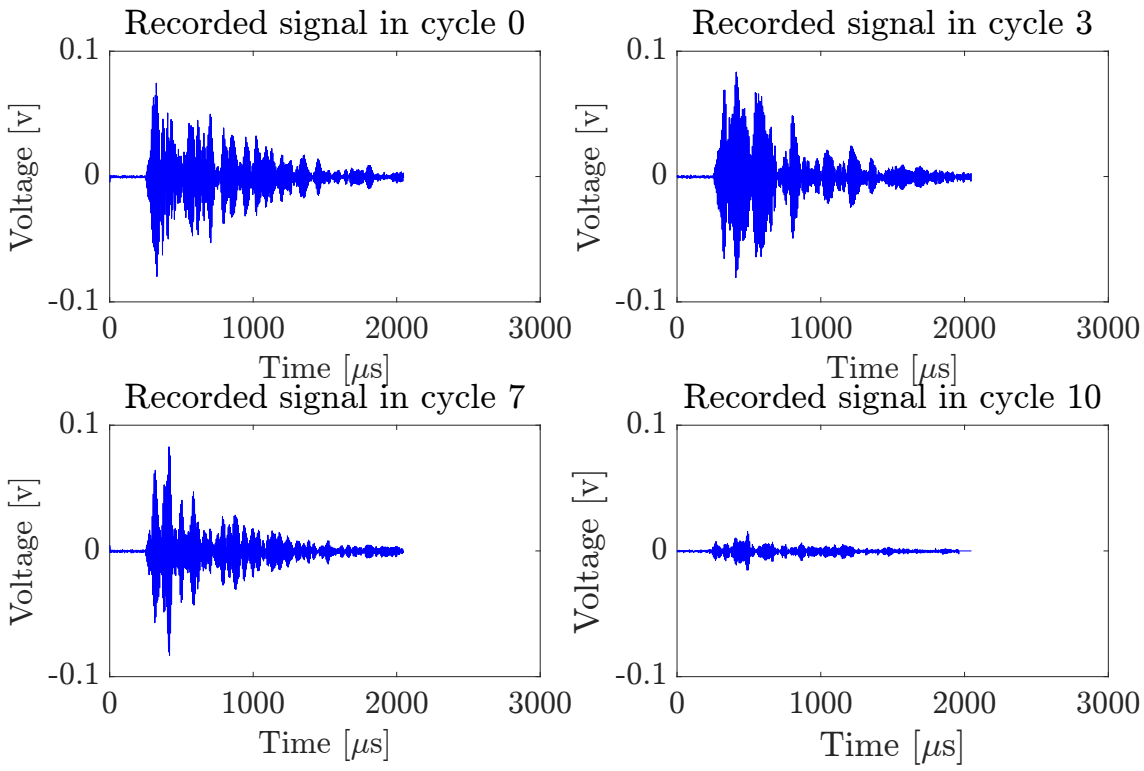

Figure 3.24: Recorded signal waveform by sensor 1 in different cycles

The coefficient of correlation obtained in all the cycles is then summarized in the Fig 3.26. A significative decease of the coefficient of correlation is observed from the initial cycle 0 to cycle 1, indicating that some changes within material is detected even in the elastic domain. This observation is not found in the AE analysis. And then this coefficient is relatively constant till the cycle 4. Another decrease of coefficient is observed from the cycle 4 to cycle 5, corresponding to the micro cracking initialization and formation. Compared with the classical ultrasonic parameter analysis, the NCC method is more sensitive to the micro cracking.

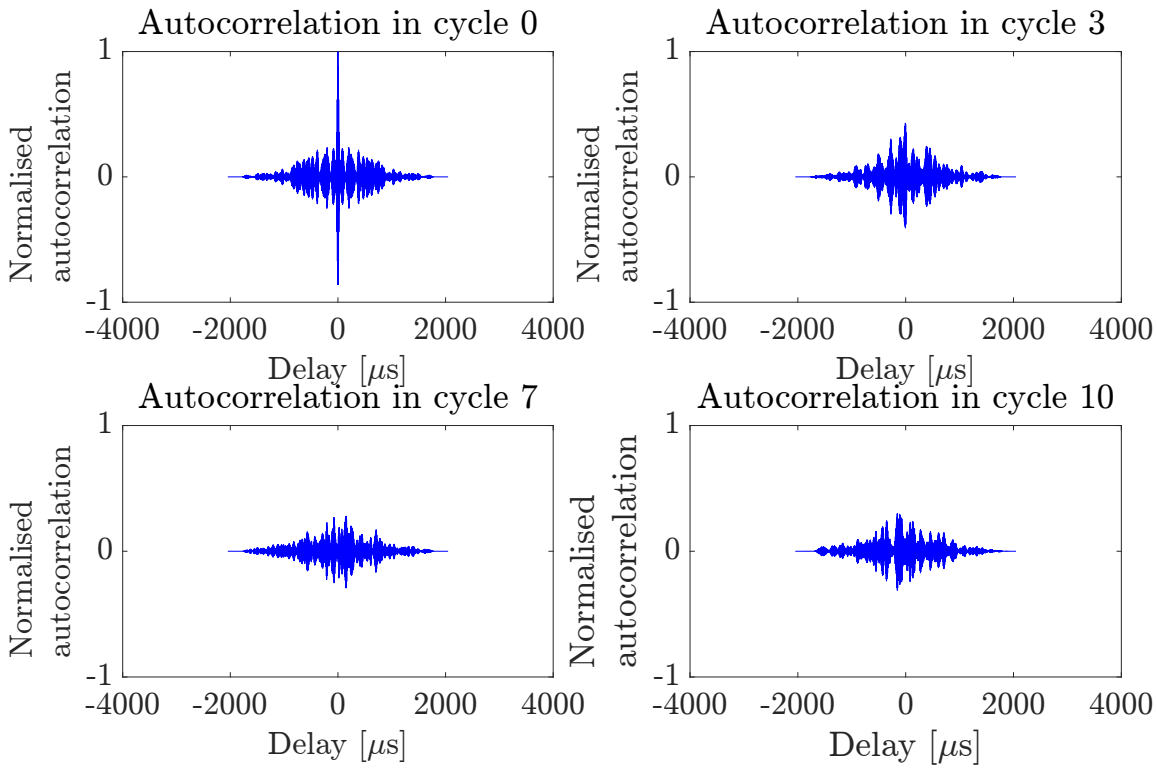

Figure 3.25: Normalized cross correlation between the signal in different cycle and the referent

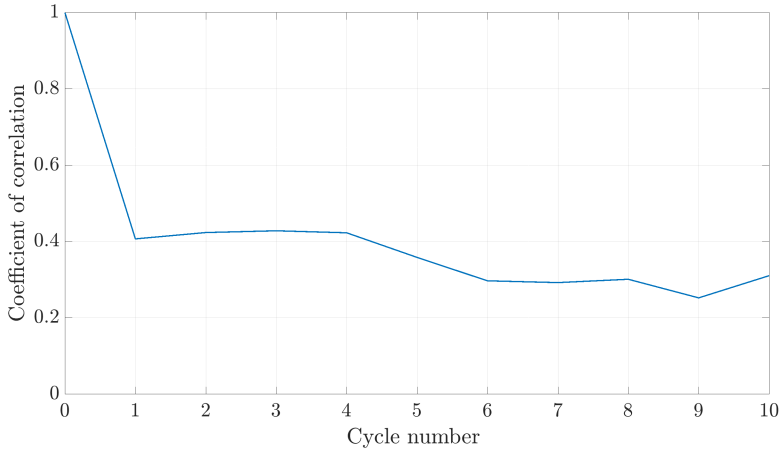

Figure 3.26: Correlation coefficient vs. Cycle number

3.4 Shear test

As mentioned previously, the shear damage in the mortar interface is also a major cause in the masonry ruin in case of wind and seismic loading. Thus this section aims to study the damage development of triplet specimen subjected to shear loading under a normal compressive stress. The mechanical behavior of material as well as the damage process are also discussed by the interpretation of AE activities. Besides three possible factors the influencing the AE signature are investigated including the loading rate, material variability and the normal stress level.

3.4.1 Experimental equipment setup

The specimen was composed by three stones, bonded by mortar with 7mm (see part 3.2.1). The specimen was positioned horizontally at the metal plate. The two extreme stones were clamped to limit the rotation of specimen during the test. Two small rectangular plates were positioned on the central stone, at the vicinity of mortar interface to adjust the position where the loading was applied. The applied load was transmitted, via a special equipage. The ball joint in this equipage was used to equilibrate the loading applied in each side (Fig 3.27) ensuring a free rotation boundary condition. For more details of the mechanical tensile test and shear test setup, see [Venzal, 2020].

Four HBM were positioned across the mortar to measure the shear displacement. Eight AE sensors were placed as shown in Fig 3.27, the arrangement of these sensors was determined to minimize the error in AE location. The sensor positioned at the two extreme blocks were deviated 20mm from the boundary of stone or the interface to avoid side effects. The sensors at the central stone are positioned at the symmetry axe and also deviated 20mm from the upper boundary of stone. The PLB was carried out before each test to examine the adherence of sensors.

3.4.2 Load test procedure

In shear test, a normal loading was firstly applied horizontally at the two extreme blocs. This normal loading was set at 0.4, 0.6 and 0.8MPa. A shear vertical loading was then carried out by imposing a vertical displacement to the central block leading to shearing of the mortar joint.

Four HBM were positioned across the mortar to measure the shear displacement.

(a)

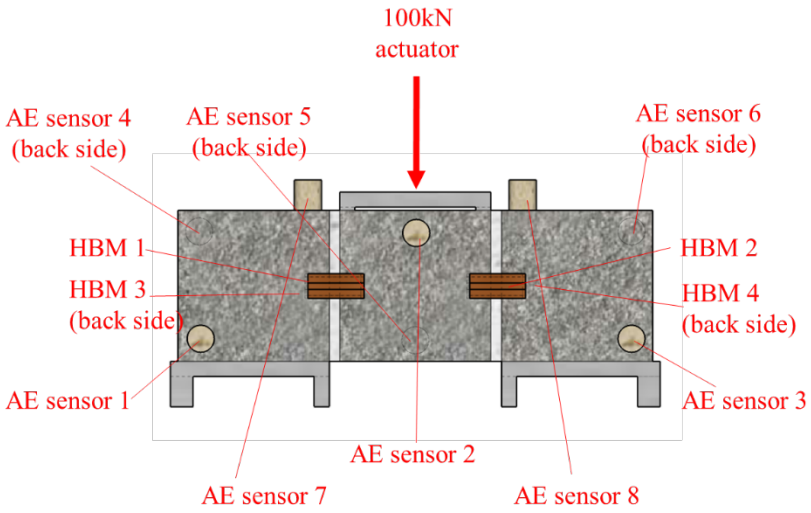

(b)

Figure 3.27: Shear test setup and instrumentations

Before the beginning of the test, 3 cycles of preloading of 20N were carried out, ensuring a contact of loading and material. This test is also displacement-rate controlled, and three loading regimes are concerned. The different loading regimes were designed to discover the influence on the AE parameters brought by the displacement rate. The detailed information concerning the loading regime for each specimen is presented in the Tab 3.6. Each loading regime is explained in the Fig 3.28 which illustrates the imposed the displacement vs. the time. So that the slope refers to the displacement rate. For the loading regime 'Monotone', the imposed displacement rate remains the same value 0.04mm/min during the whole test. The regime 'variable1' means the displacement rate changes in 6 sections of time, the initial displacement rate was set as 0.005mm/min, then this rate was doubled in the following section. The difference is the regime 'Variable2' is the rate in the last section was

Table 3.6: Loading regime in shear test

Specimen	Loading regime
S0.4-1	Variable1
S0.4-2	Variable1
S0.4-3	Monotone
S0.6-1	Variable1
S0.6-2	Variable1
S0.6-3	Monotone
S0.6-4	Monotone
S0.6-5	Monotone
S0.6-6	Monotone
S0.8-1	Variable1
S0.8-2	Variable1
S0.8-3	Variable2
S0.8-4	Monotone

the same in the 5^{th} section.

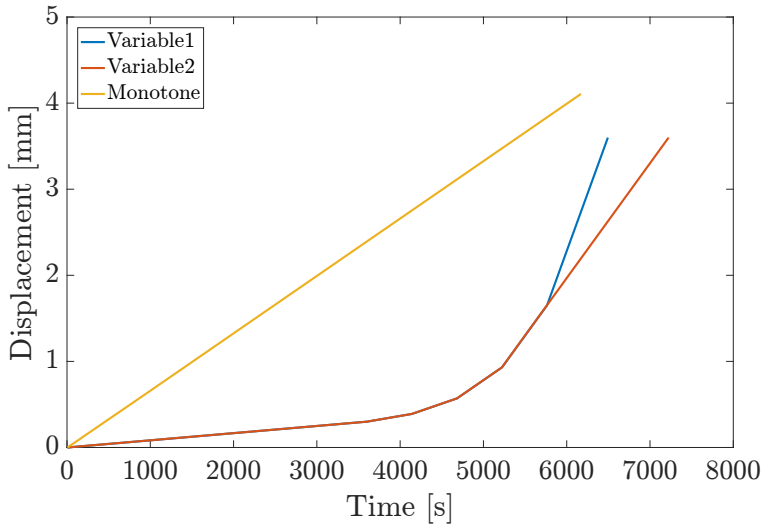

Figure 3.28: Imposed displacement rate in three loading regimes

3.4.3 Results and discussions

3.4.3.1 Mechanic behavior

In the Fig 3.29 the results of test under each compression level were presented in a similar color. The method 'moving average' is firstly applied on the raw data to smooth out the outlier data. The new data are obtained, resulted from the moving average of 50000 points. The data number recorded by The trend in all curves is quite similar regardless of normal stress value. At initial step, all the specimens present an elastic behavior, and that shifted to be no linear till the curve reach to the max shear stress. At the post-peak curve, the stress reduced gradually. Due to the participation of compression stress inducing friction effect, the stress will never descend to null value. It can be also observed that the max shear stress raised with increasing compressive stress. That explains how the confinement stress affect the specimen's mechanic behavior under shear stress. More detailed information including the peak stress, the stiffness and the residual stress of each test is summarized in the Tab 3.7. The stiffness is calculated in the range of 0-25% of maximal load, this range can be considered as an elastic domain. The residual stress is calculated as the averaged stress of the displacement between 3 to 3.6mm.

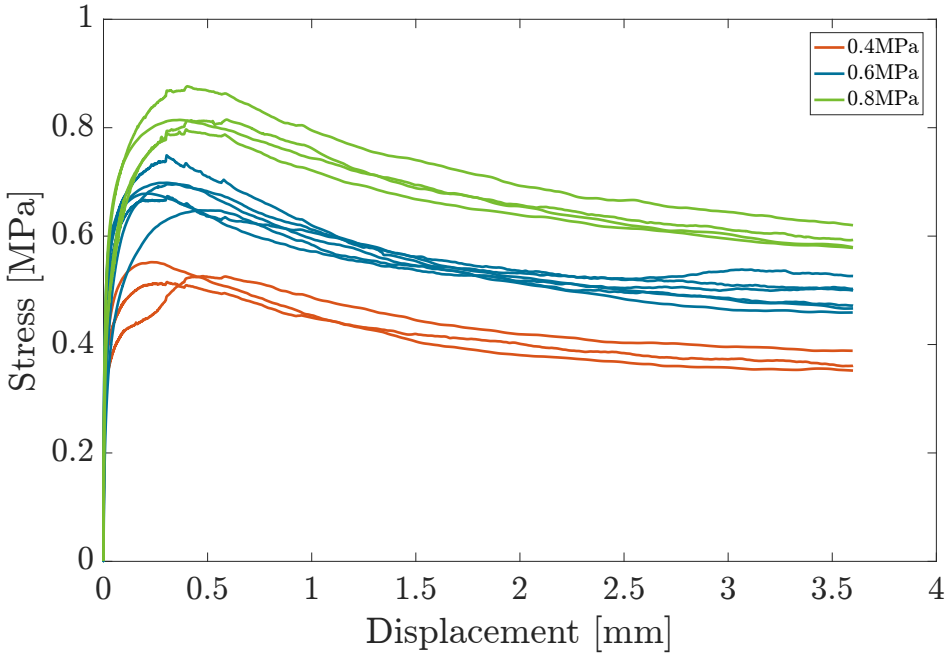

Figure 3.29: Summarized load-displacement curve in shear test

Table 3.7: Summarized mechanical properties in shear test

Specimen	Peak stress (MPa)	Stiffness (GPa/m)	Residual stress (Mpa)
S0.4-1	0.515	152.05	0.36
S0.4-2	0.526	128.24	0.4
S0.4-3	0.552	92.09	0.37
S0.6-1	0.674	153.65	0.49
S0.6-2	0.749	136.71	0.48
S0.6-3	0.696	78.96	0.5
S0.6-4	0.64	35.77	0.53
S0.6-5	0.67	120.51	0.50
S0.6-6	0.69	179.09	0.47
S0.8-1	0.815	148.4	0.61
S0.8-2	0.797	149.81	0.61
S0.8-3	0.876	122.22	0.64
S0.8-4	0.814	132.11	0.60

The mechanical properties of each specimen are summarized in the Tab 3.8, according to the compressive stress level. It can be obtained that the variability in the stiffness is much higher than that in the peak stress and residual stress. As mentioned previously, the stiffness is calculated as the slope of a regression determined at a fixed range of loading of 0-25% of maximal load. In fact, several methods can be used for the determination of this regression, ones is to find the maximal value of slope, varying the load range. Another one is to find the regression corresponding to the maximal coefficient of determination by the method of least squares. However, the sectioned zone from these two methods sometimes drops at a narrow range of load such as 0-10% of maximal stress. This range cannot be considered as a pure elastic domain in the most of time, because the stabilization of material is also observed at the beginning of the test. Thus, the method used in this study to calculate the stiffness is a comprising result, taking account of the coefficient of determination in a linear regression determination and the reasonable range corresponding to an elastic behavior of material. This results in the fact that the stiffness calculated in some cases is lower than that calculated by other methods.

A correlation can be obtained between the peak stress and compressive stress in Fig 3.30. A linear regression is observed with a good coefficient of determination. This correlation shows how the confinement effect influences the peak stress. Moreover, it enables a prediction of peak stress of such a kind of material.

Table 3.8: Summarized information in the 3 compressive stress level

Compressive stress (Mpa)	Peak stress (MPa)	Stiffness (GPa/m)	Residual stress (Mpa)
0.4	0.53 (±2.9%)	124 (±19.9%)	0.38 (±4.7%)
0.6	0.71 (±4.5%)	123 (±26.0%)	0.49 (±2.1%)
0.8	0.83 (±3.7%)	138 (±8.3%)	0.62 (±2.4%)

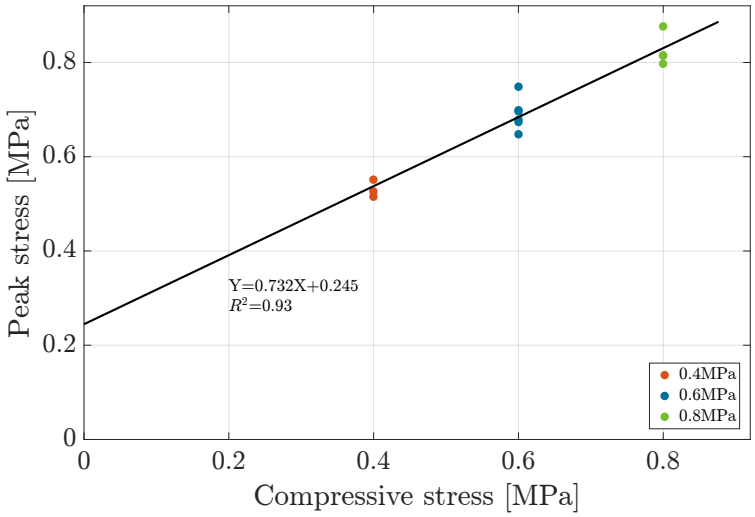

Figure 3.30: Correlation between the peak stress and compressive stress

With respect to the residual stress and compressive stress, the coefficient of friction μ, when interface Is fully damaged, can also be obtain according to the equation:

$$\sigma_{resi} = \mu\sigma_N \tag{3.4}$$

Where σ_N is the normal compressive stress, σ_{resi} is the residual stress and σ_N is the applied normal stress. In fact, while the interface is totally damaged and only the friction participates, the residual stress can be considered as the unique frictional stress[NF EN 1015-11, 2000]. The friction coefficient is obtained by linear regression of which the intercept is forced to 0 as shown in the Fig 3.31. This friction coefficient 0.81 can be used in the model potentially.

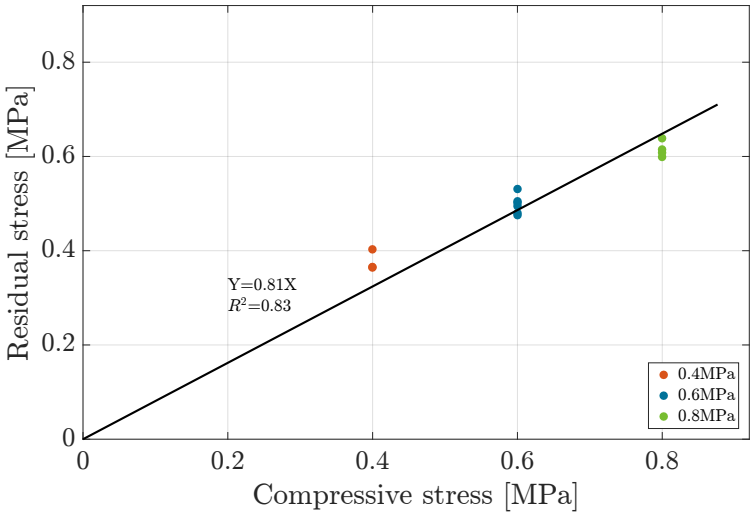

Figure 3.31: Correlation between the residual stress and compressive stress

3.4.3.2 Acoustic emission activities analysis

The mechanical behavior shows differences between mode II (shear) and mode I. Three stages can be identified, according to the load-displacement curve in Fig 3.32: elastic domain OA, transition phase ABC, pure fiction CD. At initial step OA, the specimen presents an elastic behavior at first 2μm, at this stage, the number and the energy of recorded signals is lower than the following phase. However it should be noticed that a pronounced number of signals with relative low energy are detected at the first few millimeter, which could be result from the contact between the plate and sample when the load was applied.

The transitions stage ABC corresponds to the interface decohesion stage from elastic behavior to full friction stage. The mechanical behavior as well as acoustic emission are discussed in the stages before (AB) and after (BC) peak stress. In the phase AB, the load-displacement curve shifts to be no linear until it reaches the peak shear stress. A considerable increase of the hits number rate resulted from increasing damage surface is observed before the peak. However, the energy of hits is still at a relative low value.

At the post-peak curve (phase BC), the stress reduces gradually. This rate increases more slowly at the downward curve phase. With respect to absolute energy, more energetic signals are recorded after peak stress. This trend is likely associated to crack initiation, crack propagation with partial friction after cracking.

Due to the participation of compression normal stress on the interface, the stress never drops to null value and a full frictional behavior is reached at about 3mm. and finally remains relatively constant during the full frictional stage. At this stage, the number of recorded signals per displacement of 1μm is observed also constant, compared with the previous stage. However, the energy rate is not as constant as the hits number, the occurrence of some signals with a pronounced energy cannot be predicted. Because even at the full friction phase, the damaged mortar interface is still heterogonous, the generated signal depends on the roughness of cracked interface.

Another parameter "duration" can be also used to be correlated with the mechanical behavior as shown in Fig 3.33. When the friction was induced, the duration turns to be higher, the maximal duration exceeds 2ms. At the post-peak phase, the full frictional behavior is reached, the value of duration remains constant and much higher (12ms) than that observed in the previous phase (3ms). It should be noticed that some long signals at about 0.3μm are probably resulted from composition crush, the compact of composition, the loading setup, the sliding when the specimen started to be loaded.

As the same reason explained in the tensile test, several factors influence the detection of signals, however, it is worthy to compare the hits and energy of all the specimen. In the Fig 3.34, the cumulative hits and energy of hits are illustrated in the terms of displacement, taking into account of all the specimen with different compressive stress. These cumulative are normalized by the total value of hits number or energy, respectively. It can be observed that, the form of theses curve of hit number or energy is quite different from that in tensile test. And compared between the shear tests, the curve shows a similarity regardless of compressive stress. In the curves of normalized cumulative number of hits, the most part of curve is almost linear, except at the beginning. This observation confirms that at the number of signals is constant at the full friction phase. The rate of the beginning curve increases and then reaches to a constant value, which is related to the elastic domain and the transition stage from elastic behavior to full friction stage. Regarding to the energy of hits, the curves are generally linear when the displacement exceeds 2mm. Compared with that of hits number, they are less smooth due to the little steps, resulted from the pronounced energy. This observation is also explained in the no cumulative curve.

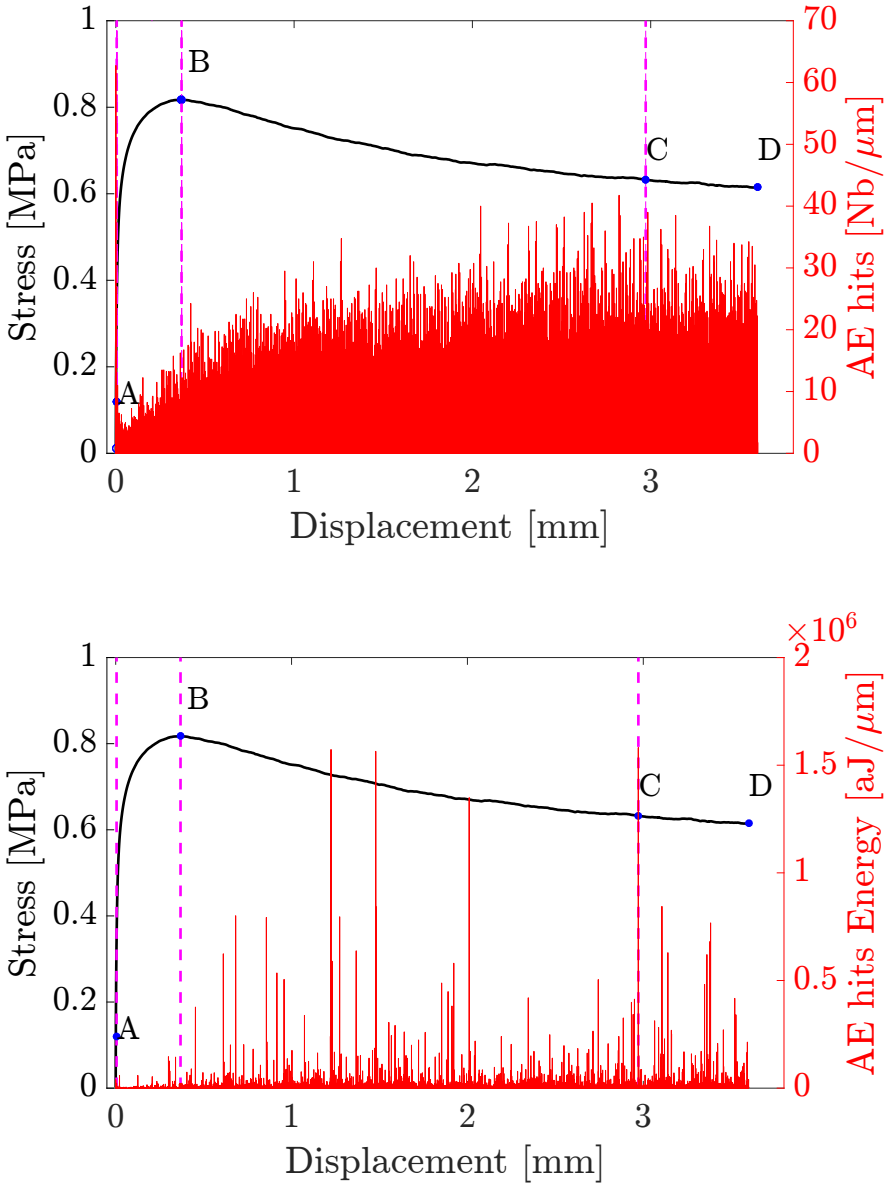

Figure 3.32: Stress and AE hit number/ AE energy vs. displacement of specimen S0.8-4

3.4.3.3 Three factors influencing AE signature

Effect of loading rate on AE signature

We have acknowledged some factors [Aggelis et al., 2012],[Aggelis et al., 2017] resulting to the AE signal distortion. In this part, three influencing factors are studied on the AE waveform signature. We will firstly illustrate the influence of loading rate on the AE signature.

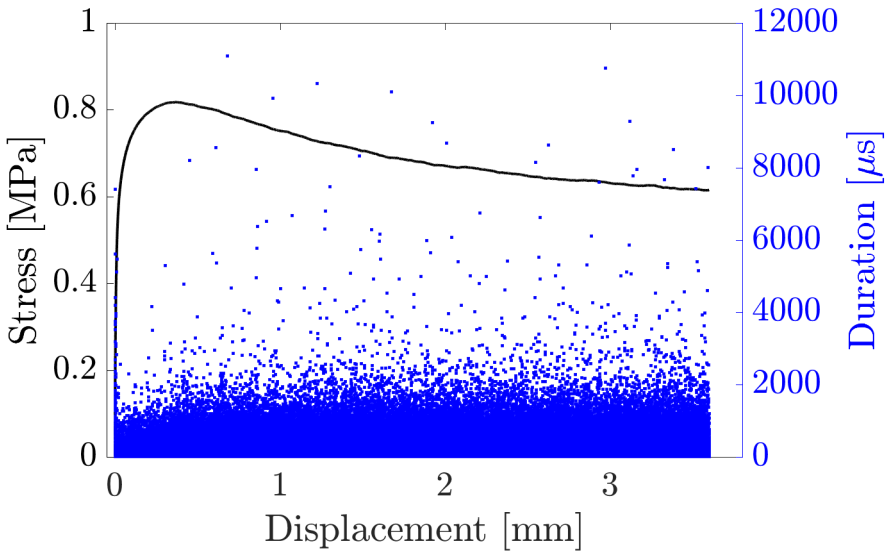

Figure 3.33: Stress/duration vs. displacement of specimen S0.8-4

Three tests under 0.8MPa with different loading regimes are compared: S0.8-2 and S0.8-3 and S0.8-4. the regime 'Variable1' and 'Variable2' and 'Monotone' were applied, respectively in those tests. Two parameters amplitude and duration are selected which are the basic parameters of a recorded AE signal. The averaged value is calculated from the method 'moving average', based on each 50000 points. In the Fig 3.35, the dashed magenta line present the moment where the displacement rate is changed (for the regimes 'Variable 1' and 'Variable 2'). Six sections can be identified according to the displacement rate. For the 'Variable1', the displacement rate is twice in the last section than that in previous section, while the displacement is the same in the last two sections in the loading regime 'Variable2'(see Tab 3.6). And the regime 'Monotone' corresponds to a constant displacement rate during the whole tests. A pronounced increase of parameter value is observed between the two last sections under the loading regime 'Variable 1'. While no evident variation is found for the other loading regimes. This observation is found both in the amplitude and duration. This observation confirms the influence of loading rate on the AE parameter.

Material variability in AE signature

It always remains difficult to characterize a AE signal, which is not only because of its complex damaged source, it is also related to signal distortion. This distortion depends on propagation path, the attenuation and, which are associated with the heterogeneous material. So how the AE signal or its parameter perform with the material variability is another issue which will be discussed in here.

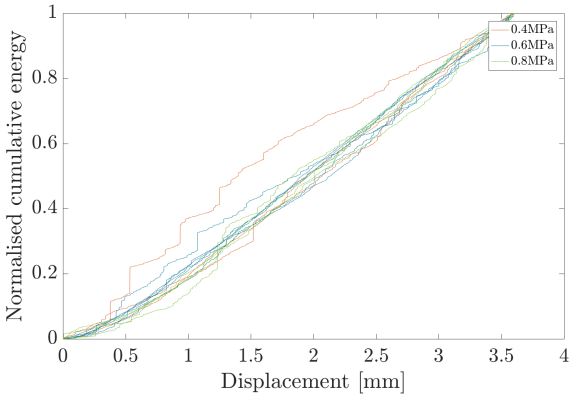

(a)

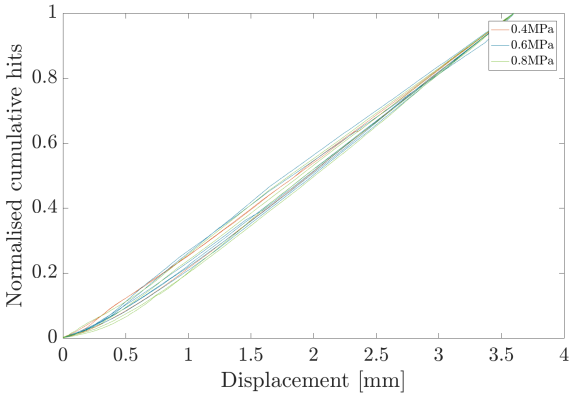

(b)

Figure 3.34: Summary of cumulative hits number/ hits energy vs. displacement in shear test

In the Fig 3.36, the AE parameter amplitude and duration are presented against the displacement. The parameter value is calculated as an averaged value, by applying the moving average, based on 50000 points. Three tests under 0.6MPa are selected, the 'monotone' loading regime is performed on these tests. It is shown that amplitude value increase on the first transition phase of the tests and keep relatively constant at the friction phase. However the variability is more distinct in the duration, varying from 330μm to 600μm. It can be concluded that the AE parameter is influenced by the material variability, and this influence also depends on the type of parameter.

Normal compressive stress effect on AE signature

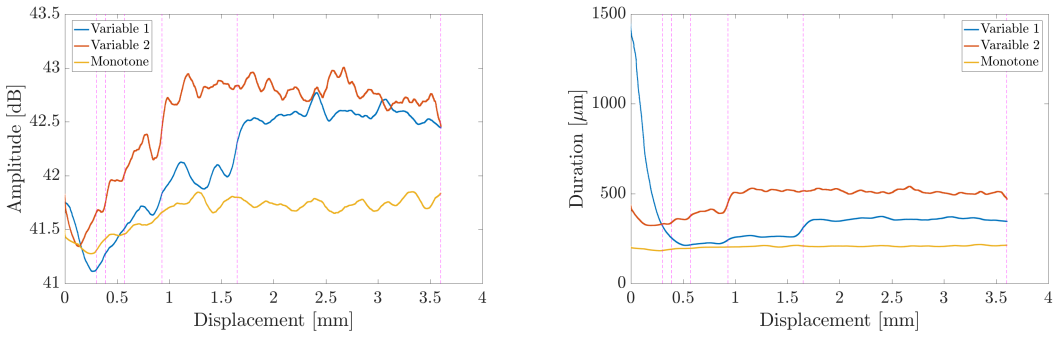

(a) (b)

Figure 3.35: Moving averaged amplitude/ duration vs. displacement under 3 loading regimes

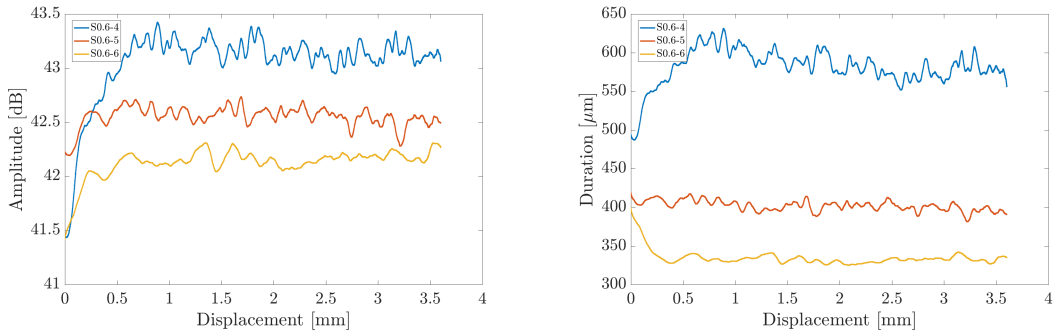

(a) (b)

Figure 3.36: Moving averaged amplitude/ duration vs. displacement of three repeated test

It is also questioned if the AE signature is correlated with the compressive stress. To answer this question, six tests are selected with 2 loading regimes under 3 different levels of compressive stress. The two regimes correspond to the 'varaible1' and 'monotone', and the compressive correspond to 0.4, 0.6 and 0.8 MPa. The same method 'moving average' was applied on the amplitude and duration of each test, and the results are shown in the Fig 3.37.

The curve resulted from different compressive stress is present in each corresponding color. It can be seen that the amplitude and duration is higher under 0.4MPa than that under 0.8MPa, and the highest value parameter is observed in the tests under 0.6MPa. Besides, taking into account the influence caused by material variability, it can be concluded that the AE parameter seems not influenced by the compressive stress.

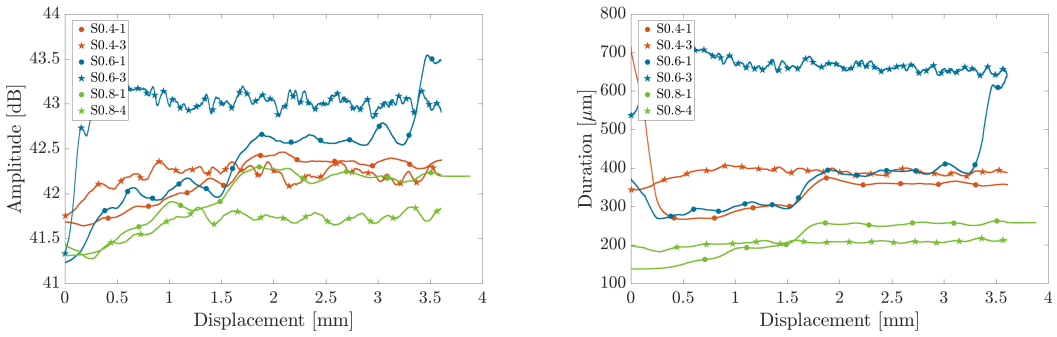

(a) (b)

Figure 3.37: Moving averaged amplitude/ duration vs. displacement under 3 different compressive stress

3.5 Source discrimination

The source discrimination is also an important topic which have been discussed in the AE analysis. Several methods such as k-means are used to cluster the signals from the different sources. These methods are usually based on the AE parameter analysis. Thus, the correlation of the AE parameters and the clustering method are studied at the first step. Then a method, based on the correlation of fracture energy and AE energy is proposed to discriminate the signal from the micro to macro cracks. This discrimination is based on the tensile test of which the signal is mostly generated from the micro and macro cracks. Then another discrimination, based on the comparison of AE parameters in both tensile and shear test is investigated. This discrimination aims to distinguish the signal from the crack decohesion to friction.

3.5.1 Correlation and cluster

3.5.1.1 Principal component analysis

As mentioned in the part of damage assessment (Part 3.3.3.2), AE energy strongly depends on damage source. This parameter is calculated as the integration of squared amplitude versus the duration, and thus the parameter amplitude is often used to represent the energy, due to the strong correlation between the amplitude and absolute energy. The Fig 3.38 represent the relation between amplitude and energy of all hits recorded in the tensile monotonic test T2. It highlights this strong correlation. Another correlation is also noteworthy, showing the relation between

amplitude and duration in tensile test.

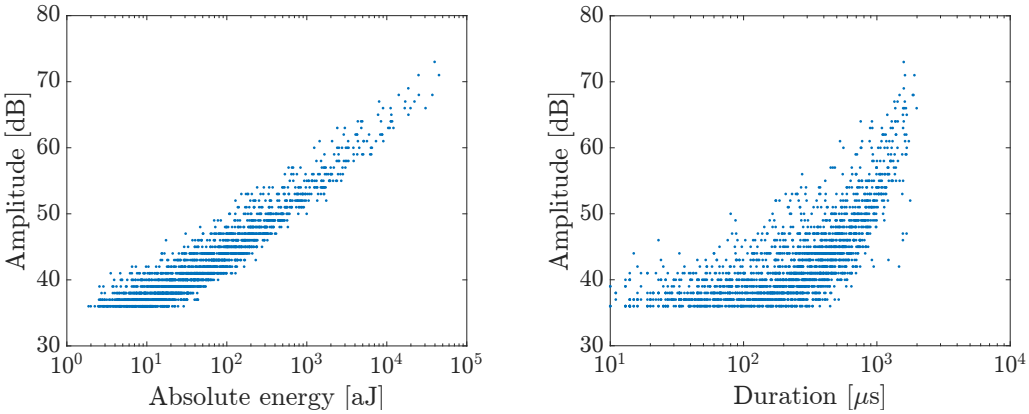

(a) (b)

Figure 3.38: Correlation of AE amplitude and absolute energy / duration of specimen T2

Some other parameters can be also obtained from received signals. To find out the appropriate parameter used in the discrimination analysis, a multivariate correlation analysis was applied. Principal component analysis (PCA), is a method which projects the variables to a new plan. By analyzing the correlation and variance of each component, it enables to reduce the parameter number, ensuring that the maximal possible information is conserved by the rest parameters. Some parameters are strongly correlated as aFrq (average frequency), iFreq (initiation frequency) and cFrq (frequency centroid).

Some correlations are not quite evident as that, as the principle axe F1 and F2 takes only 34% of total variance. That indicates lots of information was neglected in the PCA analysis as in Fig 3.39, therefore several iterations of PCA with reduced parameter number were carried out. Finally, the parameters as amplitude, rise time, duration, aFrq and cFrq are finally selected, ensuring that total variances is beyond 70% (Tab 3.9).

1.4.1.2 K-means discrimination method

In order to discriminate the signal from different sources: micro cracking, macro crack formation, friction or other phenomena, a preliminary clustering method was applied. K-means algorithm aims at partitioning n input value into k clusters. The cluster number 2 is used in this method after several iterations, separating the signals in tensile test from micro crack and macro crack. By computing the distances from each observation to each centroid, and assign each observation to its closest centroid, all the observation are clustered into 2 groups, as illustrated in Fig 3.40,

Table 3.9: Principal component scores for each selected variable of specimen T2

	F1	F2	F3	F4	F5
aFrq	-0.22	0.86	0.27	0.37	-0.05
cFrq	-0.72	0.37	0.22	-0.54	-0.04
amp	0.77	0.55	-0.15	-0.18	0.22
duration	0.92	0.21	-0.13	-0.16	-0.24
rise	0.61	-0.28	0.74	-0.04	0.03
Percent total variance (%)	47.75	26.05	14.17	9.8	2.24

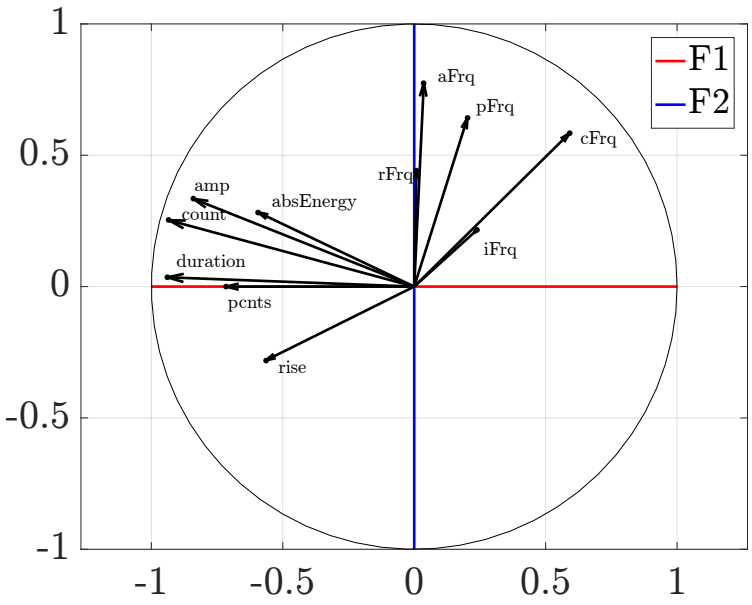

Figure 3.39: PCA score for all hits of specimen T2

two pairs of parameters are presented, one is duration vs. aFrq, considering the parameter related to frequency, another is duration vs. Absolut energy which is a crucial parameter in this study. A visible boundary clustering the points in these two presentations following the duration value of about 0,6 ms, demonstrates that the duration is a dominant parameter in clustering. However it is still questioned if the boundary value can discriminate the damage source from the micro to macro cracking source. The response to this question is studied in the following paragraph in which the AET is compared to mechanical energy.

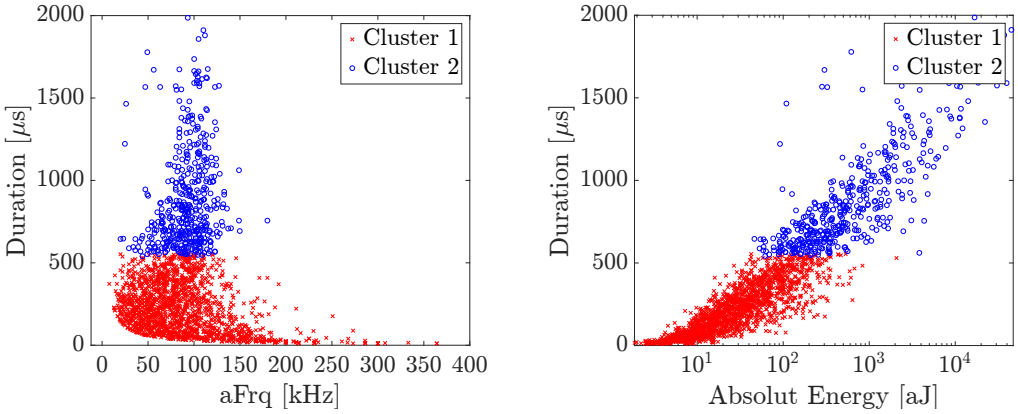

(a) (b)

Figure 3.40: Correlation of AE amplitude and absolute energy / duration of specimen T2

3.5.2 Discrimination from micro to macro crack

This discrimination is based on the tensile test of which almost only the micro and macro crack are involved. Since a momentary non-equilibrium mechanical process as micro cracking formation, crack bridging generates an acoustic emission, it is pertinent to consider the relationship of fracture energy dissipation and the AE energy at the same moment. Besides, the aforementioned analyses demonstrate that the signal energy is probably related to the damage source which could be discriminated by parameter duration. Note that this correction analysis is based on the hypothesis that a certain energy liberated by fracture should be detected by the acoustic emission monitoring system[Landis and Baillon, 2002]. Based on [Carpinteri et al., 2013], AE energy could be correlated to the surplus of elastic energy due to the snap-back instability. Moreover, the interface bloc/mortar is a brittle material and presents a global softening behavior perturbed by multiple local instabilities (micro snapback)[Carpinteri et al., 2016]. For this reason, it is reasonable to assume that there is a link between the two energy rates during a given tensile test, even if the signal distortion from the device acquisition and signal attenuation are not taken into consideration in AE energy calculation. The fracture energy is calculated based on the hypothesis of zero residual displacement. In fact, a good correlation is found between the energy calculated with and without consideration of residual displacement.

In order to compare the evolution of energy from two sources, the T2 sample is presented. A series of fracture energy rate and AE energy rate are both calculated as a sum of energy in each displacement increment (0.005mm) at post-peak phase. As

the ultimate displacement corresponding to the complete interface separation (Point C in Fig 3.6) is 0.268mm, in total 54 points are taken into account. The energy rate is defined here as the quantity of energy dissipated within a displacement increment (0.005mm). As these two energy rates are not in the same unit, the energy series are accumulated and normalized by each total energy respectively. The curve plotted in dot illustrates the normalized cumulative fracture energy versus displacement, while that in solid curves is the normalized cumulative AE energy. It is observed that the fracture energy curve is smoother, while the AE energy increase steeply in Fig 3.41.

In order to show how the duration parameter, influence the correlation between the AE energy rate and mechanical fracture energy rate and to find out the best fitting between the two energy evolutions, the AE energy is calculated from the selected signals, according to duration of which rang is incremented by 50μs each time from 0 to 1600μs. In general, 31 series of curves AE energy vs. displacement are obtained, corresponding to each duration rang value respectively. An example of 4 curves is shown in Fig 3.42, corresponding to the duration rang as 0-50μs, 450-500μs, 950-1000μs and 1450-1500μs, respectively. A good correlation was found between the two energies, resulted from the signal with duration from 0-50μs, and the AE energy curve is quite smooth, indicating that signals are generated continuously, however, the correlation is significantly worse with increasing duration, the evolution curve increases incrementally, with brutal increasing energy. According to these observations, the AE energy evolution of the signal with short duration is better correlated with fracture energy evolution than that with longer duration. As the duration is linked with the damage source, it also suggests that most fracture energy is consumed to develop micro crack, the energy which is required to associate the micro crack to macro crack cannot be observed from the load displacement curve. However, when the macro crack is formed, it generates the signal with long duration instantly.

Another parameter RMSE (Root Means Square Error) is applied to evaluate the quality of the correlation, which can be calculated by the following equations (Eq 3.5-Eq 3.6):

$$RMSE(\%) = \frac{\sqrt{\frac{1}{N}\sum_{i=1}^{N}|e_i|^2}}{\frac{1}{N}\sum_{i=1}^{N}E_{meca,i}} \tag{3.5}$$

$$e_i = E_{meca,i} - E_{EA,i} \tag{3.6}$$

Where $E_{meca,i}$ and $E_{EA,i}$ are the dissipated fracture energy and AE energy after

normalization respectively, N is the number of points counted in the curve.

The lower RMSE is, the better correlation is. Here, the RMSE obtained by the correlation of energy of each incremental range of duration, is normalized by the averaged mechanical energy, each bar corresponds to each incremental rang of 50μs in Fig 3.43. The value is relatively low when the duration is below 850μs, the RMSE shifts to higher value beyond this value, this value can be interpreted as a possible threshold to discriminate the signal in two categories: (a) signal with short duration is generated continuously and the energy evolution is better correlated with fracture energy, (b) signal with long duration recorded punctually and the evolution is quite different from the fracture energy.

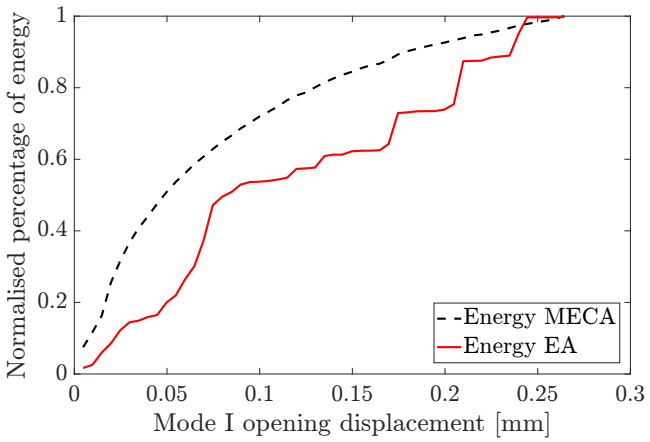

Figure 3.41: Normalized cumulative AE hits energy and fracture energy vs. displacement (all signals are considered)

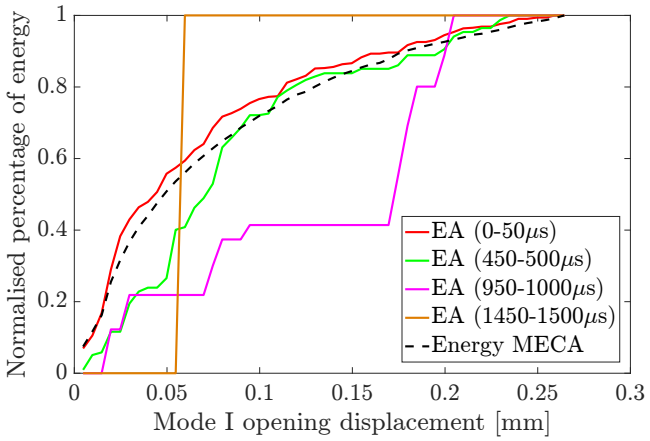

Figure 3.42: Normalized cumulative AE hits energy in different duration range and fracture energy vs. displacement

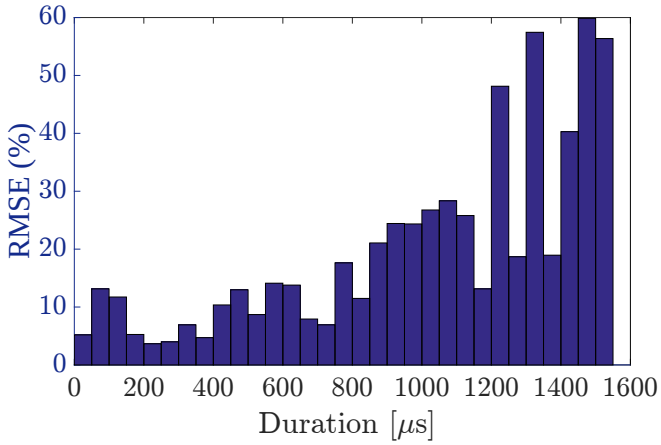

Figure 3.43: RMSE results for each duration range

3.5.3 Discrimination from macro crack to friction

This discrimination is based on the comparison of results from the tensile and shear test. As observed in the previous part, the parameter duration is a distinctive parameter which enable to distinguish the source from the micro to macro crack. We will still use this parameter to distinguish the signal from the macro crack to friction. As the absolute energy of each hit is calculated as the squared sum of amplitude in term of duration, a strong correlation is found between the duration, amplitude of a hit and its absolute energy. Thus, these two parameters corresponding to each failure mode are studied. In order to compare the AE parameter in these two tests, the distance from the damage source to sensor should also be considered[Aggelis et al., 2012],[Aggelis et al., 2017]. In the tensile test, the longest distance of signal propagation is about 13cm, corresponding to the diagonal distance. While that in the shear test is about 15cm. The maximal receiving distance is comparable at the same scale in these two different tests. On this basis, the analysis of acoustic emission in these two different failure modes can be also compared. The presentation about the amplitude vs. duration of all the signals in these two tests is shown in the Fig 3.44, respectively. The value of each grid is calculated as the number of signals in a given amplitude and duration, corresponding to the color bar.

Comparing these two presentations, it is more clear that the amplitude of signal in tensile test is generally lower than that in shear test. And the max amplitude in the latter test could reach to 85dB more even higher, against 70dB observed in the former test. The similar observation is found also in duration value. In tensile test, almost all the duration of hits is lower than 2 ms. In shear test, at

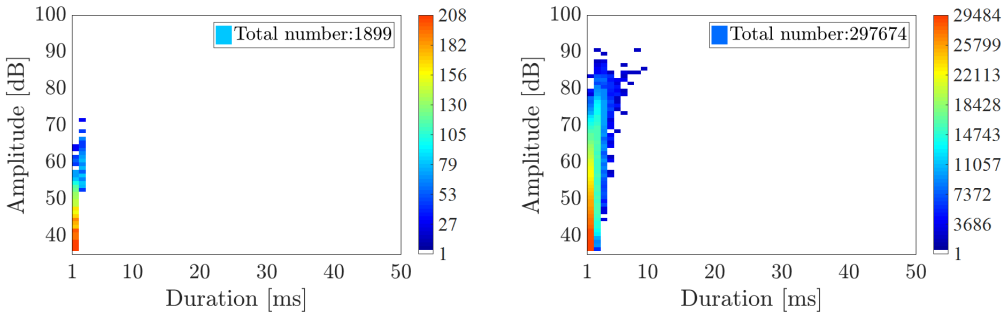

(a) (b)

Figure 3.44: Correlation of AE amplitude and absolute energy / duration of specimen T2

the linear phase, the duration of most signals is also short. It should be noticed that some long signals at pre-peak phase Fig 3.45(a) are probably resulted from composition crush, the compact of composition, the loading setup, the sliding when the specimen started to be loaded. When the friction was induced, the duration turns to be higher, the maximal duration exceeds 2ms. At the post-peak phase Fig 3.45(b), the full frictional behavior is reached, the value of duration remains constant and much higher (12ms) than that observed in the previous phase (3ms).

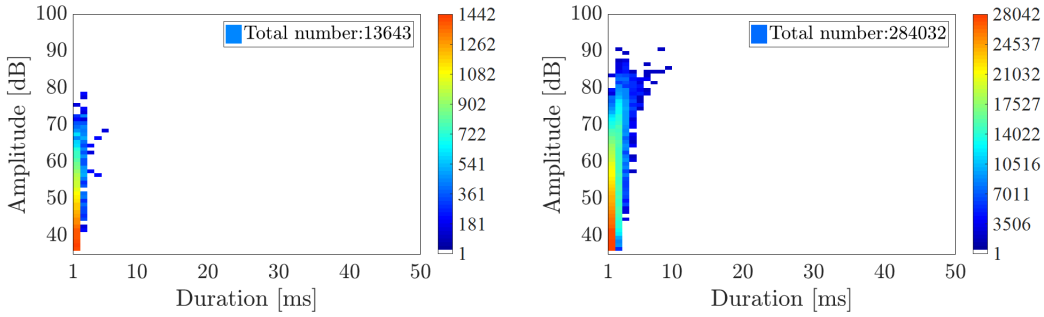

(a) (b)

Figure 3.45: Shear test : Amplitude vs duration in (a) pre-peak phase and (b) post-peak phase of sample S0.8-4

3.6 Conclusion

In this chapter, we have discussed the performance of AET at the mechanical damage monitoring and the source discrimination at an assemblage scale. The experimental tests were carried on the small scale laboratory specimens under tensile and shear

loading, and monitored by AET.

In this section, we focus on the damage development of duo specimen in masonry subjected to monotone and cyclic tensile loading and the performance of AET in the monitoring of tensile damage. We have found that the material shows a typical quasi-brittle behavior under tensile loading. And the cyclic envelop curves are quietly similar to monotonic tensile curve. The residual displacement as well as the stiffness degradation are also observed in the cyclic test. Besides the stiffness of a damaged material can recover to the initial stiffness under compression.

With respect to AET, a good agreement is found between the AE activities and mechanical damage. Further understanding of damage process particularly at the softening phase is acknowledged by AE activities analysis. The early detection of damage has been observed at the first cycle before load peak which is processing for on-site diagnosis and monitoring of masonry structures. Besides the ultrasonic measurement (amplitude and velocity) shows a good performance for the monitoring of damage but micro-craking before cracks propagation cannot be detected. Moreover, auto-correlation analysis seems to be powerful for damage detection in masonry even before peak-load. Others non-linear parameters are currently investigated for testing their sensitivity for the monitoring of mechanical damages.

In tensile test, the mechanical behavior of bed mortar interface is firstly discussed in the uniaxial monotone and cyclic test. The nonlinear phenomenon occurring in the interface block/mortar of masonry is observed in cyclic test, by analyzing the stiffness degradation and the residual displacement. Then, the interpretation of AE activities provides a good correlation with the damage development. Besides, in the cyclic test, the felicity effect is observed which refers to that the new signal appears only when more damage is accumulated in the material. The ultrasonic method also provides its ability for the damage monitoring by signal wave analysis. In shear test, the investigation is carried out under different compressive stress, by the means of AET. Different damage stages can be identified by the mechanical response and the acoustic activities. It is also found that the AE signature is also affected by the loading rate applied on the specimen.

Compared with the mechanical behavior of these two failure modes: tensile and shear. It can be found that more signals are generated in shear test, and the signals are more energetic, particularly at the phase of friction.

From the correlation of AE parameter and the cluster results, it is observed that the signal duration is a dominant parameter in the source discrimination. This parameter can distinguish the signal from micro crack to macro crack in tensile test,

based on the correlation between the evolution of AE energy and fracture energy. This can be attributed to the fact that a better correlation is observed between 2 forms of energy rates when AE energy rate is calculated with signals having lower duration. Compared with the tensile and shear test, the signal with duration beyond 2ms can be considered to be related to friction.

Chapter 4

Damage monitoring in shear wall test

4.1 Introduction

In the previous chapter, the tensile and shear failure at the bloc-mortar interface were analyzed separately by the mechanical response and by the means of acoustic emission technique. We have found that the acoustic activities show a good performance at damage monitoring including the micro crack, the macro crack as well as the friction. And by comparing the parameters of acoustic emission in these different failure modes, the signal from the different sources can be distinguished. These observations prove the capacity of this technique for damage monitoring and source discrimination in the case where the failure mode is relatively simple and controlled in a small-scale specimen.

It is then questioned if this technique still have a good performance in the damage monitoring when the failure modes are more complex at a larger scale specimen. And if this technique can distinguish the signals from the different damage source in such a situation. For this purpose, in this chapter, the performance of AET will be investigated in a masonry wall subjected to a combination of shear and normal compressive stress where more complex failures modes can be observed, based on the literature. A series of experimental tests at a masonry wall at laboratory will be firstly presented. This wall experimental campaign was carried out by Venzal in the context of his thesis[Venzal et al., 2020]. These shear wall tests were also monitored by digital image correlation (DIC) technique. This technique is a non-destructive technique which can assess strains fields and visualize the crack pattern at a real time by analyzing the displacement fields of the investigate zone.

The failure modes as well as the crack paths will be discussed, based on the

mechanical response and the observations from DIC. Then, the analysis of acoustic activities will be carried out in order to be correlated with the envelope mechanic responses and cyclic mechanic response. The source discrimination by acoustic parameters will also be studied at different zone of masonry wall. These analyses are based on the observations from the tensile and shear test.

4.2 Materials and materiel

Nine wall shear tests were carried out where the test configuration (Fig 4.1). The shear walls were built by the blocks with dimensions $0.3\times0.1\times0.15m^3$. The materials used in the construction of the walls were the same to those used in the tensile and shear test at the assemblage scale. The wall dimensions were $1.835\times1.17\times0.15m^3$ consisting of 11 layers. The nine tests concern three compressive stress levels 0.3, 0.4 and 0.5 MPa, and for each stress level, three tests were repeated. These dimensions were designed considering the test bench capacity in laboratory and the dimension observed of masonry construction in Bordeaux, according to the European Standards.

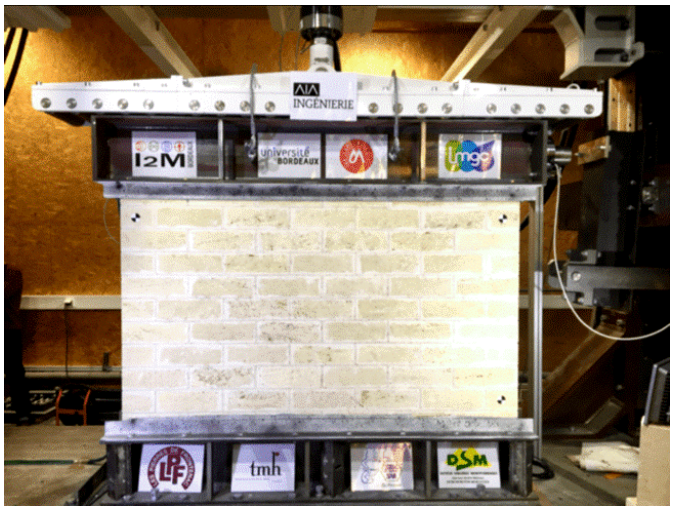

Figure 4.1: Experimental set-up of shear wall test

Firstly, the wall was glued into a metallic angle section at the top and bottom side. The bottom section was clamped on a metal profile, which was fixed into the test bench, to ensure a clamped boundary condition. A distributed vertical load, transferred by steel roller bearings was provided by a hydraulic jack system (250kN capacity), this load was raised progressively to the target normal stress value and remained constant during the rest of the test. The roller bearing beam and the

jack piston road were linked by a pivot connection to ensure a cantilever boundary condition.

A horizontal load was then applied by another hydraulic jack system of 200kN capacity. The specimen was subjected to a low-level pre-load at the beginning step of 5 kN. For a better understanding of damage evolution in shearing wall, 8 load-unload cycles were realized. Note that during each cycle, the shear load was controlled by the horizontal displacement. When the displacement reached to a certain increment, the load was unloaded gradually to the initial value of 5kN (pre-load). One displacement transduces (LVDT) was used to measure the horizontal wall-top displacement. The experimental test set-up is show in the Fig 4.1.

A DIC system was set up in front of the wall in order to visualize displacement fields and crack evolution. AET was set up at the other side to avoid perturbation of DIC measurements. The sensor placement pattern has been chosen by considering the wave attenuation and detection area (Fig 4.2).

Figure 4.2: Experimental test set-up in the EA side

4.2.1 DIC setup for shear wall

DIC is an optical non-contact technique for analyzing the full-field deformation by image matching process. Image acquisition for DIC was used by 2 cameras (PIKE F-421B) with 4 megapixel ((2048 $\times$2048 pixels) with their SCHNEIDER XENOPLAN objectives (focal length = 29.3 mm). With this camera system, one pixel corresponds approximately to one millimeter. Due to the inhomogeneity of stone, the tested wall has enough intrinsic contrasts that no pattering was needed. A calibration test was carried out before the test and one reference image was captured before each cycle. The software VIC-SNAP recorded the images with a sampling rate of 1 frame per

2 seconds depending on the overall duration of each cycle. A subset size of 55×55 pixel with step size of 4 pixel was used to compute the results, with the help of image processing software VIC-3D. Thus, a three-dimensional displacement field on the studied area is determined.

4.2.2 AE configuration

The acquisition system of AET was equipped with a Peripheral Component interface (PCI) with 8 channels boards for the data acquisition and a software for data collection and processing. The piezoelectric sensors R15 with a resonant frequency of about 150 kHz were thinly glued by a silicone grease as the coupling agent to ensure a good contact. A sampling frequency of 1MHz was use for the acquisition of 2048 samples per AE signal. The pre-amplifier gain was set at 40dB with amplitude detection threshold of 35dB. The threshold was set to eliminate the signal from the environmental bruit. The signal was filtered by a pass-band filter ranging 100-400 kHz, to eliminate the no-sensitive frequencies signal and noise. To ensure good contact of sensors, amplitude from break-pencil test near each sensor has been verified to be between 95 and 100 dB.

4.2.3 Pencil lead break test(PLB)

The pencil lead break test (PLB) is indispensable to confirm the good adherence of sensor before each test. For the shear wall, it is also interesting to perform this test to obtain the attenuation curve. This curve describes the decrease of amplitude of AE signal propagating along a structure as shown in the Fig 4.3. The attenuation curve helps to determine the maximal distance between 2 sensors necessary to record every signal. As masonry is an anisotropic composite material, consisting of stone bloc and mortar, the ultrasound wave crosses different composition. Therefore, PLB is quite necessary to show the wave attenuation and its velocity in the different directions in the tested masonry. Besides the PLB can help to determine setup parameters of AE, according to the waveform of recorded signal as in the tensile test because this artificial acoustic emission source is provided by Hsu-Nielsen source, which is similar to a nature acoustic emission source such as a crack[Grosse and Ohtsu, 2008].

PLB configuration Due to the large dimension of tested material, the tests were repeated in four zones as shown in the Fig 4.4. In each zone, fours sensors were positioned as shown in the Figure 5. This arrangement is to obtain the wave attenuation and wave velocity in three directions: the horizontal, vertical and diagonal

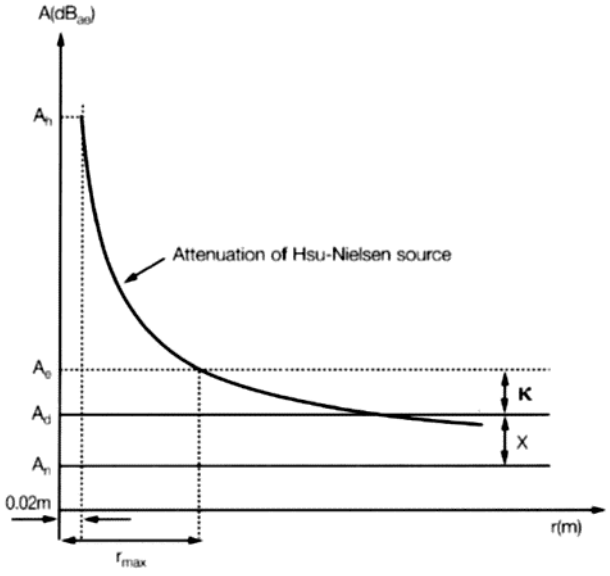

Figure 4.3: Determination of the maximum allowed sensor spacing 'rmax' from the attenuation curve[Rogers, 2013]

direction.

In order to get a full information curve including the attenuation in the limestone bloc and also in the lime mortar, the lead breaks were taken at the stone blocs and also at the mortar joint. The schema of test's position is shown in the Fig 4.5, the point in different color refers to the lead break position. In the horizontal direction, 3 stone blocs are concerned, 5 lead breaks points spaced 50 mm are involved in each bloc. 3 lead break points at mortar were added: two points were just before and after joint and the third one was exactly in the middle of mortar. In the vertical direction, 3 lead break points were concerned in each bloc, spacing 25 mm, 3 points were added at the interface as that in the horizontal direction.

Avoiding analyzing the complex phenomena in the interface following the diagonal direction, the 18 pencil lead tests were undertaken only in the stone blocs. For each direction, the PLB test was repeated 3 times.

PLB test results

The decrease of amplitude following the three directions in the zone is firstly studied. The Fig 4.6 shows the decrease of amplitude in the horizontal direction of the zone 1. The amplitude was taken from the signal recorded by the sensor 1 in each breaking. The attenuation curves are presented in two ways: with and without taking account of the lead breaking at the interface. The position of the mortar is represented by the dashed line. The brutal decrease of amplitude is observed

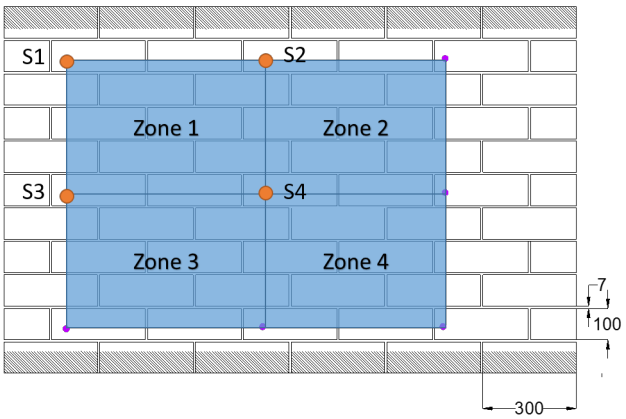

Figure 4.4: PLB test in 4 zone

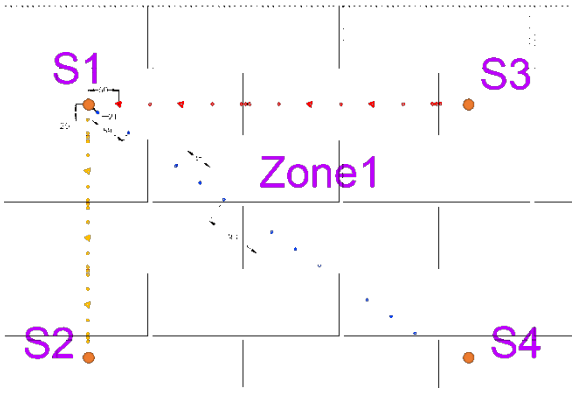

Figure 4.5: Sensor position and the lead breaking position for one zone

at the interface, indicating that the signal is greatly attenuated, resulted from the wave traversing the mortar. In order to summarize the attenuation curve in all the directions and determine the maximal distance of detection by a fitting correlation, the attenuation curve without the PLB at the mortar is also taken into account.

In the Fig 4.7, in comparison with 4 zones of a unique wall in the horizontal direction without taking into account of PLB at mortar, the variation of the four attenuation curves might be related to heterogeneity of the limestone blocks and lime mortar used to build the wall. A pronounced low amplitude in a small distance of zone 3, was due to the lead breaking in a pore. Similar curve evolution was observed in vertical and diagonal direction.

An exponential correlation is obtained according to the attenuation equation[Feng and Yi, 2017]

$$A = A_0 e^{-ax} \tag{4.1}$$

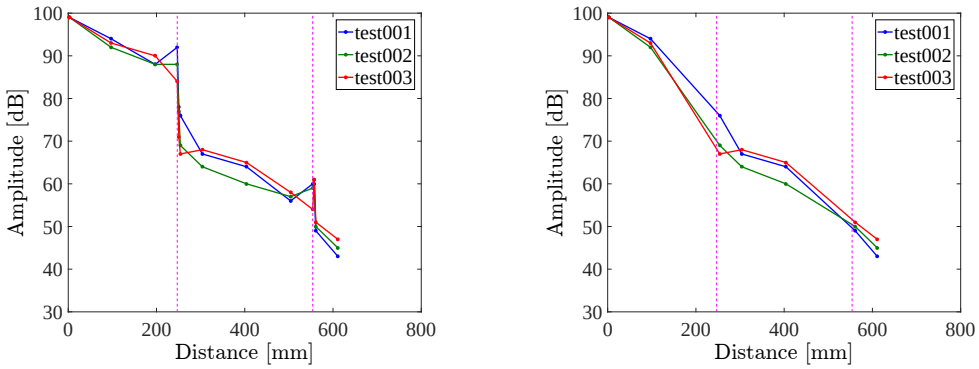

Figure 4.6: Decrease of amplitude vs. distance (a) with and (b) without lead breading at the mortar

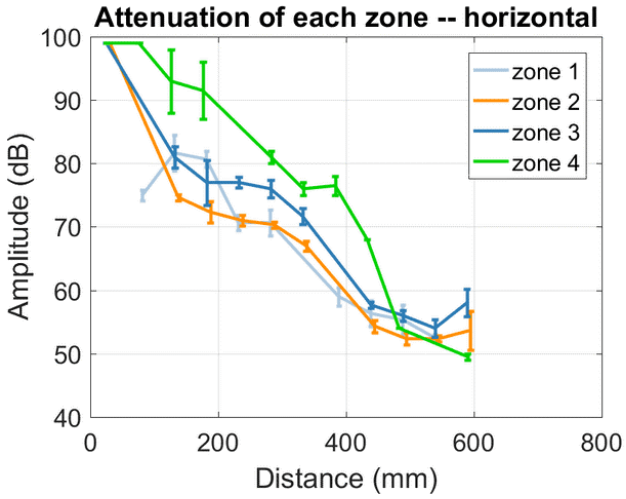

Figure 4.7: Attenuation of amplitude in horizontal direction

Where A0 is the attenuated amplitude, the amplitude A is the reduced amplitude after the wave propagation distance z. And a is the attenuation coefficient. The each solid curve corresponds to the exponential correlation fitting, which is calculated from the amplitude attenuation of the 4 zones, two dotted curves delimit the interval of variation around the theoretical value with a confidence level of 90%. More Attenuation was found in vertical, likely to be related with a higher mortar joints density in the vertical direction (Fig 4.8). According to the summarized figure, the maximal distance of signal detection in the horizontal and diagonal direction is about 800mm while that in the vertical direction is about 550mm. These difference is mainly resulted from the masonry arrangement and the crossing mortar number.

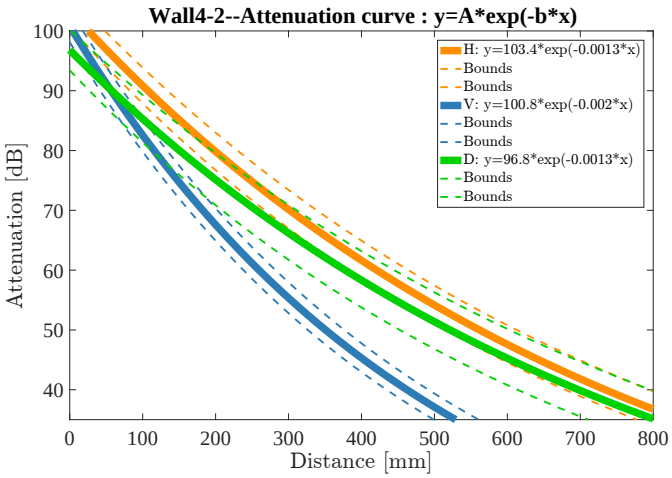

Figure 4.8: Summarized attenuation curve in the 3 directions

4.3 Experimental results and discussion

In the basis of the AE results and the mechanical response of masonry prism under the tensile and shear loading, the AET provide a good performance on the damage monitoring. Besides, the AE parameter duration is considered as a dominant parameter for the source discrimination from the micro and macro cracks as well as friction. These promising results are concluded from the test at a relative small scale, in this following part, we will apply the same methodology of analysis in the shear wall to verify if these results can be used for a larger scale structure under a cyclic loading. Thus the following study will start with the investigation of AE for the damage monitoring. This part will discuss the acoustic activities as well as AE parameters in the association with the damage evolution in a monotonic envelope analysis as well in cyclic analysis. The source discrimination will then be presented by using the AE parameter duration.

The summarized Fig 4.9 presents the load-displacement curve of each test under the constant compressive stress of 0.3, 0.4 and 0.5 MPa, respectively. From this figure, all the curves exhibit a similar tendency of load with the increasing displacement, regardless of peak load. Besides 3 phases can be observed, including the linear phase, a transition phase and a constant load phase.. Based on this similarity under different compressive stress level, in the following section, only one shear test 4-2 under constant stress of 0.4MPa will be discussed.

Fig 4.10 shows the mechanical response of the wall under the combination of a horizontal load and a constant stress 0.4MPa in all the cycles. The load-displacement

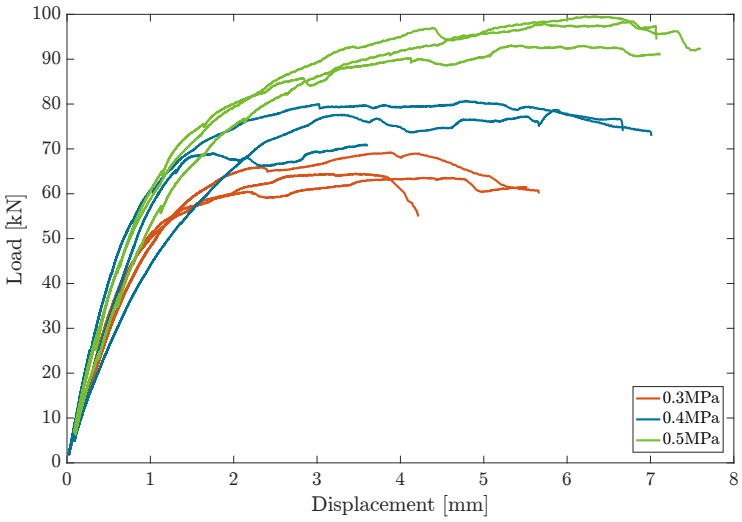

Figure 4.9: Summarized load-displacement envelop curve

curve of each cycle is plotted with each corresponding color. The envelop curve is obtain from the curve between the intersection points.

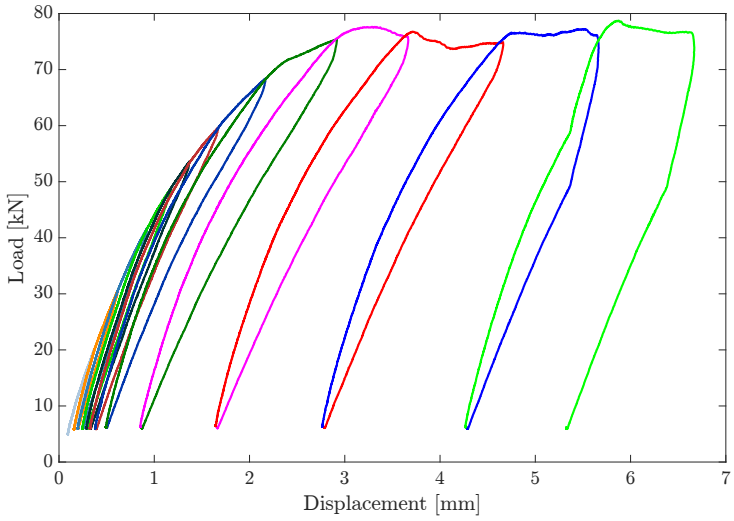

Figure 4.10: Load-displacement curve of cyclic test on a shear wall 4-2 under 0.4MPa

Based on the attenuation curve obtain from the PLB test, the distance of signal detection by the each sensor is taken into account. Besides, the main crack propagation path can be also envisaged from the literature review part. The position of sensors are determined near the damaged area of overall wall. The positions

of sensors are illustrated in the Fig 4.11 and summarized in the Tab 4.1.

Table 4.1: Position of sensors in shear wall test under compressive stress

N° Capteur	Pos.X(m)	Pos.Y(m)
2	0.91475	1.0154
3	1.7285	0.9764
4	1.25	0.5999
5	0.5065	0.5879
6	1.7075	0.1669
7	0.917	0.1299
8	0.08125	0.1239

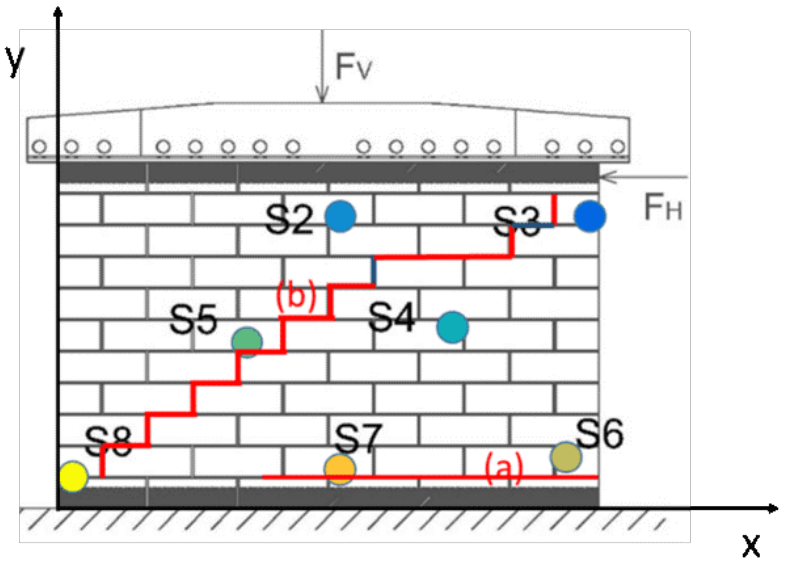

Figure 4.11: Illustration of shear wall test setup and sensor position,

Although this is a cyclic test, we will firstly present the monotonic mechanical behavior resulting from the envelop curve in this part, as shown in Fig 4.12. This envelop curve load vs. horizontal displacement illustrates firstly a linear zone until the point A at 0.58mm (Stage I) and this curve is no longer linear when the damage occurs. A horizontal crack at the bottom is initialed and propagate along the block-mortar interface at the stage II, corresponding to the point B (2.15mm). The stage III can be considered as a transition stage while micro cracks are developed and started to form into macro cracks in the diagonal direction. From the point C (3.16mm) to the point D (6.35mm), due to the formation of macro cracks, more friction participate under the combining loadings.

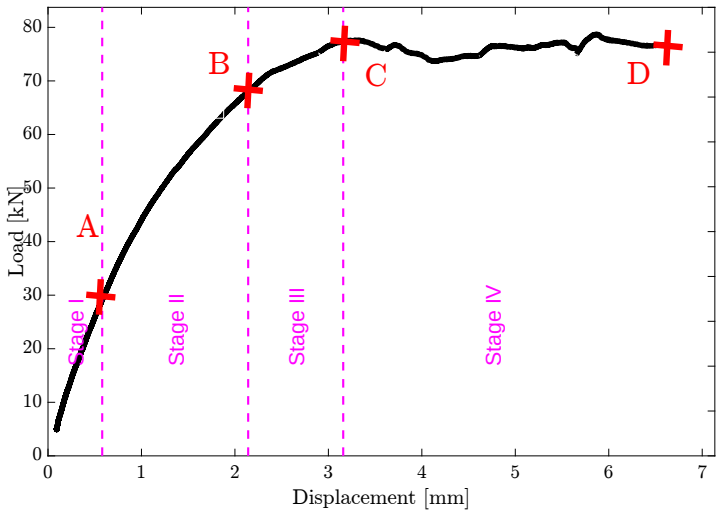

Figure 4.12: Curve load vs. displacement in shear wall test

Based on captured images and the DIC post-processing, it enables to post process the strain fields concerning the horizontal strain (ϵ_{xx}) and vertical strain (ϵ_{yy}) at the point A,B,C and D on the curve in Fig 4.12. These four points could be regarded as the end of stage I, II, III and IV. Stage II corresponds to the propagation of a horizontal crack (a) while stage IV corresponds to the propagation of a diagonal crack (b) in the Fig 4.11. Thus, four stages of crack formation and development could be identified.

Stage I: the slope of curve remains constant, indicating that the structure performed an elastic behavior with a constant stiffness (6.1×10^7 N/m). The end of this first stage takes place at the point A, which corresponds to the initiation of horizontal crack (a) propagation.

Stage II: the slope in this stage shifts to be lower. The no linear behavior in this stage is associated to the propagation of crack (a) observed at the bottom bed mortar in direction of shear load in Fig 4.11. In this area, vertical tensile stress, induced by the moment at the bottom of the wall, raises and exceeds the interface tensile strength. However, with less effective surface due to normal stress redistribution, the compression in the rest of undamaged horizontal area of the first bed increases. When this compressive stress reaches a critical value of friction, this horizontal crack (a) is prevent to propagate (Point B)[Bisoffi-Sauve, 2016]. The vertical strain at this point shows the total length of this horizontal crack at the end of its propagation in Fig 4.11(about 62 cm).

Stage III: at this transition stage, the mechanical curve tends towards flat, more micro cracks are formed with the rising horizontal loading according to the strain ϵ_{xx} ϵ_{yy} at the point C. These micro cracks are observed at the diagonal direction of wall. Some cracks initialize, however these individual cracks have not yet formed into a main diagonal crack, which will show up at the following stage.

Stage IV: Unlike the previous stages, the curve tends towards flat or even drop down which is caused by the formation of the diagonal crack (b) at the bloc-joint interface in Fig 4.11. This crack was observed from the right top to left bottom propagating the whole wall in a diagonal direction. Similar as the ruin mechanism of previously mentioned shear test, this crack appears in case that the compressive force is sufficiently strong. The horizontal strain at the point C shows the crack initiation. A pronounced strain in plane ϵ_{xx},ϵ_{yy} was shown in diagonal at the point D (Fig 4.13).

4.3.1 Comparison hit vs. event

In the analysis of AE, hit-based analysis and event-based analysis are frequently used. In fact, an event is the term given to a group of hits received from AE source[Fu, 2005]. For a two dimensional plan, an event is determined while at least 3 sensors detect signal from the same source. The use of events is to limit the influence of noise, which is more easily detected by only one sensor. The noise will affect the analysis of acoustic which is generated from the damage source. More frequently, the event is used in the crack localization. However, in some cases, it is not simple to use events instead of hits, due to the low amplitude, as that in the tensile test presented in the previous chapter. The low amplitude will probably result to a huge decrease of event number, influencing the AE result interpretation. Thus, for the shear wall test, we will firstly compare the event and hits number to determine which of hits or events will be used for the following analysis. The (Fig 4.14) shows the amplitude distribution of hits and the hits associated to the events. The hits and events studied here are taken from all the sensors in the overall test. The range of amplitude is taken from 35dB to 100dB with an interval of 1 dB. It can be found that the most of signals are concentrated at a low amplitude, the signal number decreases with the increasing amplitude. Moreover, for the most hits, it is not associated to an event. For all the hits, less than 10% of signals are formed into event according to Tab 4.2. Thus, in our case, it is suggested to analyze the hits rather than event, considering the number of events.

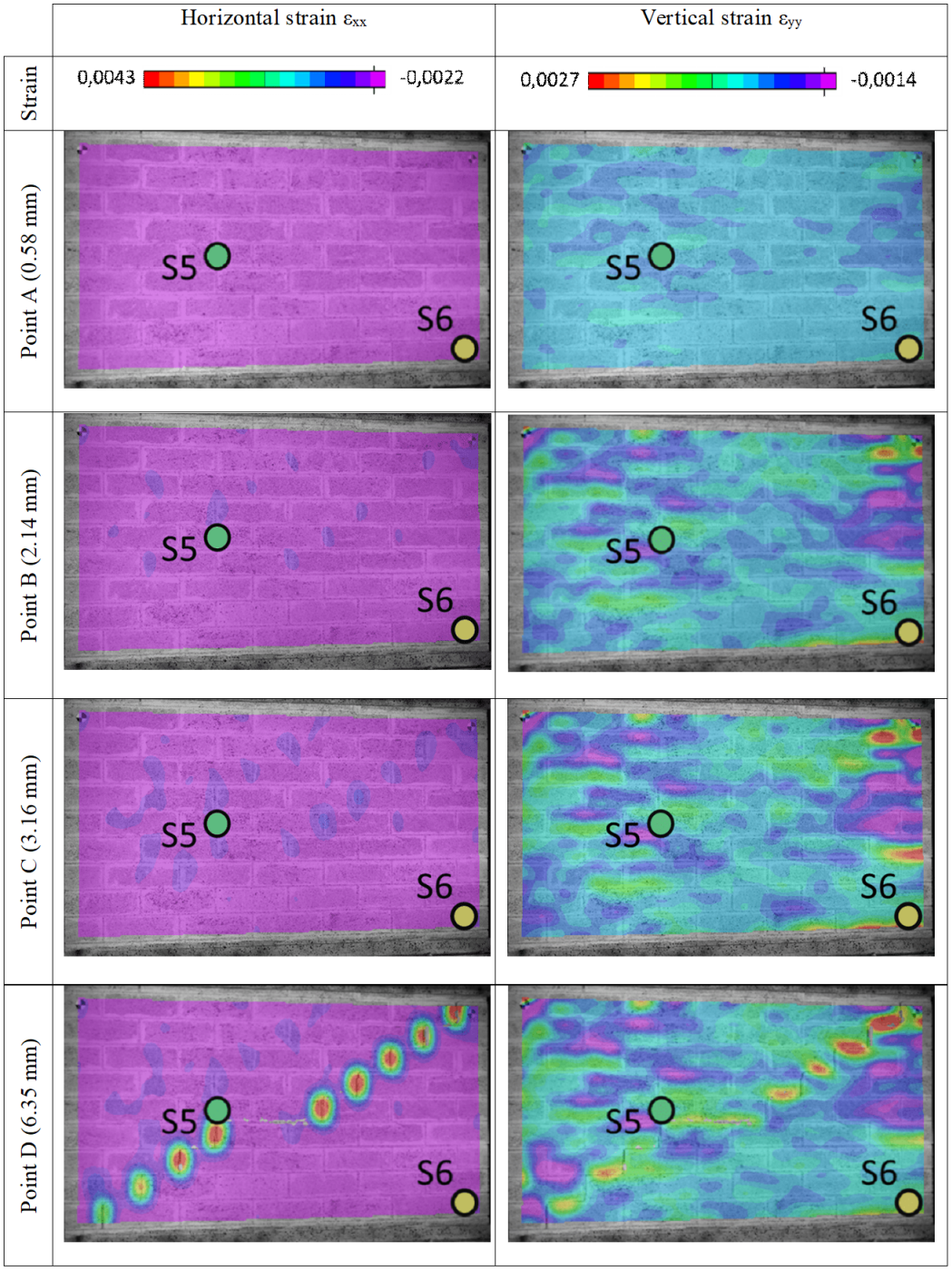

Figure 4.13: Horizontal and vertical strain at point A, B, C and D

4.3.2 Damage monitoring in monotonic envelope curve

This shear wall test was carried out by applying a cyclic shear loading. However, in order to get a more general material deterioration and compared with acoustic emission, the first analysis is based on the envelope of load-displacement curve. As

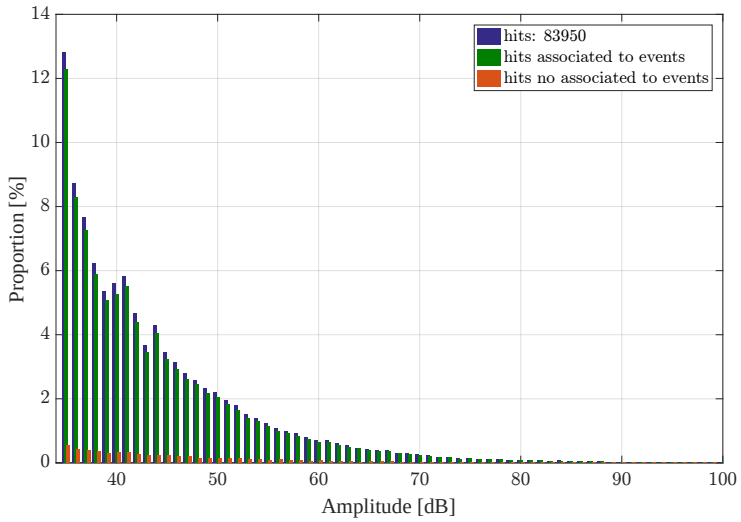

Figure 4.14: Frequency of hits, hits associated or not to event vs. amplitude

Table 4.2: Summary of event and hit number

	Total hits	Total events	Hit associated to events	Hit non-associated to events
Number	83698	1559	4897	78801
Percentage (%)	100		5.85	94.15

no crack induces no signal, the hit number and the hit energy are two elementary parameters to understand the crack initiation and formation as well as the material deterioration. As shown in the Fig 4.20, the number and energy of hits of all sensors are presented with respect to the displacement. As the same calculation method in the tensile and shear test, the value of each bar corresponds to the sum of the number or energy of hits in each 1µm imposed horizontal displacement. And according to the DIC observation, the limit of four stages are also plotted in this Fig 4.12(in dashed magenta lines).

Stage I: in this stage, the wall is considered as in an elastic domain, and no evident crack is observed. However, some signals are also detected, these signals are not energetic, indicating that these signals are likely related to the stabilization of material, the compaction of voids or some micro crack which cannot be observed from DIC results or from the envelope curve.

Stage II: the load-displacement curve is no longer linear, the crack at the bottom was initially formed and developed. An increasing rate of hits number is observed. However the energy of these signals is still at a low value. This observation is similar

as that occurred in the tensile test.

Stage III: this stage is considered as a transition stage. More micro cracks formed into macro crack at the bloc-mortar interface. These individual macro cracks are observed at the diagonal direction from the right top to left bottom of wall. A great amount of hits are then generated from the crack formation. These hits show a little more energetic than that in the previous stage. However compared with the following stage, the energy of hits remains at a low value, indicating the main diagonal crack has not yet formed from the individual macro cracks.

Stage IV: Once the main diagonal crack is formed at the interface, more friction participles, corresponding to the flat part of load-displacement curve. The number of hits per displacement is no longer increased, however this amount of hits presents a huge energy value. This observation is similar as that at the full friction phase of triplet assemblage shear test. However, the hits number in shear wall test is not constant as that in shear test. In fact, in shear wall test, the full friction phase is not evident, the instabilities as the load drop can be observed in the curve. These pronounced instabilities likely refer to the formation and propagation of macro crack. It should be noticed that a great number of hits occur immediately after the accidental instability, when the horizontal load slightly increases (drawn in red cycle). These signals related to the crack shows the energy is less than signal generated at the fiction phase.

Besides, some signals are not recorded, resulted from the saturation of signal. That means the acquisition card cannot deal with all the signals during the test, this phenomenon is observed particularly in the sensors 5 and 8 which are positioned in the zone subjected to the heavier stress.

The results are also presented in terms of the cumulative parameter. Unlike the small size specimen test (tensile and shear test), the signals recorded by each sensor are taken into account separately in shear wall test. Thus, the cumulative hits number and cumulative hits energy of each sensor are normalized by the total value of all the sensors at the end of the test. These cumulative normalized curves are shown in Fig 4.16.

Firstly, few signals are recorded at the elastic phase (Stage I), implying no damage occurred. However, sensors 7 and 8, which were located at the foot and on the left of the wall, recorded some signals probably related to the vertical compressive reclosure of micro crack or micro void at the interface of bloc-joint. When the horizontal crack occurs (Stage II), signals are generated and recorded principally by sensor 7. This sensor placed at the left of this crack records more signals. In

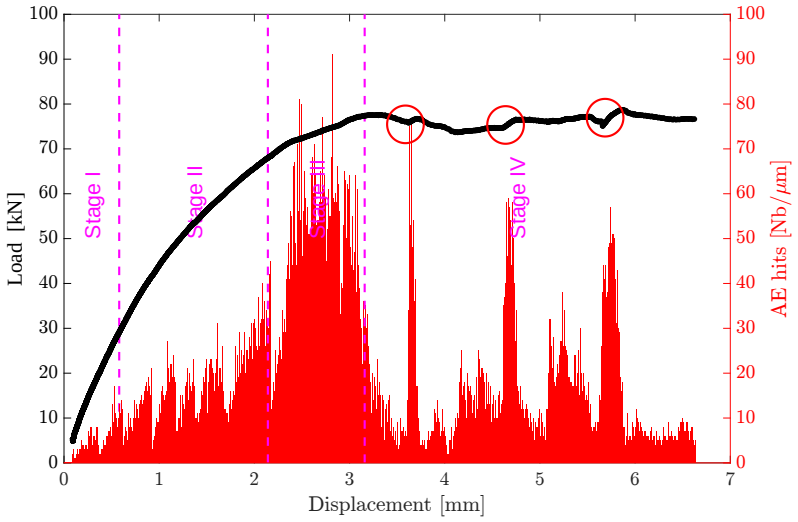

(a)

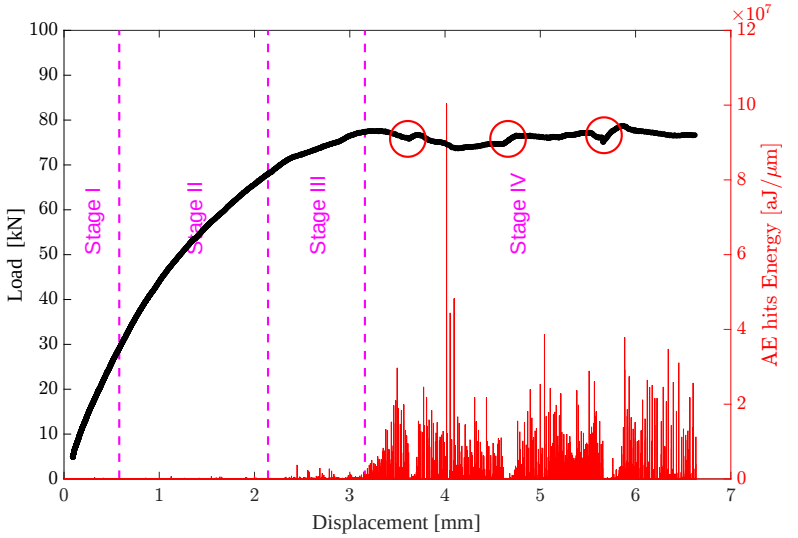

(b)

Figure 4.15: Hit number / energy by each sensor vs. displacement in shear wall test

fact, these signals with relative low energy (Fig 4.16(b))are similar as that in tensile characterization test. At the stage III, a great increase of hits are recorded by S2, S4, S4 and S5, however these hits are not energetic. This observation is agreed with the VIC results at the point C where more micro cracks are formed at this area.

With the initial formation of main diagonal crack (Stage IV), the sensors along

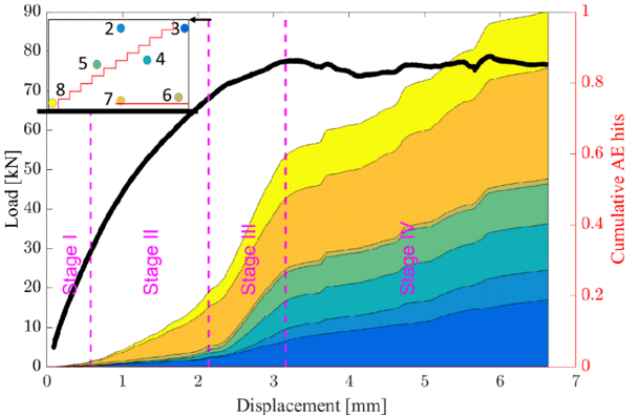

(a)

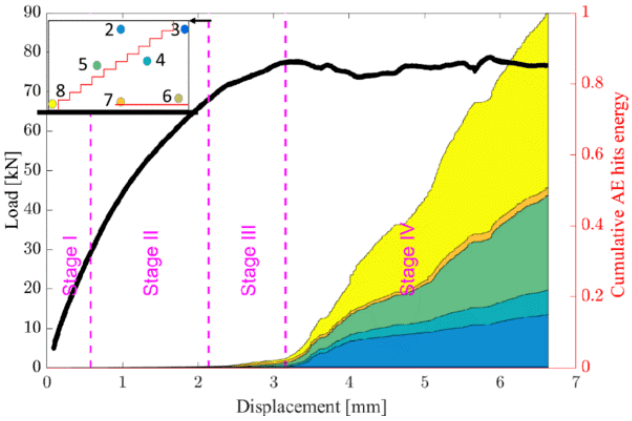

(b)

Figure 4.16: Cumulative hit number / energy by each sensor vs. displacement in shear wall test

the diagonal (S3, S4, S5, S8) which were located not far from the diagonal crack path started to record more energetic signals. The energy of associated hit increases sharply, indicating more friction is involved at the damaged interface. Note that more than 95% of energy is recorded by these four sensors during the whole test.

As mentioned previously, duration and amplitude are strongly correlated with absolute energy. Thus, another two parameters as amplitude and duration are also used to be correlated with the damage evolution in Fig 4.17. In general, the value of these parameters increases with material degradation which have been proved in the tensile and shear test. These observation are already confirmed in the tensile and shear tests. The maximum value of amplitude at linear domain is about 55dB, this maximal value reaches to 90dB and remains constant where the curve is flat. At the stage I and II, the duration of signal is generally inferior to 2 ms which corresponds

to tensile crack formation. More pronounced signal with very long duration are observed when the curve trends to be flat. The origin of these signals is complex that can be related to continuous movement as friction. In fact, these typical signals only appear at the full friction phase and also in shear characterization test, confirming that only the friction generates these long signals.

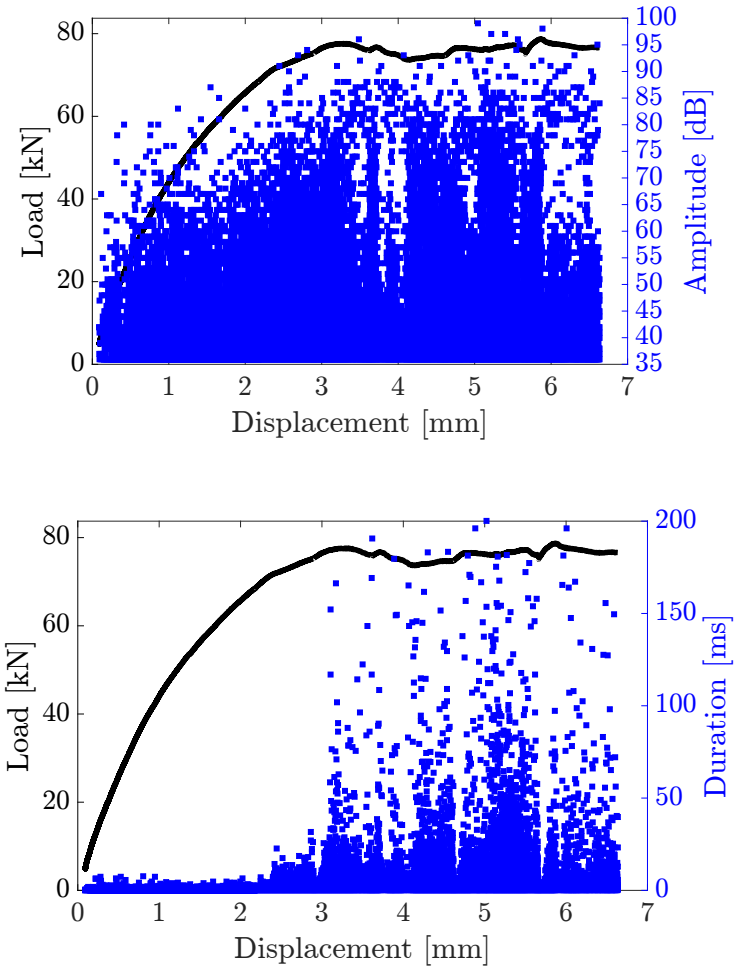

Figure 4.17: Amplitude/ duration vs. displacement in shear wall test

In the envelop curve analysis, a good agreement is observed between the acoustic activities and the mechanical response. More signals with lower energy are generated by the crack formation, more energetic signals are observed at the frictional phase. This analysis shows that the acoustic emission looks promising in the monitoring of material deterioration of masonry wall at a larger scale.

4.3.3 Damage monitoring in cyclic curve

In this part, we focus on analysis of acoustic emission in the cycle monitoring. Similar as shown in the cyclic tensile test, the load-displacement curve (Fig 4.18) can be spitted into 3 stages for any given cycle i:

- Reloading phase from the end of the previous stage which is equally the onset of this present stage (Point A) to the point of the onset of unloading at previous cycle (Point B);
- Softening phase from the point B to the load when the specimen starts to be unloaded (Point C)
- Unloading phase: from the unloading point of the present (Point B) to a constant level load which is the preloading value.

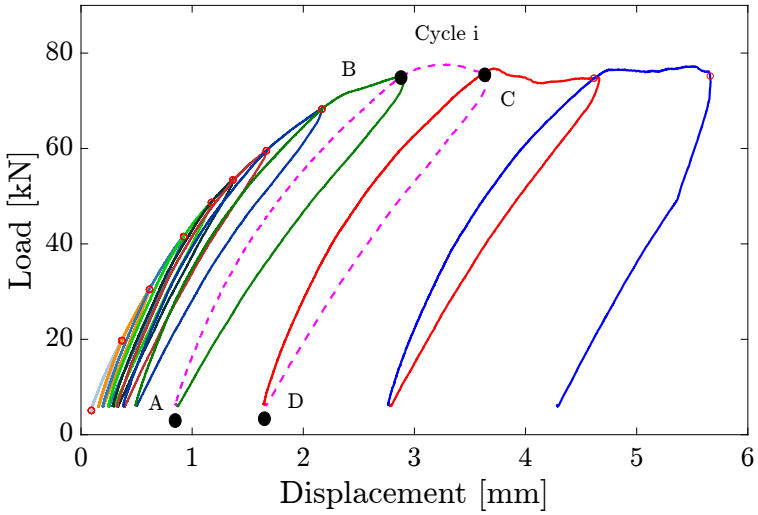

Figure 4.18: Illustration of load-displacement curve

According to DIC results, the stage I, II, III and correspond to the cycle 1-2, cycle 3-7, cycle 8 and cycle 9-12, respectively as shown in the Fig 4.19. The number and the energy of hits are analyzed in the following analysis. The hits number and hits energy are plotted vs. time in the Fig 4.20. The cumulative curve is calculated as the sum of hit number or energy in every one second. Note that this cumulative curve involves the hits at the reloading, softening and unloading phases.

Firstly, it is clear that nearly no hits is observed in the cumulative curve in the first 2 cycles in which the wall remains in the elastic phase. In the beginning of stage

II, an increasing cumulative number of hits and energy is observed. Remember that no cumulative hit energy were observed in the envelop curve at this moment. In fact, this observation highlight the fact that some hits with the significant energy occur at unloading phases. This horizontal crack reclosure seems to be energetic. At the end of stage II, the cumulative energy also shows an increasing trend, and this increasing trend is sharper after the 7th cycle in both cumulative hit number and hit energy.

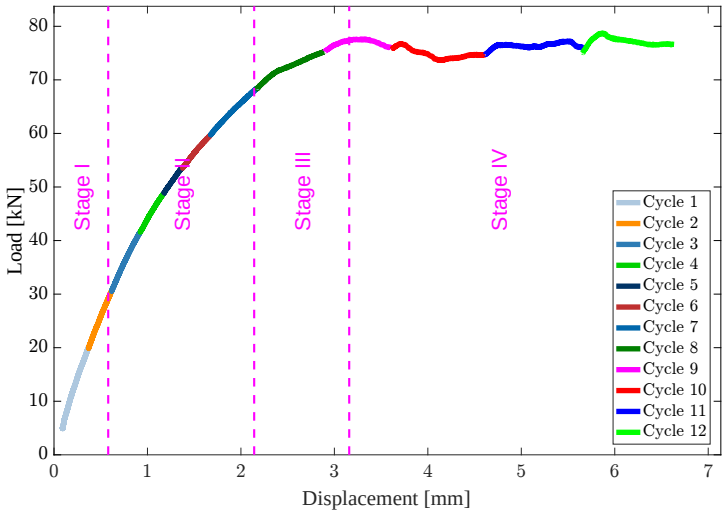

Figure 4.19: Load-displacement envelop by different cycles

In order to understand the acoustic activities in the reloading and unloading phases, the amplitude of signals is used as a parameter in the analysis. By considering the position of the sensors, the amplitude of signal received by sensors 5 and 6 are plotted following the load-time curve in different cycles in the Fig 4.22-Fig 4.24. Note that these two sensors are chosen for the analysis because of their location: sensor 5 is near the diagonal crack (b) while sensor 6 is close the horizontal crack (a). The two magenta lines represent the same level of peak load in the previous cycle and the peak load at the present cycle. Also based the results of DIC, the amplitude evolution will be discussed in three different stages.

Stage I At this stage, two cycles are concerned as shown in Fig 4.21. In cycle 1, some hits are observed at the loading and phase in sensor 6, nearly no signal is recorded by sensor 5. This observation indicates the initiation of the horizontal crack and its slight reclosure. The center area where the sensor 5 is located shows a good elastic behavior (with almost no hit recorded). In these first two cycles, the Kaiser effect can be observed in these two sensors: the new hits appear when the

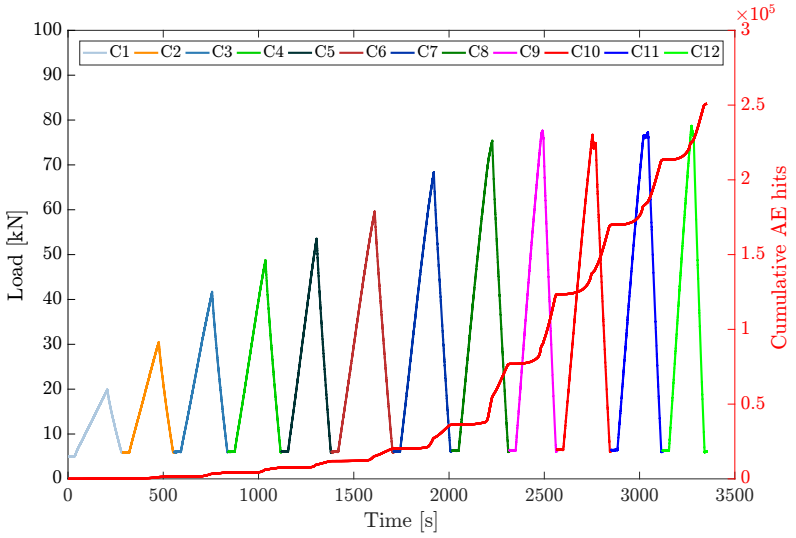

(a)

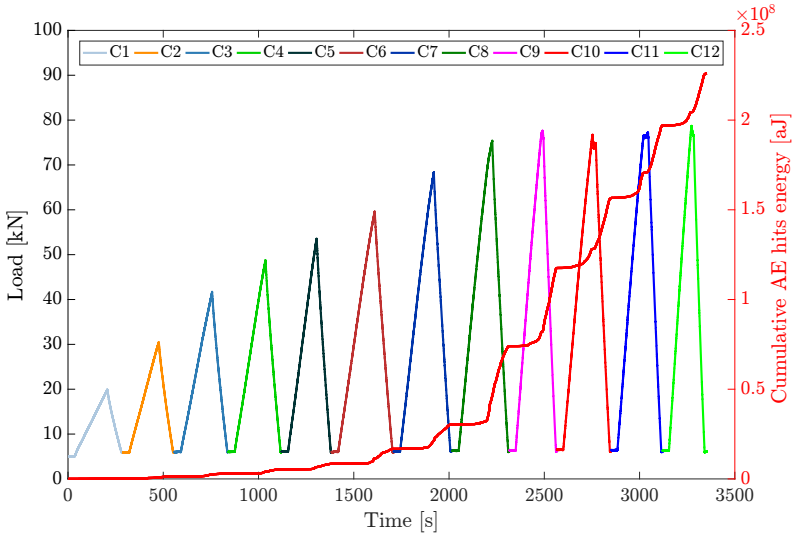

(b)

Figure 4.20: Hit number / energy by all sensors vs. displacement in shear wall test

stress level exceeds the maximal stress in the previous cycle. And in the unloading phase, nearly no signal is detected by sensor 5, and some signals received by sensor 6 indicate some crack reclosing at the right bottom of wall when it is unloaded.

Stage II The stage II involves the cycles from the 3th to the 7th one, in the following Fig 4.22, only the results in the cycle 3, 5 and 7 are plotted. With respect

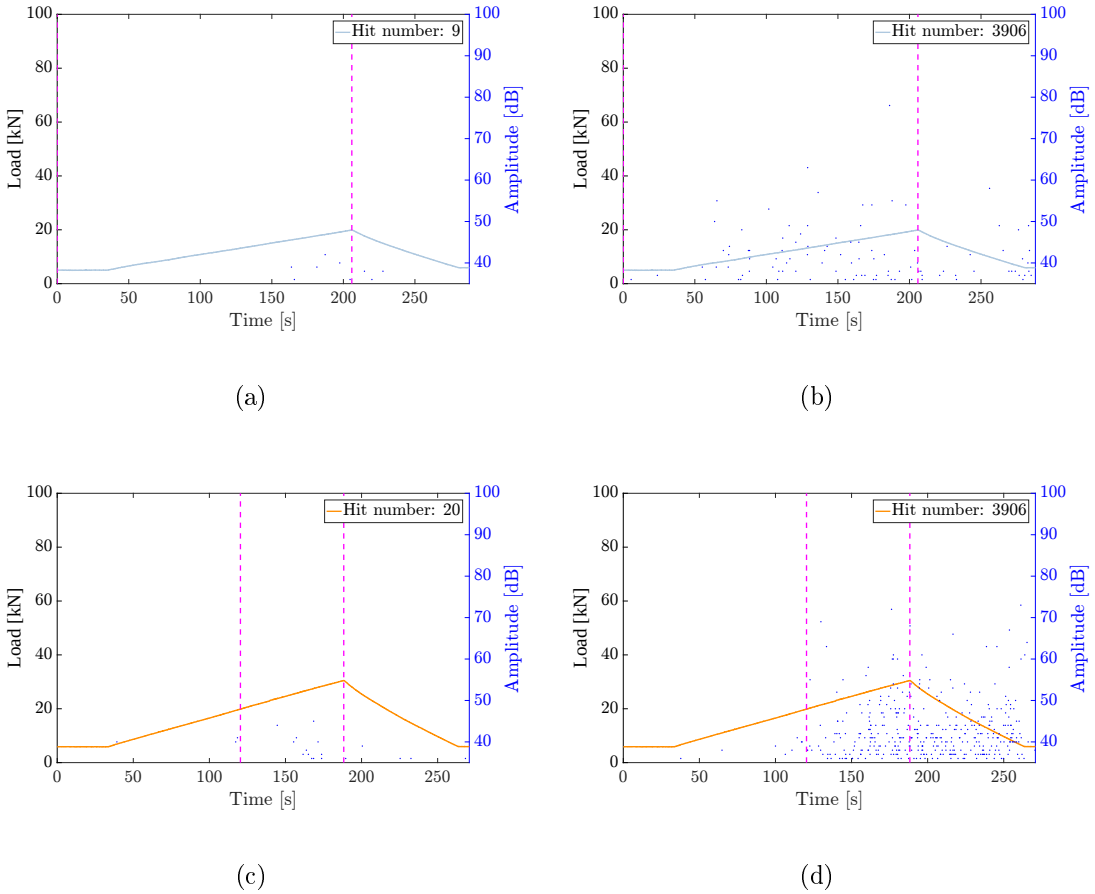

Figure 4.21: Load/amplitude vs. time of sensor 5(left) and sensor 6(right) in stage I

to the amplitude of signal received by the sensor 5, the Kaiser effect is also observed within the overall stage II. However from the sensors 6, this phenomena is no longer observed. Besides, at the unloading phase, for the sensor 5, the observation is found as the previous cycles: no signals occur at the unloading phase. However for the sensor 6, more signals with a greater amplitude are observed at the unloading phase. This observation is related to the reclosing of macro tensile crack. Besides, although the specimen is unloading with a decrease of horizontal force, it is still under a constant vertical loading. More closing surface under the compressive loading generate the signals with greater amplitude. This observation is similar as seen in the tensile-compressive test, where some energetic signals are observed when the specimen is subjected to a compressive loading. And for sensor 5, some signals are also detected in the end of the unloading phase in the cycle 7, indicating some cracks are initially formed. Thus at the unloading phase, the closing of existing crack generates the signals.

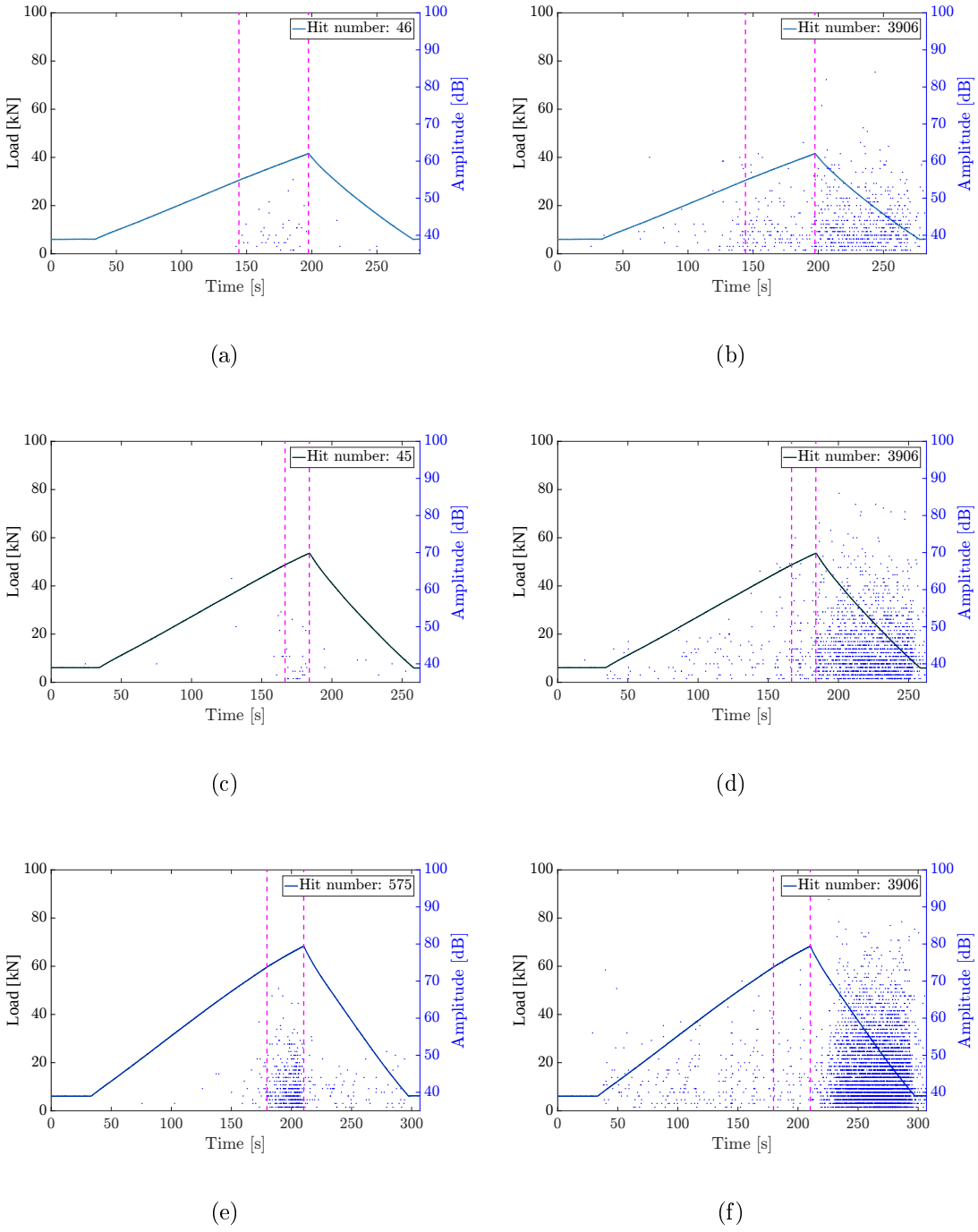

Figure 4.22: Load/amplitude vs. time of sensor 5(left) and sensor 6(right) in stage II

Stage III In softening phase of cycle 8 (Fig 4.23), more hits with greater amplitude of signal recorded by the sensor 5 support the fact that more micro are generated at the area where S5 is located. While for the sensor 6, this little amount of hits are probably resulted from the tensile crack or even the closing cracks due

to the stress redistribution. By contrast, at the unloading phase, the amplitude of signal detected by S6 shows a similar feature as in the previous cycle. An obvious increase both in hit number and amplitude is observed for the S5 at the unloading phase. This observation confirms the micro crack at the softening phase.

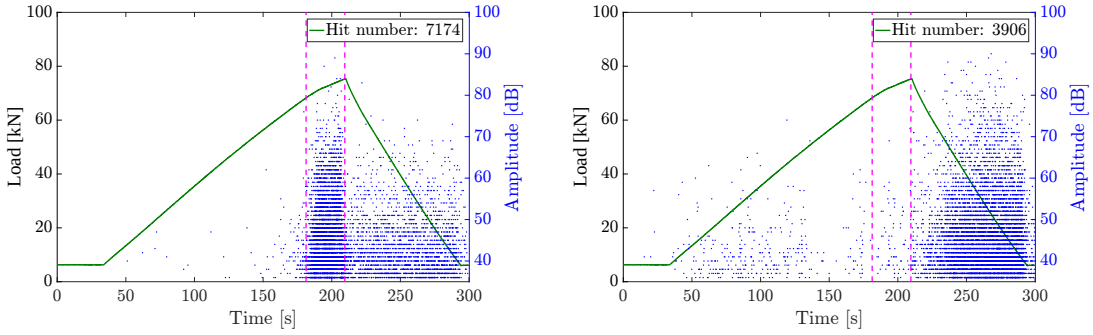

(a) (b)

Figure 4.23: Load/amplitude vs. time of sensor 5(left) and sensor 6(right) in stage III

Stage IV In the stage IV, 4 cycles are involved from the cycle 9 to cycle 12, and only an example of two cycles are presented in the Fig 4.24. The amplitude of signals recorded by sensor 5 and sensor 6 are shown in these cycles. At the unloading phase, more signals with greater amplitude are observed at the unloading phase by the sensor 5. And these signals are more energetic at the end of unloading phase. This observation confirms that more cracks are formed at the stage IV at the area of location of sensor 5, and more signals from the friction are recorded. Besides the amplitude of signals get greater at the softening phase, also implying more damaging and friction process, including the propagation of signals and the friction due to the shear and compressive stress. It should be noted that the loss of signals with lower amplitude at the softening phase is resulted from the signal saturation, which have been reported previously. For the sensor 6, the same observation is found in the reloading and unloading phase as that in the previous cycles. However, in the softening phase, the number and the amplitude of signals are no longer greater than the previous cycles. This can be explained by the fact that the horizontal crack remains completely opened in the softening phase of stage IV.

In the cyclic analysis, the acoustic activities are correlated with damage process in each cycle, including the reloading, softening and unloading phase. By analyzing the occurrence of signal and the associated amplitude, it is found that the evolution of acoustic activities is well associated to the crack initiation, crack propagation, the

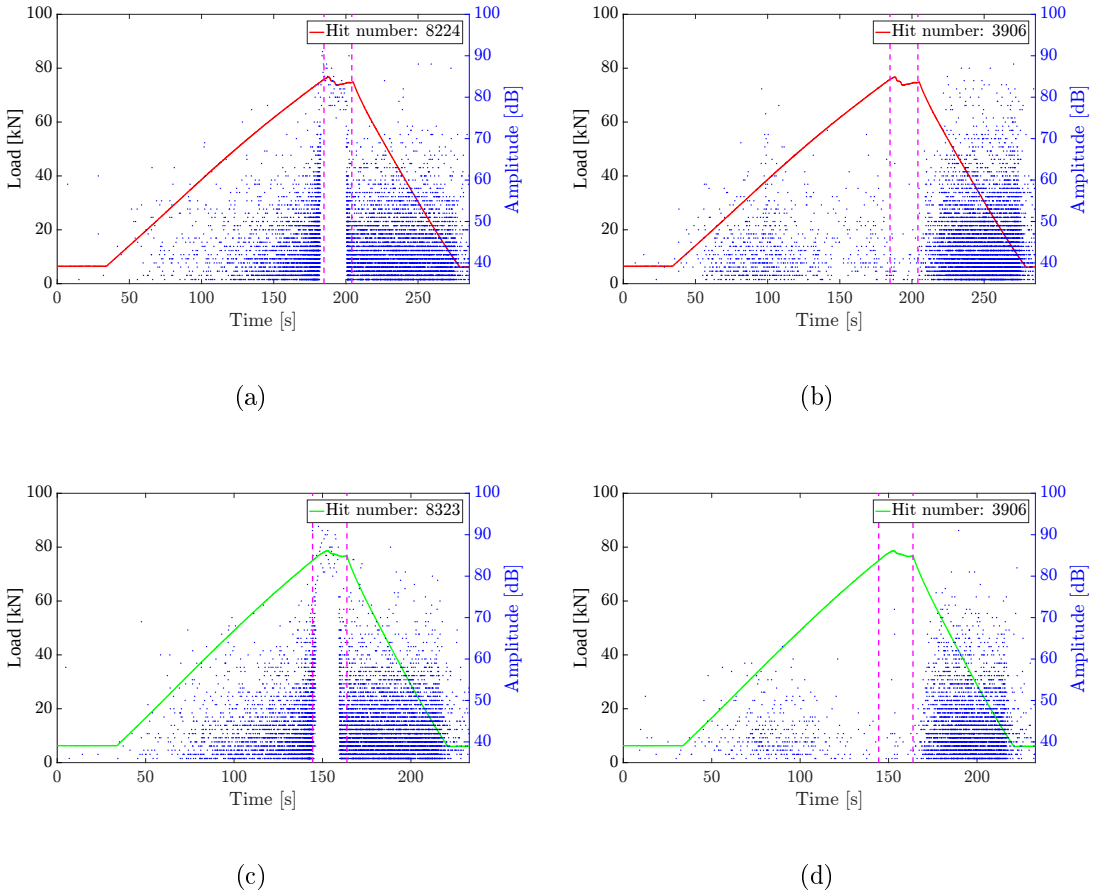

Figure 4.24: Load/amplitude vs. time of sensor 5(left) and sensor 6(right) in stage IV

crack closing as well as the friction. Besides this good coherence between the AE and the mechanical interpretation is observed in the different area, distinguished by the failure mode. Besides, the signals from tensile or shear crack with friction show a great difference both in hit number or maximal value of amplitude at the three phases, particularly in the softening and unloading phase. This result is interesting to be applied in in-situ damage monition of masonry structure.

4.3.4 Source discrimination

Based on the previous results and the results in the tensile and shear test, these two distinctive parameters (amplitude and duration) can be used to classify the damage sources from tensile crack and shear crack with friction. Another interpretation is presented in terms of distribution of amplitude-duration. These signals are obtained from all sensors on the envelope curve only. According to the phases determined by

the DIC results, 3 presentations are shown in Fig 4.25. The value of each point is calculated as the sum of hit number in a given stage within 1dB and 1ms, corresponding to the color bar value. In the stage I, the signals are concentrated at the amplitude below 60dB, a small amount of signal occur ranging from 60 dB to 70 dB. The duration of the signal is generally below 2ms. The similar observation is found in the stage II, however, the amplitude in this stage is greater than that in the stage I, the maximal value of amplitude can reach to 80dB. The most signals are also concentrated at a duration below 2ms, some are observed at 3ms.. A great change of the distribution of amplitude and duration is observed at the stage III. The signal are no longer concentrated at a limited range of amplitude and duration, the maximal value of amplitude extends to 90dB, and a lot of signals show a great value in duration, ranging from 3ms to 50ms. These long duration signals indicate the formation of shear crack with the participation of friction. It is concluded that the distribution of amplitude and duration of signals from the tensile crack, shear crack and the friction is quite different.

The signals recorded by sensor 5(S5) and sensor 6(S6) at the four stages are analyzed in Fig 4.26. The signals with a relative low amplitude were recorded by the S6. These signals from bottom are even more difficult to reach at the position of S5 due to the attenuation, resulting in a largely reduction of hit number as well as in its amplitude.

At the stage II, the S6, which was located just near the horizontal crack at the bottom of wall records the signals generated by tensile crack stage. The S5, located in middle of wall along the diagonal crack path, detected the signals mostly from shear crack and friction at the stage III.

During the stage II, S5 records 500 signals while S6 recorded 290 signals. As the S6 was located at the place of crack initiation, which is prevent to detect more signals with the crack opening. However, the S6 which was placed at the front of diagonal crack, is easier to detect more signals. Regardless of sensors position, the duration of these signals are lower than 2ms, which confirms that these signals were mostly generated from tensile crack. The presentation of S6 at stage III is similar as that at stage II. The tensile crack is prevent to propagate meanwhile the diagonal crack initializes. At this stage, S5 records largely more signals 5380 against 537 recorded in stage II. These signals are no longer concentrated at a relative lower duration, implying that the shear crack develops and the friction is involved.

At the last stage (Stage IV), the signal with longer duration ranging from 10ms to 30 ms are observed for the S5, implying the signal from the friction.

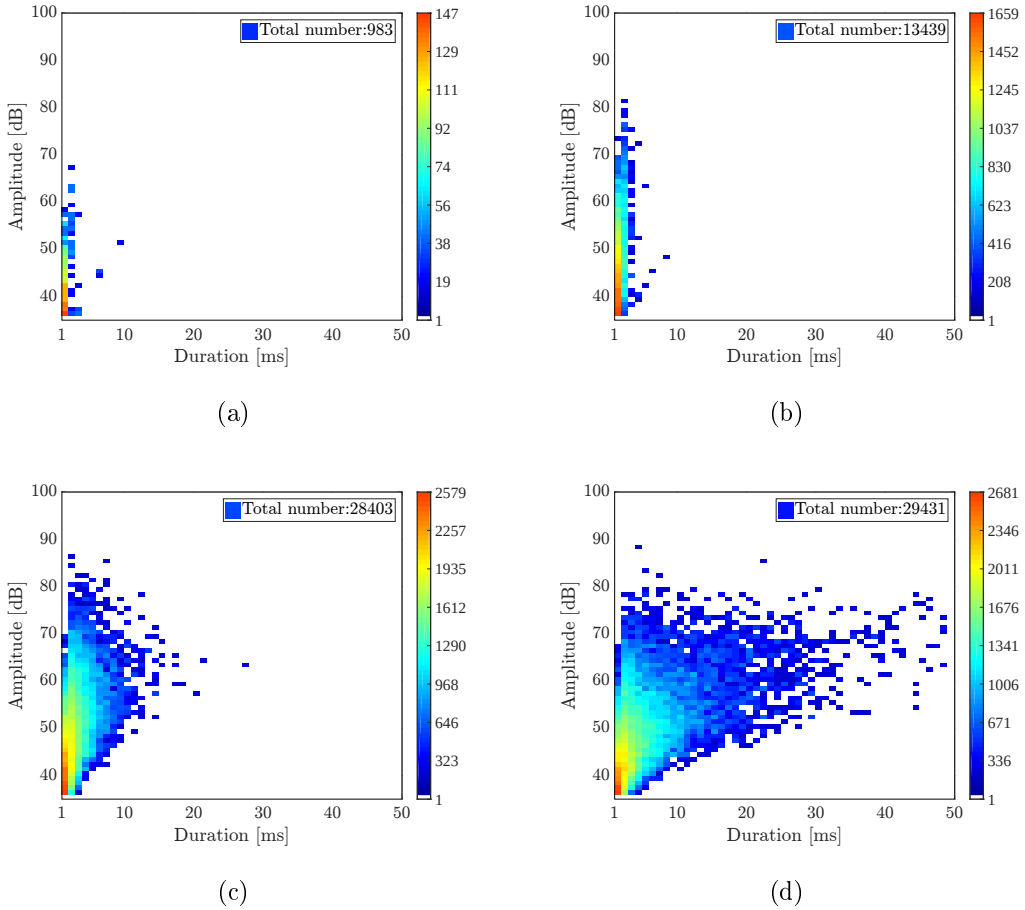

Figure 4.25: Hit intensity map of amplitude vs. duration by all signals at stage I,II,III,IV

In order to confirm similar waveform of these signals in the 3 different tests (at the assemblage scale: tensile test, shear test and at a larger scale: shear wall test), a Principal Component Analysis (PCA) is carried out to classify the signals. The signals from the 3 different tests are collected and put in the same dataset, three parameters including rise time (RT), amplitude (Amp), averaged frequency (AF) are selected, based on the total variance score which is beyond 70% in the first principle plan. Besides, these three parameters are often used to describe the signal waveform in AET. Fig 4.27 illustrates the coordinate of each signal in a new two-dimensional axe including 1st principal component (PC1) and 2end principal component (PC2) after orthogonal transformation. The PC1 explains 39.3% of total variance and the PC2 explains 35% of total variance. The contribution of each parameter to each axe is summarized in the Table 3. More clearly, the results are resolved into four presentations (Figure 26), corresponding to that in tensile test, shear test and the stage II and stage III in shear wall test, respectively. In each presentation, the signals

Table 4.3: Principal component scores for each selected variable

	PC1	PC2	PC3
RT	-0.76	-0.33	-0.56
Amp	-0.77	0.28	0.57
AF	-0.04	0.93	-0.37
Total variance (%)	*39.28*	*34.96*	*25.77*

are clustered into 2 groups according to the duration value, which is considered as a distinctive parameter in AE analysis[Peng et al., 2020]. The similar signals with duration below 2ms are found in the three tests. Another similar signals with long duration but below 10ms are observed in the shear test. Only a minority of signals of this type are observed in tensile test and in stage II of shear wall test. At the stage III of shear wall test, some particular points should be noticed: a band of point clouds, ranging from -40 to -10 in the PC1. These signals represent a high RT and amplitude, according to the correlation coefficient score in Tab 4.3. Besides the duration of these signals is beyond 10ms, the long signal may be caused by the long propagation path and more sliding surface. Indeed, some overlapped points are also observed in these two groups which needs a further analysis.

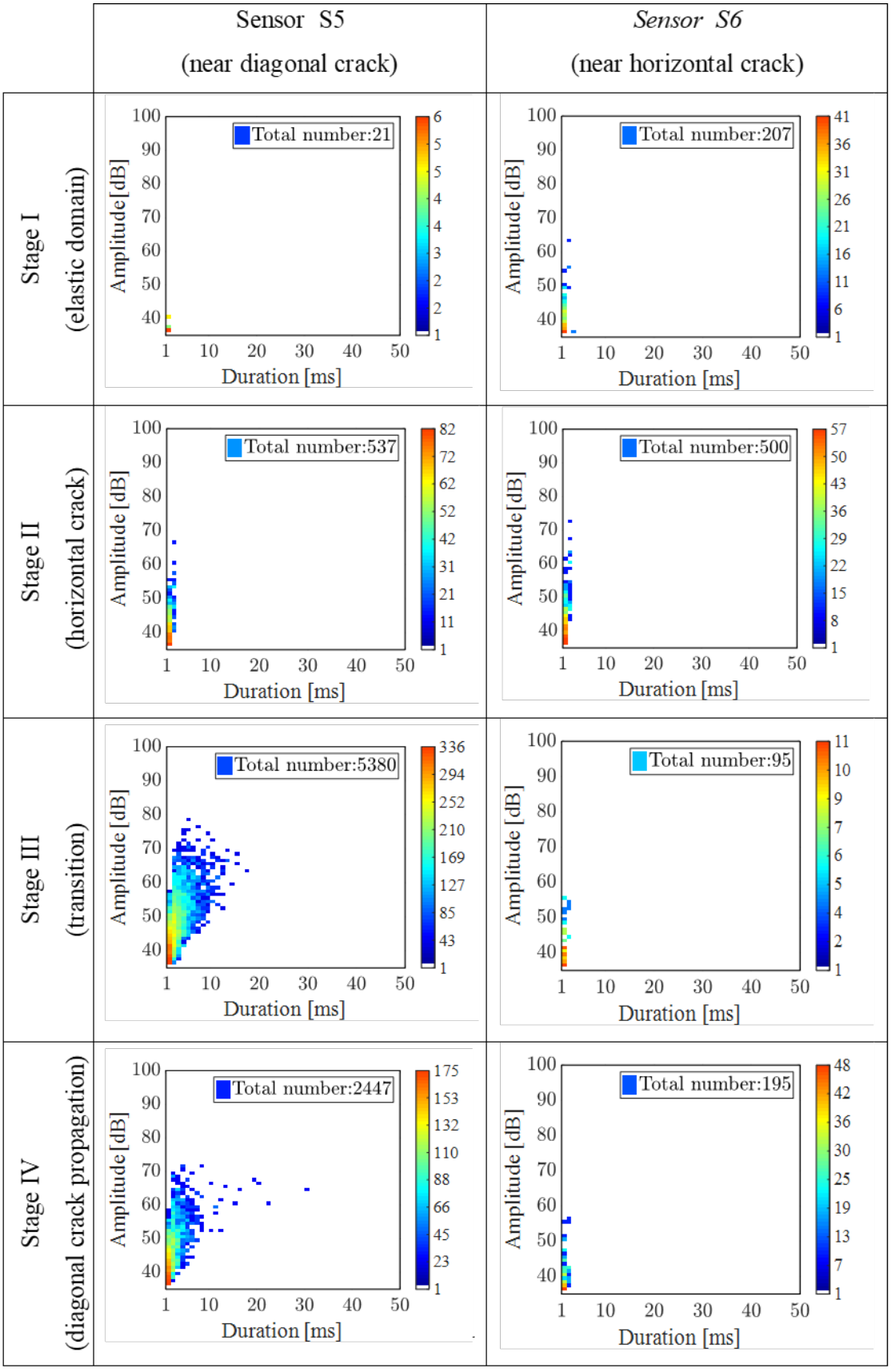

Figure 4.26: Hit intensity map of amplitude vs. duration by sensor 5 and 6 at the four stages

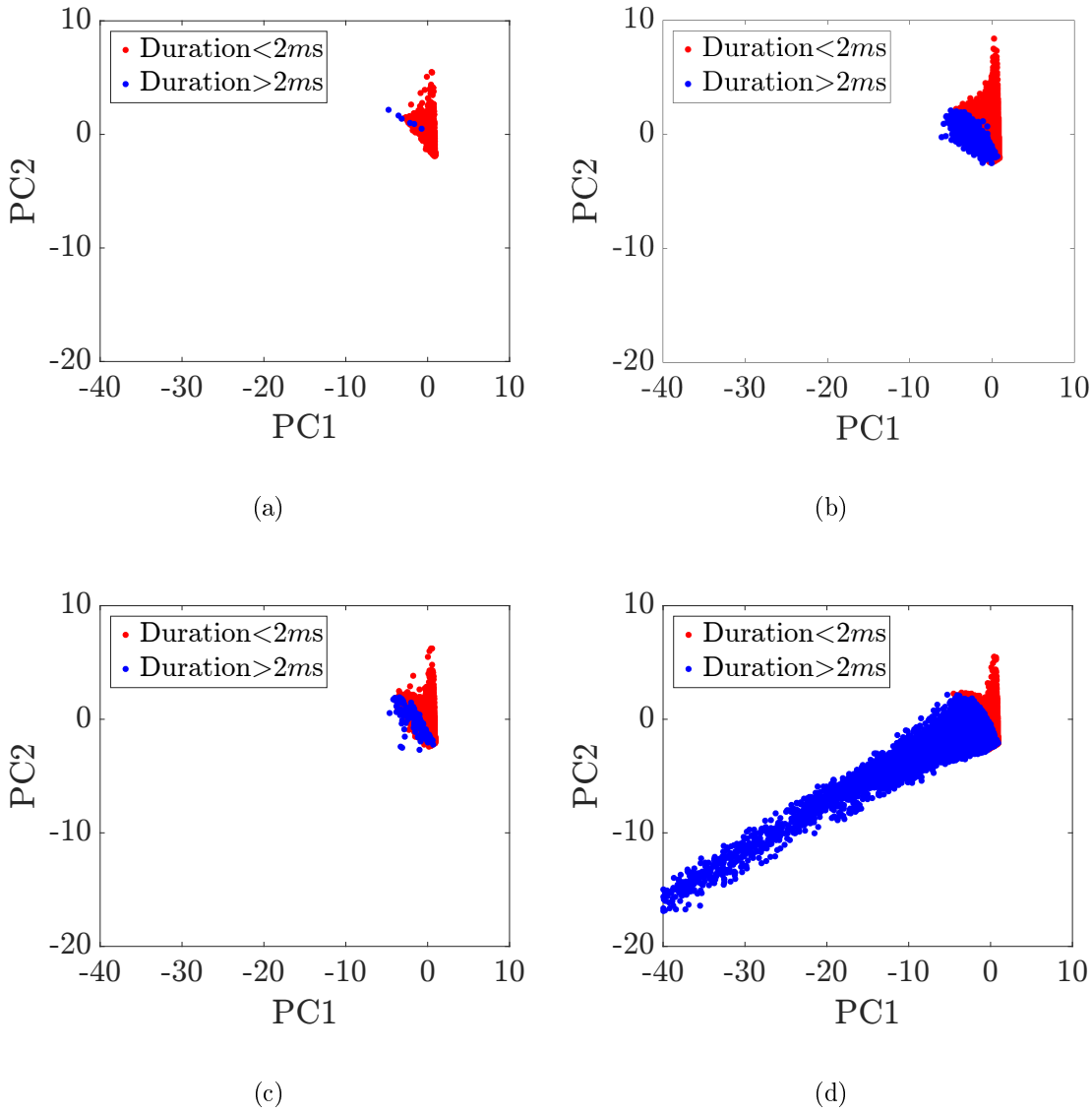

Figure 4.27: Principal component analysis results in (a) tensile test, (b) shear test, (c) stage II of shear wall test, (d) stage III and IV of shear wall test

4.4 Conclusion

In this chapter, the performance of AE in shear wall test was investigated in the damage monitoring and source discrimination. The damage process and the crack pattern were firstly analyzed by the mechanical response and the DIC observations. Then damage monitoring by acoustic activities were investigated. This investigation concerned the envelop analysis and cyclic analysis. For the former one, only the damage process corresponding to the softening phase is demonstrated in the mechanical load-displacement curve. A good correlation is found between the overall material deterioration and the no-cumulative acoustic activities. Moreover, the analysis of the cumulative activates by each sensor shows a good agreement of the different failure modes observed from the DIC results.

For the cyclic analysis, the acoustic activities is investigated at each cycle including the reloading, softening and unloading phase. In these three stages, the crack opening, crack development as well as crack closing are interpreted by the cyclic load-time curve and the DIC observations. Besides, the acoustic activities in each cycle shows a good coherence with the different status of crack in different area. This observation seems promising in the analysis in a real building in situ such a historic building subjected to a seismic loading.

By analysis the amplitude and duration of acoustic emission, we can also distinguish the signal from the different source such as cracking and friction. This source discrimination can be applied at the different damaged area where more complex failure modes occur.

Conclusions and perspectives

In the context of conservation of building heritage, the proper diagnostic investigation can be invented for a better material or structure condition assessment. The objective of this thesis is to investigate the non-destructive techniques for the material characterization and damage characterization of stone masonry structure. As the masonry is a composite material made of mortar and stone, its structure behavior depends on the mechanical characteristic of each component and also on the interaction. Thus the material characterization of the masonry component was introduced and the mechanical behavior of masonry specimen subjected to different loading was also discussed.

For the first step, our study focus on the mechanical characteristic of stone. Based on the literature review, it is known the moisture is a major cause in the material degradation of stone. Thus in the Chapter 2, the influence of water on the mechanical properties of 3 different types of stone are studied. The studied stones have a porosity ranging from 10% to 30%. They were firstly characterized by their nature properties. Then the modulus of elasticity of stone sample at different degree of saturation were derived from the load-displacement curve. These experimental curve were obtained from the compressive tests, which were also carried out in two directions: parallel and perpendicular to the bedding. By comparing the modulus in these two directions, we have found the modulus of elasticity in direction perpendicular to the bedding is generally greater than that in direction parallel to bedding at the tested degree of saturation. Exception for the non-marble, due to its anisotropy, the modulus is more sensitive to the degree of saturation in the parallel direction than the perpendicular directions. Besides, a significant decrease of modulus of elasticity is observed with an increasing degree of saturation for the three type of stones. Another parameter the porosity reduces the deformability following an exponential trend. Moreover, the presence of water weakens the strength of stone by comparing the compressive strength of sample at dry and saturated condition.

The three non-destructive techniques were also investigated on the water estim-

ation. For the method of ultrasound, the ultrasound velocity was measured as a ND parameter. The results show that no significant variability in the velocity in terms of degree of saturation for the low porous stone. For the stone with relative higher porosity, the evolution of ultrasound velocity follows a trend in the form of 'convex' with the increasing water content.

In the method of radar, the dielectric permittivity of sample is mainly affected by the presence of water. The permittivity of sample increases with an increasing degree of saturation. This increase is more significant for the stone with a higher porosity. A modelling based on the complex refractive index model is also compared with experimental data. Through the high coefficient of determination and the low RMSE, a good agreement is concluded between the experimental and modeled permittivity.

Regarding to the method of resistivity, the electrical resistivity as another parameter shows an exponential decreasing trend with an increasing degree of saturation. Comparing with the measured resistivity, the model-calculated resistivity is well predicted by the model of each type stone. However, this model is not a general model for all type stones, because of the great variability of resistivity of stone under a relativity dry condition.

Each non-destructive technique shows its sensitive to the moisture detection for the low porous stones. The promising results from modelling is help for the future intervention of water assessment of a building in-situ. Besides, an inversion method can be envisaged to combine the different techniques to interpreter the nature or mechanical parameters from the measured non-destructive parameters.

Another main research aims at investigating the AET for damage monitoring in masonry, particularly focusing on two cracking modes at the unit-mortar interface: opening (mode I) and in-plane shear (mode II). The performance of AET was thus analyzed at multiscale experimental tests from the mesoscopic scale (bloc-mortar-bloc) to the macroscopic scale (shear wall).

At the mesoscopic scale (Chapter 3), tensile test and shear test were carried out at small-scale laboratory specimens by the means of AET. In the tensile test, both the monotone and cyclic test were conducted to get a further understanding of the non-linear damage mechanics. The cyclic envelop curves are quietly similar to monotonic tensile curve, the residual displacement and elastic stiffness can be derived from the correlation with the unloading displacement. Besides the correlation is established regardless of peak strength of material. With respect to the acoustic emission analysis, two elementary AE indices (hit number and hit energy)

were correlated with damage accumulation to identify its response to each loading. Three stages can identified according to the occurrence of hits and its corresponding energy. From experimental tests it is found that the signal duration is a dominant parameter which can distinguish the signal from micro crack to macro crack, based on the correlation between the evolution of AE energy and fracture energy. This can be attributed to the fact that a better correlation is observed between 2 forms of energy rates when AE energy rate is calculated with signals having lower duration. However, this duration value for all the test is not always the same due to the material heterogeneity and wave propagation path, conducting the signal distorting even if it comes from the same type of cracking. Besides not only the emission is participated in the energy dissipation, some dissipated energy turned into the heat, which influence the correlation of evolution of the discussed two energies. The scale effect is also interesting to be taken into account in the future study. As the mechanical analysis of masonry specimen under tensile loading is concentrated in the mesoscale, while the emission is received in a micro scale, more fundamental research is needed to uncover this relation at microscale.

In the shear test, the mechanical response of a triplet sample subjected to a combined shear and compressive loading is also correlated with acoustic emission activities. A good correlation is found between the damage process and the acoustic emission activities. Besides, three factor influencing the AE parameters of the recorded signals is also presented.

The parameter duration which is related to AE energy shows the distinctive signature of different damage sources. By comparing both the tests, it can be concluded that more signals were generated in shear test than that in tensile test, moreover these signals were more energetic and longer, and the signal with duration superior to 2ms could be associated with friction.

At macroscopic scale(Chapter 4), a series of full scale test as a shearing wall under compression was carried out in parallel with the AET. Digital image correlation (DIC) was also induced as a referent technique to demonstrate crack patterns. The same strategies of AE processing as at the mesoscopic scale were applied to assess the integrated damage deterioration of structure to discriminate the damage modes, confronted with the DIC results. The first analysis is based on the envelope mechanical response. Different damage process stages can be characterized according to the DIC results and mechanical response of shear wall. The acoustic emission activities show a good correspondence to the damage process stage. The second analysis is applied on each cycle of mechanical responses. More fundamental results shows a good agreement of acoustic activities in the reloading, softening and un-

loading phases in different damage accumulation. The source discrimination is also undertaken, supporting the source discrimination from the cracking to the friction in the damaged area where the tensile or shear crack is observed. These results confirm the performance of AET in case of more complex mechanism of ruin. Furthermore, this technique is more sensitive to detect the micro void or micro crack than DIC. Thanks to these promising results, this technique can be envisaged to be implemented at a historic monument for the condition assessment in the future.

Bibliography

[Aggelis et al., 2017] Aggelis, D. G., El Kadi, M., Tysmans, T., and Blom, J. (2017). Effect of propagation distance on acoustic emission fracture mode classification in textile reinforced cement. 152:872–879.

[Aggelis et al., 2013] Aggelis, D. G., Mpalaskas, A. C., and Matikas, T. E. (2013). Investigation of different fracture modes in cement-based materials by acoustic emission. 48:1–8.

[Aggelis et al., 2012] Aggelis, D. G., Mpalaskas, A. C., Ntalakas, D., and Matikas, T. E. (2012). Effect of wave distortion on acoustic emission characterization of cementitious materials. 35:183–190.

[Aggelis et al., 2011] Aggelis, D. G., Soulioti, D. V., Sapouridis, N., Barkoula, N. M., Paipetis, A. S., and Matikas, T. E. (2011). Acoustic emission characterization of the fracture process in fibre reinforced concrete. 25(11):4126–4131.

[Alani et al., 2020] Alani, A. M., Tosti, F., Ciampoli, L. B., Gagliardi, V., and Benedetto, A. (2020). An integrated investigative approach in health monitoring of masonry arch bridges using GPR and InSAR technologies. page 102288.

[Almeida et al., 2014] Almeida, J. C., Lourenço, P. B., and Barros, J. A. (2014). Characterization of brick and brick–mortar interface under uniaxial tension. page 10.

[Anbazhagan et al., 2020] Anbazhagan, P., Bittelli, M., Pallepati, R. R., and Mahajan, P. (2020). Comparison of soil water content estimation equations using ground penetrating radar. 588:125039.

[Archie, 1942] Archie, G. (1942). The electrical resistivity log as an aid in determining some reservoir characteristics. 146(1):54–62.

[Aydin, 2014] Aydin, A. (2014). Upgraded ISRM suggested method for determining sound velocity by ultrasonic pulse transmission technique. 47(1):255–259.

[Bai et al., 2013] Bai, W., Kong, L., and Guo, A. (2013). Effects of physical properties on electrical conductivity of compacted lateritic soil. 5(5):406–411.

[Beck, 2006] Beck, K. (2006). Étude des propriétés hydriques et des mécanismesd'altération de pierres calcaires à forte porosité. page 245.

[Beck et al., 2007] Beck, K., Ramézani, H., and Al-Mukhtar, M. (2007). Mechanical strength and water content of porous limestones.

[Benavent-Climent et al., 2012] Benavent-Climent, A., Gallego, A., and Vico, J. M. (2012). An acoustic emission energy index for damage evaluation of reinforced concrete slabs under seismic loads. 11(1):69–81.

[Bennacer et al., 2014] Bennacer, R., Abahri, K., and Belarbi, R. (2014). 3 - intrinsic properties controlling the sustainability of construction. In Khatib, J. M., editor, *Sustainability of Construction Materials (Second Edition)*, Woodhead Publishing Series in Civil and Structural Engineering, pages 33–53. Woodhead Publishing.

[Binda et al., 1998] Binda, L., Lenzi, G., and Saisi, A. (1998). NDE of masonry structures: use of radar tests for the characterisation of stone masonries. 31(6):411–419.

[Binda et al., 1994] Binda, L., Roberti, G. M., and Abbaneo, S. (1994). The diagnosis research project. 10(1):151–170. Publisher: SAGE Publications Ltd STM.

[Bisoffi-Sauve, 2016] Bisoffi-Sauve, M. (2016). ÉTUDE DES OUVRAGES MAÇONNÉS EN PIERRE PAR LA MÉTHODE DES ÉLÉMENTS DISCRETS - CARACTÉRISATION ET MODÉLISATION DU COMPORTEMENT COHÉSIF DES JOINTS. page 190.

[Bisoffi-Sauve et al., 2019] Bisoffi-Sauve, M., Morel, S., and Dubois, F. (2019). Modelling mixed mode fracture of mortar joints in masonry buildings. 182:316–330.

[Boniface et al., 2019] Boniface, A., Saliba, J., Sbartaï, Z. M., Ranaivomanana, N., and Balayssac, J.-P. (2019). Evaluation of the acoustic emission 3d localisation accuracy for the mechanical damage monitoring in concrete. page 106742.

[Broekmanweg et al., 2004] Broekmanweg, V. M., Box, P. O., and Delft, A. (2004). Shear tests on masonry panels; literature survey and proposal for experiments. page 36.

[Bungey et al., 2006] Bungey, J. H., Millard, S. G., and Grantham, M. (2006). *Testing of concrete in structures*. Taylor & Francis, 4th ed edition. OCLC: ocm61247215.

[Cardani et al., 2013] Cardani, G., Cantini, L., Munda, S., Zanzi, L., and Binda, L. (2013). Non invasive measurements of moisture in full-scale stone and brick masonry models after simulated flooding: Effectiveness of GPR. In Büyüköztürk, O., Taşdemir, M. A., Güneş, O., and Akkaya, Y., editors, *Nondestructive Testing of Materials and Structures*, RILEM Bookseries, pages 1143–1149. Springer Netherlands.

[Carpinteri et al., 2013] Carpinteri, A., Corrado, M., and Lacidogna, G. (2013). Heterogeneous materials in compression: Correlations between absorbed, released and acoustic emission energies. 33:236–250.

[Carpinteri and Lacidogna, 2007] Carpinteri, A. and Lacidogna, G. (2007). Damage evaluation of three masonry towers by acoustic emission. 29(7):1569–1579.

[Carpinteri et al., 2016] Carpinteri, A., Lacidogna, G., Corrado, M., and Di Battista, E. (2016). Cracking and crackling in concrete-like materials: A dynamic energy balance. 155:130–144.

[Carpinteri et al., 2007] Carpinteri, A., Lacidogna, G., and Pugno, N. (2007). Structural damage diagnosis and life-time assessment by acoustic emission monitoring. 74(1):273–289.

[Costigan and Pavía, 2012] Costigan, A. and Pavía, S. (2012). Influence of the mechanical properties of lime mortar on the strength of brick masonry. In Válek, J., Hughes, J. J., and Groot, C. J. W. P., editors, *Historic Mortars*, RILEM Bookseries, pages 359–372. Springer Netherlands.

[D'Altri et al., 2018] D'Altri, A. M., de Miranda, S., Castellazzi, G., and Sarhosis, V. (2018). A 3d detailed micro-model for the in-plane and out-of-plane numerical analysis of masonry panels. 206:18–30.

[Daniels, 2004] Daniels, D. J. (2004). *Ground Penetrating Radar*. IET. Google-Books-ID: iZpEbaJEOy0C.

[De Santis and Tomor, 2013] De Santis, S. and Tomor, A. K. (2013). Laboratory and field studies on the use of acoustic emission for masonry bridges. 55:64–74.

[du Plooy et al., 2013] du Plooy, R., Palma Lopes, S., Villain, G., and Dérobert, X. (2013). Development of a multi-ring resistivity cell and multi-electrode resistivity probe for investigation of cover concrete condition. 54:27–36.

[El-Husseiny et al., 2019] El-Husseiny, A., Vega, S., and Nizamuddin, S. (2019). The effect of pore structure complexity and saturation history on the variations of acoustic velocity as function of brine and oil saturation in carbonates. 179:180–191.

[EN 1052-3, 2002] EN 1052-3 (2002). Methods of test for masonry - part 3: Determination of initial shear strength.

[Endres and Bertrand, 2006] Endres, A. and Bertrand, E. (2006). A pore-size scale model for the dielectric properties of water-saturated clean rocks and soils. 71.

[Farhidzadeh et al., 2014] Farhidzadeh, A., Mpalaskas, A. C., Matikas, T. E., Farhidzadeh, H., and Aggelis, D. G. (2014). Fracture mode identification in cementitious materials using supervised pattern recognition of acoustic emission features. 67:129–138.

[Feng and Yi, 2017] Feng, H. and Yi, W. (2017). Propagation characteristics of acoustic emission wave in reinforced concrete. 7:3815–3819.

[Fowler, 2017] Fowler, T. J. (2017). The origin of CARP and the term "felicity effect". page 8.

[Fu, 2005] Fu, G. (2005). *Inspection and Monitoring Techniques for Bridges and Civil Structures*. Elsevier. Google-Books-ID: iFqpAgAAQBAJ.

[G. et al., 2002] G., Y., M., O., and J., P. (2002). Laboratory study of landfill leachate effect on resistivity in unsaturated soil using cone penetrometer. 43(1):18–28.

[Ghiassi et al., 2014] Ghiassi, B., Verstrynge, E., Lourenço, P. B., and Oliveira, D. V. (2014). Characterization of debonding in FRP-strengthened masonry using the acoustic emission technique. 66:24–34.

[Godio et al., 2019] Godio, M., Vanin, F., Zhang, S., and Beyer, K. (2019). Quasi-static shear-compression tests on stone masonry walls with plaster: Influence of load history and axial load ratio. 192:264–278.

[Griffiths, 1976] Griffiths, D. H. (1976). Application of electrical resistivity measurements for the determination of porosity and permeability in sand-stones. 14(3):207–213.

[Grosse and Ohtsu, 2008] Grosse, C. and Ohtsu, M. (2008). Acoustic emission testing.

[Han et al., 1986] Han, D., Nur, A., and Morgan, D. (1986). Effects of porosity and clay content on wave velocities in sandstones. 51(11):2093–2107.

[Hassine et al., 2018] Hassine, M. A., Beck, K., Brunetaud, X., and Al-Mukhtar, M. (2018). Use of electrical resistance measurement to assess the water saturation profile in porous limestones during capillary imbibition. 165:206–217.

[ISRM, 2007] ISRM (2007). The complete ISRM suggested methods for rock.

[Kaushik et al., 2007] Kaushik, H. B., Rai, D. C., and Jain, S. K. (2007). Stress-strain characteristics of clay brick masonry under uniaxial compression. 19(9):728–739.

[Kazmi et al., 2016] Kazmi, D., Qasim, S., Siddiqui, F. I., and Azhar, S. B. (2016). Exploring the relationship between moisture content and electrical resistivity for sandy and silty soils. page 6.

[Khamrat et al., 2016] Khamrat, S., Archeeploha, S., and Fuenkajorn, K. (2016). Pore pressure effects on strength and elasticity of ornamental stones. 42(2):121.

[Kim and Changani, 2016] Kim, E. and Changani, H. (2016). Effect of water saturation and loading rate on the mechanical properties of red and buff sandstones. 88:23–28.

[L. Davies and Bouldin, 1979] L. Davies, D. and Bouldin, D. (1979). A cluster separation measure. PAMI-1:224–227.

[Landis and Baillon, 2001] Landis, E. N. and Baillon, L. (2001). Acoustic emission measurements of fracture energy. 1:389–394.

[Landis and Baillon, 2002] Landis, E. N. and Baillon, L. (2002). Experiments to relate acoustic emission energy to fracture energy of concrete. 128(6):698–702.

[Lang, 2002] Lang, K. (2002). Seismic vulnerability of existing buildings. Artwork Size: 188 S. Medium: application/pdf.

[Lataste, 2010] Lataste, J. F. (2010). 12 - electrical resistivity for the evaluation of reinforced concrete structures. In Maierhofer, C., Reinhardt, H.-W., and Dobmann, G., editors, *Non-Destructive Evaluation of Reinforced Concrete Structures*, volume 2 of *Woodhead Publishing Series in Civil and Structural Engineering*, pages 243–275. Woodhead Publishing.

[Lataste and Göller, 2018] Lataste, J.-F. and Göller, A. (2018). Microwave reflection. In Nilsson, L.-O., editor, *Methods of Measuring Moisture in Building Materials and Structures: State-of-the-Art Report of the RILEM Technical Committee 248-MMB*, RILEM State-of-the-Art Reports, pages 123–140. Springer International Publishing.

[Lataste et al., 2018] Lataste, J.-F., Thiel, C., and Franzoni, E. (2018). Electrical resistance. In Nilsson, L.-O., editor, *Methods of Measuring Moisture in Building Materials and Structures: State-of-the-Art Report of the RILEM Technical Committee 248-MMB*, RILEM State-of-the-Art Reports, pages 55–66. Springer International Publishing.

[Laurenco et al., 1995] Laurenco, P. B., Rots, J. G., and Blaauwendraad, J. (1995). Two approaches for the analysis of masonry structures: Micro and macro-modeling.

[Laurens et al., 2005] Laurens, S., Balayssac, J. P., Rhazi, J., Klysz, G., and Arliguie, G. (2005). Non-destructive evaluation of concrete moisture by GPR: Experimental study and direct modeling. 38(9):827–832.

[Lavrov, 2003] Lavrov, A. (2003). The kaiser effect in rocks: principles and stress estimation techniques. 40(2):151–171.

[Li et al., 2018] Li, D., Wei, J., Di, B., Ding, P., Huang, S., and Shuai, D. (2018). Experimental study and theoretical interpretation of saturation effect on ultrasonic velocity in tight sandstones under different pressure conditions. 212(3):2226–2237.

[Li et al., 2012] Li, D., Wong, L. N. Y., Liu, G., and Zhang, X. (2012). Influence of water content and anisotropy on the strength and deformability of low porosity meta-sedimentary rocks under triaxial compression. 126:46–66.

[Li et al., 2016] Li, Q., Xu, S., and Zeng, Q. (2016). The effect of water saturation degree on the electrical properties of cement-based porous material. 70:35–47.

[Lourenço et al., 2005] Lourenço, P. B., Almeida, J. C., and Barros, J. A. O. (2005). Experimental investigation of bricks under uniaxial tensile testing.

[Lourenço and Pina-Henriques, 2006] Lourenço, P. B. and Pina-Henriques, J. (2006). Validation of analytical and continuum numerical methods for estimating the compressive strength of masonry. 84(29):1977–1989.

[Lourenço and Ramos, 2004] Lourenço, P. B. and Ramos, L. F. (2004). Characterization of cyclic behavior of dry masonry joints. 130(5):779–786.

[Lourenço and Rots, 1994] Lourenço, P. B. and Rots, J. G. (1994). UNDERSTANDING THE BEHAVIOUR OF SHEAR WALLS: A NUMERICAL REVIEW. page 10.

[Lourenço and Rots, 1997] Lourenço, P. B. and Rots, J. G. (1997). Multisurface interface model for analysis of masonry structures. 123(7):660–668. Publisher: American Society of Civil Engineers.

[Macorini and Izzuddin, 2011] Macorini, L. and Izzuddin, B. A. (2011). A non-linear interface element for 3d mesoscale analysis of brick-masonry structures. 85(12):1584–1608. _eprint: https://onlinelibrary.wiley.com/doi/pdf/10.1002/nme.3046.

[Martinez and Byrnes, 2001] Martinez, A. and Byrnes, A. P. (2001). Modeling dielectric-constant values of geologic materials: An aid to ground-penetrating radar data collection and interpretation. page 16.

[Matsushita and Onoue, 2006] Matsushita, H. and Onoue, K. (2006). Influence of surface energy on compressive strength of concrete under static and dynamic loading. 4:409–421.

[MIT, 2009] MIT (2009). Ministry of infrastructures and transportation, circ. n. 617 of 2/2/2009: Istruzioni per l'applicazione delle nuove norme tecniche per le costruzioni di cui al decreto ministeriale 14 gennaio 2008. italy.

[Mohammed and Mahmood, 2018] Mohammed, A. and Mahmood, W. (2018). Statistical variations and new correlation models to predict the mechanical behavior and ultimate shear strength of gypsum rock. 8(1):213–226.

[Moradian and Li, 2017] Moradian, Z. and Li, B. Q. (2017). Hit-based acoustic emission monitoring of rock fractures: Challenges and solutions. In Shen, G., Wu, Z., and Zhang, J., editors, *Advances in Acoustic Emission Technology*, Springer Proceedings in Physics, pages 357–370. Springer International Publishing.

[Nabawy, 2018] Nabawy, B. S. (2018). Impacts of fossil anisotropy on the electric and permeability anisotropy of highly fossiliferous limestone: a case study. 39(4):537–550.

[Neyrat, 2009] Neyrat, M. (2009). Contribution à l'étude de g.p.r. (ground penetrating radar) multicapteurs : méthodes directes et inverses en temporel. page 162.

[NF EN 1015-11, 2000] NF EN 1015-11 (2000). Méthodes d'essai des mortiers pour maçonnerie - partie 11 : détermination de la résistance en flexion et en compression du mortier durci.

[NF EN 1926, 1999] NF EN 1926 (1999). Natural stone test methods - determination of uniaxial compressive strength.

[NF EN 1936, 2007] NF EN 1936 (2007). Méthodes d'essai des pierres naturelles - détermination des masses volumiques réelle et apparente et des porosités ouvertes et totale.

[NF EN ISO 14580, 2011] NF EN ISO 14580 (2011). NF EN ISO 14580 - juin 2011.

[Nguyen et al., 2017] Nguyen, A. Q., Klysz, G., Deby, F., and Balayssac, J. P. (2017). Evaluation of water content gradient using a new configuration of linear array four-point probe for electrical resistivity measurement. 83:308–322.

[Nguyen, 2014] Nguyen, N. T. (2014). Évaluation non destructive des structures en béton armé: étude de la variabilité spatiale et de la combinaison des techniques. page 243.

[Nguyen-Tat et al., 2018] Nguyen-Tat, T., Ranaivomanana, N., and Balayssac, J.-P. (2018). Characterization of damage in concrete beams under bending with acoustic emission technique (AET). 187:487–500.

[Nilsson, 2018] Nilsson, L.-O. (2018). Methods of measuring moisture in building materials and structures.

[Ohtsu et al., 2007] Ohtsu, M., Isoda, T., and Tomoda, Y. (2007). Acoustic emission techniques standardized for concrete structures. page 12.

[Ojo and Brook, 1990] Ojo, O. and Brook, N. (1990). The effect of moisture on some mechanical properties of rock. 10(2):145–156.

[Oliveira et al., 2007] Oliveira, D. V., Lourenço, P. B., and Roca, P. (2007). Cyclic behaviour of stone and brick masonry under uniaxial compressive loading. 39(2):247–257.

[Orr et al., 2020] Orr, S. A., Fusade, L., Young, M., Stelfox, D., Leslie, A., Curran, J., and Viles, H. (2020). Moisture monitoring of stone masonry: A comparison of microwave and radar on a granite wall and a sandstone tower. 41:61–73.

[Orr et al., 2019] Orr, S. A., Young, M., Stelfox, D., Leslie, A., Curran, J., and Viles, H. (2019). An 'isolated diffusion' gravimetric calibration procedure for radar and microwave moisture measurement in porous building stone. 163:1–12.

[Pappalardo et al., 2016] Pappalardo, G., Mineo, S., and Monaco, C. (2016). Geotechnical characterization of limestones employed for the reconstruction of a UNESCO world heritage baroque monument in southeastern sicily (italy). 212:86–97.

[Parent et al., 2015] Parent, T., Domede, N., Sellier, A., and Mouatt, L. (2015). 102mechanical characterization of limestone from sound velocity measurement. 79:149–156.

[Pashmforoush et al., 2014] Pashmforoush, F., Khamedi, R., Fotouhi, M., Hajikhani, M., and Ahmadi, M. (2014). Damage classification of sandwich composites using acoustic emission technique and k-means genetic algorithm. 33(4):481–492.

[Peng et al., 2020] Peng, S., Sbartaï, Z. M., and Parent, T. (2020). Mechanical damage evaluation of masonry under tensile loading by acoustic emission technique. 258:120336.

[Petry and Beyer, 2014] Petry, S. and Beyer, K. (2014). Influence of boundary conditions and size effect on the drift capacity of URM walls. 65:76–88.

[Physics, University of Louisiana at Monroe and McGRAW Jr., 2020] Physics, University of Louisiana at Monroe and McGRAW Jr., D. (2020). THE MEASUREMENT OF THE DIELECTRIC CONSTANT OF UNDERGROUND CLAY PIPES. 5(2):74–93.

[Pluijm, 1999] Pluijm, R. R. V. D. (1999). Out-of-plane bending of masonry : behaviour and strength.

[Popinet et al., 2018] Popinet, A., Laage de, G., Létoffé, F., and Groupement français des entreprises de restauration de Monuments Historiques (2018). *Traité de maçonnerie ancienne: calculs matériaux diagnostic et réhabilitation*. OCLC: 1041841147.

[Prem et al., 2018] Prem, P. R., Murthy, A. R., and Verma, M. (2018). Theoretical modelling and acoustic emission monitoring of RC beams strengthened with UHPC. 158:670–682.

[Rao and Lakshmi, 2005] Rao, M. V. M. S. and Lakshmi, K. J. P. (2005). Analysis of b-value and improved b-value of acoustic emissions accompanying rock fracture. 89(9):1577–1582.

[Reboul et al., 2020] Reboul, N., Grazide, C., Roy, N., and Ferrier, E. (2020). Acoustic emission monitoring of reinforced concrete wall-slab connections. 259:119661.

[Rezaei et al., 2019] Rezaei, M., Davoodi, P. K., and Najmoddin, I. (2019). Studying the correlation of rock properties with p-wave velocity index in dry and saturated conditions.

[Rhoades et al., 1999] Rhoades, J. D., F, C., Lesch, S., Smith, M., Organization, F. F. a. A., and Rhoades, J. (1999). *Soil salinity assessment : methods and interpretations of electrical conductivity measurements*. FAO irrigation and drainage paper. FAO.

[RILEM Technical Committee (Masayasu Ohtsu), 2010] RILEM Technical Committee (Masayasu Ohtsu) (2010). Recommendation of RILEM TC 212-ACD: acoustic emission and related NDE techniques for crack detection and damage evaluation in concrete: Test method for damage qualification of reinforced concrete beams by acoustic emission. 43(9):1183–1186.

[Rogers, 2013] Rogers, L. (2013). Application of acoustic emission technology for health monitoring of ship structures. page 19.

[Ruedrich et al., 2011] Ruedrich, J., Bartelsen, T., Dohrmann, R., and Siegesmund, S. (2011). Moisture expansion as a deterioration factor for sandstone used in buildings. 63(7):1545–1564.

[Saba et al., 2019] Saba, M., Lizarazo-Marriaga, J., Hernandez-Romero, N. L., and Quiñones-Bolaños, E. E. (2019). Physico-mechanical characterization of the limestone used in cartagena walls and a proposal for their restoration process. 214:420–429.

[Saitta et al., 2007] Saitta, S., Raphael, B., and Smith, I. F. C. (2007). A bounded index for cluster validity. In Perner, P., editor, *Machine Learning and Data Mining in Pattern Recognition*, volume 4571, pages 174–187. Springer Berlin Heidelberg.

[Samouëlian et al., 2005] Samouëlian, A., Cousin, I., Tabbagh, A., Bruand, A., and Richard, G. (2005). Electrical resistivity survey in soil science: a review. 83(2):173–193.

[Sass, 1998] Sass, O. (1998). Die steuerung von steinschlagmenge und –verteilung durch mikroklima, gesteinsfeuchte und gesteinseigenschaften im westlichen karwendelgebirge (bayerische alpen). page 190.

[Sass and Viles, 2010] Sass, O. and Viles, H. A. (2010). Wetting and drying of masonry walls: 2d-resistivity monitoring of driving rain experiments on historic stonework in oxford, UK. 70(1):72–83.

[Sbartaï et al., 2006] Sbartaï, Z. M., Laurens, S., Balayssac, J. P., Arliguie, G., and Ballivy, G. (2006). Ability of the direct wave of radar ground-coupled antenna for NDT of concrete structures. 39(5):400–407.

[Sbartaï et al., 2007] Sbartaï, Z. M., Laurens, S., Rhazi, J., Balayssac, J. P., and Arliguie, G. (2007). Using radar direct wave for concrete condition assessment: Correlation with electrical resistivity. 62(4):361–374.

[Senin and Hamid, 2016] Senin, S. F. and Hamid, R. (2016). Ground penetrating radar wave attenuation models for estimation of moisture and chloride content in concrete slab. 106:659–669.

[Shetty et al., 2019] Shetty, N., Livitsanos, G., Van Roy, N., Aggelis, D. G., Van Hemelrijck, D., Wevers, M., and Verstrynge, E. (2019). Quantification of progressive structural integrity loss in masonry with acoustic emission-based damage classification. 194:192–204.

[Si et al., 2016] Si, W., Di, B., Wei, J., and Li, Q. (2016). Experimental study of water saturation effect on acoustic velocity of sandstones. 33:37–43.

[Tang et al., 2017] Tang, J., Soua, S., Mares, C., and Gan, T.-H. (2017). A pattern recognition approach to acoustic emission data originating from fatigue of wind turbine blades. 17(11).

[Tomor and Verstrynge, 2013] Tomor, A. and Verstrynge, E. (2013). A joint fatigue–creep deterioration model for masonry with acoustic emission based damage assessment. 43:575–588.

[Traore et al., 2017] Traore, O. I., Favretto-Cristini, N., Pantera, L., Cristini, P., Viguier-Pla, S., and Vieu, P. (2017). Which methods and strategies to cope with noise complexity for an effective interpretation of acoustic emission signals in noisy nuclear environment? 103(6):903–916.

[Van der Pluijm, 1997] Van der Pluijm, R. (1997). Non-linear behaviour of masonry under tension. 42.

[van Mier and van Vliet, 2002] van Mier, J. G. M. and van Vliet, M. R. A. (2002). Uniaxial tension test for the determination of fracture parameters of concrete: state of the art. 69(2):235–247.

[Vanin et al., 2017] Vanin, F., Zaganelli, D., Penna, A., and Beyer, K. (2017). Estimates for the stiffness, strength and drift capacity of stone masonry walls based on 123 quasi-static cyclic tests reported in the literature. 15(12):5435–5479.

[Vasarhelyi, 2003] Vasarhelyi, B. (2003). Some observations regarding the strength and deformability of sandstones in dry and saturated conditions. 62:245–249.

[Vasarhelyi and Davarpanah, 2018] Vasarhelyi, B. and Davarpanah, S. M. (2018). Influence of water content on the mechanical parameters of the intact rock and rock mass.

[Venzal, 2020] Venzal, V. (2020). Modélisation discrète du comportement mécanique des ouvrages maçonnés en pierre. aspects expérimentaux - analyse énergétique.

[Venzal et al., 2020] Venzal, V., Morel, S., Parent, T., and Dubois, F. (2020). Frictional cohesive zone model for quasi-brittle fracture: Mixed-mode and coupling between cohesive and frictional behaviors. 198:17–30.

[Weydert and Gehlen, 1999] Weydert, R. and Gehlen, C. (1999). ELECTROLYTIC RESISTIVITY OF COVER CONRETE: RELEVANCE, MEASUREMENT AND INTERPRETATION. page 11.

[Zhang et al., 2012] Zhang, F., Xie, S. Y., Hu, D. W., Shao, J. F., and Gatmiri, B. (2012). Effect of water content and structural anisotropy on mechanical property of claystone. 69:79–86.